THERMAL PERFORMANCE OF A FLAT-PLATE SOLAR COLLECTOR USING AQUEOUS COLLOIDAL DISPERSIONS OF CARBON-BASED NANOSTRUCTURES

WAIL SAMI WADEE SARSAM

FACULTY OF ENGINEERING
UNIVERSITY OF MALAYA
KUALA LUMPUR

2017

THERMAL PERFORMANCE OF A FLAT-PLATE SOLAR COLLECTOR USING AQUEOUS COLLOIDAL DISPERSIONS OF CARBON-BASED NANOSTRUCTURES

WAIL SAMI WADEE SARSAM

THESIS SUBMITTED IN FULFILMENT OF THE
REQUIREMENTS FOR THE DEGREE OF
DOCTOR OF PHILOSOPHY

FACULTY OF ENGINEERING
UNIVERSITY OF MALAYA
KUALA LUMPUR

2017

UNIVERSITY OF MALAYA

ORIGINAL LITERARY WORK DECLARATION

Name of Candidate: **Wail Sami Wadee Sarsam**

Registration/Matric No.: **KHA130002**

Name of Degree: **Doctor of Philosophy**

Title of Thesis: **Thermal performance of a flat-plate solar collector using aqueous colloidal dispersions of carbon-based nanostructures**

Field of Study: **Energy**

I do solemnly and sincerely declare that:

(1) I am the sole author/writer of this Work;
(2) This Work is original;
(3) Any use of any work in which copyright exists was done by way of fair dealing and for permitted purposes and any excerpt or extract from, or reference to or reproduction of any copyright work has been disclosed expressly and sufficiently and the title of the Work and its authorship have been acknowledged in this Work;
(4) I do not have any actual knowledge nor do I ought reasonably to know that the making of this Work constitutes an infringement of any copyright work;
(5) I hereby assign all and every rights in the copyright to this Work to the University of Malaya ("UM"), who henceforth shall be owner of the copyright in this Work and that any reproduction or use in any form or by any means whatsoever is prohibited without the written consent of UM having been first had and obtained;
(6) I am fully aware that if in the course of making this Work I have infringed any copyright whether intentionally or otherwise, I may be subject to legal action or any other action as may be determined by UM.

Candidate's Signature Date

Subscribed and solemnly declared before,

Witness's Signature Date

Name:

Designation:

ABSTRACT

The effects of using aqueous nanofluids containing functionalized carbon-based nanostructures as novel working fluids on the thermal performance of flat-plate solar collectors (FPSCs) have been investigated. The nanomaterials used were graphene nanoplatelets (GNPs) with specific surface areas (SSAs) of 300, 500, and 750 m^2/g; and multi-walled carbon nanotubes (MWCNTs) with outside diameters of (< 8 nm) and (20–30 nm). Water-based nanofluids with weight concentrations of 0.025%, 0.05%, 0.075%, and 0.1% were prepared. The thermophysical properties and colloidal stability of the nanofluids were investigated. To study the thermal performance of nanofluid-based FPSCs, an experimental setup was designed and built; and a MATLAB code was developed. Test runs were performed using inlet fluid temperatures of 30, 40, and 50 °C; flow rates of 0.6, 1.0, and 1.4 kg/min; and heat flux intensities of 600, 800, and 1000 W/m^2.

Higher colloidal stability was obtained at 60-min ultrasonication time. Nanofluids containing pristine nanomaterials were unstable. Non-covalent functionalization with surfactants improved the colloidal stability but created excessive foam. Triethanolamine-treated GNPs (TEA-GNPs) and β-Alanine-treated MWCNTs (Ala-MWCNTs) were synthesized as covalently-functionalized nanomaterials. The success of functionalization processes was confirmed through different characterization methods. Stability was found reliant on nanomaterial type, SSA, and weight concentration; and it increased up to relative concentrations of 0.876 and 0.955 for TEA-GNPs and Ala-MWCNTs, respectively.

The thermal conductivity, viscosity, and density of nanofluids increased, while the specific heat decreased as weight concentration increased. The temperature was directly proportional to the thermal conductivity and inversely proportional to the viscosity, density, and specific heat. The increase in SSA produced noticeable increase in the

thermal conductivity, up to 22.91% for 0.1-wt% TEA-GNPs 750. The measured thermal conductivity showed good agreement with the models of Chu et al. (2012a) for TEA-GNPs and Nan et al. (1997) for Ala-MWCNTs. For TEA-GNPs and Ala-MWCNTs, the highest increment in nanofluid viscosity was 25.69%. Since the classical viscosity models underestimated the measured values, a correlation was developed which revealed good agreement.

The FPSC's efficiency increased as the flow rate and heat flux intensity increased, and decreased as inlet fluid temperature increased. For nanofluid-based FPSC, the measured values of absorber plate temperature (AP) and tube wall temperature (TW) decreased down to 3.35% and 3.51%, respectively, with the increase in weight concentration and SSA, while the efficiency increased up to 10.53% for 0.1-wt% TEA-GNPs 750, in comparison with water. The experimental values of AP, TW, and efficiency for water very well matched the MATLAB code with maximum differences of 3.02%, 3.19%, and 3.26%, respectively. While for nanofluids, higher differences were found, up to 4.74%, 4.7%, and 13.47% for TEA-GNPs 750, respectively. The MATLAB code was considered appropriate for simulating nanofluid-based FPSCs with acceptable accuracy. Values of performance index were all > 1, and increased as weight concentration increased up to 1.104 for 0.1-wt% TEA-GNPs 750, implying higher positive effects on efficiency than negative effects on pressure drop. Accordingly, the investigated nanofluids can efficiently be used in FPSCs for enhanced energy efficiency, and the 0.1-wt% water-based TEA-GNPs 750 nanofluid was comparatively the superior one.

ABSTRAK

Kesan penggunaan cecair nano akueus yang mengandungi functionalized struktur nano berasaskan karbon sebagai cecair pemindahan haba pada prestasi haba pengumpul suria plat rata (FPSCs) telah disiasat. Bahan nano yang digunakan adalah nanoplatelet graphene (GNPs) dengan kawasan permukaan tertentu (SSA) 300, 500, dan 750 m^2/g; dan tiub nano karbon pelbagai dinding (MWCNTs) dengan diameter luar (< 8 nm) dan (20–30 nm). Cecair nano berasaskan air dengan kepekatan berat 0.025%, 0.05%, 0.075%, dan 0.1% telah disediakan. Sifat termofizikal dan kestabilan koloid untuk cecair nano telah disiasat dengan teliti. Bagi mengkaji prestasi haba FPSCs berasaskan cecair nano, persediaan eksperimen telah direka dan dibina; dan kod MATLAB telah dibangunkan. Experimen telah dilakukan dengan menggunakan suhu cecair masuk 30, 40, dan 50 °C; kadar aliran 0.6, 1.0, dan 1.4 kg/min dan keamatan fluks haba 600, 800, dan 1000 W/m^2.

Kestabilan koloid lebih tinggi telah diperolehi pada 60-min masa ultrasonikasi. Cecair nano mengandungi bahan nano pristine tidak stabil. Functionalization bukan kovalen dengan surfaktan meningkatkan kestabilan koloid tetapi mencipta buih yang berlebihan. GNPs dirawat triethanolamine (TEA-GNPs) dan MWCNTs dirawat β-Alanine (Ala-MWCNTs) telah disintesis sebagai kovalen-functionalized bahan nano. Proses functionalization disahkan berjaya melalui kaedah pencirian yang berbeza. Kestabilan adalah bergantung kepada jenis bahan nano, SSA, dan kepekatan berat badan; dan meningkat sehingga kepekatan relatif 0.876 untuk TEA-GNPs dan 0.955 untuk Ala-MWCNTs, masing-masing.

Keberaliran haba, kelikatan dan ketumpatan cecair nano meningkat, manakala haba khusus menurun apabila kepekatan berat badan meningkat. Suhu adalah berkadar terus dengan keberaliran haba dan berkadar tidak langsung kepada kelikatan, ketumpatan, dan haba khusus. Peningkatan SSA menyebabkan peningkatan ketara

dalam keberaliran haba, sehingga 22.91% bagi 0.1% berat TEA-GNPs 750. Keberaliran haba diukur menunjukkan perbandingan yang baik dengan model Chu et al. (2012a) untuk TEA-GNPs dan Nan et al. (1997) untuk Ala-MWCNTs. Bagi TEA-GNPs dan Ala-MWCNTs, kenaikan paling tinggi dalam kelikatan cecair nano adalah 25.69%. Sejak model kelikatan klasik telah mempunyai kelemahan pada nilai diukur, korelasi yang telah dibangunkan menunjukkan perbandingan yang baik.

Kecekapan FPSCs meningkat apabila kadar aliran dan keamatan fluks haba meningkat, dan menurun apabila suhu cecair masuk meningkat. Bagi FPSCs berasaskan cecair nano, nilai diukur pada suhu plat penyerap (AP) dan suhu dinding tiub (TW) menurun kepada 3.35% dan 3.51%, masing-masing, apabila kepekatan berat badan dan SSA meningkat, manakala kecekapan meningkat sehingga 10.53% bagi 0.1% berat TEA-GNPs 750 jika dibandingkan dengan air. Nilai eksperimen untuk AP, TW, dan kecekapan untuk air dipadankan dengan baik pada kod MATLAB dengan perbezaan maksima 3.02%, 3.19%, dan 3.26%, masing-masing. Manakala bagi cecair nano, perbezaan yang lebih tinggi ditemui, sehingga 4.74%, 4.7%, dan 13.47% bagi TEA-GNPs 750, masing-masing. Kod MATLAB dianggap sesuai untuk simulasi FPSCs berasaskan cecair nano dengan ketepatan yang boleh diterima. Semua nilai indeks prestasi adalah > 1, dan peningkatan kepekatan berat badan meningkat sehingga 1.104 untuk 0.1% berat TEA-GNPs 750, menyifatkan kesan positif yang lebih tinggi kepada kecekapan daripada kesan negatif kepada kejatuhan tekanan. Oleh itu, cecair nano yang disiasat boleh digunakan dalam FPSCs untuk mempertingkatkan kecekapan tenaga, dan 0.1% berat cecair nano TEA-GNPs 750 berasaskan air adalah secara perbandingan yang unggul.

ACKNOWLEDGEMENTS

First and foremost, I would like to express my heartfelt thanks and gratitude to God for his blessings throughout my life and for giving me this opportunity to successfully complete my Ph.D. degree.

Utmost and heartiest words of thanks should go to my mother, my wife, my daughter Merna, my son Fady, and my sisters for giving me strong motivation through their endless love, support, and continuous encouragement to achieve the best in my life. Honestly, my efforts would not be meaningful without your existence in my life. I also want to dedicate this work to the soul of my father; I hope he was with me in this special day.

I wish to express deep gratitude and appreciation to my supervisors Dr. Kazi Md. Salim Newaz and Dr. Ahmad Badarudin Bin Mohamad Badry for valuable suggestions, constructive discussions, support, and encouragement during my Ph.D. candidature at University of Malaya. I would also like to thank all my relatives, friends, and colleagues for their support, cooperation, and encouragement. This would be incomplete without my gratitude to the all of the faculty and staff in the Department of Mechanical Engineering at University of Malaya.

Finally, thanks are also presented to Ministry of Higher Education and Scientific Research, Iraq for funding my Ph.D. study through a scholarship and University of Malaya, Malaysia for providing the laboratory facilities and financial support for the experimental work to conduct this study.

TABLE OF CONTENTS

LIST OF FIGURES

LIST OF TABLES

LIST OF SYMBOLS AND ABBREVIATIONS

A	:	Area (m^2)
Al_2O_3	:	Aluminum oxide
Ala-MWCNTs	:	Covalently functionalized multi-walled carbon nanotubes with beta-alanine (β-Alanine)
$AlCl_3$	:	Aluminum chloride
AM	:	Air mass coefficient
AP	:	Surface temperature of the absorber plate (°C)
a.u.	:	Arbitrary unit
a_X	:	Dimension of the nanoparticle along the transverse axis (nm)
a_Z	:	Dimension of the nanoparticle along the longitudinal axis (nm)
C_b	:	Bond conductance (W/m K)
CNT	:	Carbon nanotube
C_p	:	Specific heat (J/kg K)
CTAB	:	Cetyl trimethylammonium bromide
CuO	:	Cooper oxide
Cv	:	Valve flow coefficient
d	:	Diameter of tube (m)
DASC	:	Direct absorption solar collector
DLS	:	Dynamic Light Scattering
DMA	:	N,N-dimethylacetamide
DMF	:	N,N-dimethylformamide
DPT	:	Differential pressure transmitter
DSC	:	Differential scanning calorimetry
DW	:	Distilled water
DWCNT	:	Double-walled carbon nanotube
EDS	:	Energy dispersive X-ray spectroscopy
EG	:	Ethylene glycol
ELS	:	Electrophoretic light scattering
f	:	Darcy-Weisbach friction factor
FEP	:	Fluorinated ethylene propylene
FPSC	:	Flat-plate solar collector
F_R	:	Solar collector heat removal factor
FWCNT	:	Few-walled carbon nanotube
GA	:	Gum Arabic

GNP : Graphene nanoplatelet
G_T : Incident solar radiation (W/m^2)
h_i : Convective heat transfer coefficient inside riser tube (W/m^2 K)
h_l : Total head loss across the FPSC (m)
HCl : Hydrochloric acid
HW : Hottel-whillier
HWB : Hottel-whillier-bliss
i : Enthalpy (kJ⁄kg)
$\tilde{I}$: Alternating current (A)
p : Aspect ratio of the nanoparticle
K : Thermal conductivity (W/m K)
K_L : Minor loss factor
K_s : Thermal conductivity of the interfacial boundary layer (W/m K)
K_{11}^{C} , K_{33}^{C} : Parameters defined by equation (2.17)
K_X^{eff} , K_Z^{eff} : Parameters defined by equation (2.21)
L : Length (m)
L_h : Hydrodynamic entry length (m)
L_{11} , L_{33} : Parameters defined by equations (2.13) and (2.15), respectively
MgO : Magnesium oxide
$\dot{m}$: Mass flow rate of fluid (kg/s)
MWCNT : Multi-walled carbon nanotube
n : Number of rise tubes in the FPSC
$NaNO_2$: Sodium nitrite
NPT : National pipe thread
P : Pressure (Pa)
PDI : Polydispersity index
PEG : Polyethylene glycol
PI Performance index
PP : Polypropylene
PV : Photovoltaic
q : Heat transfer rate per unit length (W/m)
Q_u : Useful energy of solar collector (W)
Q : Heat transfer rate (W)
R : Reflectance of solar energy
RTD : Resistance temperature detector
S : Absorbed solar radiation per unit area (W/m^2)

SDBS	:	Sodium dodecyl benzene sulfonate
SDS	:	Sodium dodecyl sulfate
SiO_2	:	Silicon dioxide
SSA	:	Specific surface area (m^2/g)
SWCNT	:	Single-walled carbon nanotube
T	:	Temperature (°C)
TEA-GNPs	:	Covalently functionalized graphene nanoplatelets with triethanolamine
TEM	:	Transmission electron microscopy
thk	:	Thickness (m)
TiO_2	:	Titanium dioxide
$(T_i - T_a)/G_T$	:	Reduced temperature parameter (m^2 K/W)
TW	:	Outside wall temperature of the riser tube (°C)
U_L	:	Solar collector overall heat loss coefficient (W/m^2 K)
UV-vis	:	Ultraviolet-visible spectrophotometry spectral analysis
V	:	Velocity of heat transfer fluid (m/s)
$\widetilde{V}$	:	Alternating voltage (V)
W	:	Width (m)
x	:	Length along direction of fluid flow
x/d	:	Dimensionless axial distance
ZnO	:	Zinc oxide

Special characters

α	:	Absorptance of solar energy
β	:	Reduced saturation pressure defined by equation (3.45)
β_{11} , β_{33}	:	Parameters defined by equation (2.16)
χ	:	Reduced volume defined by equation (3.47)
Δ	:	Difference
ε	:	Emittance, reduced enthalpy defined by equation (3.48)
ϕ_m	:	Weight concentration of particles in the base fluid
ϕ_v	:	Volume fraction of particles in the base fluid
γ	:	A dimensionless parameter defined by equation (2.18)
η_c	:	Energy efficiency of flat-plate solar collector
φ	:	Tilt angel of the FPSC (degree)
ρ	:	Density of fluid (kg/m^3)
σ	:	Stefan Boltzmann constant
τ	:	Transmittance of solar energy

μ : Viscosity (Pa.s)
ν : Specific volume (m^3/kg)
θ : The reduced temperature defined by equation (3.46)
ω : Uncertainty
ψ : Sphericity of particle

Subscripts
a : Ambient air
ap : Absorber plate of the FPSC
b : Bottom
bf : Base fluid
c : Collector
e : Edge
f : Fluid
g : Glass cover
i : Inner or inside
in : Inlet fluid
ins : Insulation
nf : Nanofluid
np : Nanoparticles
o : Outer or outside
out : Outlet fluid
p : Particles
rt : Riser tube of the FPSC
X : Transverse axis of the nanoparticle
Z : Longitudinal axis of the nanoparticle

CHAPTER 1: INTRODUCTION

1.1 Background

With the continuing increase in the world's population and the expansion of modernization, the worldwide demand for energy doubled in the first half of the twenty-first century, and it is expected to be tripled before the end of this century. Unfortunately, the reserves of fossil fuels are not vast or renewable; the supply is constrained. Renewable energy technologies are those technologies that can be used to produce energy from direct and indirect effects on the Earth from the sun's energy (e.g., solar energy, wind, and water falls), gravity effects (ebb and flow), and the high temperature of the Earth's center (geothermal). A future blend that incorporates renewable energy sources will help people thrive and ensure their wellbeing. Continuous escalation of the cost of generating energy is preceded by the fact of scary depletion of the energy reserve of the fossil fuels and pollution of the environment as developed and developing countries burn these fuels. To meet the challenge of the impending energy crisis, renewable energy has been growing rapidly in the last decade and becoming an influential part of energy production.

Based on the desirable environmental and safety features of solar energy, it is generally accepted that it can be used to a greater extent with the least environmental effects than other sources of renewable energy (Kalogirou, 2009; Foster et al., 2010; Otanicar et al., 2010; V. Verma & Kundan, 2013). In both the direct and indirect forms, solar energy is the best available source of renewable energy. If around 0.1% of energy emitted by the Sun is harvested with a conversion efficiency of 10%, it could generate about four times the total current generating capacity of the whole world (Thirugnanasambandam et al., 2010). Methods for collecting solar energy can basically be categorized as photovoltaic systems (PV) and thermal systems. Thermal systems convert solar energy to thermal energy while PV systems transform solar energy to electric energy. Whereas thermal systems can absorb over 95% of the incoming solar radiation, PV systems are restricted by their limited wavelengths range. Figure 1.1 presents the effective working wavelengths for both types of solar systems at air mass coefficient (AM) of 1.5. From which, it can be concluded that the solar thermal systems can utilize a higher percentage of the incoming solar radiation than the photovoltaic systems (R. Taylor, 2011). Therefore, the focus of this research is limited to the thermal type of solar collectors for the effective capture of solar energy.

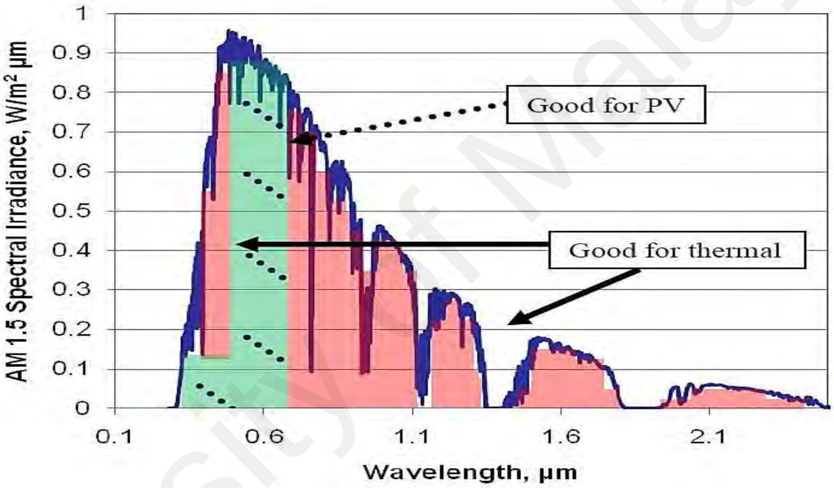

Figure 1.1: Working wavelengths for PV and thermal systems (R. Taylor, 2011).

Solar thermal collectors are a special type of heat exchangers that convert solar radiation energy to thermal energy. Numerous types of solar thermal collectors have been used to collect solar energy, as presented in Table 1.1. The flat-plate solar collector (FPSC) is the most common type and converts solar energy to thermal energy using a solid surface called an "absorber plate" (Okujagu & Adjepong, 1989; Kalogirou, 2009; Mahian et al., 2013a). The surface of the absorber plate is usually covered with matte black paint or spectrally selective coating to achieve high absorptivity of the solar spectrum with low emissivity (Bogaerts & Lampert, 1983; Duffie & Beckman, 2013). The received solar radiation is absorbed by the collector's absorber plate as heat energy and transferred to the heat transfer medium that is flowing through the collector's tubes. Figure 1.2 shows a schematic drawing of a standard FPSC (Camel-solar, 2012). Another type of flat solar collector is the direct absorption solar collector (DASC), in which the working fluid is used as the absorbing medium for solar radiation instead of limiting the absorption to the absorber plate (Otanicar, 2009; Lenert & Wang, 2012). In the DASC, the heat transfer fluid flows between the bottom wall and the glass cover at the top, as shown in Figure 1.3. The first type of solar collectors, i.e., the FPSC, will be investigated in this study.

Table 1.1: Types of solar thermal collectors (Kalogirou, 2009).

Motion	Collector Type	Absorber Type	Concentration Ratio	Operating Temperature (°C)
Stationary	Flat-plate solar collector (FPSC)	Flat	1	30–80
	Evacuated tube solar collector	Flat	1	50–200
	Compound parabolic solar collector	Tubular	1–5	60–240
Single-axis tracking			5–15	60–300
	Linear Fresnel reflector	Tubular	10–40	60–250
	Cylindrical trough collector	Tubular	15–50	60–300
	Parabolic trough collector	Tubular	10–85	60–400
Two-axis tracking	Parabolic dish reflector	Point	600–2000	100–1500
	Heliostat field collector	Point	300–1500	150–2000

Note: Concentration ratio is defined as the aperture area divided by the receiver or absorber area of the collector.

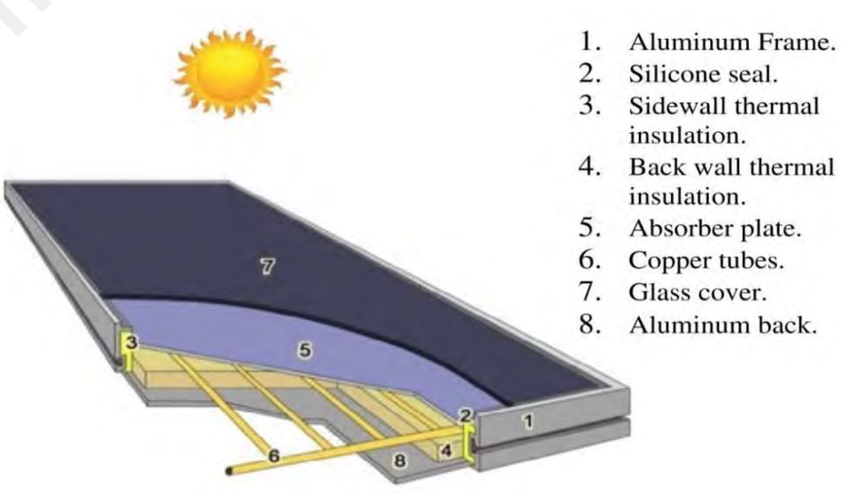

Figure 1.2: Schematic drawing of a FPSC (Camel-solar, 2012).

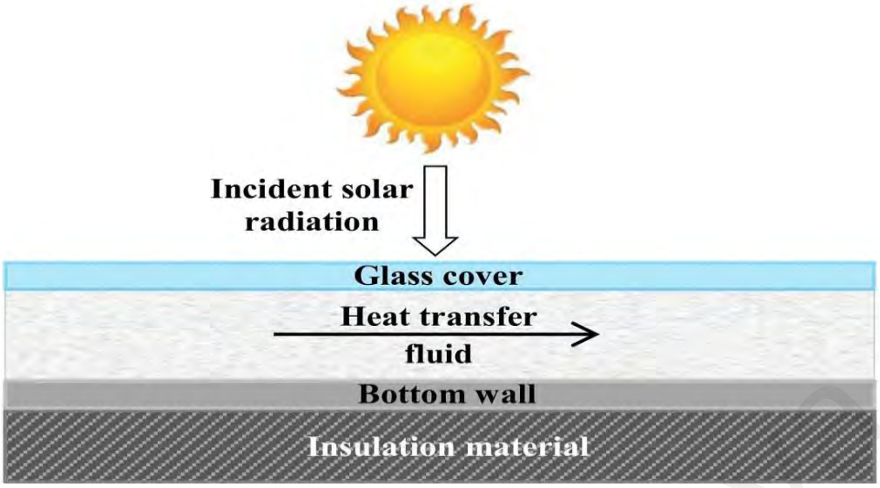

Figure 1.3: Schematic drawing of a direct absorption solar collector (DASC).

1.2 Flat-plate solar collectors (FPSCs)

The reasons for the preference of FPSCs in comparison with other solar thermal collectors are relatively low manufacturing cost, ability of collecting both beam and diffuse radiation, and needless for any sun's tracking system. The major fraction of the incident solar radiation passing through the FPSC's transparent cover is absorbed by the absorber plate. The bottom and sides of the collector's absorber plate are fully insulated to minimize heat losses by conduction and natural convection. The collector's glass cover diminishes heat losses by convection via containment of an air layer and by radiation in that it is transparent to the sun's shortwave solar radiation (greenhouse effect) but practically non-transparent to the long-wave thermal radiation emitted by the absorber plate (Kalogirou, 2009). The tubes through which the working fluid is flowing along the collector, i.e., riser tubes, can either be an implicit part of the absorber plate or welded to it. At both ends of the collector, the riser tubes are connected to the larger-diameter header tubes.

Enhancement of the FPSC's efficiency has been achieved by using several methods such as using different coatings for the absorber plate (T. N. Anderson et al., 2010; Oliva et al., 2013), varying the flow rate (Z. Chen et al., 2012), and considering different configurations and tilt angles for the FPSC (Xiaowu & Ben, 2005; Ho & Chen, 2006; Akhtar & Mullick, 2007; Skeiker, 2009; A. J. N. Khalifa & Abdul Jabbar, 2010; Bisen et al., 2011; Martín et al., 2011; Bakari et al., 2014). However, a simple and novel approach to increase the thermal efficiency of new and existing FPSCs is the use of aqueous colloidal dispersions of nanometer-sized high-thermally conductive particles, called “nanofluids” (S. U. S. Choi & Eastman, 1995), instead of the conventional heat transfer fluids to boost the rate of heat transfer from the collector’s absorber plate (Xiaowu & Ben, 2005; Wenhua Yu et al., 2008; Khullar & Tyagi, 2010; Abdin et al., 2013; Javadi et al., 2013; Mahian et al., 2013a).

1.3 Problem statement

Water and ethylene glycol are common working fluids in FPSCs and various engineering processes. Nevertheless, because of the comparatively low thermal conductivity of these heat transfer fluids, they cannot attain high rates of heat transfer in thermal applications. Through developing heat transfer fluids with enhanced heat transfer properties, mechanical equipment having higher efficiency and compactness can be designed with the resulting savings in cost.

This study aims to investigate, theoretically and experimentally, the thermal performance of a FPSC using aqueous colloidal dispersions of carbon-based nanostructures as alternative novel working fluids. The investigation will be performed at different inlet fluid temperatures, heat flux intensities, and mass flow rates using distilled water and several water-based nanofluids containing functionalized carbon-based nanostructures with different weight concentrations.

1.4 Objectives of the research

The objectives are summarized as follows:

1. To study the various parameters affecting the long-term colloidal stability of the synthesized nanofluids (such as ultrasonication time; type, weight concentration, and specific surface area (SSA) of the nanomaterial; and functionalization method) and the methods for evaluating (such as UV-visible spectrophotometry and measurement of zeta potential) and enhancing it (such as ultrasonic vibration and covalent and non-covalent functionalization of the nanomaterials).

2. To investigate the thermophysical properties of the nanofluids prepared by dispersing several types and weight concentrations of carbon-based nanostructures in distilled water. In addition, to compare the available models/correlations with the measured values of thermophysical properties in order to select the most reliable and accurate model/correlation.

3. To design and build an experimental test rig for studying the effects of using aqueous colloidal dispersions of various carbon-based nanostructures as working fluids on the thermal performance of a FPSC. Furthermore, to conduct test runs at different mass flow rates, inlet fluid temperatures, heat flux intensities, and weight concentrations of the nanomaterials in the base fluid.

4. To develop a mathematical model based on the basic conservation laws, which will be solved by a numerical calculation algorithm implemented by a MATLAB code for simulating nanofluid-based FPSC during steady-state operation. Then, to compare the experimental and simulated results for distilled water and water-based nanofluids to validate the collected data.

1.5 Outline of the thesis

This thesis consists of five chapters. “Chapter 1” is the “Introduction” that provides background about the areas of this study, highlights the current problems that motivated this research, and clarifies the objectives through which the aim of this study can be reached. “Chapter 2” is the “Literature Review” which comprehensively surveys the previous published work related to the field of study which can be categorized as: description and component parts of a FPSC; preparation procedures of nanomaterials and nanofluids, evaluation and enhancement of colloidal stability, and thermophysical properties of nanofluids; and thermal performance of nanofluid-based FPSCs. “Chapter 3” is the “Methodology” which concerns about the materials, devices, and methods used in this study for the preparation, characterization, measurement of thermophysical properties, and evaluation of colloidal stability of the nanofluids. Furthermore, the experimental test setup that is built and used for investigating the performance of nanofluid-based FPSC is fully described and presented. In addition, the mathematical model and the structure of the developed MATLAB code for simulating the nanofluid-based FPSC are thoroughly described. “Chapter 4” is the “Results and Discussion” which lists, compares, and discusses the data obtained from different sources in this study such as water run versus nanofluid, experimental data versus correlated or analytical data, and the MATLAB code results versus experimental data. All the data are presented in the form of tables and/or figures. Finally, “Chapter 5” is the “Conclusions and Recommendations” in which the important outcomes of this study are briefly summarized with some recommendations for future work in this research field.

CHAPTER 2: LITERATURE REVIEW

2.1 Introduction

Increasing the heat transfer rate from the absorber plate of any FPSC to the working fluid and from the fluid to the end user can effectively enhance the thermal performance. Accordingly, the use of nanofluid instead of conventional working fluid can boost the energy efficiency of a FPSC due to improved thermal properties of the working fluids. However, there are some important considerations that should be given considerable attention for the efficient use of a nanofluid as the heat transfer fluid in FPSCs. The first consideration should be the synthesis of the nanofluid. Since suspending solid nanoparticles in the base fluid will not result in a simple mixture, the stability of nanofluid should be investigated thoroughly (Pantzali et al., 2009a; Saidur et al., 2011; Behi & Mirmohammadi, 2012; Hordy et al., 2014). Due to the high ratio of surface area to volume, the nanoparticles would have a tendency to aggregate over time because of high surface tension between them (A. K. Gupta & Gupta, 2005; Y. Li et al., 2009; Chaji et al., 2013; Solangi et al., 2015). Such agglomeration of the nanoparticles might cause them to settle and block the flow channels, and it also could decrease the thermal conductivity of the nanofluid. Consequently, for successful application of nanofluids, it is essential to investigate the main factors that could affect the dispersion stability of the nanofluids (J. Lee & Mudawar, 2007; Y. Li et al., 2009; Wei Yu & Xie, 2012). The second point to be considered is the cost of the nanofluids, which is relatively high due to the complications in the manufacturing process of nanoparticles (J. Lee & Mudawar, 2007; Pantzali et al., 2009a; Saidur et al., 2011). Therefore, the lowest possible concentration of nanoparticles that relatively have high thermal conductivity should be used to synthesize a nanofluid with comparatively high thermal conductivity and heat transfer coefficient. This approach is important because it is known that nanofluids with lower concentrations of dispersed nanoparticles have higher stability (Behi & Mirmohammadi, 2012). Moreover, the use of a lower concentration of nanoparticles leads to the third point that must be considered, i.e., the viscosity of the nanofluid and its effect on pressure drop and pumping power. Nanofluids with higher concentrations of nanoparticles will have higher viscosities (J. Li et al., 2002; Nguyen et al., 2007; Wei Yu et al., 2011). The pressure drop associated with any flowing fluid is one of the essential factors that must be considered in evaluating its suitability for application (Saidur et al., 2011). The increase in the viscosity of the nanofluid over that of the base fluid will cause an increased pressure drop, which is closely related to the required pumping power (Duangthongsuk & Wongwises, 2010; Razi et al., 2011; Kole & Dey, 2013; Mahian et al., 2013a). This is considered to be one of the disadvantages of using nanofluids as the working fluid. Based on the aforementioned considerations, this chapter will survey the methods for the preparation of nanofluids and the techniques for the evaluation and enhancement of the colloidal stability for nanofluids in addition to their thermophysical properties. Furthermore, the previously published works in the field of nanofluid-based FPSCs will be thoroughly reviewed. Furthermore, the main components of FPSCs will be described and presented in the following sections.

2.2 Components of a FPSC

A brief description of the main components of a typical FPSC along with their functions and materials used for manufacturing will be presented and clarified in the following sections.

2.2.1 Transparent cover

Most flat-plate collectors incorporate at least one transparent cover made of glass or plastic. The cover protects the absorber and reduces the energy lost from the upper surface of the FPSC. The collector's cover diminishes heat losses by convection via containment of an air layer and by radiation in that it should exhibit a high transmittance for solar radiation (wavelengths 0.3 to 2.5 μm) in order to maximize the solar input to the absorber, and intercept the thermal radiation of wavelengths greater than about (3 μm), which is emitted by the hot absorber plate. FPSC's covers essentially perform similar functions to those of glass in a greenhouse (Gillett & Moon, 1985; Kalogirou, 2009). Therefore, optical properties of the cover plate are of considerable importance in collector design (Ting, 1980).

The main features of the transparent cover are; absorptance of solar energy (α_g), which is the absorbed portion of incident solar radiation; reflectance of solar energy (R_g), which is the reflected portion of incident solar radiation; and the transmittance of solar energy (τ_g), which is the transmitted portion of incident solar radiation. For higher FPSC's efficiency, the values of the absorptance and reflectance should be the least possible and transmittance's values should be the highest possible. The absorptance (α_g), reflectance (R_g), and transmittance (τ_g) of solar energy for the transparent cover can be linked according to the conservation of energy law as follows (Duffie & Beckman, 2013);

$$\propto_g + R_g + \tau_g = 1 \tag{2.1}$$

The most widely used material for the FPSC's cover is glass, which may be attributed to its high transmittance, around 90% of the incoming solar radiation, and high opaqueness for solar radiation emitted by the FPSC's absorber plate. The main disadvantages of glass are that it is brittle, relatively expensive, and has a high density (Gillett & Moon, 1985; Amrutkar et al., 2012).

The effect of glass cover thickness on the performance of a FPSC was experimentally investigated by Bakari et al. (2014). Four different thicknesses of glass, i.e., 3, 4, 5, and 6 mm, were used as the transparent cover for the four 0.72−m^2 FPSCs that were constructed. Results proved that varying the thickness of the glass cover affected the collector’s efficiency, and the highest efficiency was reached using the 4−mm glass thickness. Kalogirou (2009) indicated that for a spacing between the glass cover and the absorber plate in the range of 15–40 mm, the convective heat loss in the FPSC is almost independent of spacing. Consequently, a 4−mm glass with 15−mm spacing was selected as the transparent cover of the FPSC used in the experimental setup of this research.

2.2.2 Absorber plate and riser tubes

The main purpose of the absorber plate is to absorb the highest possible of the solar radiation transmitting through the transparent cover of the FPSC, to waste the lowest possible heat losses, and to transfer the collected energy to the flowing heat transfer fluid in the riser tubes (Amrutkar et al., 2012; Duffie & Beckman, 2013). An absorber plate may be made from any of a wide range of materials, or in some cases from more than one material. Copper, stainless steel, mild steel, aluminum and plastics are all used (Gillett & Moon, 1985; Kalogirou, 2009). The selection of the suitable material is dependent on many factors such as thermal conductivity, weight, cost, and availability (Amrutkar et al., 2012).

The nature and quality of the bond between the riser tubes and the absorber plate has a noticeable effect on the thermal performance of the FPSC. Better bond will provide improved heat transfer from the absorber plate to the riser tubes. Brazing, welding, press-fitting, or using high temperature solder can provide this bond. It is practically important to select a bonding system which can resist both high temperatures and temperature cycling (Gillett & Moon, 1985; Badran et al., 2008).

Using an electric resistance heater to emulate the energy input to the absorber plate from solar radiation, Badran et al. (2008) experimentally studied the bond conductance between the riser tube and absorber plate of five locally-made FPSC's samples. All the samples were enclosed with a 5-cm thick insulation to eliminate energy loss. Through evaluating the generated heat flux of the electric heater and the energy transferred to the working fluid, the bond conductance was calculated and found to be in the range of 6.3−1.8 W/m K. From all the samples tested, the one that was manufactured using the press-fit method showed the highest conductance value.

The FPSC used for performing the experimental test runs in the present study was built using a 2-mm copper absorber plate and 12.7-mm copper riser tubes. The absorber plate was solder bonded to the riser tubes all over the contact length.

2.2.3 Thermal insulation

The conduction heat losses from the edges and back side of the FPSC can be eliminated by applying insulation materials. An optimum thickness may be determined on the basis of cost and effectiveness. The three most important factors other than cost that should be considered when choosing insulation materials are their resistance to temperature, durability in the presence of moisture, and thermal conductivity. Common insulation materials are glass-wool, mineral-wool and polyurethane foam (Gillett & Moon, 1985).

2.3 Analysis of flat-plate solar collectors

The comprehensive analysis of FPSC is a complex problem. Luckily, a quite easy analysis has been presented by Duffie & Beckman (2013) with very useful results. The presented analysis has followed the basic derivation by Whillier (1953, 1977) (as cited in Duffie & Beckman (2013)) and Hottel & Whillier (1958). The model shows the important variables, how they are related, and how they affect the performance of a solar collector. To simplify the model without affecting its fundamental physical value, several assumptions were made. The resulting equation from the analysis, Equation (2.2), is known as the Hottel-Whillier (HW) or Hottel-Whillier-Bliss (HWB) equation (Kalogirou, 2009; Munich, 2013), which is the most commonly used equation for modeling the useful energy gain for FPSCs and consists of two terms, an energy gain term (term 1) and an energy loss term (term 2):

$$Q_u = A_c\, F_R\, S - A_c\, F_R\, U_L(T_{in} - T_a) \tag{2.2}$$

where, Q_u = useful energy gain (W)

A_c = collector aperture area (m^2)

F_R = collector heat removal factor

S = absorbed solar radiation per unit area (W/m^2)

U_L = collector overall heat loss coefficient (W/m^2 K)

T_{in} = inlet fluid temperature to the collector (K)

T_a = ambient air temperature (K)

The calculation of the solar energy absorbed by the FPSC's absorber plate (S) is important for predicting the performance of the FPSC. Using the transmittance-absorptance product, the absorbed solar radiation per unit area is defined as (Duffie & Beckman, 2013):

$$S = G_T\, (\tau_g\, \alpha_{ap}) \tag{2.3}$$

where, G_T = Incident solar radiation (W/m^2)

τ_g = transmittance of solar energy for the FPSC's glass cover

α_{ap} = absorptance of solar energy for the FPSC's absorber plate

Based on the inlet fluid temperature to the collector, the equation of HW is usually used for calculating the energy collected in FPSCs. However, this equation might possibly produce substantial errors due to the fact that it estimates no energy lost by convection heat transfer when the inlet fluid temperature to the FPSC is equal to that of the ambient air.

An improved model for the thermal output of a FPSC was developed by Munich (2013), which was based on using two methods for replacing the inlet fluid temperature of the collector in the HW equation. The first method was based on replacing the inlet fluid temperature with the collector average fluid temperature. While the second method used the log mean temperature difference for the heat transfer fluid in the collector instead of the inlet fluid temperature. Results obtained using these two methods were found to be comparable to the original HW equation, but not necessarily better.

Numerical and experimental investigation of the thermal performance of a FPSC was carried out by Ong (1974). For the numerical part of the work, a finite-difference method was used, while an experimental FPSC was used to perform the tests. During the main insolation period, satisfactory agreement was obtained between the experimental and theoretical results. Due to the incorrect predictions of the mean temperature of different system parts, some faults in the theory were found during the early and late periods of the day.

Ong (1976) had modified and improved his previous theoretical model for evaluation of the thermal performance of a FPSC system. The model considered the entire system to be broken up into a finite number of sections, each section having a uniform mean temperature. Energy balance was made over each section and finite difference equations were written to enable the evaluation of the mean section temperature. Good agreement was obtained during the main part of the day between the theoretical and experimental data.

A. J. N. Khalifa & Abdul Jabbar (2010) conducted an experimental comparison between the performance of a conventional domestic FPSC system and a modified solar collector with an integrated storage tank. The storage-type solar collector contained six series-connected 80–mm copper tubes acting as a storage tank and an absorber in the same time. The derivation of the HWB equation was used as the basis for deriving the modified equations for the storage-type solar collector. Good agreement was obtained between the experimental and theoretical data. Also, the storage-type solar collector system showed higher performance than the conventional one. Based on the aforementioned information, it can be concluded that HW model presented by Duffie & Beckman (2013) can give acceptable results for simulating the steady state operation of a FPSC, therefore, it will be used in the mathematical model of this study with some modifications.

Estimation of various heat losses in the FPSC is important for the evaluation of thermal performance, and top loss heat coefficient has a major contribution in the total heat losses in FPSCs. An analytical study to estimate the top loss heat coefficient of a FPSC was conducted by Bisen et al. (2011). The effects of ambient air temperature, absorber plate temperature, and wind heat transfer coefficient on the top loss heat coefficient were evaluated using MATLAB. Results showed that the top loss heat coefficient increased as the wind heat transfer coefficient and the temperatures of ambient air and absorber plate increased.

An experimental investigation of the value of top loss coefficient of a FPSC was performed by Bhatt et al. (2011) at different tilt angles. Even though energy is lost from the upper surface, bottom side, and edges of the FPSC, results proved that the collector's efficiency relies mainly on the energy lost from the upper surface. Furthermore, it was concluded that the top loss coefficient increases with the increase of the tilt angle and absorber plate temperature.

Sekhar et al. (2009) had evaluated, theoretically and experimentally, the top loss heat coefficient of a FPSC. A single glass cover FPSC was fabricated and used to run experiments under laboratory conditions. The effects of different parameters such as tilt angle, solar insolation, ambient air temperature, absorber plate temperature, type of fluid flow inside tubes, and emissivity of the glass cover and absorber plate on the top loss heat coefficient and collector's efficiency were considered. From all these parameters, the emissivity of the absorber plate showed the highest effect on the top loss coefficient while the tilt angle revealed insignificant effect. Results displayed that the collector's efficiency increased as the ambient temperature increased.

For a FPSC having an absorber plate with selectively and non-selectively coated surface, an empirical equation for calculating top heat loss coefficient (U_t) at different tilt angles was developed by Klein (1975). This equation was a modification of the empirical equation for Hottel & Woertz (1942) (as cited in Klein (1975)), which was suitable for absorber plates with nonselective coating only, and was given as follows;

$$U_t = \left(\frac{N}{\frac{CC}{T_{pm}}\left[\frac{\left(T_{pm}-T_a\right)}{(N+ff)}\right]^{0.33}} + \frac{1}{h_{wind}} \right)^{-1} + \frac{\sigma\left(T_{pm}+T_a\right)\left(T_{pm}^2+T_a^2\right)}{\frac{1}{\varepsilon_{ap}+0.005\,N\,\left(1-\varepsilon_p\right)} + \frac{2\,N+ff-1}{\varepsilon_g} - N} \tag{2.4}$$

where, N = number of glass covers

σ = Stefan Boltzmann constant = 5.67×10^{-8} W/m^2 K^4

$ff = (1 - 0.04\,h_{wind} + 0.04\,h_{wind}^2)(1 + 0.091\,N)$

$CC = 365.9\,(1 - 0.00883\,\varphi + 0.0001298\,\varphi^2)$

φ = collector tilt (deg)

ε_g = emittance of glass cover

ε_{ap} = emittance of absorber plate

T_{pm} = mean temperature of absorber plate (K)

h_{wind} = wind heat transfer coefficient (W/m^2 K)

Later, Klein (1979) (as cited in Duffie & Beckman (2013)) presented an improved equation for evaluating the top heat loss coefficient (U_t) of a FPSC following his previous work in 1975. For mean absorber plate temperatures ranging from ambient up to 200 °C, the new relationship estimated the top heat loss coefficient with an error of ±0.3 W/m^2 K (Duffie & Beckman, 2013).

$$U_t = \left(\frac{N}{\frac{CC}{T_{pm}} \left[\frac{(T_{pm} - T_a)}{(N + ff)} \right]^{ee}} + \frac{1}{h_{wind}} \right)^{-1} + \frac{\sigma (T_{pm} + T_a)(T_{pm}^2 + T_a^2)}{\frac{1}{\varepsilon_{ap} + 0.00591\, N\, h_{wind}} + \frac{2\,N + ff - 1 + 0.133\, \varepsilon_{ap}}{\varepsilon_g} - N} \tag{2.5}$$

where, $ff = (1 + 0.089\, h_{wind} - 0.1166\, h_{wind}\, \varepsilon_p)(1 + 0.07866\, N)$

$CC = 520\,(1 - 0.000051\, \varphi^2) \quad for \quad 0^o < \varphi < 70^o$

$ee = 0.430\,(1 - 100/T_{pm})$

T_{pm} = mean temperature of the absorber plate.

A numerical model for the thermal performance of a conventional FPSC with a black absorber plate was proposed by Khoukhi & Maruyama (2006). The model considered the glass cover as a media with absorption and emission. The top heat loss coefficient was calculated using the equation of Klein (1975). Results showed nearly a straight line profile for the efficiency curve when the prevailing heat transfer mode was the convection in comparison with the radiation one. It was concluded that Klein

(1975)'s equation could be used for calculating the top loss coefficient. From the abovementioned, it can be concluded that the empirical equation of Klein (1979) (as cited in Duffie & Beckman (2013)) can be used in the mathematical model of this study for calculating the top loss heat coefficient with reasonable accuracy.

ASHRAE extended the work of Hottel & Whillier (1958) to develop ASHRAE Standard 93 (2003). This standard provides a procedure for the indoor and outdoor testing of solar energy collectors and rating them in accordance with their thermal performance. Also, it carefully defined its applicability to both liquid-cooled non-concentrating and concentrating solar collectors, and collectors that use air as their working fluid. ASHRAE recommended performing the tests using a liquid flow rate value per unit area of 0.02 kg/s m^2 and tilting the solar collector at an angle between 30° and 60° for indoor testing. Accordingly, in this study, the collector was set at an angle of 30° and a fluid mass flow rate of 0.6 kg/min, which corresponds to 0.02 kg/s m^2, was used to perform the experiments in addition to another two mass flow rates of 1.0 and 1.4 kg/min.

2.4 Nanofluids and their preparation methods

An innovative idea for enhancing the thermal conductivity of common heat transfer fluids was to use ultrafine solid particles suspended in the base fluid (Ahuja, 1975a, 1975b; Sohn & Chen, 1981; Hetsroni & Rozenblit, 1994). Even though the utilization of particles with sizes in the range of millimeters or micrometers in suspensions in early studies indicated some enhancement of their thermal conductivity, there also were some negative effects such as the low stability of the suspensions that resulted in the blockage of flow channels. Unlike micrometer-sized particle suspensions, nanofluids (i.e., suspensions of nanometer-sized particles (1–100 nm) in a common base fluid) have latterly revealed to be more stable with higher thermal conductivity and better rheological properties (Yujin Hwang et al., 2008; Natarajan & Sathish, 2009; Mahian et al., 2013a). The expression ‘‘nanofluid’’ was first utilized by Choi in 1995 (S. U. S. Choi & Eastman, 1995).

In the previous studies, nanofluids were synthesized using different techniques and procedures that, so far, can generally be categorized under two preparation methods, i.e., the “one-step method” and the “two-step method” (Keblinski et al., 2005; R. A. Taylor et al., 2011b; Behi & Mirmohammadi, 2012). A brief description of each method will be presented in the following sections.

2.4.1 One-step method

In this method, the production of nanoparticles and the preparation of nanofluid are performed simultaneously. The required size of nanoparticles is prepared and concurrently dispersed with the desired concentration in the host fluid. Therefore, the output of this method is a nanofluid that can directly be used (R. A. Taylor et al., 2011b). The one-step method is desirable to prepare nanofluids containing metal nanoparticles to prevent oxidation (Wenhua Yu et al., 2008). Higher dispersion stability of nanofluids can be obtained by this method due to reduced agglomeration of nanoparticles (Ghadimi et al., 2011; R. A. Taylor et al., 2011b; Behi & Mirmohammadi, 2012). However, there are some limitations for this method such as it is only applicable to fluids with low vapor pressure, can only be used for synthesizing nanofluids in small scale, and relatively expensive (Y. Li et al., 2009; R. A. Taylor et al., 2011b; Wei Yu & Xie, 2012). A water-based Cu nanofluid was prepared by Liu et al. (2006) using the one-step chemical reduction method for the first time. Without using any surfactant, Cu-water nanofluids were prepared with volume concertation less than 0.2%. Using a one-step method, J. A. Eastman et al. (2001) had synthesized ethylene glycol (EG)-based Cu nanofluids. In the preparation method, the contact between a metallic vapor (Cu) and a flowing low vapor pressure liquid (EG) resulted in a direct condensation of Cu nanoparticles. The diameter of the prepared Cu nanoparticles was less than 10 nm and volume concentration was about 0.3%.

2.4.2 Two-step method

In this method, preparation of any nanofluid requires two steps. In the first step, the nanoparticles are produced as dry powders. Then, the second step is the dispersion of these nanoparticles in any suitable host fluid. The stability of the nanofluids prepared by this method represents a challenge because suspending solid nanoparticles in a base fluid will not result in a simple mixture (Pantzali et al., 2009a; Saidur et al., 2011; Behi & Mirmohammadi, 2012; Hordy et al., 2014). Owing to the high specific surface area (SSA) of nanoparticles, they will have a capability to agglomerate over time due to high surface tension between them. Agglomeration of the nanoparticles will cause them to settle down and block the flow channels (Y. Li et al., 2009; Chaji et al., 2013). This is a drawback for this method, but its main feature is the ability for synthesizing nanofluids in large scale for industrial applications. There are several methods available to prevent or reduce the effect of agglomeration such as the addition of surfactants or using ultrasonication (Keblinski et al., 2005; Ghadimi et al., 2011; Wei Yu & Xie, 2012). These methods will be discussed in the following sections.

Using a two-step method, Said et al. (2013a) prepared water/aluminum oxide (Al_2O_3) and EG-water/Al_2O_3 nanofluids with volumetric concentrations of 0.05 – 0.1% using 13-nm Al_2O_3 nanoparticles, an ultrasonic probe, and a high pressure homogenizer. Yousefi et al. (2012c) had synthesized water-based multi-walled carbon nanotubes (MWCNTs) nanofluids using the two-step method. The MWCNTs/water nanofluid was prepared by using MWCNTs with an outer diameter of 10–30 nm, a ratio of 1:350 Triton X-100 surfactant, and 30 min of probe ultrasonication.

2.5 Stability of nanofluids

Producing a stable nanofluid is essential for its successful use as a working fluid in any heat transfer application. When dispersing particles at the nanoscale in a base fluid, the colloidal stability will no longer be affected by gravity and buoyancy and other body forces. As a replacement, the stability will mainly be governed by the Brownian motion, which is "the random movement of nanoparticles inside the mixture caused by molecular interactions" (Vandsburger, 2010; Mahmood, 2012). Methods for evaluating and enhancing the dispersion stability of nanofluids will be presented in the following sections.

2.5.1 Evaluating the stability of nanofluids

There are several methods that can usually be used to evaluate the colloidal stability of nanofluids such as the sediment photograph capturing, zeta potential, and ultraviolet-visible spectrophotometry (UV-vis) spectral analysis. A short explanation of each method is given below.

2.5.1.1 Sediment photograph capturing method

The estimation of colloidal stability for nanofluids by this primary method was considered as the most simple and dependable method. Photos should be captured for the sample at regular time interval, and through comparison between successive photos, sedimentation will be visible and can be evaluated. This is a time-consuming method that requires a long time for monitoring the samples (Y. Li et al., 2009; Ghadimi et al., 2011).

2.5.1.2 Zeta potential

Zeta potential is defined as the "electric potential in the interfacial double layer at the location of the slipping plane versus a point in the bulk fluid away from the interface, and it shows the potential difference between the dispersion medium and the stationary layer of fluid attached to the dispersed particle" (Wei Yu et al., 2012). Measurement of zeta potential for a colloidal dispersion is one of the common procedures to evaluate the colloidal stability of the prepared nanofluids via the investigation of the electrophoretic behavior (H. Zhu et al., 2007; Ghadimi et al., 2011). The importance of zeta potential is that its value can be linked directly to the stability of a colloidal suspension (Amrollahi et al., 2009). The relationship between suspension stability and zeta potential arises from the mutual repulsion that occurs between like-charged particles. For this reason, particles with a high surface charge tend not to agglomerate, since contact is opposed (J.-H. Lee et al., 2008; Vandsburger, 2010). So, a nanofluid suspension with an absolute value of the measured zeta potential above 30 mV is considered to have a good colloidal stability (Vandsburger, 2010; Wei Yu & Xie, 2012).

2.5.1.3 Ultraviolet-visible spectrophotometry spectral analysis

Measurement of light absorbance of a nanofluid using UV–vis spectroscopy can provide a quantitative characterization of the stability. By measuring the values of light absorbance for the base fluid and the fresh nanofluid sample, a linear relation can be obtained between the concentration of the supernatant nanoparticles and the light absorbance. Using special quartz cuvettes suitable for UV region, the light absorbance of the sample should be measured at certain time intervals. The decrease in the value of light absorbance can provide a quantitative evaluation for the colloidal stability. The superiority of this method is its appropriateness for all the viscosities of base fluids, while zeta potential has some limitations (Ghadimi et al., 2011; Wei Yu & Xie, 2012). This UV–Vis spectrophotometry was first proposed as a suitable method for evaluating the colloidal stability of nanofluids by Jiang et al. (2003).

2.5.2 Enhancing the stability of nanofluids

Colloidal stability of nanofluids continues to be a technical challenge to the researchers due to strong van der Waals relations between the nanoparticles resulting from high SSA (C.-C. Teng et al., 2011; G.-J. Lee & Rhee, 2014). Accordingly, long-term dispersion stability should be thoroughly investigated for the effective utilization of nanofluids (Amiri et al., 2015a).

The main three techniques for increasing the colloidal stability that commonly were used can be summarized as (Ghadimi et al., 2011; Jeon et al., 2011; Behi & Mirmohammadi, 2012; Wei Yu & Xie, 2012):

1. Addition of surfactant,
2. Surface modification method, and
3. Ultrasonic vibration.

The first two methods were used to enhance the dispersivity of nanometer-sized particles in colloidal suspensions by preventing or minimizing the agglomeration of nanoparticles. Contrarily, the third method was used to augment the colloidal stability by breaking down the agglomerated nanoparticles instead of preventing their formation. Some researchers have used all three techniques to enhance the stability of nanofluids such as (Ding et al., 2007a; X. F. Li et al., 2008; Huang et al., 2009; X.-j. Wang et al., 2009; D. Zhu et al., 2009; Yousefi et al., 2012c; He et al., 2013), while others just applied one technique such as (J.-H. Lee et al., 2008; Wei Yu et al., 2009; Chandrasekar et al., 2010a; Azari et al., 2013), or two techniques such as (Pak & Cho, 1998; Y. Hwang et al., 2006; Otanicar et al., 2010; Sani et al., 2010; R. Taylor, 2011; R. A.

Taylor et al., 2011b; Yousefi et al., 2012a; Yousefi et al., 2012b; Kahani et al., 2013; S.-H. Lee & Jang, 2013; Vijayakumaar et al., 2013; Halelfadl et al., 2014).

2.5.2.1 Addition of surfactant

The colloidal stability of the nanofluid can be enhanced using different methods. However, the most cost-effective method is by adding surfactants to increase the stability of the dispersion of nanoparticles in the nanofluid (Madni et al., 2010; Ghadimi & Metselaar, 2013). Addition of surfactants is one of the methods for preparing non-covalently functionalized nanoparticles (Jeon et al., 2011; Wei Yu et al., 2012). The main advantage of the non-covalent functionalization is that it preserves the original structural properties of the nanomaterial (Jeon et al., 2011). Addition of surfactants is a simple method to avoid or minimize agglomeration and sedimentation of nanoparticles by modifying the hydrophobic nature of the surfaces of nanoparticles to become hydrophilic and it increases the wettability, which is the contact between the nanoparticles and the surrounding fluid medium. Thus, it improves the colloidal stability of the nanofluid. However, due to the cooling and heating cycles that occur in heat transfer applications, some of the surfactants have a tendency to create foam, which has negative effects on the viscosity and thermal conductivity of the nanofluids, a phenomenon that must be examined carefully (L. Chen et al., 2008; Aravind et al., 2011; Mingzheng et al., 2012). Furthermore, at temperatures greater than 60 °C, the stability of a nanofluid prepared by the addition of surfactant will be reduced, and sedimentation will occur due to the loss of connection between the surfactant and the nanoparticles (Assael et al., 2005; X.-Q. Wang & Mujumdar, 2007, 2008b; Wen et al., 2009; Hordy et al., 2014).

Surfactants have a hydrophilic polar head group and hydrophobic tail portion, and can be categorized according to the structure of the head as (Wei Yu et al., 2012):

1. Nonionic surfactants in which the head doesn’t have any charge group such as Triton X-100,
2. Anionic surfactants in which the head have negatively charged head groups such as sodium dodecyl sulfate (SDS), gum Arabic (GA), and sodium dodecyl benzene sulfonate (SDBS),
3. Cationic surfactants in which the head have positively charged head groups such as cetyl trimethylammonium bromide (CTAB) , and
4. Amphoteric surfactants in which pH value specifies the charge of the head.

Selecting the right concentration of any surfactant has the same importance as choosing the correct surfactant for any application. For preparing a nanofluid with high stability, the concentration of the surfactant should be sufficient to produce an effective coating of nanoparticles capable of inducing sufficient electrostatic repulsion to counteract the van der Waals forces (Jiang et al., 2003; Goodwin, 2004; Wei Yu et al., 2012). The addition of surfactants will increase the surface charge of the nanoparticles resulting in an increase in the zeta potential which ultimately will increase the repulsion forces between the nanoparticles suspended in the host fluid (Y. Hwang et al., 2007; Ghadimi et al., 2011). Nanofluids in the previous research were synthesized using different surfactants such as;

- SDS: (Y. Hwang et al., 2006; Y. Hwang et al., 2007; Natarajan & Sathish, 2009; Otanicar, 2009; Sani et al., 2010; Nasiri et al., 2011; R. Taylor, 2011).
- SDBS: (Wen & Ding, 2004; X. Li et al., 2007; Ding et al., 2007a; D. Zhu et al., 2009; M. E. Meibodi et al., 2010; He et al., 2013; Halelfadl et al., 2014).
- CTAB: (Assael et al., 2005; Chaji et al., 2013; S.-H. Lee & Jang, 2013).
- Triton X-100: (Yousefi et al., 2012b; Yousefi et al., 2012c; Chaji et al., 2013).
- GA: (Ding et al., 2006; J. H. Lee, 2009).

2.5.2.2 Surface modification method

The disadvantages of adding surfactants have been addressed in previous section, i.e., the formation of foam and loss of colloidal stability at high temperatures. Therefore, the use of surface modified nanoparticles, i.e., covalently functionalized nanoparticles, is a promising technique to prepare nanofluids with long-term colloidal stability and use their enhanced thermal performance as working fluids in heat transfer applications (L. Chen et al., 2008; Aravind et al., 2011). All the efforts have been applied to prepare a nanofluid using highly-dispersed nanoparticles decorated with non-corrosive hydrophilic groups in a base fluid. By preparing covalently functionalized nanoparticles with highly-charged surface, nanofluids with high colloidal stability can be obtained due to the strong repulsive forces between the nanoparticles (Huang et al., 2009; X.-j. Wang et al., 2009; D. Zhu et al., 2009; Ghadimi et al., 2011).

Using covalent and non-covalent functionalization with carboxyl groups and SDBS surfactant, respectively, water-based graphene nanoplatelets (GNPs) nanofluids with weight concentrations of 0.025%, 0.05%, and 0.1% were prepared by Amiri et al. (2015a). Higher dispersion stability in water was obtained by the two functionalization methods in comparison with pristine GNPs. However, nanofluids containing non-covalently functionalized GNPs showed higher viscosity than those with covalently functionalized GNPs. Also, thermal conductivity for water-based covalently functionalized GNPs nanofluids was higher than that for non-covalently functionalized GNPs with SDBS. Using acid treatment for preparing covalently functionalized GNPs with carboxyl and hydroxyl groups, Yarmand et al. (2016b) prepared water-based nanofluids with long term dispersion stability. Nanofluids with weight concentrations of 0.02%, 0.06%, and 0.1% were prepared. After 240 h, the sedimentation of the nanofluids that were prepared was less than 7%. Amiri et al. (2016c) had prepared a stable water/EG-based nanofluid containing functionalized GNPs with hydroxyl groups.

Nanofluids with weight concentrations of 0.01%, 0.05%, 0.1%, and 0.2% were synthesized using a volumetric ratio for water to EG of (40:60) and a 10-min probe sonication.

2.5.2.3 Ultrasonic vibration

Through breaking down the agglomerated nanoparticles, ultrasonic vibration can enhance the colloidal stability of nanofluids that were prepared using pristine or functionalized nanoparticles, in the presence or absence of surfactants (Ghadimi et al., 2011; Jeon et al., 2011; Behi & Mirmohammadi, 2012; Wei Yu & Xie, 2012).

Garg et al. (2009) studied the effect of ultrasonication time on the dispersion stability of water-based 1−wt% MWCNTs nanofluid. Four different ultrasonication times of 20, 40, 60, and 80 min were used. GA was used as a surfactant to disperse nanotubes with an outside diameter of about 10–20 nm in water. Ultrasonication had dual effects on the water-based MWCNTs nanofluid. The stability increased as ultrasonication time increased. However, the thermal performance of the water-based MWCNTs nanofluid increased as ultrasonication time increased until an optimum time of 40 min was reached and then decreased. This was attributed to the decreased aspect ratio of the MWCNTs resulting from increased damage of the nanotubes.

Nanofluids with volume concentration of 0.5−4% of GNPs in EG as a base fluid were prepared by G.-J. Lee & Rhee (2014) using intensive ultrasonication and without any functionalization. The nanofluids were proven to be stable by a reproducibility test of thermal conductivity. Using a two-step method, Ghadimi & Metselaar (2013) prepared water-based 0.1−wt% titanium dioxide (TiO_2) nanofluid. Ultrasonic probe and bath, 0.1−wt% SDS surfactant, and 25−nm nanoparticles were used. Results showed that the highest colloidal stability was reached using an ultrasonic bath for 3 hours.

2.6 Thermophysical properties of nanofluids

For the effective use of nanofluids in various heat transfer applications, thermophysical properties should positively change once nanoparticles are loaded. To address the suitability of a nanofluid for any heat transfer application, its thermophysical properties such as thermal conductivity, viscosity, density, and specific heat should be thoroughly investigated and compared to those of the base fluid (Wong & De Leon, 2010; Zubir et al., 2016). A complete knowledge for the effects of adding nanoparticles to a base fluid on the thermophysical properties is essential for preparing a nanofluid with selected properties suitable for a specific heat transfer application. The complicated relationship between the thermophysical properties and effective parameters of nanofluids is presented in Figure 2.1. For any weight concentration of nanoparticles in a nanofluid, the volumetric concentration can be calculated using equation (2.6) presented by Pak & Cho (1998). The thermophysical properties of nanofluids will be reviewed in the following sections.

$$\emptyset_v = \frac{1}{(100/\emptyset_m)\left(\rho_p/\rho_{bf}\right)+1} \times 100\% \tag{2.6}$$

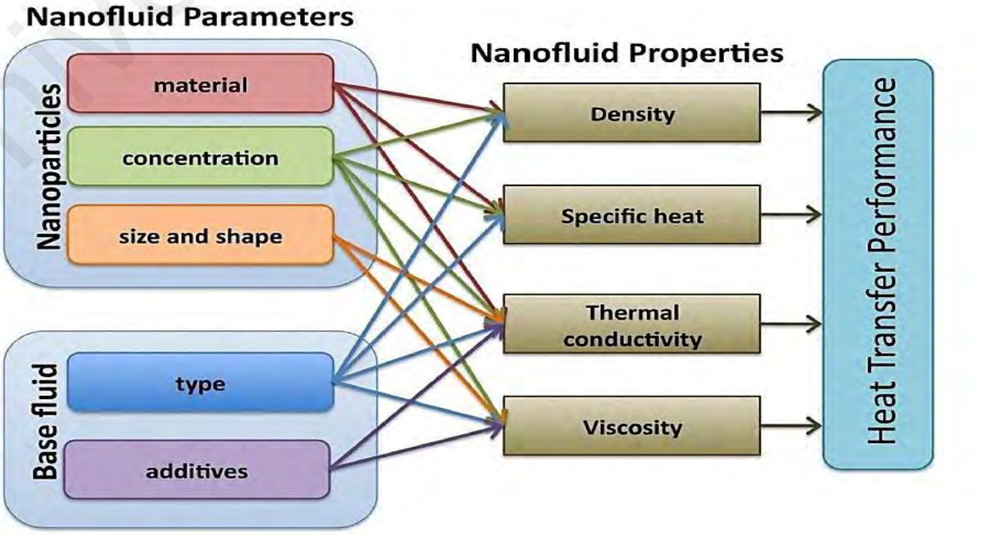

Figure 2.1: The relationship between the thermophysical properties and effective parameters of nanofluids (Timofeeva, 2011).

2.6.1 Thermal conductivity of nanofluids

Common working fluids such a water, engine oil, and ethylene glycol in various engineering processes show relatively low thermal conductivity (Daungthongsuk & Wongwises, 2007). The addition of nanoparticles to the base fluids (nanofluids) for enhancing their thermal conductivity was an innovative idea (S. U. S. Choi et al., 2001; Xuan & Li, 2003; Sarit Kumar Das et al., 2006). By developing heat transfer fluids with improved thermal performance, mechanical equipment having higher efficiency and compactness can be designed with the consequent savings in capital and operating costs (Maïga et al., 2005; Garg et al., 2009; Natarajan & Sathish, 2009; Labib et al., 2013; Sundar et al., 2014). There are several interesting characteristics behind selecting nanoparticles as possible candidates for dispersion in base fluids such as high SSA, lower particle energy, and high movability (Sarit Kumar Das et al., 2006). In order to elucidate the reasons for the increase in the thermal conductivity of nanofluids, Keblinski et al. (2002) and Jeffrey A Eastman et al. (2004) suggested four potential mechanisms, i.e., molecular-level layering of the liquid at the liquid/particle interface, Brownian motion of the nanoparticles, the nature of heat transport in the nanoparticles, and the effects of nanoparticle clustering.

It was proved from previous research that the thermal conductivity of nanofluids relies on numerous factors, such as temperature, volume fraction, thermal conductivities of the suspended nanoparticles and base fluid, shape or geometry of nanoparticles, interfacial thermal resistance, and surface area. With incorporating one or more of these factors, several researchers had developed theoretical models and correlations for calculating the thermal conductivity of nanofluids (Nan et al., 1997; S. U. S. Choi & Eastman, 2001; S. U. S. Choi et al., 2001; Huxtable et al., 2003; Kang et al., 2006; X.-Q. Wang & Mujumdar, 2008a; L. Godson et al., 2010; Marconnet et al., 2013).

The first model for calculating the thermal conductivity of a suspension contains liquid and solid was developed by Maxwell (1881) (as cited in (Chandrasekar et al., 2010a)). The model, shown in equation (2.7), is suitable for low volume fraction of relatively large solid particles. The particles should have uniform size and dispersed in the host fluid randomly (Wenhua Yu et al., 2008; Chandrasekar et al., 2010a).

$$\frac{K_{nf}}{K_{bf}} = \frac{K_{np} + 2\,K_{bf} + 2\,\emptyset_v\left(K_{np} - K_{bf}\right)}{K_{np} + 2K_{bf} - \emptyset_v\left(K_{np} - K_{bf}\right)} \tag{2.7}$$

where, K_{nf} = thermal conductivity of the nanofluid (W/m K)

K_{bf} = thermal conductivity of the base fluid (W/m K)

K_{np} = thermal conductivity of the nanoparticles (W/m K)

ϕ_v = volume fraction of nanoparticles in base fluid

The value of thermal conductivity calculated from this model depends on the volume fraction of suspended particles and the values of thermal conductivity of the particles and base fluid (Y. Li et al., 2009). The above correlation can be written in a simpler form suitable for particles with spherical shape, relatively high thermal conductivity, and low volume fraction as follows (S. U. S. Choi et al., 2001; Nan et al., 2003; Timofeeva et al., 2007; Gong et al., 2014);

$$K_{nf} = K_{bf}\,(1 + 3\,\emptyset_v) \tag{2.8}$$

The equation of Maxwell didn’t take into consideration the effect of some influential parameters on the value of thermal conductivity such as particle’s shape and diameter, SSA, effect of Brownian motion, and the thermal resistance that originates between the solid particles and the base fluid. Therefore, the predicted values of thermal conductivity were not in good agreement when compared with experimental data. Consequently, using the Maxwell model, effective medium theory (EMT) (which theoretically describes a medium based on the volume fraction and properties of its components), and taking into consideration more effective factors, several models were proposed as modification and improvement for the Maxwell model (Y. Li et al., 2009; Chandrasekar et al., 2010a).

By considering the effect of particle's shape on the effective thermal conductive of solid particles suspended in host liquid, Hamilton & Crosser (1962) modified the model of Maxwell as follows;

$$\frac{K_{nf}}{K_{bf}} = \frac{K_{np} + (n-1)K_{bf} - (n-1)\emptyset_v\left(K_{bf-}K_{np}\right)}{K_{np} + (sf-1)K_{bf} + \emptyset_v\left(K_{bf-}K_{np}\right)} \tag{2.9}$$

where, sf = shape factor = $(3/\psi)$ (sf = 3 for spherical particle)

$$\psi = \text{Sphericity of the particle} = \frac{\text{Surface area of a sphere with the same volume}}{\text{Surface area of the particle}}$$

The interfacial thermal resistance (R_K), known as the Kapitza resistance, is a thermal resistance that originates between ingredients in a composite due to weak adhesion at the interface and the dissimilarity in thermal expansion. The enhancement in thermal conductivity of composites/nanofluids is limited by the existence of the Kapitza resistance (Nan et al., 1997; Huxtable et al., 2003; Chu et al., 2012a; Chu et al., 2012b; Warzoha & Fleischer, 2014). Kapitza radius (a_K) is defined as the product of the thermal conductivity of the base fluid and the thermal resistance of the interfacial boundary layer (R_K).

$$a_K = R_K\, K_{bf} \tag{2.10}$$

$$R_K = c/K_s \tag{2.11}$$

where, (c) and (Ks) are the thickness and thermal conductivity of the interfacial boundary layer shown in Figure 2.2, respectively. The value of the predicted thermal conductivity for composites is highly affected by the interfacial thermal resistance, with higher values obtained with considering perfect interface, i.e., ($a_K = 0$) (Nan et al., 1997). To address the influence of this effective parameter, Nan et al. (1997) improved the correlation of MG-EMT by taking into consideration the effects of shape of ellipsoidal particles and interfacial thermal resistance, resulting in a new model for thermal conductivity:

$$\frac{K_{nf}}{K_{bf}} = \frac{3 + \emptyset_v[2\beta_{11}(1 - L_{11}) + \beta_{33}(1 - L_{33})]}{3 - \emptyset_v(2\beta_{11}L_{11} + \beta_{33}L_{33})} \tag{2.12}$$

where L_{11} and L_{33} are geometrical factors that depend on the shape of particle and were given by:

$$L_{11} = \begin{cases} \dfrac{p^2}{2(p^2 - 1)} - \dfrac{p}{2(p^2 - 1)^{3/2}} \cosh^{-1} p \quad , \ \text{for}\, p > 1 \\ \dfrac{p^2}{2(p^2 - 1)} + \dfrac{p}{2(1 - p^2)^{3/2}} \cos^{-1} p \quad , \ \text{for}\, p < 1 \end{cases} \tag{2.13}$$

With reference to Figure 2.2, the aspect ratio (p) is defined as:

$$p = \frac{a_Z}{a_X} \ , \ \begin{cases} \text{for a prolate ellipsoid} \quad p > 1 \\ \text{for an oblate ellipsoid} \quad p < 1 \end{cases} \tag{2.14}$$

$$L_{33} = 1 - 2L_{11} \tag{2.15}$$

And, K_{11}^C and K_{33}^C are the equivalent thermal conductivities of the ellipsoidal particles with the surrounding interface layer of thickness (c) along transverse (x-axis) and longitudinal (z-axis) axes, respectively, as shown in Figure 2.2.

$$\beta_{11} = \frac{K_{11}^C - K_{bf}}{K_{bf} + L_{11}\left(K_{11}^C - K_{bf}\right)} \ , \ \beta_{33} = \frac{K_{33}^C - K_{bf}}{K_{bf} + L_{33}\left(K_{33}^C - K_{bf}\right)} \tag{2.16}$$

$$K_{ii}^{C} = \frac{K_p}{1 + \gamma L_{ii} K_p / K_{bf}} \quad , \qquad \text{for ii = 11 and 33} \tag{2.17}$$

The dimensionless parameter γ was defined as:

$$\gamma = \begin{cases} \left(2 + {}^{1}\!/_{p}\right) \dfrac{a_K}{a_X} \ , \ \text{for} \ \ p \geq 1 \\ (1 + 2p) \dfrac{a_K}{a_Z} \ , \ \text{for} \ \ p \leq 1 \end{cases} \tag{2.18}$$

Furthermore, Nan et al. (2003) presented a simple model for calculating the effective thermal conductivity for composites that modified the MG-EMT correlation to take into account the geometry of carbon nanotubes. This model uses equations (2.12) to (2.15) for the calculation of nanofluid thermal conductivity and geometrical factors of Nan et al. (1997) model in addition to the following equation:

$$\beta_{11} = \frac{K_X - K_{bf}}{K_{bf} + L_{11}\left(K_p - K_{bf}\right)} \ \ , \ \ \beta_{33} = \frac{K_Z - K_{bf}}{K_{bf} + L_{33}\left(K_p - K_{bf}\right)} \tag{2.19}$$

By employing the effect of aspect ratio of GNPs and using the theories of the differential effective medium and interfacial thermal resistance, Chu et al. (2012a) developed a model for effective thermal conductivity of GNP composites. GNPs were considered as large-aspect ratio oblate spheroids surrounded by an interfacial boundary layer having thickness (c) and thermal conductivity (K_S) (Figure 2.2). The effective thermal conductivity of the enclosed-GNPs was modeled as:

$$9(1 - \emptyset_v) \frac{K_{nf} - K_{bf}}{2K_{nf} + K_{bf}} = \emptyset_v \left[\frac{2K_X^{eff}}{K_{nf}} - \frac{K_{nf}}{K_Z^{eff}} - 1 \right] \tag{2.20}$$

where, K_X^{eff} and K_Z^{eff} (Equation (2.21)) are the effective thermal conductivities of the GNP along transverse (x-axis) and longitudinal (z-axis) axes, respectively, with incorporating the effect of the interfacial thermal resistance (R_K).

$$K_X^{eff} = \frac{K_X}{2R_K K_X/a_x + 1} \quad , \quad K_Z^{eff} = \frac{K_Z}{2R_K K_Z/a_z + 1} \tag{2.21}$$

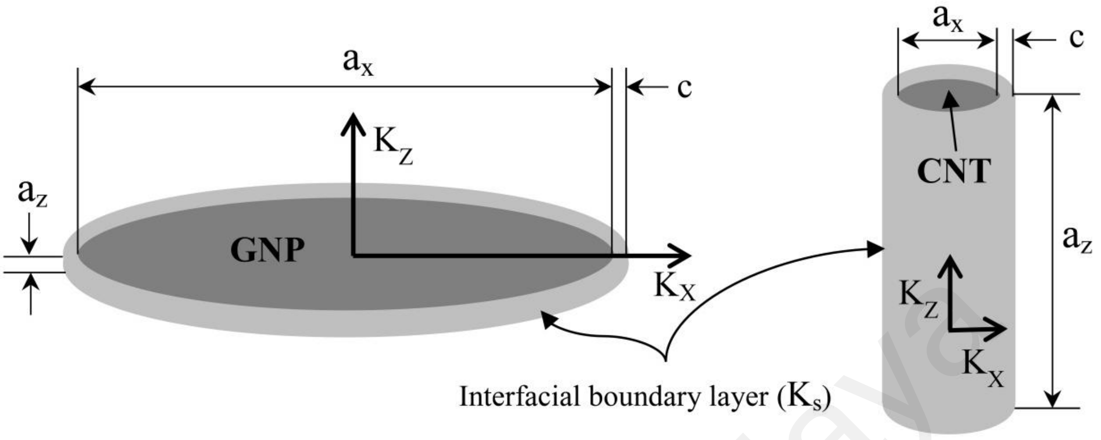

Figure 2.2: Schematic representation of the interfacial boundary layer.

Using Al_2O_3 nanoparticles with diameters of 11, 20, and 40 nm, Timofeeva et al. (2007) prepared water- and EG-based nanofluids with volume concentrations of 0.5−10%. The two-step method was followed for synthesizing the nanofluids using continuous bath sonication for 5−20 h. For water-based nanofluids, the highest enhancement in thermal conductivity of about 24% at 10 vol% was reached by the 40−nm nanoparticles, followed by the 11−nm and 20−nm nanoparticles, respectively. While for the EG-based nanofluid, the maximum increase in the thermal conductivity was 29% at 10 vol% and the effect of nanoparticle size was almost insignificant. It was also found that effective medium theory was in good agreement with the thermal conductivity data.

The thermophysical properties of water/Al_2O_3 and EG-water/Al_2O_3 nanofluids were investigated by Said et al. (2013a). Nanofluids with volumetric concentrations of 0.05–0.1% were synthesized by a two-step method using 13-nm Al_2O_3 nanoparticles, an ultrasonic probe, and a high pressure homogenizer. The stability of water/Al_2O_3 nanofluid was better than that of the EG-water/Al_2O_3 nanofluid. Results indicated almost a linear increase in the measured thermal conductivity with concentration. From the two nanofluids that were studied, it was concluded that the effective medium theory is only suitable for predicting the thermal conductivity of EG-water/Al_2O_3 nanofluids.

The thermophysical properties of MWCNTs/water nanofluids were investigated by Natarajan & Sathish (2009) and compared with the properties of water as a conventional heat transfer fluid. Two-step method, volume concentration of nanoparticles in the range of 0.2–0.1%, SDS surfactant at 1.0 wt%, and ultrasonication were used to synthesize the nanofluids. The prepared nanofluids were deemed to be stable based on UV-vis spectrophotometry, which revealed a decrease in concentration of 10% after 400 hr. Thermal conductivity increased with volume fraction of MWCNTs up to 41% at 1.0 vol% MWCNTs.

Jang & Choi (2004) have discovered that the thermal behavior of nanofluids is mainly governed by the Brownian motion. A theoretical model for estimating the thermal conductivity of nanofluids taking into account the effects of temperature, nanoparticle's size, and weight concentration was developed. For water-based Al_2O_3 and cooper oxide (CuO) nanofluids and EG-based CuO and Cu nanofluids, very good agreement was found between the calculated values of thermal conductivity with the published experimental data.

Using EG, oil, and water as the base fluids, Y. Hwang et al. (2007) investigated the thermal conductivity of nanofluids containing fullerene, MWCNTs, CuO, and silicon dioxide (SiO_2) nanomaterials. Excluding the water-based fullerene nanofluid, the thermal conductivity increased as the volume fraction increased. The thermal conductivity of water was higher than water-based fullerene nanofluid which was attributed to the low thermal conductivity of fullerene.

Water-based 25–nm Cu nanofluid was prepared by X. F. Li et al. (2008) using two-step method to study the effect of SDSB surfactant and pH on the thermal conductivity. Results proved the high dependency of thermal conductivity on the concentration of SDBS surfactant, pH value, and weight concentration. Using optimized values of SDBS concentration and pH, a maximum enhancement in the thermal conductivity of 10.7% was reached at 0.1wt%.

Using EG/water (60:40) as a base fluid, Al_2O_3, CuO, and zinc oxide (ZnO) nanofluids with up to 10 vol% was produced by Vajjha & Das (2009b) to examine the thermal conductivity in the temperature range of 25–90 °C. The thermal conductivity increased as temperature and volumetric concentration increased. Comparison of the experimental data with some available models for thermal conductivity showed bad agreement. Consequently, new correlations were proposed and showed good agreement with the experimental data.

Thermal conductivity and stability of water-based Al_2O_3 and Cu nanofluids were studied by X.-j. Wang et al. (2009) considering various SDBS concentrations and pH values. At 0.8 wt% and using optimized values of SDBS concentration and pH, maximum augmentations in the thermal conductivity of 15% and 18% were reached using Al_2O_3 and Cu nanoparticles, respectively. Furthermore, thermal conductivity enhanced with better dispersion of nanoparticles in the base fluid.

Stability and thermal conductivity of water based SWCNTs and MWCNTs nanofluids were experimentally studied by M. E. Meibodi et al. (2010). The effects of weight concentration, nanoparticle’s shape, temperature, surfactant type, pH value, time lapse after preparation, and power of ultrasonication were all considered. Directly after ultrasonication, the value of thermal conductivity changed with time. While after longer time, it became unrelated to time. The thermal conductivity increased as particle concentration and temperature increased. Also, it was found that the sample with higher thermal conductivity did not necessarily have better colloidal stability.

Using the large amount of experimental data in the literature, Corcione (2011) developed an empirical correlation for estimating the thermal conductivity of nanofluids in the ranges of 10–150 nm for diameter of nanoparticle, 0.2%–9.0% for volume fraction, and 21–51 °C for temperature. For a specific base fluid and material for nanoparticle, the thermal conductivity ratio of the nanofluid to the base liquid increased as the temperature and volume fraction increased, and decreased as the diameter of nanoparticle increased.

Water-based nanofluids containing SWCNTs, double-walled carbon nanotubes (DWCNTs), few-walled carbon nanotubes (FWCNTs), and two different MWCNTs were prepared by Nasiri et al. (2011) to study their thermal conductivity. The dispersion of CNTs in water was performed using different combinations of ultrasonic probe, SDS surfactant, ultrasonic bath, and covalent functionalization. Thermal conductivity increased as temperature increased, and decreased with different trends as time lapse after preparation increased. Nanofluids with functionalized CNTs showed higher thermal conductivity, better colloidal stability, and slighter trend with time.

Ghadimi & Metselaar (2013) had synthesized water-based 0.1−wt% titanium dioxide (TiO_2) nanofluid using a two-step method to examine the effects of ultrasonication time and SDS surfactant on the stability and thermal conductivity. Ultrasonic probe and bath, 0.1−wt% SDS surfactant, and 25−nm nanoparticles were used. Results showed that the highest thermal conductivity and colloidal stability was reached using 0.1−wt% SDS and ultrasonic bath for 3 hours.

2.6.2 Dynamic viscosity of nanofluids

The positive change of the thermophysical properties of conventional heat transfer fluids once nanoparticles are loaded is essential to justify the use of nanofluids as effective working fluids in various heat transfer applications. The thermal conductivity of the base fluids may enhance with the addition of nanoparticles; however, the viscosity of nanofluids will negatively be affected. In industrial and practical applications, the viscosity and pumping power are very important factors from an economical point of view (Behi & Mirmohammadi, 2012). Consequently, the rheological and heat transfer properties of the nanofluid should be optimized since they have direct effect on its applicability as a working fluid in engineering applications (Garg et al., 2009). It was verified from previous research that the viscosity of nanofluids relies on numerous factors, such as shear rate, concentration of nanoparticles, nanofluid temperature, and nanoparticle size. Several models were proposed and presented by the researchers in this field for estimating the viscosity of nanofluids (Y. Li et al., 2009).

The formula of Einstein (1906) (as cited in Mahbubul et al. (2012) and presented by equation (2.22)), is one of the first correlations for evaluating the effective viscosity of a mixture, which is suitable for low volume fractions (≤ 2%) of solid particles with spherical shapes. For higher volume fractions, Einstein's formula will predict underestimated values for viscosity (Y. Li et al., 2009; Mahmood, 2012). The innovative work of Einstein was mainly used as a source for deriving several modified formulas based on the linear viscous fluid theory for estimating the viscosity of particle suspension.

$$\text{Einstein formula,} \qquad \frac{\mu_{nf}}{\mu_{bf}} = 1 + 2.5\, \emptyset_v \tag{2.22}$$

For predicting the viscosity of mixtures with medium volume concentrations (≤ 4%) of particles, Brinkman (1952) modified and extended the formula of Einstein as follows:

Brinkman formula, $$\frac{\mu_{nf}}{\mu_{bf}} = \frac{1}{(1-\emptyset_v)^{2.5}} \tag{2.23}$$

The effect of Brownian motion of particles on viscosity was first introduced in the modified formula proposed by Batchelor (1977) (as cited in Y. Li et al. (2009)) as:

Batchelor formula, $$\frac{\mu_{nf}}{\mu_{bf}} = 1 + 2.5\,\emptyset_v + 6.5\emptyset_v^2 \tag{2.24}$$

In a wide range of weight concentration of nanoparticles in nanofluids, almost none of the above-mentioned standard models are able to estimate an accurate viscosity value. Therefore, a common method to estimate the viscosity of nanofluids is curve fitting (Y. Li et al., 2009; Mahmood, 2012).

The viscosity of water-based CuO nanofluids was measured by J. Li et al. (2002) using a capillary viscometer in the temperature range of 30–80 °C and a weight concentration of 0.02%–0.1%. Results indicated that for the range of weight concentrations investigated, the viscosity of the nanofluid was highly affected by the value of temperature, whereas the influence of the weight concentration was not very noticeable.

The effect of shear rate, temperature, nanoparticle's diameter, and volume fraction on the viscosity of propylene glycol-based Al_2O_3 (alumina) nanofluids were presented by Prasher et al. (2006). Volume fractions of 0.5%, 2%, and 3%, temperatures in the range of 30–60 °C, and Al_2O_3 diameter of 27, 40, and 50 nm were utilized to perform the experiments at various shear rates using a rheometer with a double-gap fixture. The viscosity of nanofluids was found to have a weak dependence on nanoparticle's diameter and temperature, and a strong dependence on volume fraction of nanoparticles.

Water-based Al_2O_3 and CuO nanofluids were synthesized by Nguyen et al. (2007) to investigate the effect of the nanoparticle's size and temperature on the viscosity using a viscometer with a cylindrical measurement cavity. Temperatures in the range of ambient−75 °C, Al_2O_3 diameters of 36 and 47 nm, CuO diameter of 29 nm, and volume fractions in the range of 0.15%−13% were used. No notable effect of nanoparticle's size on the viscosity of Al_2O_3 nanofluid was observed at volume fractions <4%, while for higher volume fractions, the 47−nm Al_2O_3 nanofluid obviously showed higher viscosities. Moreover, the CuO nanofluids displayed higher viscosities than the Al_2O_3 nanofluids. The calculated values of viscosity using the formula of Einstein and other formulas arising from the linear fluid theory were in bad agreement with experimental data for nanofluids.

Using a two-step method, volume concentrations in the range of 0.01%–0.3% of water-based Al_2O_3 nanofluids were prepared by J.-H. Lee et al. (2008). Different ultrasonication times of 0, 5, 20, and 30 h were used to disperse the 30±5 nm Al_2O_3 nanoparticles in the aqueous host fluid. The values of the viscosity substantially decreased as temperature increased, and revealed nonlinear relation with the volume concentration. Moreover, the formula of Einstein underestimated the values of viscosity predictions and displayed a linear relation with concentration.

Using the huge amount of experimental data in the literature, Corcione (2011) proposed an empirical correlation for predicting the dynamic viscosity of nanofluids in the ranges of 25–200 nm for diameter of nanoparticle, 0.01%–7.1% for volume fraction, and 20–50 °C for temperature. For a specific base fluid and material for nanoparticle, the viscosity ratio of the nanofluid to the base liquid increased as the volume fraction increased, decreased as the diameter of nanoparticle increased, and nearly remained independent of temperature.

Using a two-step method with ultrasonication and without any surfactant, Chandrasekar et al. (2010a) prepared water-based Al_2O_3 nanofluids to study their thermophysical properties at room temperature. Nanoparticles with nominal diameter of

43 nm were used with a concentration range of 0.33–5.0 vol%. The viscosity increased as the volume concentration of nanoparticles increased. Also, the increase in the viscosity was significantly higher than that for the thermal conductivity.

The effects of nanoparticle's concentration, temperature, ultrasonication time, and size of nanoparticle on the viscosity of nanofluid were studied by Behi & Mirmohammadi (2012). The viscosity measurements were made by a rotating coaxial cylinder viscometer. The viscosity of nanofluids increased as the concentration of nanoparticles increased, and decreased as the temperature increased. It was concluded that there were optimum values for the nanoparticle's size and time of ultrasonication.

The effect of ultrasonication time on the viscosity and thermal performance of water-based MWCNT nanofluid was studied by Garg et al. (2009). Weight concentrations of MWCNT and GA of 1% and 0.25%, respectively, ultrasonication times of 20, 40, 60, and 80 min, and MWCNTs with diameter of 10–20 nm were used to prepare the nanofluids using the two-step method. Viscosity of the nanofluids increased as the time of ultrasonication increased up to a maximum value and decreased afterwards.

2.6.3 Density and specific heat of nanofluids

The ratio of two extensive properties for any material is an intensive property. Therefore, the material's density which is the ratio of its mass to volume, i.e., two extensive properties, is an intensive property of that material. The density of the nanofluid can be calculated using the equation of Pak & Cho (1998) as follows:

$$\rho_{nf} = (1 - \emptyset_v)\, \rho_{bf} + \emptyset_v\, \rho_{np} \tag{2.25}$$

The specific heat (C_p) is an intensive property of a substance and defined as "the energy required to raise the temperature of a unit mass of a substance by one degree"

(Çengel, 2003). The specific heat of a nanofluid can be determined using the following two equations presented by Xuan & Roetzel (2000) and Pak & Cho (1998), respectively;

$$C_{P_{nf}} = \frac{(1-\emptyset_v)(\rho C_P)_{bf} + \emptyset_v(\rho C_P)_{np}}{\rho_{nf}} \tag{2.26}$$

$$C_{P_{nf}} = (1-\emptyset_v)\, C_{P_{bf}} + \emptyset_v\, C_{P_{np}} \tag{2.27}$$

The density of EG/water-based nanofluids containing different volume fractions of aluminum oxide and zinc oxide nanoparticles was measure by Vajjha et al. (2009) at a temperature range of 0–50 °C. It was observed that the values of density were in direct proportion to volume fraction and inverse proportion to temperature. Using three weight concentrations of 0.5%, 1.0%, and 1.5%, T.-P. Teng & Hung (2014) prepared water-based aluminum oxide nanofluids and investigated their density and specific heat values at different temperatures. Results proved that the measured density of nanofluids increased as weight concentration increased and decreased as temperature increased. The measured values of specific heat decreased with an increase in weight concentration. Furthermore, the effect of temperature on the specific heat value was not apparent. Using volume fractions of 0.0% to 21.7% of Al_2O_3 in water, Zhou & Ni (2008) presented that the experimental values of the specific of the water-based nanofluids slowly decreased as the volume fractions increased. Kulkarni et al. (2008) showed that the measured values of specific heat for EG/water-based aluminum oxide nanofluids increased as temperature increased and decreased as weight concentration increased. Vajjha & Das (2009a) investigated the specific heat of water-based SiO_2 nanofluids at volume concentrations of 2% to 10%. The experimental results showed that the specific heat of nanofluids increased as temperature increased, and decreased considerably as volume concentration increased. Saeedinia et al. (2012b) measured the specific heat of oil-based CuO nanofluids at different weight concentrations of 0.2% to 2%. It was found that the specific heat values decreased as weight concentration and temperature increased.

2.7 Use of nanofluids in flat-plate solar collectors

In the last few years, the effects of using nanofluids as heat transfer fluids on the performance of FPSCs have been investigated both experimentally and theoretically by many researchers. They have used a variety of nanoparticles with different concentrations, diameters, and different preparation methods. Also, several researchers have investigated the effects of various entities on the performance of FPSCs, e.g., heat transfer coefficients and thermophysical properties, such as viscosity, thermal conductivity, specific heat capacity, and the density of nanofluids. In this section, we have incorporated our reviews of previous studies related to the effects of replacing conventional working fluids with nanofluids on the performance of FPSCs.

The performance of a FPSC during steady state operation can be described by an energy balance. In this case, the energy balance indicated that the incident solar radiation was distributed into optical losses, useful energy gain, and thermal losses (by conduction, convection, and infrared radiation) (Duffie & Beckman, 2013). Hottel & Whillier (1958) developed a mathematical model and procedure for evaluating the performance of FPSCs, which was extended by ASHRAE to develop ASHRAE Standard 93 (2003). This standard provides a procedure for the indoor and outdoor testing of solar energy collectors and rating them in accordance with their thermal performance. The solar collector efficiency is defined as;

$$\eta_c = \frac{\text{Actual useful energy collected}}{\text{Solar energy intercepted by the collector area}} \tag{2.28}$$

$$\Rightarrow \eta_c = \frac{Q_u}{G_T\, A_c} = \frac{\dot{m}\, C_p\, (T_{out} - T_{in})}{G_T\, A_c} \tag{2.29}$$

To enhance the performance of a solar collector, the absorption of energy from the sun should be increased and heat losses to the surroundings (such as the reflection of sun's radiation, radiation from the hot surface of the collector, and heat lost by convection from the collector to the surroundings) should be decreased. Also, the rate of heat transfer from the absorber plate to the working fluid and from the fluid to the end user should be improved (Javadi et al., 2013). Therefore, enhancement of the thermal properties of the working fluid by using a nanofluid in order to transfer the maximum amount of heat from the absorber plate to the end users is one way to improve the thermal efficiency of a solar collector (X.-Q. Wang & Mujumdar, 2007; Lazarus Godson et al., 2010; Javadi et al., 2013).

2.7.1 Experimental studies on using nanofluids in FPSCs

Natarajan & Sathish (2009) had investigated the heat transfer properties of MWCNT/water nanofluid and compared them with the properties of water as a conventional heat transfer fluid. Volume concentration of nanoparticles in the range of 0.2 – 0.1%, SDS surfactant at 1.0 wt%, and ultrasonication were used to synthesize the nanofluids. The prepared nanofluid was deemed to be stable based on UV-vis spectrophotometry, which revealed a decrease in concentration of 10% after 400 hr from preparation. Thermal conductivity increased with volume fraction of MWCNTs up to 41% at 1.0 vol% MWCNT. Accordingly, it was concluded that the efficiency of conventional FPSCs could increase if nanofluids are used as the heat transfer fluids. From this research, it can be concluded that carbon nanostructure-based nanofluids, represented by the MWCNT nanofluids used in this research, are strong candidates for use as heat transfer fluids in FPSCs and other heat transfer applications.

The effect of using silver/water nanofluid on the performance of a FPSC was investigated by Polvongsri & Kiatsiriroat (2011). Silver nanoparticles with 20-nm diameter were dispersed in water at concentrations of 1,000 and 10,000 ppm, and the nanofluids were used as working fluids in three identical 1.0 × 0.15-m FPSCs. The tests were performed following ASHRAE Standard 93, and they were conducted around 12:00 P.M. The flow rate of working fluid was 0.8–1.6 l/min m^2, and the inlet temperature was controlled in the range of 35–65 °C. For 1,000 ppm of silver nanoparticles, insignificant results were obtained compared with water, but, for 10,000 ppm, the nanofluid had a higher thermal conductivity, so obtained a greater heat rate from the solar collector. Also, as the concentration of the nanofluid increased, improvements were observed in both the temperature difference between the inlet and outlet fluids and the efficiency of the collector. It was concluded that the temperature difference between the inlet and outlet fluids decreased as the mass flow rate and the temperature of the inlet fluid increased. It can be concluded that using a silver/water nanofluid as the heat transfer fluid in FPSCs can improve their performance, but the improvement was less than that of MWCNTs. Note that the article did not provide any information about the stability of nanofluids.

The effect of using a MWCNTs/water nanofluid as the heat transfer fluid on the efficiency of a 2-m^2 FPSC was investigated experimentally by Yousefi et al. (2012a). MWCNTs were used that had outer diameters in the range of 10−30 nm and weight fractions of 0.2% and 0.4%. Triton X-100 was selected as the surfactant (Rastogi et al., 2008). They used an aluminum frame, a copper absorber plate with a selective coating, copper header and riser tubes with 22 and 10 mm diameters, respectively, and a 4-mm float glass cover to build the solar collector. An electrical pump was used to circulate the fluid in the forced-convection test setup. Also, the solar system had a 41-liters tank with an internal heat exchanger to absorb the heat from the solar collector. The flow rate of the nanofluid was in the range of 0.0167–0.05 kg/s, and tests were performed between 10:00 A.M. and 3:00 P.M. ASHRAE Standard 93 was chosen as the basis for performing the tests. The nanofluids that were synthesized without surfactant were unstable and separated quickly, while those with Triton X-100 surfactant were stable up to 10 days. The results showed that, at a weight concentration of 0.2% MWCNT nanofluid and without using a surfactant, the efficiency of the collector was lower than that when water was used as the working fluid, and a considerable enhancement of the efficiency was observed when the weight concentration was increased from 0.2 to 0.4%. In addition, it was found that the use of Triton X-100 as a surfactant had a deleterious effect on efficiency due to the extensive formation of foam. It also had been concluded that there was an increase in efficiency by adding surfactant to the 0.2 wt% MWCNT nanofluid at a specific range. From this research, it can be inferred that using the MWCNT nanofluid resulted in a good increase in FPSC's performance. But, both the stability of the nanofluid and the reduction of performance associated with the use of the surfactant should be considered with equal emphasis. Also, this research did not present any information about the effect of the high temperatures of the solar collectors, which usually are greater than 60 °C (A.-J. N. Khalifa, 1999), on the stability of the nanofluid in the presence of a surfactant. Note that, at temperatures greater than 60 °C, the stability of the nanofluid will be reduced, and sedimentation will occur due to the loss of connection between the surfactant and the nanoparticles (Assael et al., 2005; X.-Q. Wang & Mujumdar, 2007, 2008b; Wen et al., 2009; Hordy et al., 2014).

Utilizing the test setup of their preceding work, Yousefi et al. (2012b) investigated the effect on the performance of the FPSC of using Al_2O_3/water nanofluid (with and without Triton X-100 surfactant) as the heat transfer fluid. Nanoparticles with 15-nm diameters were used at weight concentrations of 0.2% and 0.4%. The flow rate of the nanofluid was in the range of 1 to 3 l/min. The nanofluid samples without surfactant were unstable, and those with surfactant were stable for about three days. At a flow rate of 3 l/min and without surfactant, the collector's efficiency with the Al_2O_3 nanofluid was higher than that of water, and the collector's efficiency within a widespread range of the reduced temperature parameter ((Ti - Ta)/G_T) was higher for 0.2 wt% than for 0.4 wt%. For 0.2 wt%, the efficiency was 28.3% higher than that of water. Also, it was found that adding Triton X-100 surfactant to the 0.4 wt% Al_2O_3/water nanofluid had a positive influence on the collector's efficiency, with a maximum enhancement of 15.63%. From this research, it can be found that using Al_2O_3 nanofluid caused an increase in the FPSC's performance but less than that associated with the use of MWCNT. The stability of the nanofluids that were prepared should be investigated further, especially at temperatures higher than 60 °C.

Yousefi et al. (2012c) had also conducted experiments to investigate the effect of variations in pH on the performance of an MWCNT/water nanofluid-based FPSC using the previous test setup. The MWCNT/water nanofluid was prepared by using a ratio of 1:350 Triton X-100 dispersant and 30 min of ultrasonication. They used MWCNT with an outer diameter of 10–30 nm, a weight concentration of 0.2%, and pH values of 3.5, 6.5, and 9.5. ASHRAE Standard 93 was chosen as the basis for performing the tests. The prepared nanofluids were stable up to 10 days. The results showed that the positive effect of the nanofluid on the collector's efficiency increased when the pH value was changed to any value that was higher or lower than that of the isoelectric point (7.4 for MWCNT), at which no electrical charge is carried by the molecules. This positive effect was attributed to the increased stability of the nanofluid. Therefore, it can be concluded that the stability of the nanofluid is one of the main factors that affect the effective application of a nanofluid as an improved working fluid in FPSCs.

A 0.5 × 0.2-m FPSC was fabricated by Chaji et al. (2013) to investigate the effect of using 20-nm TiO_2/water nanofluid as the working fluid. The collector consisted of a 5-mm glass cover, a 1-mm copper absorber plate with black matte paint, a 3-mm inner diameter copper riser tube, and 50-mm Rockwool insulation material. In spite of increased stability of the nanofluid resulting from the use of surfactants, the efficiency of the collector decreased due to the creation of foam in the nanofluid. Consequently, no surfactant was used thereafter. The prepared nanofluid was found to be stable for at least 4 h. Four weight concentrations, i.e., 0%, 0.1%, 0.2%, and 0.3%; three inlet fluid temperatures, i.e., ambient, 52, and 74 °C; and three flow rates, i.e., 36, 72, and 108 l/m^2 hr were investigated. The first two flow rates were in the laminar flow region, and the third one was in the transient flow region. The results indicated that the collector's efficiency improved at all flow rates, but the least improvement was observed at the highest flow rate. From this research, it can be concluded that the enhancement in the efficiency of the collector resulting from the use of the TiO_2 nanofluid was less than that of MWCNT. Also, the attempt to increase the stability in heat transfer applications by using surfactants was unsuccessful because the formation of foam had a severe adverse effect on collector's efficiency. Therefore, other methods for increasing the stability of the nanofluid should be studied further. Also, it can be concluded that the nanoparticles had a more significant and beneficial effect in the laminar flow region.

The effect of using water-based 1-nm SWCNTs nanofluid on the performance of a natural-circulation FPSC was studied experimentally by Vijayakumaar et al. (2013). Two identical 0.74 × 0.485-m FPSCs were fabricated. The weight fractions of nanoparticles were kept at 0.40%, 0.50%, and 0.60%, the mass flow rate of the nanofluid varied around 5 l/min, and Polysorbate80 was added as a surfactant. The collector's absorber plate and tubes were copper, and it had a single 5-mm glass cover; a 50-mm thickness of glass wool insulation was used. ASHRAE Standard 93 was selected as a basis for calculating the efficiency of the collector. Tests were performed between 11:00 A.M. and 2:00 P.M. In comparison to water, the results showed a maximum increase in the efficiency of the collector about 39% using 0.5 wt% SWCNT/water nanofluid. It can be concluded that the use of carbon nanostructure-based nanofluids (SWCNT/water) as working fluids can result in a good increase in the efficiency of the collector at low weight concentrations. It is important to mention that no information was provided about the stability of the nanofluids that were prepared.

The thermophysical properties of water/Al_2O_3 and ethylene glycol (EG)-water/Al_2O_3 nanofluids and their effect on the pumping power were investigated for a FPSC by Said et al. (2013a). Nanofluids with volumetric concentrations of 0.05–0.1% were synthesized by a two-step method using 13-nm Al_2O_3 nanoparticles, an ultrasonic probe, and a high pressure homogenizer. The stability of water/Al_2O_3 nanofluid was better than that of the EG-water/Al_2O_3 nanofluid. The results showed almost a linear increase in the measured thermal conductivity with concentration. The measured viscosity of the nanofluid was dependent significantly on the base fluid that was used, volume concentration, and temperature. At low volume concentration, the calculated values of pressure drop and pumping power were very close to those of the base liquid. Thus, it was concluded that nanofluids can successfully be used to increase heat transfer rates in various heat transfer applications. It could be noted that no information was provided about the stability of the nanofluids that were synthesized.

Jamal-Abad et al. (2013) had synthesized Cu/water nanofluids with weight concentrations of 0.05% and 0.1% using the one-step method and studied the effect of using them as heat transfer fluids on the efficiency of the FPSC. ASHRAE Standard 93 was used as basis for the experimental tests. The nanofluids were prepared using 35-nm Cu nanoparticles and sodium dodecyl sulfate (SDS) surfactant at a ratio of 1-1 SDS-Cu. A 1.0 × 0.67-m FPSC tilted at an angle of 35° was used in this work. Based on the experimental results, the efficiency of the collector increased as the weight concentration of the nanoparticles increased. In comparison with water, there was an increase of approximately 24% in efficiency at 0.05-wt% nanofluid. Thus, it was concluded that nanofluids could have significant potential as working fluids in FPSCs. Note that the effect on the performance of the collector due to the foam that was created when the SDS surfactant was used had not been considered, and no information was provided about the stability of the nanofluids in the presence of surfactant, especially at temperatures greater than 60 °C.

The effect of utilizing SiO_2-EG/water nanofluid as a working fluid in a 1.59-m^2 FPSC was studied by S. S. Meibodi et al. (2015). The average size of the nanoparticles was 40 nm, the volume concentrations were 0.5%, 0.75%, and 1.0%, the ratio of EG to water was (1:1), and the considered mass flow rates were 0.018, 0.032, and 0.045 kg/s. Using visual observations made with the naked eye, it was concluded that the nanofluids were stable since no sedimentation was observed two weeks after they were prepared. Even with the low thermal conductivity of SiO_2, the results indicated that there was an improvement of up to 8% in the thermal efficiency of the collector, in comparison with water, when 1.0-vol% SiO_2-EG/water nanofluid was used (Figure 2.3). Since the values of the thermal efficiencies obtained with the 0.75% and 1.0% volume concentrations were close to each other, it was preferred to use the lower concentration to decrease the cost and increase the stability. The results clarified the possibility of using SiO_2 nanofluid to increase the efficiency of the FPSC. However, it can be concluded from the results of this research that the increase in FPSC's performance was lower than the increase that was obtained by other researchers using carbon nanostructure-based nanofluids with lower volume fractions. Also, no information was provided about the long-term stability of the nanofluid samples that were prepared.

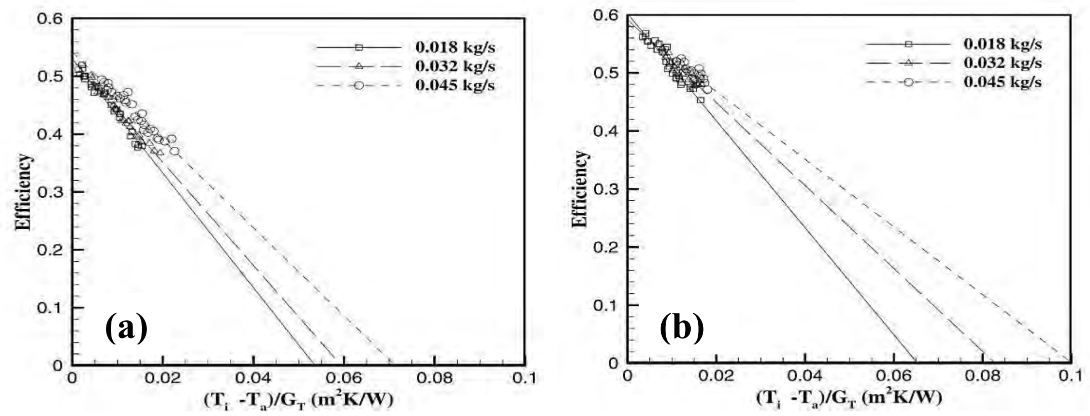

Figure 2.3: Efficiency of the FPSC used by S. S. Meibodi et al. (2015) at different flow rates using (a) water and (b) 1.0-vol% SiO_2-EG/water nanofluid.

Said et al. (2015a) had studied the performance of a 1.84-m^2 FPSC using TiO_2-water nanofluid as its working fluid. The FPSC was tilted at an angle of 22°, and it had an aluminum alloy frame, a 4-mm tempered glass, 22-mm diameter header tubes, and 10-mm diameter riser tubes. Two methods were used to increase the colloidal stability: a high pressure homogenizer and use of polyethylene glycol 400 (PEG 400) surfactant. The volume fractions were 0.1% and 0.3%, the mass flow rates were 0.5, 1.0 and 1.5 kg/min, and dimensions of the nanoparticles ranged between 20 and 40 nm. Thirty days after the working fluid was prepared, the zeta potential values of all of the nanofluid samples were greater than 30 mV. The results showed that thermal conductivity increased as the volume fraction increased up to 6% at 0.3% TiO_2. Furthermore, viscosity increased as concentration increased and decreased as temperature increased. In comparison to water, the energy efficiency of the solar collector using the TiO_2-water nanofluid was greater, up to 76.6% at 0.1% volume fraction and a flow rate of 0.5 kg/min. The pressure drop and pumping power data for TiO_2 nanofluid were very close to the data obtained using the base fluid. From this research, it can be observed that at high flow rates, the energy efficiency of the collector was lower than that obtained by other researchers using carbon nanostructure-based nanofluids. Furthermore, because of the presence of surfactant, the stability of the nanofluid at temperatures above 60 °C should be investigated.

Moreover, utilizing the test setup of the preceding work (Said et al., 2015a), the effect of using water-based SWCNT nanofluid as a working fluid on the energy efficiency of a FPSC was investigated by Said et al. (2015b). SDS was used as a surfactant for synthesizing the nanofluid. The length of the SWCNT used was 1–3 μm and the diameter was 1–2 nm. Volume concentrations of 0.1% and 0.3% and flow rates of 0.5, 1.0, and 1.5 kg/min were used. Nanofluid with a SWCNT/SDS ratio of 1:1 was found to be stable for more than 30 days. A linear increase in thermal conductivity was observed as concentration and temperature increased, but both viscosity and specific heat increased as concentration increased and decreased as temperature increased. The maximum value of energy efficiency that was attained using nanofluid was 95.12%, whereas with water it was 42.07%. From this research, it can be noticed that the collector reached high energy efficiency when carbon nanostructure-based nanofluid was used. However, the effect of the foam created from the presence of SDS surfactant on the performance of the collector was not considered. Also, no information was provided concerning the stability of the nanofluid in the presence of surfactant at temperatures greater than 60 °C.

Michael & Iniyan (2015) had conducted experiments to study the effect of using CuO/water nanofluid as the working fluid on the performance of a 2.08 × 1.05-m FPSC. Tests were performed with both natural and forced circulations. SDBS surfactant and a 0.05% volumetric concentration of CuO were used. Higher enhancement of the collector's performance occurred when natural (thermosyphon) circulation was used rather than forced circulation. A maximum increase of 6.3% in the efficiency of the collector was obtained using the CuO/water nanofluid. From this research, it can be observed that the efficiency of the collector was lower than that obtained when using carbon nanostructure-based nanofluids. Also, no information was provided about the long-term stability of the nanofluid, and no consideration was given to the effect of the foam that resulted from the SDBS surfactant on the efficiency of the collector. In addition, the stability of the nanofluid in the presence of the surfactant at temperatures greater than 60 °C was not addressed.

The thermophysical properties of GNPs/water nanofluid in addition to the effects of using this nanofluid as a working fluid on the thermal performance of a FPSC were investigated by Ahmadi et al. (2016). Two-step method with 60-min ultrasonication time was followed to synthesize nanofluids with weight concentrations of 0.01% and 0.02%. The 0.47 × 0.27-m FPSC was built using 1.0-mm copper plate, 6.3-mm copper tube, and single glass cover. The value of pH was controlled to reach higher values of zeta potential, i.e., better colloidal stability, and a pH value of 11.6 led to a maximum zeta potential value of about (-49). Thermal conductivity increased as temperature and weight concentration increased, up to 11.37% and 13.7% for 0.01-wt% and 0.02-wt% GNPs/water nanofluids, respectively (Figure 2.4a). The absorbed energy and outlet fluid temperature of the FPSC increased as weight concentration increased (Figure 2.4b). In comparison with water, results revealed that the zero heat loss thermal efficiency of the FPSC was enhanced by 12.19% and 18.87% when 0.01 and 0.02 wt% of GNPs/water nanofluids were used, respectively (Figure 2.5a). The theoretical values of thermal efficiency were calculated using the mathematical model of Duffie & Beckman (2013) and presented with experimental values of efficiency in Figure 2.5a. From which, it is clear that the mathematical model underestimates the thermal efficiency values obtained from test runs. From this research, it can be noted that relatively high enhancement in collector’s energy efficiency was attained using very low concentrations of carbon nanostructure-based nanofluid. However, the SSA and other GNP’s specifications are not available and no information was provided about long-term colloidal stability of the nanofluids that were prepared.

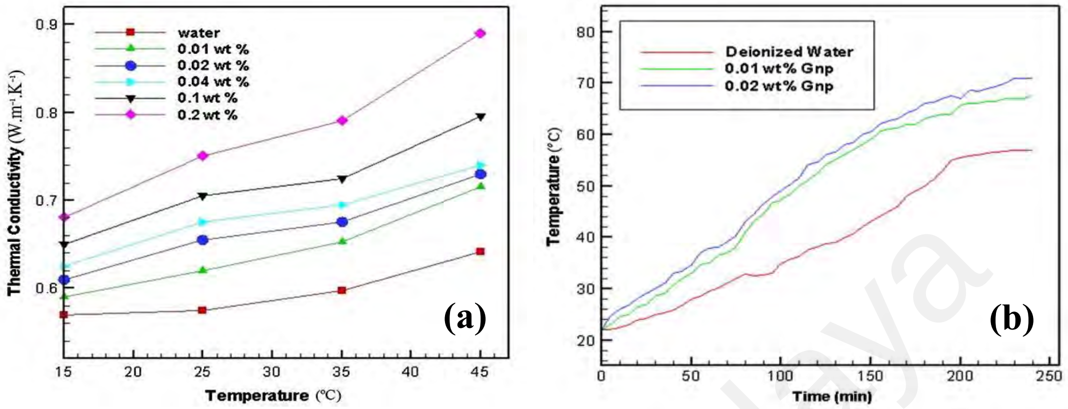

Figure 2.4: (a) Variation of thermal conductivity with temperature and weight concentration, and (b) variation of outlet fluid temperature of the FPSC with time for water and GNPs/water nanofluids (Ahmadi et al., 2016).

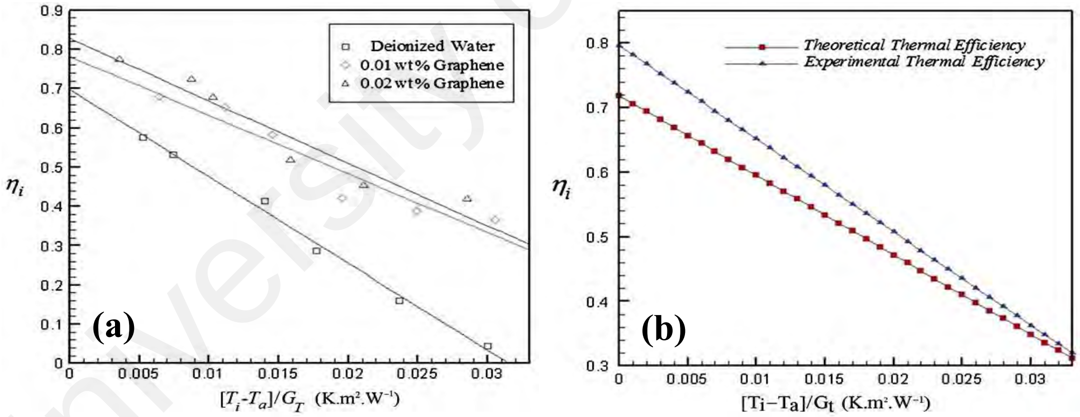

Figure 2.5: (a) Thermal efficiency of the FPSC for water and GNPs/water nanofluids, and (b) experimental versus theoretical efficiency of the FPSC (Ahmadi et al., 2016).

The thermal performance of a 107 × 107-cm FPSC using SiO_2/water nanofluid as its working fluid was experimentally studied by Noghrehabadi et al. (2016). The 1.0-wt% nanofluid was prepared using the two-step method with 12-nm nanoparticles, 60-min ultrasonication, and without any surfactant. The collector was constructed using 1.5-mm copper plate, 6.2-mm copper tube, and 6-mm glass cover. The FPSC was tested at different values of flow rate (0.35–2.8 l/min), solar radiation, and temperature. The use of nanofluid had increased the efficiency in comparison to water. As the flow rate increased, the collector efficiency increased and the difference between inlet and outlet temperatures decreased. From this research, it can be realized that the enhancement in the thermal efficiency in the presence of 1.0-wt% SiO_2/water nanofluid is lower than that found using nanofluids containing carbon-based nanostructures with lower weight concentrations Also, no information was given about the colloidal stability of the nanofluids that were prepared.

The energy efficiency of a 1.84-m^2 FPSC using aqueous colloidal dispersions of Al_2O_3 as its working fluids was investigated by Said et al. (2016). The efficiency of the FPSC was evaluated based on ASHRAE Standard 93. Nanofluid with volume fraction of 0.1% was prepared by the two-step method using 13- and 20-nm nanoparticles. The FPSC was tested at mass flow rates of 0.5, 1.0, and 1.5 kg/min and made from 4-mm tempered glass cover, 10-mm riser tube, 20-mm header tube, and aluminum frame. The pH of the nanofluid was varied to control the colloidal stability. The stability of the nanofluids was found to increase with the decrease in the volume fraction and size of nanoparticles. It was found that thermal conductivity and energy efficiency improved with the addition of Al_2O_3 nanoparticles to the base fluid, but higher improvement was reached with the smaller nanoparticles, i.e., the 13-nm Al_2O_3. When compared with water, the energy efficiency increased up to 73.7% for the 13-nm Al_2O_3/water nanofluid at 1.5 kg/min and 70.7% for the 20-nm Al_2O_3/water at 1.0 kg/min. From this research, it can be noted that no information was given about the long-term stability of the nanofluids that were prepared. It can also be observed that for the type and weight concentration of nanoparticles used in this research, the enhancements in thermal conductivity and energy efficiency are extremely high in comparison to the work of other researchers in this research field.

S. K. Verma et al. (2016) had experimentally tested a FPSC at flow rates of 0.5, 1.0, 1.5, 2.0, and 2.5 l/min using Magnesium oxide (MgO)/water nanofluid as its working fluid. A commercially available 18-wt% aqueous colloidal dispersion of 40-nm MgO nanoparticles with CTAB surfactant was used to prepare the nanofluids with volume concentrations of 0.25%, 0.5%, 0.75%, 1.0%, 1.25%, and 1.5%. A 75 × 50-cm FPSC was used in the research and consisted of 4-mm single glass cover, 10-mm copper tube, and copper absorber plate. The experimental test runs were performed indoor using solar simulator. Results revealed that the thermal conductivity increased as volume fraction and temperature increased (Figure 2.6a). It was observed that the thermal efficiency had increased with the increase of incident solar radiation (Figure 2.6b). When compared to water, the highest increment in energy efficiency of 9.34% was recorded at a volume fraction of 0.75% and flow rate of 1.5 l/min. From this research, it can be noticed that FPSC's efficiency was lower than that obtained when using carbon nanostructure-based nanofluids. Also, no information is found about the effect of the foam that can be created from the existence of CTAB surfactant on the efficiency of the collector. Also, the stability of the nanofluid at temperatures higher than 60 °C in the presence of the surfactant was not investigated.

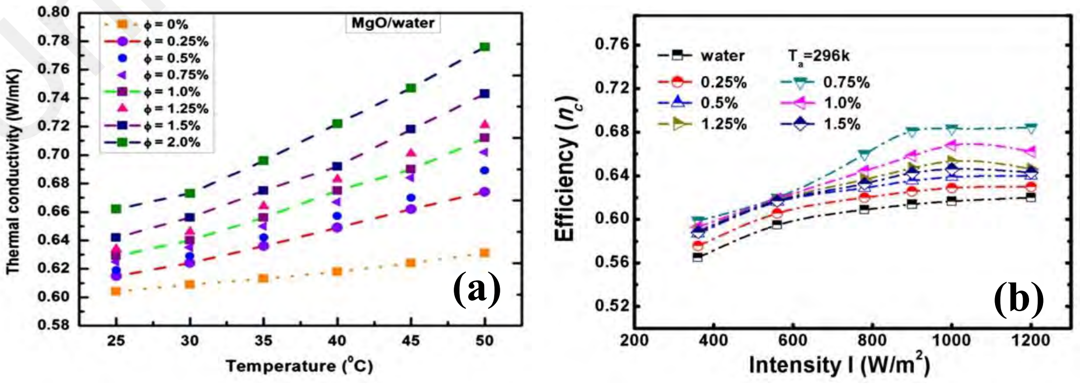

Figure 2.6: (a) Variation of thermal conductivity with temperature at different volume fractions, and (b) energy efficiency versus incident solar radiation for water and MgO/water nanofluids (S. K. Verma et al., 2016).

S. K. Verma et al. (2017) had synthesized water-based nanofluids of CuO, Al_2O_3, TiO_2, SiO_2, Graphene, and MWCNT and investigated the influence of using them as working fluids on the performance of a FPSC. Experiments were completed utilizing the same test setup of their earlier work (S. K. Verma et al., 2016). Aqueous Colloidal dispersions of Al_2O_3, TiO_2, SiO_2, CuO, Graphene, and MWCNT with weight concentrations of 23%, 35%, 30%, 18%, 20%, and 20%, respectively, were used to prepare the nanofluids. Using these dispersions, which are commercially available and contain Triton X-100 as a surfactant, water-based nanofluids with volume fractions of 0.25%, 0.5%, 0.75%, 1.0%, 1.5%, and 2.0% were prepared by the two-step method with ultrasonication. Experiments showed that the thermal conductivity increased as volume fraction and temperature increased (Figure 2.7a). As volume concentration increased, the density of nanofluids increased (Figure 2.7b) while the specific heat decreased (Figure 2.8a). Based on the enhancement in energy efficiency of the FPSC in comparison with water, the sequence of water-based nanofluids was MWCNT > Graphene > CuO > Al_2O_3 > TiO_2 > SiO_2 with 23.47%, 16.97%, 12.64%, 8.28%, 5.09%, and 4.08%, respectively (Figure 2.8b). From the presented figures, it can be concluded that the aqueous colloidal dispersions of carbon-based nanostructures, i.e., Graphene and MWCNT, showed better enhancement in thermal conductivity and energy efficiency than those containing oxide nanoparticles, i.e., Al_2O_3, TiO_2, and SiO_2. From this research, it can also be observed in the presence of Triton X-100, no information is presented about the effect of the foam that can be generated on collector's efficiency and the stability of the nanofluid at temperatures higher than 60 °C. Moreover, no information was provided about the long-term stability of the nanofluids that were prepared.

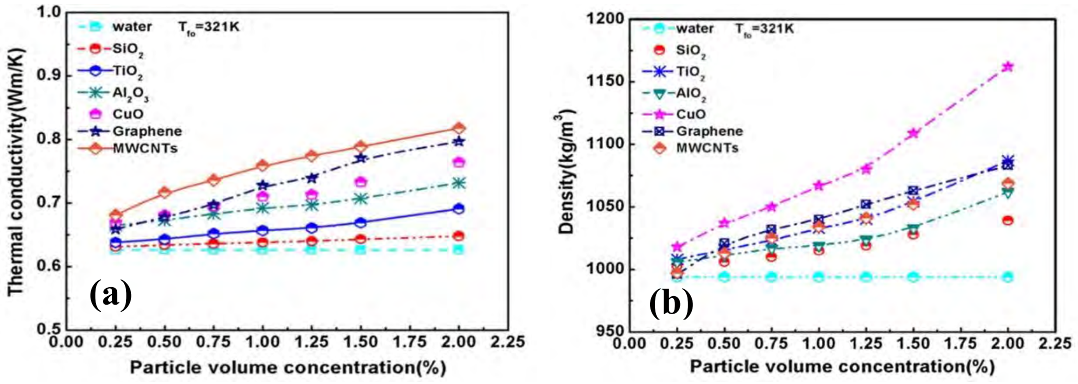

Figure 2.7: Thermal conductivity (a) and density (b) versus volume fraction for water and different aqueous nanofluids (S. K. Verma et al., 2017).

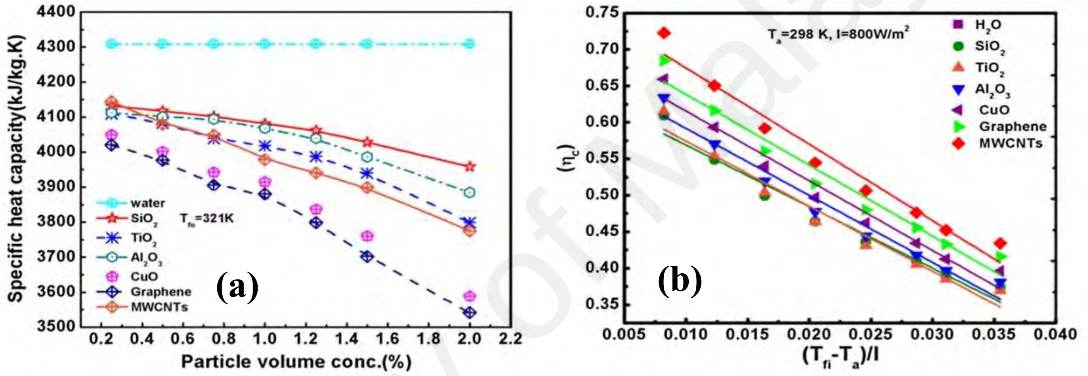

Figure 2.8: (a) Specific heat versus volume fraction, and (b) efficiency versus reduced temperature parameter for water and different nanofluids (S. K. Verma et al., 2017).

2.7.2 Theoretical studies on using nanofluids in FPSCs

The effect of using MWCNT/water nanofluid as the working fluid instead of water on the size of a 2-m^2 FPSC was analyzed by Faizal et al. (2013a). The analysis was based on different mass flow rates and weight fractions of nanoparticles. Calculations of the reduction in the size of the collector were performed using equation (2.30) and data provided by Yousefi et al. (2012a) and Foster et al. (2010). At 12:00 P.M. and for the same temperature of the exit fluid, the calculations showed a reduction of the area of the collector by as much as 37% when the MWCNT/water nanofluid was used, as shown in Figure 2.9a. Therefore, they concluded about the possibility of designing a smaller solar collector without any loss in efficiency, which could reduce the cost required to manufacture solar collectors. However, just one equation was presented in the article for calculating the size of the solar collector, and no clear mathematical model or methodology was presented.

$$A_c = \frac{\dot{m}\, C_p\, (T_o - T_i)}{\eta_c\, G_T} \tag{2.30}$$

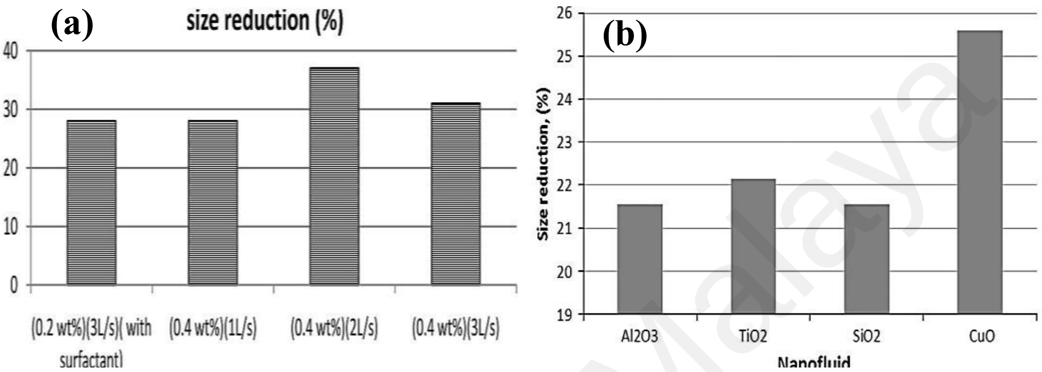

Figure 2.9: Predicted reduction in FPSC's size using: (a) MWCNT nanofluids (Faizal et al., 2013a) and (b) different nanofluids (Faizal et al., 2013b).

Furthermore, Faizal et al. (2013b) maintained the same temperature of the exit fluid and studied the probable reduction in the size of a FPSC using metal oxide nanofluid as a working fluid instead of water. Calculations of the efficiency of the collector and the possible decrease in size, cost, and embodied energy were performed depending on the data of Yousefi et al. (2012a) and other data published in the literature. The metal oxide nanofluids used in the calculations were CuO, SiO_2, TiO_2, and Al_2O_3. The embodied energy considered was only the energy used to manufacture the solar collector, which is more than 70% of the total embodied energy (Ardente et al., 2005). The volume fraction of nanoparticles used was 3% and the volumetric flow rates ranged from 1.0 to 3.8 l/min. Calculations showed that the efficiency of the collector was improved by 38.5% using CuO nanofluid instead of water and by 28.8% using Al_2O_3, SiO_2, and TiO_2 nanofluids instead of water. Based on the calculated efficiencies and using equation (2.30), estimated reductions in area of the collector were as much as

25.6%, 21.6%, 22.1%, and 21.5% using CuO, SiO_2, TiO_2, and Al_2O_3, respectively (Figure 2.9b). Consequently, the reductions in the total weight when manufacturing 1,000 collectors were 10239, 8625, 8857, and 8618 kg for CuO, SiO_2, TiO_2, and Al_2O_3, respectively. Moreover, reductions in embodied energy and CO_2 emission of about 220 MJ and 170 kg, respectively, were predicted. Note that the methodology for calculating the reductions in the areas of the collectors was not clear in the article. Also, the calculations were based on the properties of nanofluids found from correlations published in the literature, which may not provide accurate results due to the various factors that affect them. Therefore, the reliability of data was not high. Also, it can be concluded that the low concentration of MWCNT nanofluid used in a previous article (Faizal et al., 2013a) resulted in the collector's having a higher efficiency and a more significant reduction in size than the oxide nanofluids used in this article.

The influence of Al_2O_3 nanofluid as the working fluid on the performance of a 1 × 2-m FPSC was studied theoretically by Tiwari et al. (2013). ASHRAE Standard 93 and published experimental data were used to calculate the efficiency of the collector. Flow rates of 0.5, 1, 1.5, and 2 l/min and nanoparticle volume fractions of 0.5%, 1%, 1.5%, and 2% were investigated in the study. The results showed that there was a maximum increase of 31.64% in the efficiency of the collector using a flow rate of 2 l/min and 1.5% volume fraction of Al_2O_3 rather than water. Note that the calculations of efficiency were based on the properties of the nanofluids obtained from published correlations, which may not give accurate results due to numerous factors that affect them. Therefore, the validity of data is not considered to be highly reliable.

Tora & Moustafa (2013) had developed a numerical model for simulating the heat transfer performance of a 2-m^2 FPSC using Al_2O_3/water nanofluid as its working fluid. Nanoparticle sizes of 15, 30, 60, and 90 nm at volumetric concentrations of 0.01–0.5% were considered. The model was based on the model of Duffie & Beckman (2013) with the addition of the effects of specific heat, viscosity, thermal conductivity, and the density of nanofluid on the performance of the solar collector. The collector's efficiency using alumina/water nanofluid was higher than that of water data, and it increased as the volume concentration and nanoparticle size increased, and it decreased as (T_i–T_a) increased. Efficiency was increased by 14.7 and 37.44% at volume concentrations of 0.01 and 0.5%, respectively. Note that the calculations of efficiency in this research were based on the properties of nanofluids obtained from published correlations, which may not give accurate results due to the numerous factors that affect them. Also, at a volume concentration of 0.5%, the improvement in the collector's efficiency was found to be much higher than it was in previous research (Tiwari et al., 2013; Faizal et al., 2013b). Thus, due to lack of detailed experimental data (Javadi et al., 2013) and the inconsistency in the numerical results, it can be concluded that developing a highly reliable numerical model for a nanofluid-based FPSC is a challenging task.

In an analytical study, Mahian, Kianifar, Sahin, & Wongwises (2015) examined the effect of using SiO_2/water nanofluid in a FPSC on the heat transfer, pressure drop, and generation of entropy. Turbulent fluid flow was considered, and the volume concentration of SiO_2 used was 1%. Two pH values, i.e., 5.8 and 6.5, and two nanoparticle sizes, i.e., 12 and 16 nm, were used. The results showed that higher heat transfer coefficients and collector efficiencies were obtained using nanofluid rather than water if the viscosity values used in the analysis were calculated from the model of Brinkman (1952) instead of experimental data. Also, by using nanofluids, a higher outlet temperature and a lower entropy generation rate were attained. Note that the difference between the values of the collector's efficiency for water and the different cases investigated were only as high as 0.6%, which is quite low when compared with the results of other researchers in this field.

2.8 Summary

From previous investigations on the use of nanofluids in FPSCs, it is apparent that nanofluids can be effectively used to enhance the performance of FPSCs. While many nanofluids have been investigated as working fluids in solar collectors, additional research is needed to investigate the effect on solar collectors' performance of using some newly-developed nanomaterials with high thermal conductivities. Most researchers have concentrated on using Al_2O_3 and MWCNTs nanofluids, and a few researchers have investigated various other nanofluids, such as Ag, TiO_2, GNPs, ZnO, Fe_2O_3, CuO, MgO, SiO_2, graphene, and SWCNTs. In reviewing the data from various experimental research efforts, it was found that better enhancements in energy efficiency of FPSCs have been achieved using aqueous dispersions with relatively low weight concentrations of carbon-based nanostructures, i.e., GNPs, MWCNTs, graphene, and SWCNTs. On the other hand and using higher weight concentrations of non-carbon-based nanomaterials, lower enhancements in energy efficiency of FPSCs were attained. Therefore, it can be concluded that carbon-based nanostructures are the most promising type of nanomaterials that can be dispersed in water at very low concentrations to efficiently enhance the thermal performance of FPSCs. Lower concentration nanofluids will subsequently have higher dispersion stability, lower cost, with minor increases in viscosity, pressure drop, and pumping power. Accordingly, five carbon-based nanostructures were selected for preparing water-based nanofluids in this study, i.e., graphene nanoplatelets (GNPs) with three different SSAs and multi-walled carbon nanotubes (MWCNTs) with two different outsides diameters.

Covalent and/or non-covalent functionalizations are important for preparing stable nanofluid dispersion. The negative effects of the addition of surfactants, i.e., one of the methods for non-covalent functionalization, on the thermophysical properties of both the base fluid and the nanofluid have been addressed in previous research. Therefore, synthesizing nanofluids using covalently-functionalized nanomaterials is recommended to prepare high-stability nanofluids and use their enhanced thermal performance as working fluids in heat transfer applications (Aravind et al., 2011). Covalent functionalization is a very effective method for converting the behavior of nanomaterials from hydrophobic to hydrophilic, hence it will be easier to disperse them in water and attain higher stability. In this study, covalent and non-covalent functionalization processes will be experimentally investigated. In addition, the effect of various factors on the thermophysical properties of the prepared nanofluids and thermal performance of the FPSC will be carefully considered. The previous theoretical and experimental investigations on the use of nanofluids as working fluids in FPSCs are summarized in Table 2.1.

Table 2.1: Previous investigations on the use of nanofluids in FPSCs.

Author	Base fluid type	Nanomaterial			Surfactant	FPSC specifications	Highlights and Remarks
		Type	Size (nm)	Concentration			
Experimental Studies							
Natarajan & Sathish (2009)	Water	MWCNT	N/A	0.2 to 1.0 vol%	SDS	N/A	• Stability tests showed a concentration of 90% after 400 hours. • At 1.0 vol%, thermal conductivity increased 41%. • Effect of temperature > 60°C on surfactant is not considered.
Polvongsri & Kiatsiriroat (2011)	Water	Ag (Silver)	20	0.1 and 1.0 wt%	Without	1.0 × 0.15 m	• No information was presented in the paper about the colloidal stability of the prepared nanofluid. • The increase in FPSC's performance was less than that when using MWCNT.
Yousefi et al. (2012a)	Water	MWCNT	10 - 30	0.2 and 0.4 wt%	Triton X-100	2 m^2	• Unstable nanofluid samples without surfactant. • Low stability with surfactant, up to 10 days. • At 0.4 wt%, good increase in performance found. • Effect of temperature on surfactant is not considered.
Yousefi et al. (2012b)	Water	Al_2O_3	15	0.2 and 0.4 wt%	Triton X-100	2 m^2	• Unstable nanofluid samples without surfactant. • Low stability with surfactant, up to 3 days. • Increase in performance was less than that using MWCNT. • Effect of temperature on surfactant is not considered.
Yousefi et al. (2012c)	Water	MWCNT	10 - 30	0.2 wt%	Triton X-100	2 m^2	• Low stability with surfactant, up to 10 days. • Better stability with pH values higher or lower than isoelectric point, (7.4 for MWCNT). • Increased efficiency with the increase in nanofluid stability. • Effect of temperature on surfactant is not considered. • It can be concluded that nanofluid stability is one of the main effective factors on performance.

Table 2.1, continued

Author	Base fluid type	Nanomaterial			Surfactant	FPSC specifications	Highlights and Remarks
		Type	Size (nm)	Concentration			
Chaji et al. (2013)	Water	TiO_2	20	0, 0.1, 0.2 and 0.3 wt%	Without	0.5 × 0.2 m	• Less increase in efficiency than that using MWCNT. • No surfactants were used because of high foam. • Low stability without surfactant, about 4 hours. • Nanofluid was more effective in laminar flow region.
Vijayakumaar et al. (2013)	Water	SWCNTs	1	0.40, 0.50 and 0.60 wt%	Polysorbate 80	0.74 × 0.485 m	• At 0.5 wt%, the increase in FPSC's performance was close to that using MWCNT. • Effect of temperature on surfactant is not considered. • No information about nanofluid stability is presented.
Said et al. (2013a)	Water and EG / water 60:40	Al_2O_3	13	0.05–0.1 vol%	Without	N/A	• Water/Al_2O_3 has better stability than EG-water/Al_2O_3. • Increased thermal conductivity with concentration. • Viscosity highly depends on base fluid used, volume concentration, and temperature. • Pressure drop and pumping power values were very close to base liquid at low volume concentration. • No information about long term stability is provided.
Jamal-Abad et al. (2013)	Water	Cu	35	0.05 and 0.1 wt%	SDS	1.0 × 0.67 m	• At 0.05 wt%, the increase in efficiency was around 24%. • No information about nanofluid stability is presented. • Effect of temperature > 60°C on surfactant is not considered. • The effect of foam created from the existence of SDS surfactant on collector's performance is not considered.
S. S. Meibodi et al. (2015)	EG / water 1:1	SiO_2	40	0.5, 0.75, and 1.0 vol%	Without	1.59 m^2	• The prepared nanofluids were concluded to be stable when no sedimentation was observed after two weeks from preparation. • At 1.0 vol%, increase in FPSC's efficiency was up to 8%. • Close efficiencies obtained with the 0.75 and 1.0 vol%. • The increase in FPSC's performance is less than that when using carbon nanostructure-based nanofluids. • No information about long term stability is provided.

Table 2.1, continued

Author	Base fluid type	Nanomaterial			Surfactant	FPSC specifications	Highlights and Remarks
		Type	Size (nm)	Concentration			
Said et al. (2015a)	Water	TiO_2	20 and 40 nm	0.1 and 0.3 vol%	PEG 400	1.84 m^2	• After 30 days, zeta potential was higher than 30 mV. • Thermal conductivity increased up to 6% at 0.3% TiO_2. • Viscosity increased with vol% and decreased with temp. • Energy and exergy efficiencies of the FPSC when using nanofluids were higher than those for water. • Pressure drop and pumping power for nanofluids were very close to water. • Collector's energy efficiency presented is lower than that obtained using carbon nanostructure-based nanofluids. • Effect of temperature > 60°C on surfactant is not considered.
Said et al. (2015b)	Water	SWCNTs	Length = 1–3 µm, Diameter = 1–2 nm	0.1 and 0.3 vol%	SDS	1.84 m^2	• Water-based 1:1 SWCNT/SDS nanofluid was found to be stable after 30 days. • Thermal conductivity for nanofluids increased as vol% and temperature increased. • Viscosity and specific heat increased with concentration and decreased with temperature. • Energy and exergy efficiencies reached 95.12% and 26.25%, while water was 42.07% and 8.77%, respectively. • The effect of foam created from the existence of SDS surfactant on collector's performance is not considered. • Effect of temperature > 60°C on surfactant is not considered.
Michael & Iniyan (2015)	Water	CuO	0.3 and 0.21 nm	0.05 vol%	SDBS	2.08×1.05 m	• Higher enhancement in performance was found in natural (thermosyphon) circulation than forced circulation. • With the use of nanofluid, a maximum increase of 6.3% in collector's efficiency. • Collector's energy efficiency reached is lower than that obtained using carbon nanostructure-based nanofluids. • The effect of foam created from the existence of SDBS surfactant on collector's performance is not considered. • Effect of temperature > 60°C on surfactant is not considered.

Table 2.1, continued

Author	Base fluid type	Nanomaterial			Surfactant	FPSC specifications	Highlights and Remarks
		Type	Size (nm)	Concentration			
Ahmadi et al. (2016)	Water	GNPs	N/A	0.01 and 0.02 wt%	Without	0.47 × 0.27 m	• Thermal conductivity increased as wt% and temperature increased up to 11.37% for 0.01-wt% and 13.7% for 0.02-wt%. • pH value of 11.6 led to a maximum zeta potential of about (-49). • Absorbed energy and outlet temperature increased with wt%. • Thermal efficiency enhanced with GNPs/water nanofluids up to 12.19% for 0.01-wt% and 18.87% for 0.02-wt%. • The mathematical model underestimates the thermal efficiency values obtained from experimental test runs. • Relatively high enhancement in energy efficiency using very low concentrations of carbon nanostructure-based nanofluid. • SSA and other specifications of the GNPs used are not available. • No information was provided about long-term colloidal stability.
Noghrehabadi et al. (2016)	Water	SiO_2	12 nm	1.0 wt%	Without	107 × 107 cm	• The two-step method was used with 60-min ultrasonication. • Volume flow rate range was (0.35–2.8 l/min). • Nanofluids increased thermal efficiency in comparison to water. • As flow rate increased, the collector efficiency increased and the difference between inlet and outlet temperatures decreased. • Enhancement in efficiency with 1.0-wt% nanofluid is lower than those using carbon-based nanostructures with lower wt%. • No information about the colloidal stability of the nanofluids.
Said et al. (2016)	Water	Al_2O_3	13 and 20 nm	0.1 vol%	N/A	1.84 m^2	• The pH of the nanofluid was varied to control the stability. • Stability increased as vol% and size of nanoparticles decreased. • Higher improvement in thermal conductivity and energy efficiency with the smaller nanoparticles, i.e., the 13-nm Al_2O_3. • Energy efficiency increased up to 73.7% for the 13-nm Al_2O_3 at 1.5 kg/min and 70.7% for the 20-nm Al_2O_3 at 1.0 kg/min. • No information was given about the long-term stability.

Table 2.1, continued

Author	Base fluid type	Nanomaterial			Surfactant	FPSC specifications	Highlights and Remarks
		Type	Size (nm)	Concentration			
S. K. Verma et al. (2016)	Water	MgO	40 nm	0.25, 0.5, 0.75, 1.0, 1.25, and 1.5 vol%	CTAB	75 × 50 cm	• The test runs for the FPSC were performed indoor by using a solar simulator. • Thermal conductivity of nanofluid increased as vol% and temperature increased. • Thermal efficiency of the FPSC increased as incident solar radiation increased. • The highest enhancement in energy efficiency of 9.34% was at 0.75 vol% and flow rate of 1.5 l/min. • Energy efficiency was lower than that obtained when using carbon nanostructure-based nanofluids. • No information about the effect of the foam that can be created from the existence of CTAB surfactant on the efficiency. • Effect of temperature higher than 60°C on surfactant and stability is not considered.
S. K. Verma et al. (2017)	Water	CuO, Al_2O_3, TiO_2, SiO_2, Graphene, and MWCNTs		0.25, 0.5, 0.75, 1.0, 1.5, and 2.0 vol%	Triton X-100	75 × 50 cm	• The test runs for the FPSC were performed indoor by using a solar simulator. • Thermal conductivity of nanofluid increased as vol% and temperature increased. • As vol% of nanomaterials increased, density increased and Cp decreased. • The sequence of enchantment in energy efficiency was MWCNT > Graphene > CuO > Al_2O_3 > TiO_2 > SiO_2 with 23.47%, 16.97%, 12.64%, 8.28%, 5.09%, and 4.08%, respectively. • Graphene and MWCNT showed better enhancement in thermal conductivity and energy efficiency than Al_2O_3, TiO_2, and SiO_2. • No information about the effect of the foam that can be created from the existence of Triton X-100 surfactant on the efficiency. • Effect of temperature higher than 60°C on surfactant and stability is not considered. • No information about the long-term stability of nanofluids.

Table 2.1, continued

Author	Base fluid type	Nanomaterial			Surfactant	FPSC specifications	Highlights and Remarks
		Type	Size (nm)	Concentration			
Theoretical Studies							
Faizal et al. (2013a)	Water	MWCNT	10 - 30	0.2 and 0.4 wt%	N/A	2 m^2	• Estimated reduction of collector's area of up to 37%. • No mathematical model is provided. • Methodology used is not clear.
Faizal et al. (2013b)	Water	CuO, SiO_2, TiO_2 and Al_2O_3	N/A	3.0 vol%	N/A	2 m^2	• Efficiency improved 38.5% using CuO and 28.8% using Al_2O_3, SiO_2, and TiO_2 nanofluids. • Reduction in collector's area of 25.6, 21.6, 22.1 and 21.5% using CuO, SiO_2, TiO_2, and Al_2O_3, respectively. • Methodology used is not clear. • Nanofluid properties calculated from correlations. • Using lower wt% MWCNT, performance was higher.
Tiwari et al. (2013)	Water	Al_2O_3	N/A	0.5, 1, 1.5, and 2% vol%	N/A	1.0 × 2.0 m	• Maximum increase of 31.64% in collector's efficiency using volume fraction of 1.5% Al_2O_3 at 2 l/min. • Effect of high concentration (1.5% Al_2O_3) on viscosity and pumping power is not considered. • Nanofluid properties calculated from correlations.
Tora & Moustafa (2013)	Water	Al_2O_3	15, 30, 60, and 90	0.01, 0.05, 0.1 and 0.5 vol%	N/A	2 m^2	• Efficiency increased by 14.7 and 37.44% at volume concentrations of 0.01 and 0.5%, respectively. • Efficiency increased with volume concentration, nanoparticle size, and with the decrease of $(T_i - T_a)$. • Nanofluid properties calculated from correlations. • Higher increase in efficiency than previous researches.
Mahian et al. (2015)	Water	SiO_2	12 and 16	1.0 vol%	N/A	3.0 × 3.5 m	• Type of fluid flow considered was turbulent. • Collector's efficiency with nanofluid was higher than water if the viscosity was calculated instead of experimental data. • Using nanofluid, higher (T_o) and lower entropy was reached. • It can be noticed that increase in efficiency was up to 0.6%, which is quite low when compared with other researches in this field.

CHAPTER 3: METHODOLOGY

3.1 Introduction

The present study aims at investigating, theoretically and experimentally, the effect of using aqueous colloidal dispersions of carbon-based nanostructures, i.e. nanofluids, as working fluids on the thermal performance of a FPSC. The objective of this chapter is to present comprehensive details of the methodology employed to fulfill the requirements of this study and reach the intended aim. This includes detailed information about the materials used, synthesis of nanofluids, measurement of colloidal stability, characterization, thermophysical properties, experimental setup, testing procedure, mathematical model, and the MATLAB code for simulating the thermal performance of nanofluid-based FPSCs.

3.2 Materials

The materials used in this study are listed and categorized in the following sections. Distilled water was used as the base fluid in all the nanofluids that were prepared in this study.

3.2.1 Nanomaterials

The specifications of the different carbon-based nanostructures that were used in this study are as follows:

3.2.1.1 Graphene nanoplatelets (GNPs)

Pristine graphene nanoplatelets (GNPs) (grade C) with three different SSAs of 300, 500, and 750 m^2/g were used in this work and purchased from XG Sciences, Inc., Michigan, USA. Each graphene nanoplatelet is made up of a few graphene sheets with a total thickness and lateral size of about 2 nm and 2 μm, respectively. Detailed specifications are shown in Table 3.1.

Table 3.1: Specifications of the pristine graphene nanoplatelets (GNPs) Grade C.

Item	Specification
Supplier company	XG Sciences, Inc., Michigan, USA
Appearance	Powder
Color	Black
Carbon content	> 99.5%
Bulk density	0.1 - 0.14 g/cm^3
True density	2.2 g/cm^3
Average specific surface area	300, 500, and 750 m^2/g
Average lateral size	< 2 μm
Average thickness	≈ 2 nm
Thermal conductivity { Parallel to GNP surface Perpendicular to GNP surface	3000 W/m.K 6 W/m.K

3.2.1.2 Multi-walled carbon nanotubes (MWCNTs)

Pristine MWCNTs with purity higher than 95%, length of 10–30 μm, and two different outside diameters of less than 8 nm and 20–30 nm were used in this work and procured from Nanostructured & Amorphous Materials, Inc., USA. Specifications in detail are presented in Table 3.2.

Table 3.2: Specifications of the pristine multi-walled carbon nanotubes (MWCNTs).

Item	Specification	
Supplier company	Nanostructured & Amorphous Materials, Inc., USA.	
Appearance	Powder	
Color	Black	
Purity	> 95%	
Outside diameter	< 8 nm	20–30 nm
Inside diameter	2–5 nm	5–10 nm
Length	10–30 μm	10–30 μm
True density	2.1 g/cm^3	2.1 g/cm^3
Average specific surface area	> 500 m^2/g	> 110 m^2/g

3.2.2 Surfactants

The non-covalent functionalization process of the GNPs in this study was implemented using four surfactants, i.e., gum Arabic (GA), cetyl trimethylammonium bromide (CTAB), sodium dodecyl sulfate (SDS), and sodium dodecyl benzene sulfonate (SDBS). All surfactants were bought from Sigma-Aldrich.

3.2.3 Chemicals

In this study, the covalent functionalization processes for the different pristine nanomaterials were performed using several analytical grade chemicals: Aluminum chloride ($AlCl_3$), hydrochloric acid (HCl), N,N-dimethylacetamide (DMA), beta-alanine (β-Alanine), N,N-dimethylformamide (DMF), ethanol, methanol, and sodium nitrite ($NaNO_2$) from Sigma-Aldrich; and triethanolamine (TEA) from Merck.

3.3 Preparation of nanofluids

The two-step method was used to prepare all the nanofluids in this work, which was selected based on the available devices in the laboratories of the University of Malaya. Nanomaterials were dispersed in distilled water using an ultrasonication probe (Sonics Vibra-Cell, VC 750, Sonics & Materials, Inc., USA) having an output power of 750 W and a power supply with a frequency of 20 kHz. Heat generated during the sonication process caused a large increase in the temperature of the sample and evaporation of water with the subsequent change in the weight concentration of the sample. Hence, water bath was used to keep the temperature at an acceptable level. The required weight of nanomaterials was measured using OHAUS balance (model: OHAUS PA214, Pioneer Series of analytical and precision balances, New Jersey, USA) having a maximum capacity of 210 g with a readability and repeatability of 0.1 mg. In an aqueous solution, the measurement of pH is important to evaluate the acidity or basicity of the solution. The pH for the water-based nanofluids that were prepared in this study was measured by Mettler Toledo EL2 portable pH meter.

3.4 Functionalization of nanomaterials

Covalent or non-covalent functionalization is important to increase the long-term dispersion stability of nanomaterials in base fluids. The functionalization processes that were carried out in this study are summarized in the following two sections.

3.4.1 Non-covalent functionalization using surfactants

The nanomaterials that were used in the non-covalent functionalization process were GNPs with 300-m^2/g SSA. Since GNPs are carbon-based nanostructures that have a hydrophobic surface, they cannot be stably dispersed in water in the absence of a surfactant (Z. Zhang & Lockwood, 2004). It is noteworthy that the GNPs supplier suggested that they can be dispersed in water with probe sonication and by using surfactants. Therefore, non-covalent functionalization was performed using four different surfactants; GA, CTAB, SDS, and SDBS. Five different ultrasonication times of 15, 30, 60, 90, and 120 min were used. Nineteen different nanofluids with 0.1% weight concentration of GNPs were prepared via the two-step method. A weight concentration of 0.1% GNPs was kept constant in the synthesis of all the samples. The surfactant-GNPs weight ratios used were; GA-GNPs (0.25-1, 0.5-1, 0.75-1), CTAB-GNPs (0.5-1, 1-1, 1.5-1), SDS-GNPs (0.5-1, 1-1, 1.5-1), and SDBS-GNPs (0.5-1, 1-1, 1.5-1) (see Table 3.3). The ratio of GA-GNPs selected was less than other surfactants because of the fact that it substantially increases nanofluid viscosity (Garg et al., 2009; Amiri et al., 2015a). The pH values of the nanofluids that were prepared are presented in Table 3.3.

Table 3.3: Details of the samples prepared in the non-covalent functionalization process of GNPs with 300-m^2/g SSA and pH values after preparation.

Sample No.	Ultrasonication time (min)	Surfactant type	Surfactant – GNPs ratio	pH
1	15	–	–	8.82
2	30	–	–	8.71
3	60	–	–	7.48
4	90	–	–	6.75
5	120	–	–	6.65
6	15	SDBS	1.0 – 1.0	7.41
7	30		1.0 – 1.0	7.53
8	60		1.0 – 1.0	7.46
9	60		0.5 – 1.0	7.54
10	60		1.5 – 1.0	7.60
11	60	GA	0.25 – 1.0	8.53
12	60		0.50 – 1.0	7.08
13	60		0.75 – 1.0	6.58
14	60	SDS	0.5 – 1.0	7.17
15	60		1.0 – 1.0	6.48
16	60		1.5 – 1.0	7.42
17	60	CTAB	0.5 – 1.0	4.71
18	60		1.0 – 1.0	4.70
19	60		1.5 – 1.0	4.78

3.4.2 Covalent functionalization (Surface modification)

The covalent functionalization processes that were implemented in this study for the different pristine carbon-based nanostructures are described in the subsequent sections.

3.4.2.1 Covalent functionalization of GNPs

An electrophilic addition reaction is applied for the covalent functionalization of GNPs with triethanolamine. The present approach is completed in the presence of $AlCl_3$ under mild sonication. Further, the same functionalization procedure was followed for the three SSAs of GNPs used in this work, i.e., 300, 500, and 750 m^2/g. The covalently functionalized GNPs with triethanolamine (TEA-GNPs) were morphologically and chemically characterized to analyze the degree of functionalization. For each SSA of the

TEA-GNPs, four different weight concentrations of water-based nanofluids were prepared, i.e., 0.025%, 0.05%, 0.075%, and 0.1%. The colloidal stability and thermophysical properties of the water-based TEA-GNPs nanofluids that were synthesized have been thoroughly investigated and reported.

For preparing covalently functionalized GNPs with triethanolamine (TEA-GNPs), each SSA of the pristine GNPs (10 g) and aluminum chloride ($AlCl_3$) (185.4 g) were mixed and grinded with an agate mortar and pestle for several minutes. The obtained mixture was then poured into a 2-l glass vessel filled with 500-ml Triethanolamine and 1.5-l N,N-dimethylacetamide (DMA), then sonicated and stirred for 6 h and 36 h, respectively, to get a visually homogeneous suspension. During stirring at 80 °C, concentrated hydrochloric acid (5 ml) was added drop by drop to the suspension. The mixture was repeatedly centrifuged and washed with abundant distilled water, followed by N,N-dimethylformamide (DMF), dilute hydrochloric acid, and ethanol to remove unreacted materials, then dried overnight at 60 °C. The mechanism of the reaction can be summarized as follows: With a Lewis acid ($AlCl_3$) as a catalyst and a trifle amount of concentrated hydrochloric acid (HCl) to protonate TEA, an electrophilic addition reaction was carried out between TEA and GNPs through a sonication method. The reaction resulted in the attachment of TEA and hydroxyl groups to the surface of the GNP (Figure 3.1). The hot plate stirrer used in the preparation process was FAVORIT (model: HS0707V2, 4.5 A).

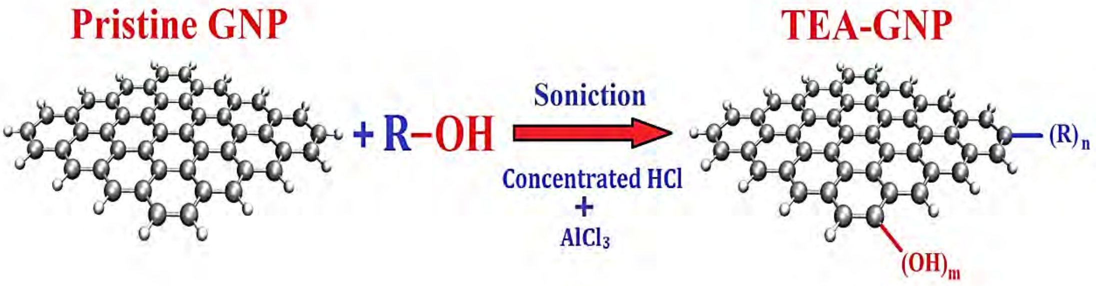

Figure 3.1: Electrophilic addition reaction of GNPs with TEA.

3.4.2.2 Covalent functionalization of MWCNTs

The mechanism for the functionalization of MWCNTs with β-Alanine, shown in Figure 3.2, comprises of generating a semi-stable diazonium ion and initiating a radical reaction with the surface and cap of the MWCNT (Bahr & Tour, 2001; Price & Tour, 2006; Amiri et al., 2011). In a typical experiment, β-Alanine (400 mg) has been sonicated in DMA (20 ml) for 2 h at 60 °C. Then, 200 mg of pristine MWCNTs, 100 mg of $NaNO_2$, and 0.5 ml of HCl were added, followed by 15 min sonication. HCl was added drop by drop in order to avoid side reactants. The mixture was bath-sonicated for 24 h. With an oil bath, the temperature of reaction was maintained at 80 ºC. Then, the resulted Alanine-treated MWCNT (Ala-MWCNT) samples were cooled to the room temperature, and then centrifuged and washed thoroughly. The functionalized MWCNTs were washed several times with DMF, ethanol, and acetone to remove any unreacted materials, and then dried for 96 h at 60 °C. The same functionalization procedure was followed for the two outside diameters of MWCNTs used in this work, i.e., less than 8 nm and 20–30 nm.

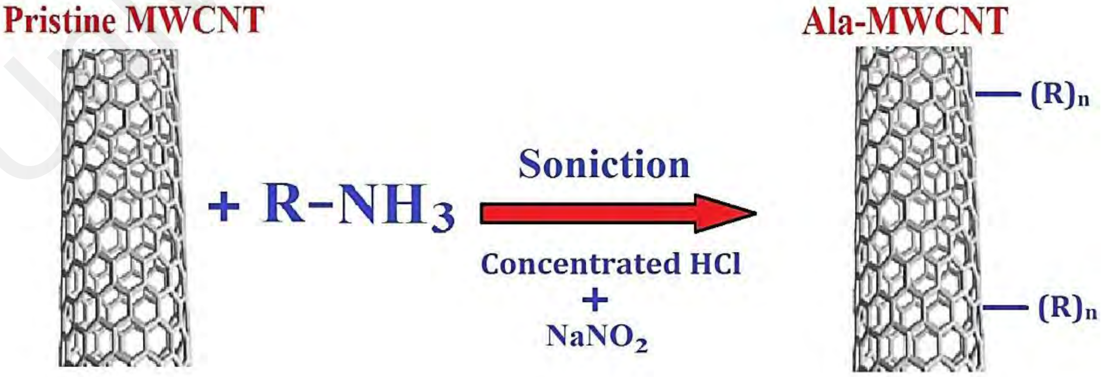

Figure 3.2: Electrophilic addition reaction of MWCNTs with β-Alanine.

3.5 Characterization

Characterization of the various nanomaterials and nanofluids that were prepared in this study was performed using different methods including transmission electron microscopy (TEM), Fourier transform infrared spectroscopy (FTIR), Raman spectroscopy, energy dispersive X-ray spectroscopy (EDS), and measurement of average particle size.

TEM is very beneficial tool to characterize the scattering, size, and shape of the nanomaterials. However, due to the use of dried samples in this method of characterization, the actual state of the nanomaterials in the nanofluid cannot be obtained (Ghadimi et al., 2011). In this method for microscopy, an ultra-thin specimen is used and interacts with a beam of electrons as it passes through it. The image formed from the interaction is enlarged and focused onto an imaging device. In this study, two TEM devices were used: a high-contrast/high-resolution digital TEM from Hitachi (HT7700) with an accelerating voltage of 120 kV and a LEO 912 AB electron microscope with an accelerating voltage of 100 kV. For preparing the specimen for TEM, a drop of dilute nanofluid with a ratio of (1:40) was placed onto a lacey carbon grid and oven-dried at 45 °C overnight.

Fourier transform infrared spectroscopy (FTIR) is a method in which an infrared spectrum of absorption or emission can be obtained for a liquid, solid, or gas. In FTIR, when the infrared radiation passes through a sample, some is transmitted and the other is absorbed by the sample. The spectrum obtained from this test represents the absorption and transmission of molecules, and thus generating a unique fingerprint for the molecules in the sample (Thermo, 2001). In this study, Bruker (IFS 66/S) was used for characterization with FTIR.

Raman spectroscopy is a method used to detect the rotational, vibrational, and other low-frequency modes in a system through which an identification pattern for the molecules can be obtained. It depends on the scattering, of monochromatic light such as laser in the visible, near infrared, or near ultraviolet range. The energy of the laser photons is shifted up or down when it interacts with molecules in the system. The identification pattern is detected from the information about the vibrational modes in the system given by this shift in energy (Smith & Dent, 2013). The Raman spectrometer used in the present study was (Renishaw confocal spectrometer at 514 nm).

Energy dispersive X-ray spectroscopy (EDS) is a procedure based on the interaction of a sample with some source of X-ray excitation and used for the elemental analysis or chemical characterization. The characterization using this technique is based on the essential theory that the unique atomic structure of any element has its unique set of peaks in the X-ray emission spectrum (Goldstein et al., 2003). Desktop scanning electron microscope (Phenom ProX, Netherlands) was used for EDS in this study.

The average particle size (Z-average) was measured in this study using the dynamic light scattering (DLS) principle. DLS is an analytical method in physics that can be used to generate a profile for the size distribution of nanomaterials in colloidal dispersion. In a DLS system, a laser beam is concentrated on a dilute dispersion of a sample contained in a special quartz cuvette, and as it transmits through the colloidal dispersion, the laser light is scattered at different intensities in all directions by the Brownian motion of the dispersed particles. From the analysis of the scattered light and using the Stokes-Einstein relationship, the particle size distribution can be calculated (J. H. Lee, 2009). DLS tests were performed using Zetasizer Nano ZS (Malvern Instruments Ltd, Malvern, UK).

3.6 Measurement devices

The devices used in the evaluation of stability and measurement of thermophysical properties in this work are described in the following two sections.

3.6.1 Stability of nanofluids

The long-term stability of the nanofluids is considered to be essential for their successful use as working fluids in heat transfer applications. The colloidal stability of water-based nanofluids that were prepared in this work was evaluated using two methods: UV–vis spectral analysis and zeta potential.

Measurement of light absorbance of a suspension by UV-vis spectroscopy can provide a quantitative characterization of the colloidal stability. The UV-vis used was Shimadzu UV-spectrometer operating in the range of wavelengths 190-1100 nm (UV-1800, Shimadzu Corporation, Kyoto, Japan). Using special quartz cuvettes suitable for UV region, the light absorbance of all the samples in this study was measured at different time intervals for a period of time (more than 50 days). All samples were diluted with distilled water at a ratio of 1:20 to permit appropriate light transmission through them (Nanda et al., 2008; Vandsburger, 2010; W. Yu et al., 2010; Ghadimi et al., 2011; Harish et al., 2012). Each absorbance reading from the UV-vis spectrophotometer was repeated twice to validate the repeatability of the device, and a maximum difference of 0.08% was obtained.

The measurement of zeta potential for a colloidal dispersion is one of the procedures used by the researchers to evaluate the colloidal stability by determining the degree of repulsion between close particles of the same charge in nanofluid dispersions (H. Zhu et al., 2007; J.-H. Lee et al., 2008; Vandsburger, 2010). Utilizing the principle of electrophoretic light scattering (ELS), the value of zeta potential for the dilute nanofluids that were prepared was measured using Zetasizer Nano ZS (Malvern Instruments Ltd, Malvern, UK).

3.6.2 Thermophysical properties

The measurement devices for thermophysical properties used in this study are presented in the following sections.

3.6.2.1 Thermal conductivity

Thermal conductivity of water-based nanofluids that were prepared was measured using KD2 Pro thermal properties analyzer device (Decagon devices, Inc., USA), which has an accuracy of about 5%. Its operation principle is based on the transient hot wire method using the KS-1 probe which consists of a single needle sensor with 1.3 mm diameter and 60 mm long (shown in Figure 3.3a and b). The main problem encountered towards obtaining a low error reading was the alignment of the probe in the center of sample's vial (shown in Figure 3.3b and c). This problem is more serious when dealing with carbon nanostructure-based nanofluid due to its dark color which makes the visual alignment of probe impossible. Therefore, a modified probe holder was designed and fabricated in order to ensure the highest aliment of the probe inside the vial without the need for frequent check of alignment. The holder consists of two Teflon pieces interconnected with three bolts and nuts embedded in the lower part. The lower Teflon part is connected by a thread to the sample's vial, while the KD2 Pro probe is trapped between the two Teflon pieces. The use of the modified probe holder significantly reduced the error of the readings that were obtained from the KD2 Pro thermal properties analyzer. Details of this probe holder are shown in Figure 3.3d–f. Two water baths were used to keep the samples at the desired temperature during measurements. At 35°C or below, a refrigerated bath circulator "WiseCircu WCR-P6" (Daihan Scientific Co., Ltd., Korea) with 1.4 kW and an accuracy of 0.1°C was used. While a heating bath circulators "Lab. Companion CW-05G" (Jeiotech Co., Ltd., Seoul, Korea) with 1.04 kW and an accuracy of 0.1°C was used for higher temperatures. After filling the vial with the sample and fixing the probe using the modified holder, the vial was placed inside one of the water baths for about thirty minutes before starting measurements to permit for the temperatures of the sample and needle to equilibrate with the temperature of water bath. More than twelve readings were taken for each measuring point with a time period of fifteen minutes between successive readings to allow the temperature of the sample to equilibrate. Readings with device error less than 0.01 were considered and the thermal conductivity of the sample at each point was calculated as the average value of eight readings with the lowest error.

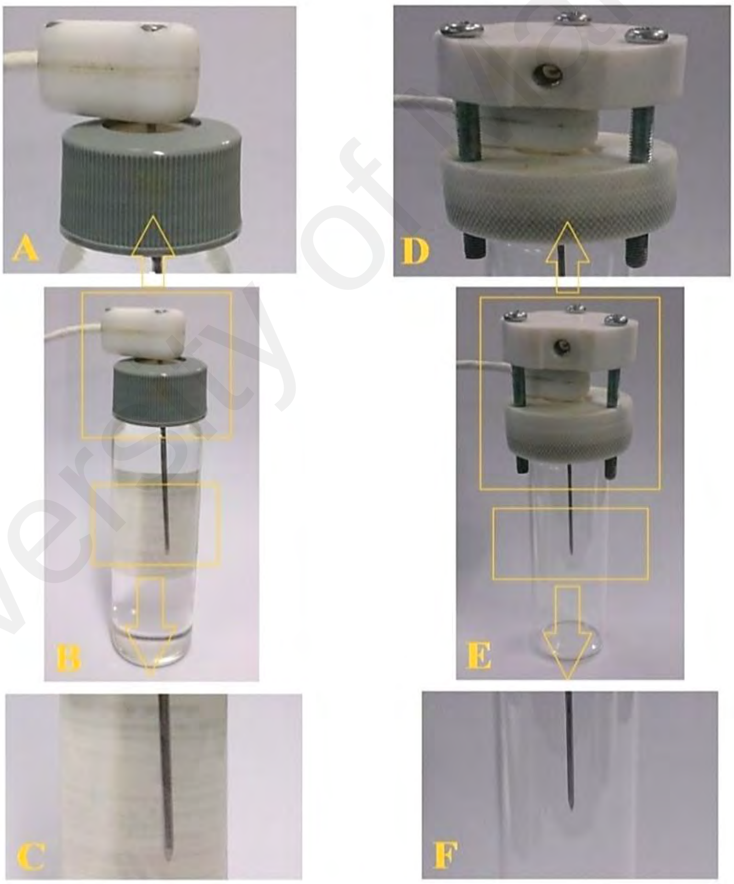

Figure 3.3: Pictorial details of the designed probe holder for KD2 Pro thermal property analyzer. (A–C) Sample's vial with the original cup and probe. (D–F) Sample's vial with the modified cup holder and probe.

3.6.2.2 Dynamic viscosity

The viscosity of any nanofluid is an important factor in specifying its suitability for using as a heat transfer fluid for its direct effect on pressure drop and pumping power. In this study, viscosity of water and water-based nanofluids was measured on a shear-rate controlled Anton Paar rotational rheometer (model Physica MCR 301, Anton Paar GmbH) by using the double gap DG 26.7 measuring system. Shear rates in the range of 20–200 1/s were used to perform the tests at different temperatures.

3.6.2.3 Density

The density of nanofluids that were prepared was measured at different temperatures and weight concentrations using Mettler Toledo density meter (DM40). The measurement range for this device is 0.0–3.0 g/cm^3 with an accuracy of 0.1 mg/cm^3. The principle of measurement for this density meter is based on measuring the period of oscillation of a U-shaped glass tube containing the sample by a sensor. The oscillations are induced by an electromagnetic transmitter with a magnet attached to the U-shaped tube. Using a special relation, the density can be calculated from the period of oscillation. For each sample, the measurement of density at each temperature was repeated for three times and the average value of them was considered as the density of the sample at this temperature.

3.6.2.4 Specific heat

The specific heat can be measured by differential scanning calorimetry (DSC), which is a thermo-analytical technique that monitors the difference between the heat flows supplied to a reference and sample as a function of temperature. In present study, the specific heat of the nanofluids that were prepared was measured at different temperatures and weight concentrations using (DSC-Q2000, TA Instruments).

3.6.2.5 Contact angle

The ability of adhesion for a liquid on a solid surface, i.e., the degree of wetting when a solid and liquid interact, is called wettability. The adhesive and cohesive forces control the wettability, which can be characterized by measuring the contact angle (C. Choi & Kim, 2011; Ortiz-Young et al., 2013). The contact angle was measured for distilled water and water-based nanofluids when they spread on a solid surface (glass slide) at room temperature using OCA15EC of Dataphysics Co. GmbH, Germany. The OCA15EC device uses an optical method and a contour analysis system to determine the contact angle.

3.7 Experimental setup

The test rig used in this study for investigating the thermal performance of nanofluid-based FPSC is presented in Figure 3.4. The experimental system consists of a FPSC, flow loop, refrigerated water bath circulator, data logger, and devices for control and measurement. An electric centrifugal pump was used for circulating the working fluid in the forced convection system. The description of test setup was divided into two sections, i.e., the FPSC section and the flow loop section.

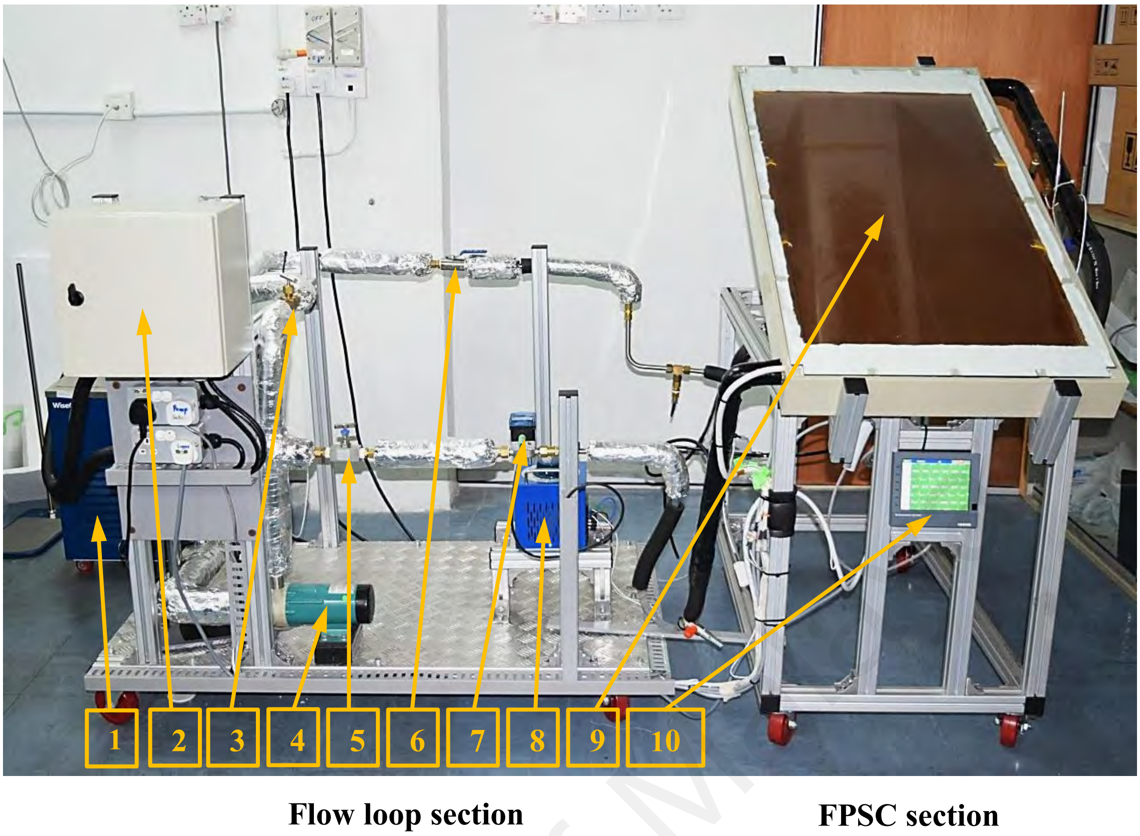

Figure 3.4: Photograph of the full experimental setup used in the present study. The numbered components are as follows; (1) refrigerated water bath circulator, (2) main electrical control box, (3) bypass loop needle valve, (4) electric pump, (5) flow line needle valve, (6) shutoff ball valve, (7) flow meter, (8) variable voltage transformer, (9) the FPSC, and (10) data logger.

3.7.1 Description of the FPSC section

Due to large fluctuations in the solar radiation intensity (irradiance) in Malaysia caused by the intermittent cloudy weather (Nawayseh et al., 1999), the outdoor testing of FPSCs is difficult and it will not provide accurate results. In addition, the cost of solar simulator for indoor testing is relatively high (Codd et al., 2010). Therefore, in this study, the FPSC is tested indoor using a flexible adhesive heater fixed to the upper surface of the absorber plate which generates a constant heat flux analogous to that of the solar radiation (Badran et al., 2008).

The materials used for the fabrication of the FPSC section, shown in Figure 3.5, are as follows: 2-mm copper absorber plate, copper riser and header tubes, glass cover, polypropylene (PP) sheet frame, T-slotted structural aluminum profile stand, adjustable-angle base, and thermal insulation. The detailed specifications of the FPSC section used in the present study are presented in Table 3.4. The copper absorber plate was directly soldered to the copper rise tubes all over the contact length and on both sides of each tube using Tin (Sn)/Silver (Ag) alloy (96.5/3.5). The selection of 2 mm rather than 1 mm for the thickness of the 91.44 × 50.8-cm copper absorber plate was to assure that the plate will remain flat without any corrugations after applying the heat required for the soldering process between the copper absorber plate and riser tubes. The flatness of absorber plate is essential for the perfect installation of the flexible adhesive heater on the top surface of absorber plate. Isowool ceramic fibers blanket with a thermal conductivity of 0.07 W/m K at 400°C was used for thermal insulation. Four parallel 12.7-mm copper riser tubes were used and connected on both sides to 22.2-mm copper header tubes.

The flexible adhesive heater used for generating the constant heat flux analogous to that of solar radiation consists of six separate 30.48 × 25.4-cm insulated flexible heaters (Figure 3.6b) connected together to a variable voltage transformer (Figure 3.6a) for controlling the heat flux of the heater. The heaters were supplied with a pressure sensitive adhesive layer and imported from Omega, USA (model KH-1012/(2.5)-P). Each heater is around 0.14-mm thickness and consists of a layer of an etched foil element of about 0.015-mm thickness surrounded by two insulation layers of 0.05-mm Kapton polyimide film and one layer of 0.025-mm fluorinated ethylene propylene (FEP) adhesive. The total wattage of each heater is 300 W at 115 V with a watt density of 0.39 W/cm^2 (2.5 W/in^2). The wattage of this heater, which is currently the minimum available in the list of products presented at Omega's website, is much higher than the wattage density required in this work. Moreover, the highest working voltage presently available for this type of heaters is 115 V, which is not compatible with the 230-V supply voltage here in Malaysia. Consequently, the heaters are connected in series and parallel in a certain way to reduce the total wattage density and increase the working voltage, as shown in Figure 3.8. The resulting heater has a total wattage of about 800 W at 230 V. In this study, the values of alternating current and voltage for the electric heater were measured using digital AC clamp meter from Kyoritsu (model Kew Snap 2017). The manufacturer specifications showed that the accuracies of measurements for the clamp meter are 1.5% and 1% for current and voltage, respectively.

In this work, surface temperatures of the absorber plate and two riser tubes were measured using T-type self-adhesive surface thermocouples with 2-m fiberglass-insulated wires from Omega, USA (model SA1XL-T-72) (Figure 3.7a). Twelve calibrated T-type thermocouples were installed on the back side of the absorber plate at four different axial positions from the edge of the absorber plate, i.e., 114, 343, 572, and 801 mm (as presented in Figure 3.10). In addition, two calibrated resistance temperature detectors (RTDs) (type PT100) (Figure 3.7b) were installed at the inlet and outlet tubes of the FPSC using copper tees and compress fittings to record the bulk temperatures of the working fluid. Within the range of temperatures used in the experimental test runs, the supplier data showed that the tolerances for the T-type thermocouples and RTDs were ±0.75% and ±(0.15 + 0.002* |T|) °C, respectively. Furthermore, an adjustable-angle base in the range of 0°–60° was used for regulating the tilt angle of the FPSC (Figure 3.9a), which was fixed at 30°.

Omega (PX154-001DI) wet/wet low differential pressure transmitter (DPT) with a range of 0–1 in H_2O (0–249 Pa) (shown in Figure 3.14a) was used to measure the pressure loss across the FPSC and connected through two tapping points at the inlet and outlet tubes. Two pressure snubbers (Omega PS-8E) were connected to both sides of the DPT to eliminate the damaging effects of fluid hammer on the transducer. All thermocouples, RTDs, and DPT were connected to an eighteen-channel Ecolog paperless recorder (EC18) data logger for viewing and recording the experimental data (shown in Figure 3.9b). This data logger comes with six universal analog input/output cards (AI183), each card with three channels. The FPSC is connected to the flow loop using half-inch flexible silicone hoses. Since the diameter of the header tube is bigger than the silicone hose, two custom machined tapered-cone copper connection were used to connect them in order to minimize the disturbance in fluid flow.

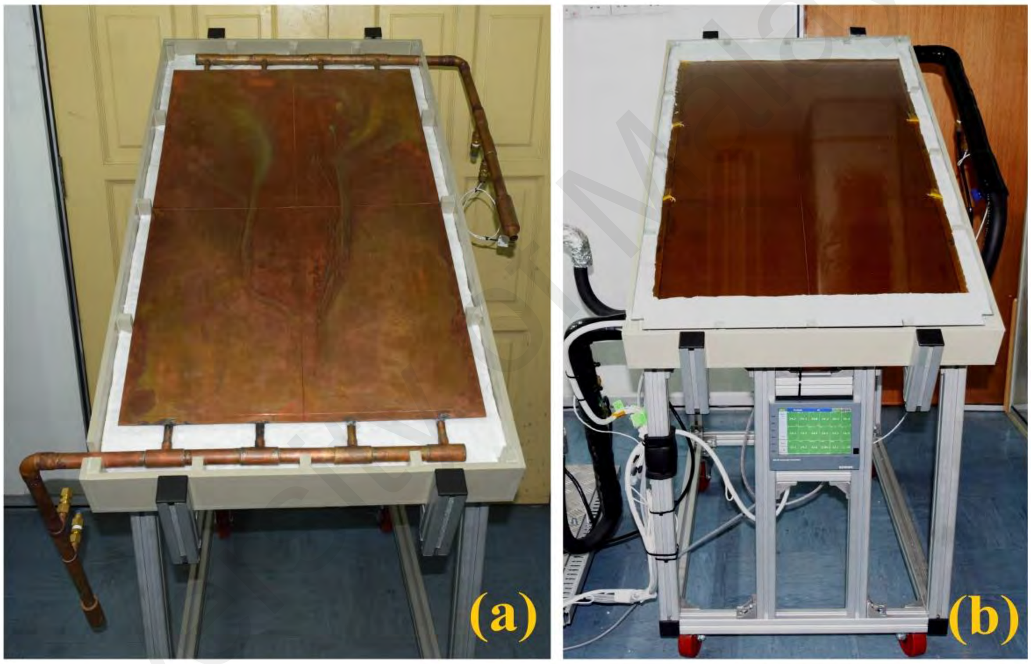

Figure 3.5: (a) The FPSC during the manufacturing process and (b) in the final form after adding the insulation, surface heaters, thermocouples, glass cover, and data logger.

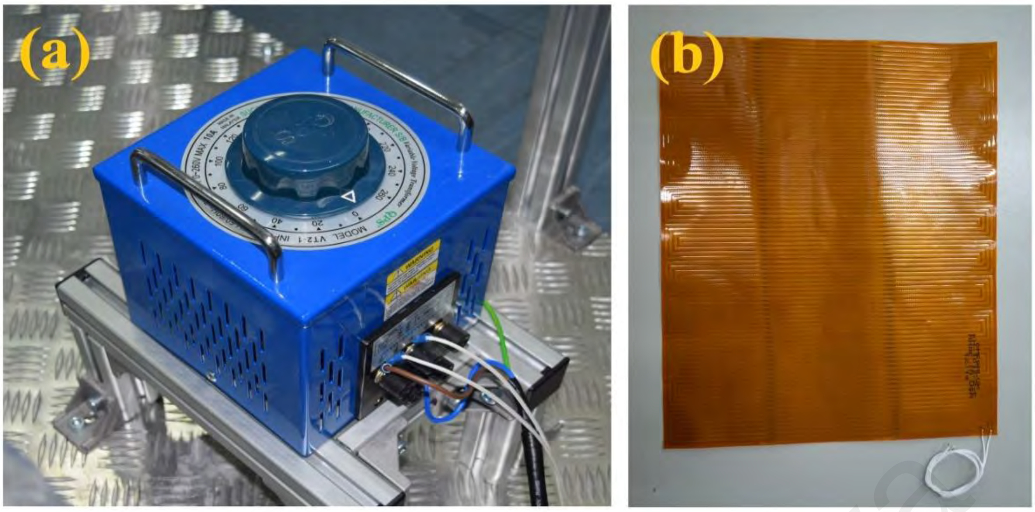

Figure 3.6: The variable voltage transformer (a) and the flexible adhesive heater (b) used in this study.

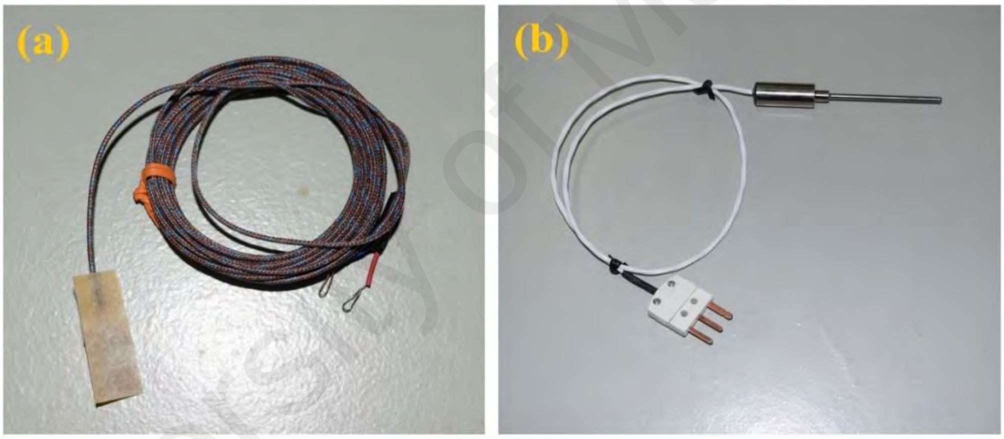

Figure 3.7: T-type surface thermocouple (a) and RTD (PT100) (b) used in this study.

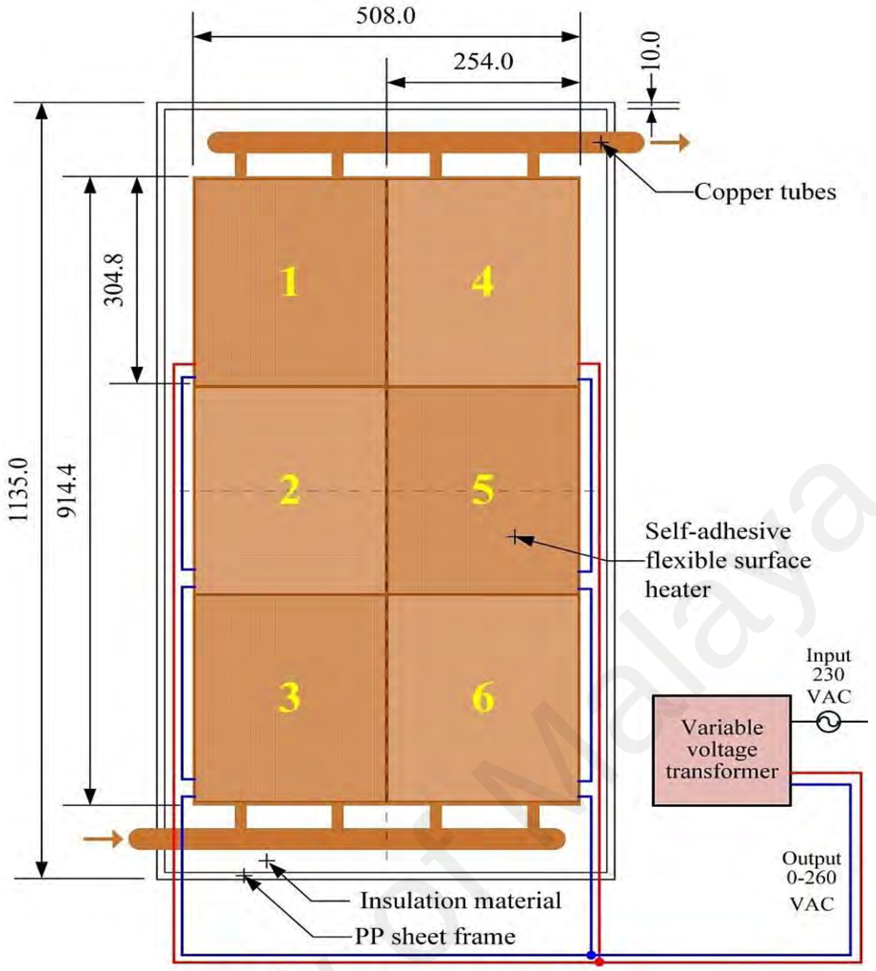

* All dimensions are in mm.

Figure 3.8: Configuration of the electric heaters on the top surface of the copper absorber plate with the wiring diagram and variable voltage transformer.

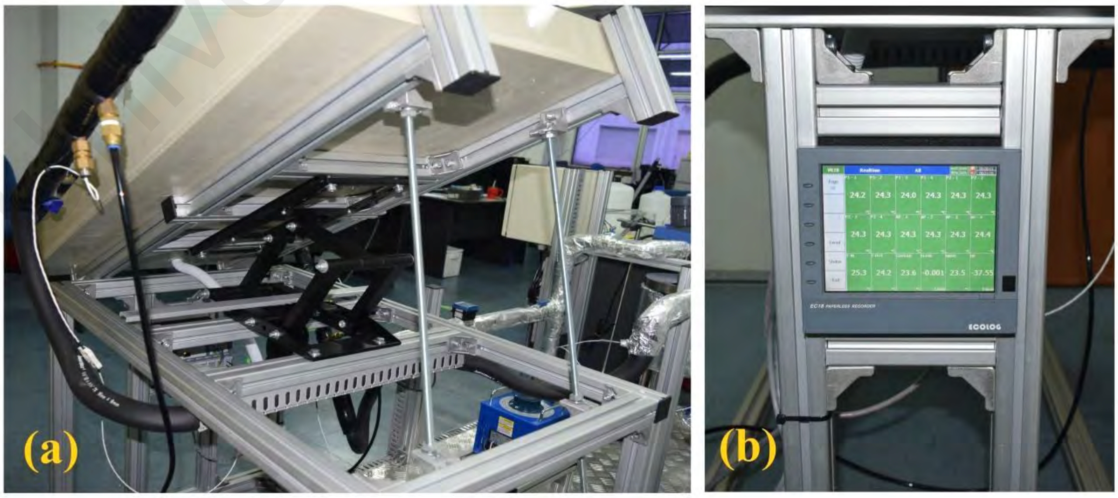

Figure 3.9: (a) The adjustable-angle base of the FPSC with the aluminum profile stand. (b) The Ecolog EC18 data logger used in the present work.

Table 3.4: Specifications of the devices and components used in the FPSC section of the experimental setup.

Item	Material / Brand	Dimensions / Model No.	Units / Specifications	Qty.
Cover	Glass (float)	Thickness = 5	mm	1
Insulation	Ceramic fibers blanket	Thickness = 50 (Back) 30 (Sides)	mm mm	–
Absorber plate	Copper	Thickness = 2 L×W = 914.4 × 508.0	mm mm	1
Riser tube	Copper	Outer diameter = 12.7 Thickness = 1.1 Length ≅ 1020 Spacing ≅ 128	mm mm mm mm	4
Header tube	Copper	Outer diameter = 22.2 Thickness = 1.3 Length ≅ 600	mm mm mm	2
Insulated flexible heaters with pressure sensitive adhesive	Etched foil element with Kapton polyimide film insulation	Thickness ≅ 0.14 Watt density = 0.39 (2.5) L×W = 30.48 × 25.4 (10 × 12) Total watt/heater = 300	mm W/cm^2 (W/in^2) cm (in) W	6
Frame	PP sheet	Thickness = 10	mm	–
Air gap between the glass cover and absorber plate	–	Thickness = 20	mm	–
Stand for the FPSC	T-slotted structural aluminum profile	Profile 40 x 40	mm	–
T-type surface thermocouple	Omega SA1XL with fiberglass-insulated wires	Wire length = 2	m	12
RTD	PT100 Class A 3-wire	Sensor length = 85	mm	2
Wet/wet low DPT	Omega	PX154-001DI	0–1 in H_2O (0–249 Pa)	1
Data logger	ECOLOG	EC18	18 channels	1
Digital AC clamp meter	Kyoritsu	Kew Snap 2017	–	1
Tapered-cone connection at inlet and outlet tubes	Copper	–	Custom machined	2
1/2″ Tee with compress fitting for RTD and DPT	Copper	–	–	4

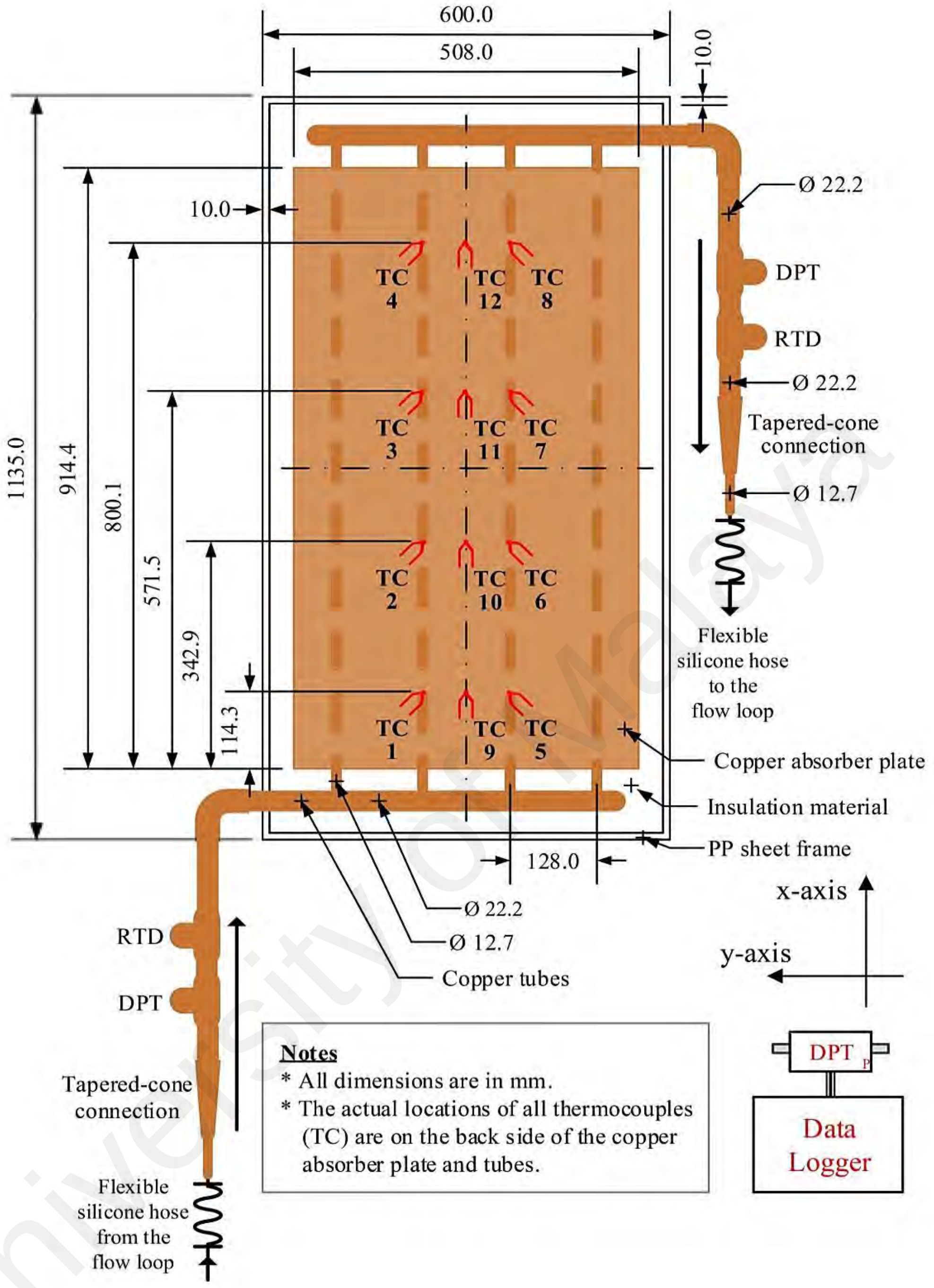

Notes

* All dimensions are in mm.

* The actual locations of all thermocouples (TC) are on the back side of the copper absorber plate and tubes.

Figure 3.10: Schematic diagram of the FPSC.

3.7.2 Description of the flow loop section

The flow loop section is schematically presented in Figure 3.11 and consists of electric centrifugal pump, thermally insulated jacketed tank with overhead stirrer, stainless steel tubes with thermal insulation, digital flow meter, two different needle valves, refrigerated water bath, and main electrical control box with an electrical board.

Detailed specifications of the parts used in the flow loop section of the test setup are listed in Table 3.5. A magnetic-drive centrifugal electric pump (model Araki EX-30R (M)) was used in the test rig having a maximum flow rate and head of 32 l/min and 3.8 m, respectively (Figure 3.12c). A needle valve with a valve flow coefficient (Cv) of 0.35 was installed at the fluid flow line before the flow meter to facilitate precise control of fluid flow rate (Figure 3.13a). A bypass loop containing a needle valve with larger Cv of 1.05 (Figure 3.13b) was added after the pump so that the minimum flow rate required, i.e., 0.6 kg/min, can be reached with reduced load on the pump (presented in Figure 3.11). An 8-l stainless steel jacketed tank with thermal insulation (Figure 3.12a, b) was installed and used as a storage for the working fluid and a heat exchanger with the refrigerated water bath to maintain a constant fluid temperature at the inlet of the FPSC. A refrigerated bath circulator “WiseCircu WCR-P22” (Daihan Scientific Co., Ltd., Korea) with 3.4 kW and an accuracy of 0.1°C was used with the insulated jacketed tank for absorbing the heat load from the FPSC section. An overhead stirrer (model IKA RW 20 digital) was connected to the jacketed tank (shown in Figure 3.12d) to increase the blending of fluid inside the tank and enhance the exchange of heat between the cooling water flowing inside the jacket and the bulk fluid inside tank. An inline paddle wheel digital flow rate transmitter (model Burkert, SE32 PV) (Figure 3.14b) was installed at the discharge line of the pump to measure the flow rate of fluid. A ball valve was added at the return line of the fluid from the FPSC to the jacketed tank (Figure 3.11), which was used to build up the pressure inside the FPSC for the cleaning process and also for purging the air from the DPT. The temperatures of bulk fluid inside the jacketed tank and the cooling fluid flowing inside the jacket were measured by two RTDs (PT100) connected to the same Ecolog EC18 data logger located in the FPSC section of the test setup.

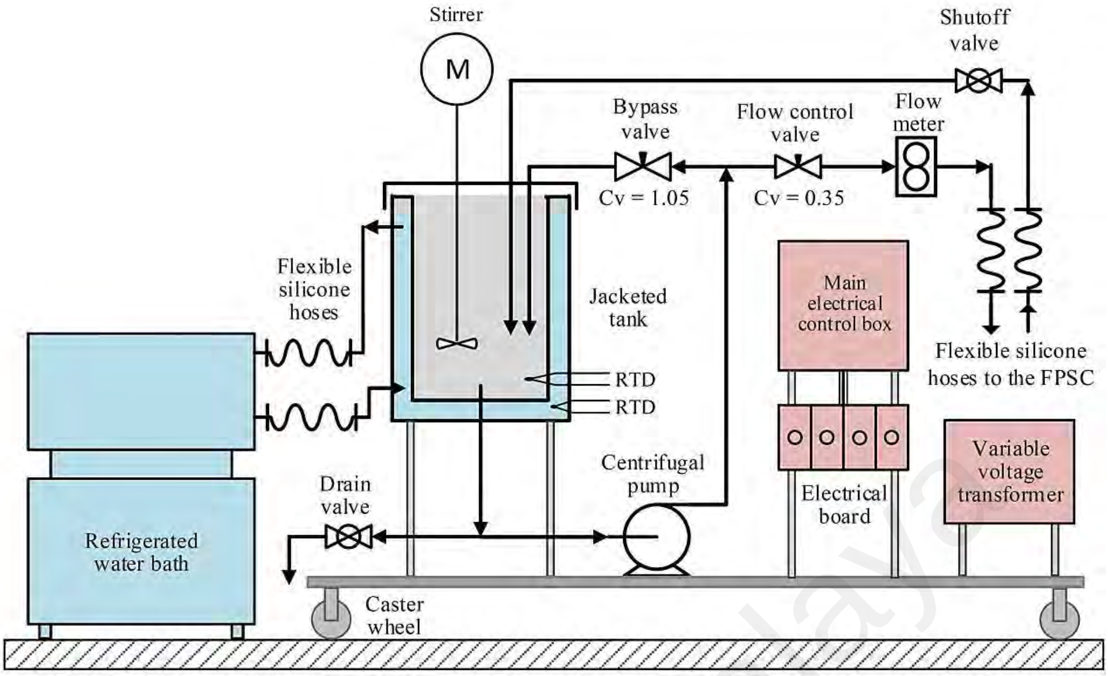

Figure 3.11: Schematic diagram of the flow loop section.

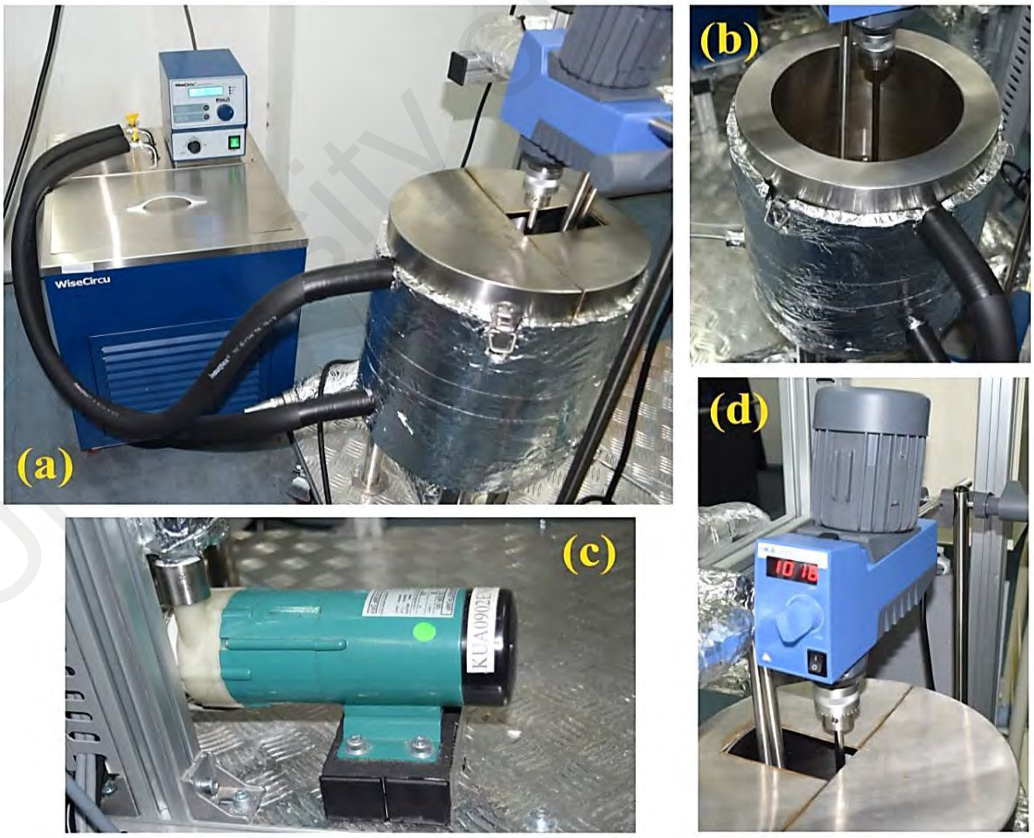

Figure 3.12: Different parts of the test rig; (a, b) refrigerated water bath circulator with the jacketed tank, (c) magnetic drive centrifugal pump, and (d) IKA overhead stirrer.

Table 3.5: Specifications of the devices and components used in the flow loop section of the experimental setup.

Item	Type	Brand	Model No.	Specifications	Qty.
Electric pump	Magnetic-drive centrifugal pump	Araki	EX-30R (M)	230 V - 50 Hz Max. flow = 32 l/min Max. head = 3.8 m Speed = 2800 rpm	1
Jacketed tank	Stainless steel tank with thermal insulation	Local custom made	Grade 316	OD = 27.4 cm OD = 19.8 cm Height = 26 cm Capacity ≅ 8 l	1
Stirrer	Overhead	IKA	RW 20 digital	220-240 V 50/60 Hz 72 W	1
Valve (Flow line)	Needle Body material: 316 stainless steel	Parker	HNVS8FF	1/2″ NPT (Female) Cv = 0.35 Orifice = 4.0 mm	1
Valve (Bypass line)	Needle Body material: Brass	Parker	8F-V12LN-B	1/2″ NPT (Female) Cv = 1.05 Orifice = 7.9 mm	1
Valve (Return line)	Ball	JSV	–	1/2″ NPT (Female)	2
Flow meter	Inline paddle wheel transmitter with display	Burkert	SE32 PV	Range = 0.3–8.0 l/min	1
Transformer	Variable voltage	QPS	VT2-1	Input = 230 V Output = 0–260 V Capacity = 10 A	1
Tubes (Flow and bypass lines)	Stainless steel with thermal insulation	N/A	Grade 316	OD = 12.7 mm ID = 10.21 mm	N/A
Water bath circulator	Refrigerated	Daihan, Korea	WiseCircu WCR-P22	3.4 kW	1
RTD	PT100	N/A	Class A 3-wire	Sensor length = 85 mm	2

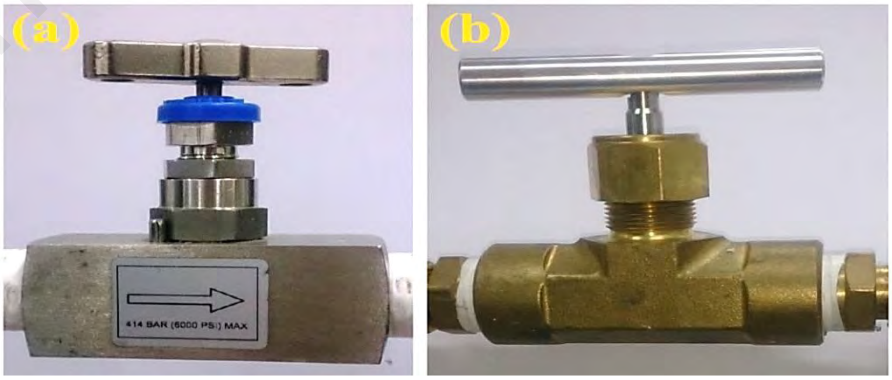

Figure 3.13: Photographs of the two needle valves from Parker used in this study with different values of valve flow coefficient (Cv) of (a) 0.35 and (b) 1.05.

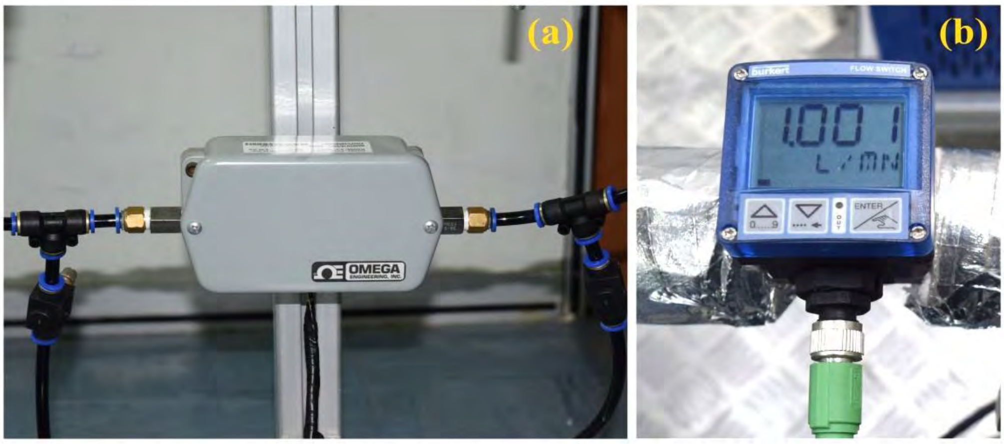

Figure 3.14: (a) Low differential pressure transmitter (DPT) (PX154-001DI) from Omega and (b) digital flow meter (SE32 PV) from Burkert.

3.8 Mathematical model and MATLAB code

In this study, the mathematical model for simulating the thermal performance of a FPSC using nanofluids as its working fluids is based on the HW model presented by Duffie & Beckman (2013) with some modifications. The model is developed based on some assumptions to simplify the problem without affecting the basic principles. The assumptions can be summarized as follows:

1. The operation of the FPSC is steady state.
2. The fluid flows uniformly through all the riser tubes of the collector.
3. The flow of heat through back insulation is one-dimensional.
4. The temperature around the wall of the riser tube is uniform.
5. The temperature gradients in the absorber plate (along y-axis) (Figure 3.15b) and in the direction of flow (along x-axis) (Figure 3.10) are treated separately.
6. The nanofluids used are well dispersed and with high colloidal stability.
7. The nanofluid is considered as a single phase fluid.
8. Heat losses from the top, edge, and bottom of the FPSC take place from the absorber plate at an average temperature (T_{ap}) to a common sink temperature, i.e., the ambient temperature (T_a).

Using the above-mentioned assumptions, a MATLAB code was developed for solving the mathematical model and simulating the nanofluid-based FPSC. The flowchart for this MATLAB code is presented in Figure 3.16.

In a FPSC, for calculating the total heat loss, the collector overall heat loss coefficient (U_L) should be estimated, which is the summation of the top (U_t), edge (U_e), and bottom (U_b) heat loss coefficients, and can be expressed as:

$$U_L = U_t + U_e + U_b \tag{3.1}$$

The top loss coefficient (U_t) was calculated using the equation (2.5), i.e., the empirical equation of Klein (1979) (as cited in Duffie & Beckman (2013)), after estimating the mean temperature of the absorber plate (T_{ap}). For the bottom heat loss coefficient (U_b), the conduction heat loss from the absorber plate to the ambient can be described using Fourier's law as:

$$Q_b = K_{ins_b}\, A_c\, \frac{\left(T_{ap} - T_a\right)}{thk_{ins_b}} = U_b\, A_c\left(T_{ap} - T_a\right) \tag{3.2}$$

$$\Rightarrow U_b = \frac{K_{ins_b}}{thk_{ins_b}} = \frac{\text{Thermal conductivity of insulation at the bottom}}{\text{Thickness of insulation at the bottom}} \tag{3.3}$$

Similarly, the edge heat loss from the FPSC to the surrounding is presented as:

$$Q_e = K_{ins_e}\, A_e\, \frac{\left(T_{ap} - T_a\right)}{thk_{ins_e}} \tag{3.4}$$

Since all heat loss coefficients should be referenced to the same area, which is the collector area (A_c), therefore, equation (3.4) is revised as:

$$Q_e = \frac{K_{ins_e}\, A_e}{A_c}\, A_c\, \frac{\left(T_{ap} - T_a\right)}{thk_{ins_e}} = U_e\, A_c\left(T_{ap} - T_a\right) \tag{3.5}$$

$$\Rightarrow U_e = \frac{K_{ins_e}\, A_e}{thk_{ins_e}\, A_c} = \frac{\text{Thermal conductivity of insulation at the edge} \times \text{Edge area}}{\text{Thickness of insulation at the edge} \times \text{Collector area}} \tag{3.6}$$

In the experimental setup of this study, the absorber plate of the FPSC is in contact with four riser tubes. Only one tube was taken into consideration in the mathematical model with the assumption that fluid flows uniformly through all the riser tubes of the collector working in a parallel channel arrangement.

The region of the FPSC's absorber plate extending from the outside diameter (d_o) of the riser tube to the centerline separating two riser tubes is considered as a fin with a length equal to [(W-d_o)/2], as shown in Figure 3.15 (a, b). From the first law of thermodynamics, considering an element in this fin of width (Δy) (Figure 3.15b), with a unit length in the direction of flow, and at a temperature (T_y), an energy balance displayed in Figure 3.15c will give the following equation:

$$S\,\Delta y - U_L\,\Delta y\left(T_y - T_a\right) + \left(-K_{ap}\,t_{ap}\,\frac{dT}{dy}\right)\bigg|_y - \left(-K_{ap}\,t_{ap}\,\frac{dT}{dy}\right)\bigg|_{y+\Delta y} = 0 \tag{3.7}$$

As (Δy) approaches zero, finding the limit for the previous equation results in:

$$\because\ \lim_{\Delta y \to 0} \frac{\left.\frac{dT}{dy}\right|_{y+\Delta y} - \left.\frac{dT}{dy}\right|_y}{\Delta y} = \frac{d^2T}{dy^2} \tag{3.8}$$

$$\therefore\ \frac{d^2T}{dy^2} = \frac{U_L}{K_{ap}\,t_{ap}}\left(T_y - T_a - \frac{S}{U_L}\right) \tag{3.9}$$

For solving equation (3.9), which is a second-order differential equation, and finding the temperature distribution in the absorber plate, two boundary conditions (B.C.) should be presented. From Figure 3.15 (b, d), the two boundary conditions are:

$$\text{B.C. 1}:\ \left.\frac{dT}{dy}\right|_{y=0} = 0 \tag{3.10}$$

$$\text{B.C. 2}:\ T|_{y=(W-d_o)/2} = T_b \tag{3.11}$$

Finite difference analysis was used to solve this second-order differential equation. Discretization and arrangement of nodes is presented in Figure 3.15d. The fin was divided into (n) nodal points. Three set of equations should be derived, one for the interior nodal points (2 to (n-1)), and two for boundary conditions at nodes (1) and (n). For interior nodal points 2 to (n-1), the centered finite-difference approximation for the second-order differential equation (3.9) is:

$$\frac{\left.\frac{dT}{dy}\right|_{y+\frac{\Delta y}{2}} - \left.\frac{dT}{dy}\right|_{y-\frac{\Delta y}{2}}}{\Delta y} = \frac{T_{y+1} - 2\,T_y + T_{y-1}}{\Delta y^2} = \frac{U_L}{K_{ap}\,t_{ap}}\left(T_y - T_a - \frac{S}{U_L}\right) \tag{3.12}$$

$$\Rightarrow \left(\frac{K_{ap}\,t_{ap}}{U_L\,\Delta y^2}\right)T_{y-1} - \left(1 + \frac{2\,K_{ap}\,t_{ap}}{U_L\,\Delta y^2}\right)T_y + \left(\frac{K_{ap}\,t_{ap}}{U_L\,\Delta y^2}\right)T_{y+1} = \left(-\frac{S}{U_L} - T_a\right) \tag{3.13}$$

For nodal point 1 which is considered as half element with a width of (Δy/2), the finite-difference approximation using B.C. 1 results in,

$$\frac{\left.\frac{dT}{dy}\right|_{y+\frac{\Delta y}{2}} - 0}{\frac{\Delta y}{2}} = \frac{2}{\Delta y^2}(T_2 - T_1) = \frac{U_L}{K_{ap}\,t_{ap}}\left(T_1 - T_a - \frac{S}{U_L}\right) \tag{3.14}$$

$$\Rightarrow \left(1 + \frac{2\,K_{ap}\,t_{ap}}{U_L\,\Delta y^2}\right)T_1 + \left(\frac{2\,K_{ap}\,t_{ap}}{U_L\,\Delta y^2}\right)T_2 = \left(-\frac{S}{U_L} - T_a\right) \tag{3.15}$$

For nodal point n with B.C. 2, the finite-difference approximation results in,

$$\frac{T_b - 2\,T_n + T_{n-1}}{\Delta y^2} = \frac{U_L}{K_{ap}\,t_{ap}}\left(T_n - T_a - \frac{S}{U_L}\right) \tag{3.16}$$

$$\Rightarrow \left(\frac{K_{ap}\,t_{ap}}{U_L\,\Delta y^2}\right)T_{n-1} - \left(1 + \frac{2\,K_{ap}\,t_{ap}}{U_L\,\Delta y^2}\right)T_n = \left(-\frac{S}{U_L} - T_a - \frac{K_{ap}\,t_{ap}}{U_L\,\Delta y^2}\,T_b\right) \tag{3.17}$$

The three equations (3.15), (3.13), and (3.17) can be revised by introducing the constants (a, b, c, and d) as presented in equations (3.18) to (3.20), respectively. This set of equations forms a tridiagonal matrix with (n) rows shown below. This matrix was solved in MATLAB using Thomas algorithm to find the temperature distribution in the absorber plate of the FPSC.

$$b_1 T_1 - c_1\, T_2 = d_1 \tag{3.18}$$

$$a_y T_{y-1} - b_y\, T_y + c_y T_{y+1} = d_y \quad , \qquad \text{for y = 2 to (n - 1)} \tag{3.19}$$

$$a_n T_{n-1} - b_n\, T_n = d_n \tag{3.20}$$

$$\begin{bmatrix} b_1 & c_1 & & & & 0 \\ a_2 & b_2 & c_2 & & & \\ & a_3 & b_3 & c_3 & & \\ & & \ddots & \ddots & \ddots & \\ & & & a_{n-1} & b_{n-1} & c_{n-1} \\ 0 & & & & a_n & b_n \end{bmatrix} \begin{bmatrix} T_1 \\ T_2 \\ T_3 \\ \vdots \\ T_{n-1} \\ T_n \end{bmatrix} = \begin{bmatrix} d_1 \\ d_2 \\ d_3 \\ \vdots \\ d_{n-1} \\ d_n \end{bmatrix} \tag{3.21}$$

The energy transferred per unit length to the riser tube from the fins on both sides was calculated using Fourier's law as:

$$q_{rt}|_{fin} = 2\, K_{ap}\, thk_{ap}\, \frac{(T_n - T_b)}{\Delta y} \tag{3.22}$$

Energy is also collected from the region above the riser tube and can be expressed per unit length as:

$$q_{rt}|_{top} = S\, d_o - U_L\, d_o\, (T_b - T_a) \tag{3.23}$$

Thus, the useful energy gain which is the total energy transferred to the riser tube per unit length is the sum of equations (3.22) and (3.23) as follows:

$$q_{rt} = q_{rt}|_{fin} + q_{rt}|_{top} = 2\, K_{ap}\, thk_{ap} \frac{(T_n - T_b)}{\Delta y} + [S\, d_o - U_L\, d_o (T_b - T_a)] \tag{3.24}$$

Eventually, the useful gain should be transferred to the heat transfer fluid flowing inside the riser tube passing through three thermal resistances, i.e., the bond between riser tube and absorber plate, tube wall thickness, and the convection heat transfer coefficient inside riser tube. Referring to Figure 3.15b, the equation for heat transfer rate per unit length to the working fluid inside the riser tube can be written as:

$$q_{rt} = \frac{T_b - T_f}{\frac{\ln(d_o/d_i)}{2\,\pi\, K_{rt}} + \frac{1}{C_b} + \frac{1}{h_i\, \pi\, d_i}} \tag{3.25}$$

where, C_b = the bond conductance between absorber plate and riser tube.

$= \frac{K_{bond}\, W_{bond}}{thk_{bond}}$ (W/m K)

K_{bond} = thermal conductivity of the bond material (W/m K).

W_{bond} = width of the bond (mm).

thk_{bond} = thickness of the bond (mm).

The convective heat transfer coefficient inside the riser tube (hi) was calculated using Shah equation (Shah, 1975) for laminar fluid flow with constant heat flux.

$$Nu_x = \frac{h_{i_x}\, d_i}{K_f} = \begin{cases} 1.953 \left(Re\, Pr\, \frac{d_i}{x}\right)^{1/3} & \text{for } \left(Re\, Pr\, \frac{d_i}{x}\right) \geq 33.3 \\ 4.364 + 0.0722\, Re\, Pr\, \frac{d_i}{x} & \text{for } \left(Re\, Pr\, \frac{d_i}{x}\right) < 33.3 \end{cases} \tag{3.26}$$

where, Re = Reynolds number $= \frac{\rho_f\, V_f d_i}{\mu_f}$ (3.27)

Pr = Prandtl number $= \frac{C_{P_f}\, \mu_f}{K_f}$ (3.28)

x = length along direction of fluid flow.

Since fluid temperature at the inlet of each elemental length of the riser tube (T_f) is known, thus, for estimating the value of (T_b), an iteration procedure was followed in which (q_{rt}) is calculated from equations (3.24) and (3.25) separately, and the value of (T_b) is adjusted until a convergence between the two (q_{rt}) values is reached within a specified tolerance.

The length of the collector's riser tube was divided into (m) elements in the direction of flow with a length of (Δx) for each element (Figure 3.15e). From the first law of thermodynamics, an energy balance displayed in Figure 3.15f will give the following equation:

$$\frac{\dot{m}}{n}\, C_p\, T_f\Big|_x + \, q_{rt}\, \Delta y = \frac{\dot{m}}{n}\, C_p\, T_f\Big|_{x+\Delta x} \qquad (3.29)$$

where $\dot{m}$ and n re the total mass flow rate and the number of riser tubes, respectively.

As (Δx) approaches zero, finding the limit for the previous equation results in:

$$\dot{m}\, C_p\, \frac{dT_f}{dx} - n\, q_{rt} = 0 \qquad (3.30)$$

Using the boundary condition of known fluid temperature at inlet (T_{in}), the first-order differential equation (3.30) can be solved using forward finite-difference approximation to find the temperature of the fluid along the riser tube as follows:

$$T_{x+1} - T_x = \frac{n\, q_{rt}\, \Delta x}{\dot{m}\, C_p} \;, \quad \text{for } x = 1 \text{ to } m \qquad (3.31)$$

After reaching the end of the riser tube, the average value of the surface temperature for the whole absorber plate is calculated and compared with the estimated temperature used for calculating the top loss coefficient (U_t). If the difference between them is higher than a certain tolerance, the estimated value is corrected and the whole calculations are repeated from the beginning until convergence is reached.

The calculations procedure requires the values of thermophysical properties at each step. For water, the complete set of equation is presented in the following section. While for calculating the thermophysical properties of different nanofluids used in this study, several models and correlations were used depending on the type and shape of nanomaterial and presented in the “Results and Discussion” chapter.

The efficiency of the FPSC is defined as (Duffie & Beckman, 2013);

$$\eta_c = \frac{\text{Actual useful energy collected}}{\text{Solar energy intercepted by the collector area}} = \frac{Q_u}{G_T\, A_c} = \frac{\dot{m}\, C_p\, (T_{out} - T_{in})}{G_T\, A_c} \tag{3.32}$$

In this study, a flexible adhesive electric heater is used for generating a constant heat flux similar to that of solar radiation. Therefore, the above equation can be rewritten in a suitable form with this approach using equation (2.3). Here, the absorbed solar radiation multiplied by collector area ($S\ A_c$) represents the power input from the electric heater, i.e., current ($\tilde{I}$) × voltage ($\tilde{V}$).

$$\eta_c = \frac{Q_u}{\frac{S}{\tau_g\, \alpha_{ap}} A_c} = \frac{\dot{m}\, C_p\, (T_{out} - T_{in})}{\frac{S\ A_c}{\tau_g\, \alpha_{ap}}} \tag{3.33}$$

The collector heat removal factor (F_R) was defined to relate the actual FPSC’s useful energy to the useful gain if the whole surface of the FPSC is at the fluid inlet temperature (T_{in}) (Duffie & Beckman, 2013).

$$F_R = \frac{Q_u}{A_c\, G_T\left(\tau_g\, \alpha_{ap}\right) - A_c\, U_L(T_{in} - T_a)} = \frac{\dot{m}\, C_p\, (T_{out} - T_{in})}{A_c\, S\ - A_c\, U_L(T_{in} - T_a)} \tag{3.34}$$

$$\Rightarrow Q_u = \dot{m}\, C_p\, (T_{out} - T_{in}) = [\, A_c\, F_R\ \ S] - [\, A_c\, F_R\, U_L(T_{in} - T_a)\,] \tag{3.35}$$

Accordingly, from equations (3.32) to (3.35), the energy efficiency of the FPSC can be expressed as:

$$\eta_c = F_R\left(\tau_g\,\alpha_{ap}\right) - F_R\,U_L\,\frac{(T_{in} - T_a)}{G_T} = F_R\left(\tau_g\,\alpha_{ap}\right) - F_R\,U_L\,\frac{(T_{in} - T_a)}{\frac{S}{\tau_g\,\alpha_{ap}}} \tag{3.36}$$

A graph of energy efficiency values calculated from equation (3.36) against the reduced temperature parameter produces a straight line. This line will intersect the vertical axis of energy efficiency when the inlet fluid temperature to the FPSC matches the ambient temperature. At this point, the energy efficiency of the FPSC is at its maximum value and called zero-loss efficiency. On the other hand, the FPSC' energy efficiency will be equal to zero when this line intersects the horizontal axis of reduced temperature parameter. This intersection called the stagnation point and normally occurs when no fluid flows in the FPSC. The zero-loss efficiency will be used for calculating the percentage enhancements in energy efficiency of the FPSC in the subsequent sections of this study (Kalogirou, 2009; H. K. Gupta et al., 2015; Vakili et al., 2016).

To evaluate the effectiveness and usefulness of using different nanofluids as working fluids in FPSCs, a performance index (PI) is selected as an appropriate parameter. Based on previous research (Razi et al., 2011; Heris et al., 2013; Amiri et al., 2016d), the PI can by defined in a form which is suitable for FPSCs as follows:

$$PI = \frac{(\eta_c)_{nf}\ /\ (\eta_c)_{bf}}{(\Delta P)_{nf}\ /\ (\Delta P)_{bf}} = \frac{R_{\eta_c}}{R_{\Delta P}} \tag{3.37}$$

When the performance index is greater than 1, it means that the nanofluid can be advantageously used in the FPSC instead of the base fluid for enhanced thermal performance. On the other hand, when the performance index less than 1, then the nanofluid is not a suitable replacement (Razi et al., 2011; Heris et al., 2013).

The pressure drop across the FPSC can be obtained by applying the energy equation between the inlet and outlet tubes where the DPT is connected (Figure 3.10) as follows (Cengel & Cimbala, 2006; Mahian et al., 2015):

$$P_{in} + \frac{\rho\, V_{in}^2}{2} + \rho\, g\, Z_{in} = P_{out} + \frac{\rho\, V_{out}^2}{2} + \rho\, g\, Z_{out} + \Delta P_{loss} \tag{3.38}$$

where ΔP_{loss} is total pressure loss across the FPSC. Considering equal velocity heads at inlet and outlet of the FPSC, resulting from equal diameters, and expressing the vertical distance (Z_{out}-Z_{in}) as (L_{rt} Sin φ), the above equation can be reduced to the following equation for calculating the pressure drop across the FPSC;

$$\Delta P_{FPSC} = P_{in} - P_{out} = \rho\, g\, L_{rt}\, \sin\varphi + \Delta P_{loss} \tag{3.39}$$

The total pressure loss (ΔP_{loss}) is the sum of the pressure loss in the riser tube and minor pressure losses in fittings, bends, tees, inlets, and exits and can be calculated as (Cengel & Cimbala, 2006);

$$\Delta P_{loss} = (\Delta P_{loss})_{\text{riser tube}} + (\Delta P_{loss})_{\text{minor}} = (\Delta P_{loss})_{\text{riser tube}} + \left(\frac{\rho\, V^2}{2}\sum K_L\right) \tag{3.40}$$

Since the inlet and outlet tubes of the FPSC are on opposite sides and the riser tubes are parallel, the frictional pressure loss through each of the riser tubes should be identical considering uniform fluid flow through all tubes. The values of the minor loss factor (K_L) for the tube entrance (sharp-edged), tee (branch flow), tee (line flow), tube exit, and smooth bend (90°) are 0.5, 1.0, 0.2, 2.0, and 0.3, respectively (Cengel & Cimbala, 2006). During fluid flow in the hydrodynamic entrance region of a tube, the pressure is lost due to the acceleration of fluid in addition to the wall shear. Accordingly, the correlation proposed by Bender (1969) was used for calculating the pressure loss in the laminar hydrodynamic entry length (equation (3.42)). The length of the hydrodynamic entrance region (L_h) can be calculated from the following equation (Cengel & Cimbala, 2006):

$$L_h = \text{hydrodynamic entry length} = 0.05\, Re\, d_i \tag{3.41}$$

$$(\Delta P_{loss})_{\text{riser tube}} = \frac{\rho\, V^2}{2}\left(13.74\sqrt{\frac{x}{d_i\, Re}} + \frac{1.25 + 64\frac{x}{d_i\, Re} - 13.74\sqrt{\frac{x}{d_i\, Re}}}{1 + 0.00018\left(\frac{x}{d_i\, Re}\right)^{-2}}\right) \tag{3.42}$$

For fully developed laminar flow in a circular pipe, i.e., $L > L_h$, the pressure loss can be calculated as (Cengel & Cimbala, 2006);

$$(\Delta P_{loss})_{\text{riser tube}} = f\ \frac{L}{D}\ \frac{\rho\, V^2}{2} \tag{3.43}$$

$$\text{where, } f = \text{Darcy-Weisbach friction factor} = \frac{64}{Re} \tag{3.44}$$

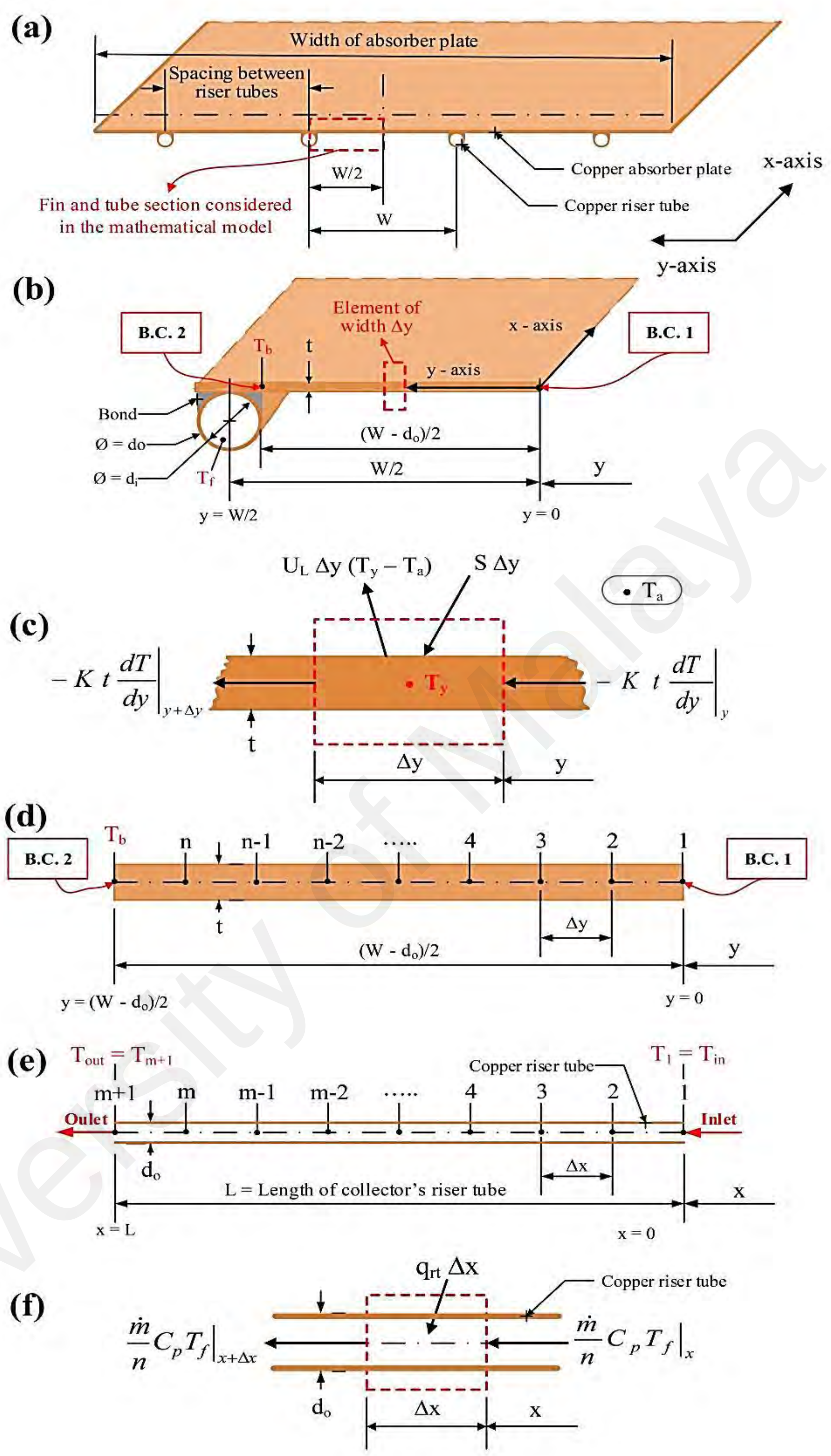

Figure 3.15: (a) The fin and tube section considered in the mathematical model, (b) location of the element with a width of Δy, (c) energy balance on an element in the fin with a width of Δy and temperature of T_y, (d) discretization of the fin length into n nodes, (e) discretization of the riser tube length into m elements, and (f) energy balance on an element in the riser tube with a length of Δx.

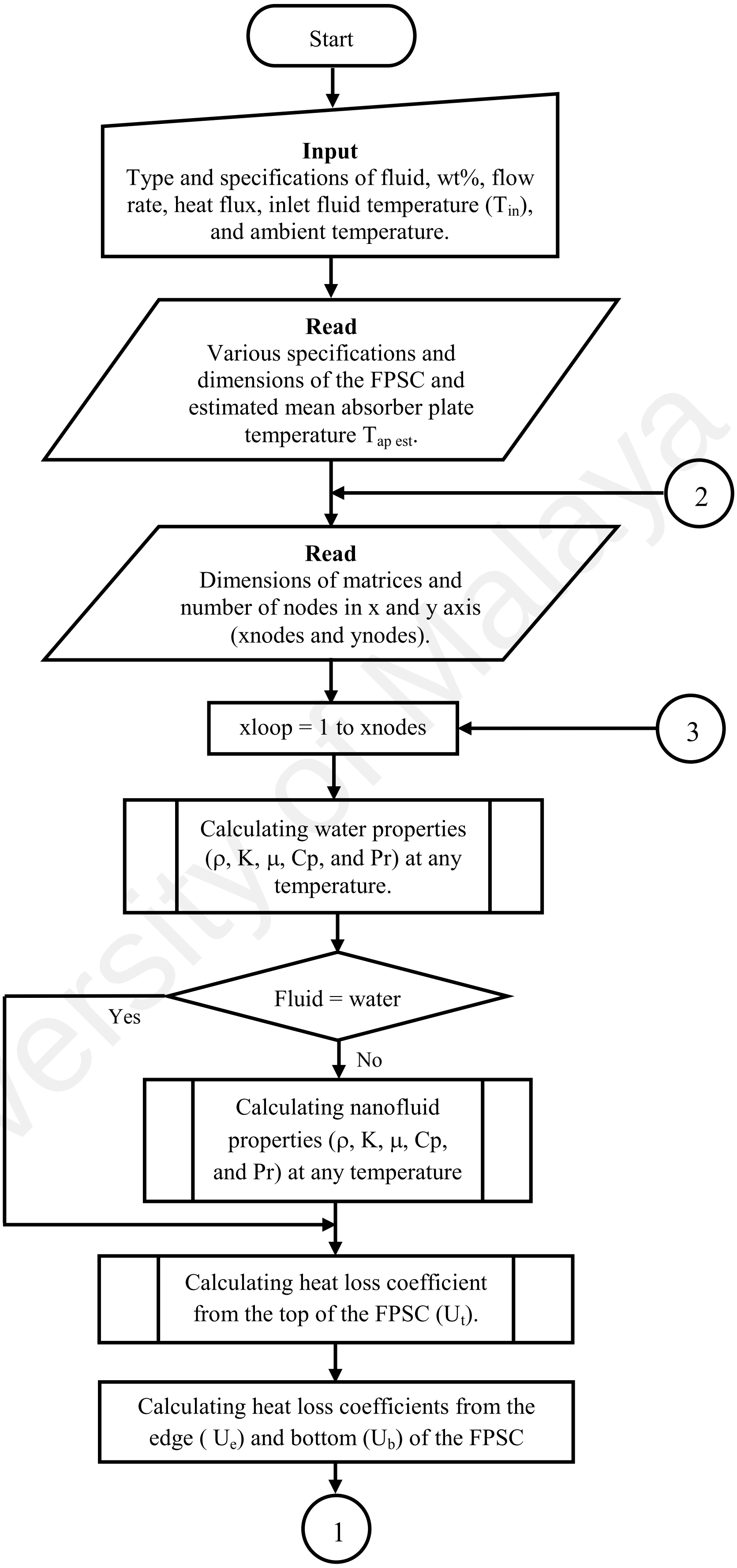

Figure 3.16: Flowchart of the MATLAB simulation code.

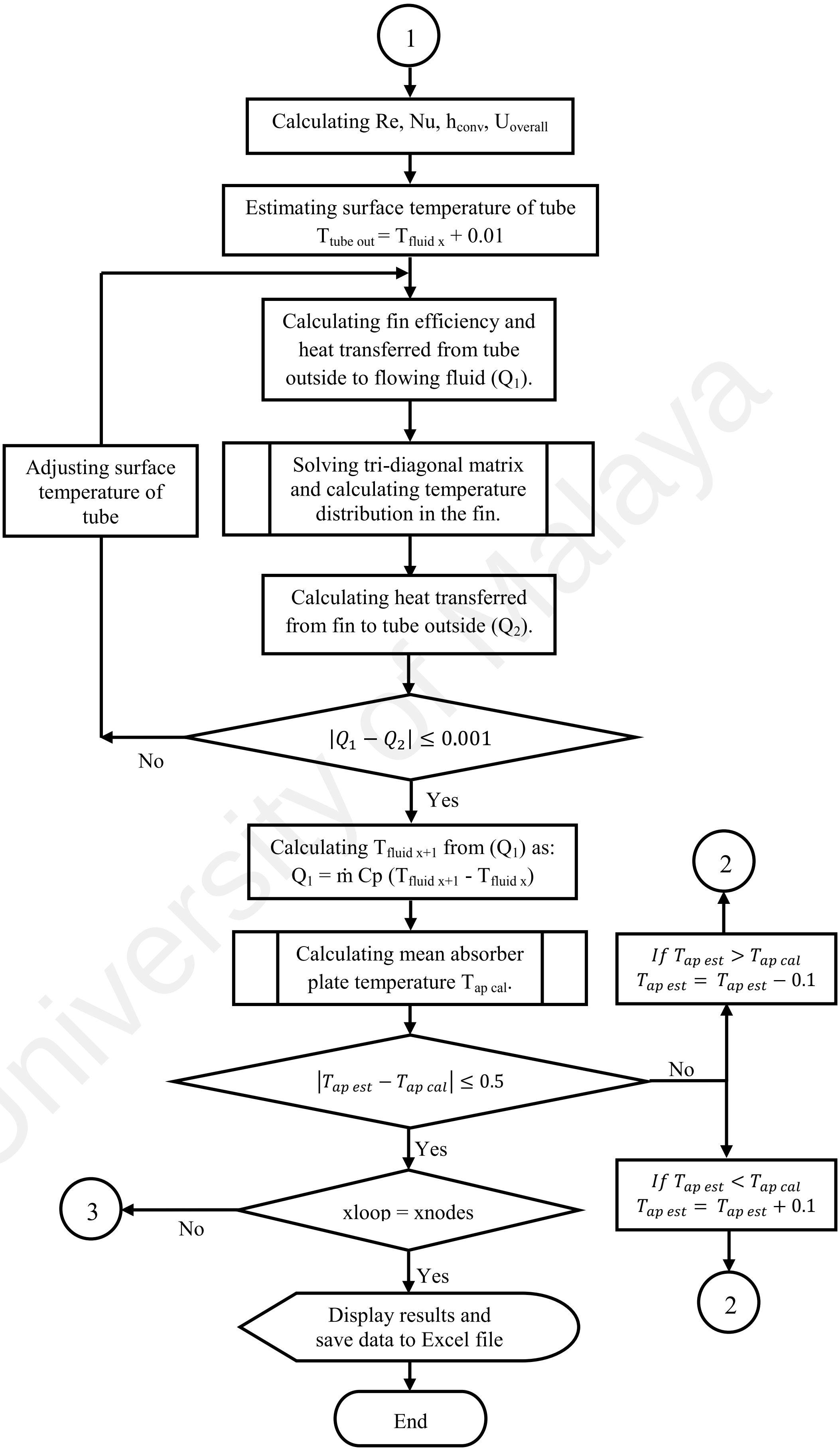

Figure 3.16, continued

3.9 Thermophysical properties of water

The thermophysical properties of water versus temperature were calculated using special correlation techniques including some numerical constants presented by Arnold (1970) and Schmidt (1981). The calculations were performed using MATLAB program and the developed script was used as a function for the main MATLAB simulation code. The calculation procedure requires the definition of the following reduced dimensionless quantities (Arnold, 1970; Schmidt, 1981):

$$\beta = \frac{P_{sat} \quad \text{(in bar)}}{221.2}, \quad \text{the reduced saturation pressure} \tag{3.45}$$

$$\theta = \frac{T \quad \text{(in °K)}}{647.3}, \quad \text{the reduced temperature} \tag{3.46}$$

$$\chi = \frac{\nu \quad (\text{in m}^3/\text{kg})}{0.00317}, \quad \text{the reduced volume} \tag{3.47}$$

$$\varepsilon = \frac{i \quad (\text{in kJ/kg})}{70.1204}, \quad \text{the reduced enthalpy} \tag{3.48}$$

The reduced saturation pressure (β) as a function of the reduced temperature (θ) was calculated using the following equation (Arnold, 1970):

$$\beta = \exp\left[\frac{\frac{1}{\theta}\sum_{n=1}^{5} k_n(1-\theta)^n}{1 + k_6(1-\theta) + k_7(1-\theta)^2} - \frac{+(1-\theta)}{+k_8(1-\theta)^2 + k_9}\right] \tag{3.49}$$

All values of the numerical constants are listed in tables presented in appendix (A). The correlations were sub-divided as follows:

3.9.1 Density of water

The density of water, which is the reciprocal of specific volume (ν), was calculated using equation (3.47) and the following correlation (Arnold, 1970):

$$\begin{aligned}\chi &= A_{11}a_5Z^{-5/17} + [A_{12} + A_{13}\theta + A_{14}\theta^2 + A_{15}(a_6 - \theta)^{10} + A_{16}(a_7 + \theta^{19})^{-1}] \\ &-[(a_8 + \theta^{11})^{-1}(A_{17} + 2A_{18}\beta + 3A_{19}\beta^2)] \\ &-[A_{20}\theta^{18}(a_9 + \theta^2)\{-3(a_{10} + \beta)^{-4} + a_{11}\}] \\ &+3A_{21}(a_{12} - \theta)\beta^2 + 4A_{22}\theta^{-20}\beta^3\end{aligned} \tag{3.50}$$

3.9.2 Specific heat of water

The specific heat (C_p) of water was calculated from the basic definition of specific heat at constant pressure, which states that the value of the C_p at any temperature T represents the slope of temperature-enthalpy (T-i) curve at that temperature. Accordingly, using centered finite difference approximation, C_p was calculated from the following equation:

$$C_p\Big|_T = \frac{\Delta i}{\Delta T}\Big|_T = \frac{i_{T+\Delta T} - i_{T-\Delta T}}{2\,\Delta T} \tag{3.51}$$

The enthalpy (i) of water was calculated using equation (3.48) and the following correlation (Arnold, 1970):

$$\begin{aligned}\varepsilon &= A_0\theta - \sum_{n=1}^{10}(n-2)A_n\theta^{n-2} + A_{11}\left[Z\left\{17\left(\frac{Z}{29} - \frac{Y}{12}\right) + 50\frac{Y'}{12}\right\} + a^4\theta - (a^3 - 1)\theta YY'\right]Z^{-5/17} \\ &+\{A_{12} - A_{14}\theta^2 + A_{15}(90 + a_6)(a_6 - \theta)^9 + A_{16}(20\theta^{19} + a_7)(a_7 + \theta^{19})^{-2}\}\beta \\ &-(12\theta^{11} + a_8)(a_8 + \theta^{11})^{-2}(A_{17}\beta + A_{18}\beta^2 + A_{19}\beta^3) \\ &+A_{20}\theta^{18}(17a_9 + 19\theta^2)\{(a_{10} + \beta)^{-3} + a_{11}\beta\} + A_{21}a_{12}\beta^3 + 21A_{22}\theta^{-20}\beta^4\end{aligned} \tag{3.52}$$

where, $Z = Y + (a_3Y^2 - 2a_4\theta + 2a_5\beta)^{1/2}$ (3.53)

$$Y = 1 - a_1\theta^2 - a_2\theta^{-6} \tag{3.54}$$

$$Y' = -2a_1\theta + 6a_2\theta^{-7} \tag{3.55}$$

3.9.3 Dynamic viscosity of water

The dynamic viscosity (μ) of water was calculated using the following correlation (Schmidt, 1981):

$$\mu = \mu_0 * \exp\left[\frac{1}{\chi} \times \sum_{i=0}^{5} \sum_{j=0}^{4} \left(BB_{i,j} \left(\frac{1}{\theta} - 1\right)^{i} \left(\frac{1}{\chi} - 1\right)^{j} \right)\right] \tag{3.56}$$

$$\text{where, } \mu_0 = \left\{ [\theta]^{1/2} \left[\sum_{i=0}^{3} AA_i \left(\frac{1}{\theta}\right)^{i} \right]^{-1} \right\} \times 10^{-6} \tag{3.57}$$

3.9.4 Thermal conductivity of water

The thermal conductivity (K) of water was calculated using the following correlation (Arnold, 1970):

$$\begin{aligned} K * 10^3 &= a_{\mathrm{o}} + a_1 \left[\frac{T}{T_{\mathrm{o}}}\right] + a_2 \left[\frac{T}{T_{\mathrm{o}}}\right]^2 + a_3 \left[\frac{T}{T_{\mathrm{o}}}\right]^3 + a_4 \left[\frac{T}{T_{\mathrm{o}}}\right]^4 \\ &+ (P - P_{sat}) \left\{ b_{\mathrm{o}} + b_1 \left[\frac{T}{T_{\mathrm{o}}}\right] + b_2 \left[\frac{T}{T_{\mathrm{o}}}\right]^2 + b_3 \left[\frac{T}{T_{\mathrm{o}}}\right]^3 \right\} \\ &+ (P - P_{sat}) \left\{ c_{0\mathrm{o}} + c_1 \left[\frac{T}{T_{\mathrm{o}}}\right] + c_2 \left[\frac{T}{T_{\mathrm{o}}}\right]^2 + c_3 \left[\frac{T}{T_{\mathrm{o}}}\right]^3 \right\} \end{aligned} \tag{3.58}$$

3.10 Uncertainty analysis

In any experimental work, there are some errors in the collected data that cannot be avoided. Such type of error results in some amount of uncertainty in the experimental data (Kline & McClintock, 1953; Holman, 2012). The uncertainty analysis is a method that evaluates the uncertainty in the experimentally calculated quantity depending on the uncertainties in the experimentally measured quantities that are used in the calculation procedure. Therefore, the accuracy of the FPSC's efficiency calculated from the experimental data in this work was evaluated using the uncertainty analysis. The efficiency of the FPSC used in this work can be expressed in a proportional form as:

$$\eta_c \propto \frac{\text{Actual useful energy collected}}{\text{Electric heat flux of surface heater}} \propto \frac{\rho\, \dot{Q}\, C_p\, (T_{out} - T_{in})}{\tilde{V}\, \times\, \tilde{I}} \tag{3.59}$$

$$\Rightarrow \eta_c \propto\ \rho\, \dot{Q}\, C_p\ V_{AC}^{-1}\, I_{AC}^{-1}\, (T_{out} - T_{in})\ \propto\ \rho\, \dot{Q}\, C_p\ \tilde{V}^{-1}\, \tilde{I}^{-1}\, \Delta T \tag{3.60}$$

Considering R as an outcome of a product function that is dependent on a series of independent variables (x1, x2, x3, . . . , xn) and given as:

$$R = x_1^{a1}\ x_2^{a2}\ x_3^{a3}\ \dots\ x_n^{an} \tag{3.61}$$

According to Holman (2012) and Kline & McClintock (1953), the uncertainty (ω) in the value of R can be estimated using the following relation:

$$\frac{\omega_R}{R} = \left[\sum_{i=1}^{n} \left(\frac{a_i\, \omega_{x_i}}{x_i}\right)^2\right]^{1/2} \tag{3.62}$$

Consequently, using equation (3.60), the uncertainty in the value of FPSC's efficiency calculated from the experimental data can be determined using the following relation:

$$\frac{\omega_{\eta_c}}{\eta_c} = \left[\left(\frac{\omega_\rho}{\rho}\right)^2 + \left(\frac{\omega_{\dot{Q}}}{\dot{Q}}\right)^2 + \left(\frac{\omega_{C_p}}{C_p}\right)^2 + \left(\frac{\omega_{\tilde{V}}}{\tilde{V}}\right)^2 + \left(\frac{\omega_{\tilde{I}}}{\tilde{I}}\right)^2 + \left(\frac{\omega_{\Delta T}}{\Delta T}\right)^2\right]^{1/2} \tag{3.63}$$

The uncertainty for the temperature difference term can be expressed according to Moffat (1985) as:

$$\frac{\omega_{\Delta T}}{\Delta T} \le \left[\left(\frac{\omega_{T_{out}}}{T_{out}}\right)^2 + \left(\frac{\omega_{T_{in}}}{T_{in}}\right)^2\right]^{1/2} \tag{3.64}$$

The uncertainty values of the six independent variables utilized in this work can be respectively specified as 0.04%, 1.67%, 2.75%, 1.0%, 1.5%, and 0.67%. Hence, the uncertainty in the measured efficiency of the FPSC was estimated to be 3.75%.

CHAPTER 4: RESULTS AND DISCUSSION

4.1 Introduction

In the present study, the colloidal stability and thermophysical properties of varies weight concentrations of novel water-based nanofluids containing different carbon-based nanostructures have been investigated. In addition, the thermal performance of nanofluid-based FPSC during steady-state operation has been studied. In this chapter, the data collected from the various tests, calculations, and investigations throughout this study have been presented in pictorial, graphical, and tabular formats, elucidated, and compared for validation.

4.2 Colloidal stability of water-based nanofluids

The two-step method was used to prepare all the water-based nanofluids in this study using different types of nanomaterials with different dimensions and SSAs. Furthermore, different functionalization methods were used to enhance the colloidal stability of the prepared nanofluids. In the flowing sections, colloidal stability for the different nanofluids that were synthesized has been presented.

4.2.1 Effect of surfactants on the stability of water-based GNPs nanofluids

In order to recognize which ultrasonication time and surfactant were the most suitable for generating high stability aqueous GNPs dispersion; different ultrasonication times (15, 30, 60, 90, and 120 min) and surfactants (SDBS, SDS, CTAB and GA) with different concentrations were used to disperse pristine GNPs with 300-m^2/g SSA in distilled water. Stability of the prepared nanofluids was investigated using UV–vis spectroscopy and measurement of zeta potential and average particle size.

The UV–vis spectrum for pristine and different non-covalently functionalized GNPs dispersed in distilled water is shown in Figure 4.1. From which it is clear that the peak absorption due to the presence of GNPs in all the samples is located in the wavelength range of 255–269 nm, after that peak and within the wavelengths range shown in Figure 4.1, a decrease in absorbance was observed in all the samples. The relative concentration, defined as the ratio of subsequent weight concentration of the sample to that of the fresh one, was calculated for all samples and shown in Figure 4.2. From Figure 4.2a, it is clear that pristine GNPs/water dispersion cannot maintain high stability for the range of ultrasonication times investigated, therefore, it can be concluded that non-covalent or covalent functionalization is essential for obtaining high colloidal stability GNPs/water nanofluids. Also, Figure 4.2a depicts that the 60-min ultrasonication time sample has slightly higher relative concentration after 60 days from the date of preparation. Thus, 60 min ultrasonication time can be considered as the most effective time for preparing nanofluids in this study. This conclusion was validated in Figure 4.2b, which showed that the SDBS-GNPs sample with 60 min ultrasonication time resulted in a higher stability than the other two samples for the same number of days. For SDBS, SDS, and CTAB, Figure 4.2 (c, d, and f), respectively, show that a (1-1) surfactant-GNPs ratio leads to better stability compared with the other ratios investigated. While for GA, Figure 4.2e presented that the highest stability is found at a ratio of (0.5-1) GA-GNPs. Furthermore, water-based GNPs nanofluids with the highest stability from those shown in Figure 4.2 are re-presented in Figure 4.3 to evaluate the most effective surfactant for dispersing GNPs in water from the four surfactants investigated. According to Figure 4.3, it is clear that all the surfactants enhanced the stability of the GNPs dispersions, however, they can be sorted from best to worst depending on the stability level of nanofluids after 60 days as; (SDBS, GA, CTAB, and SDS) with the relative concentrations of (82, 60, 54, and 53%), respectively.

Consequently, it can be concluded that using 0.1 wt% SDBS to disperse 0.1 wt% GNPs in distilled water with 60-min of ultrasonication resulted in the highest stability of nanofluid from all the prepared samples. Figure 4.4 shows a pictorial view of the five nanofluids shown in Figure 4.3. Figure 4.4a is after preparation with shaking the samples to display the formation of foam, while Figure 4.4b is after two months from preparation without any movement. Figure 4.4a clearly displays that due to the presence of SDBS, SDS, and CTAB surfactants, considerable foam was formed in the nanofluids. Therefore, care should be taken when using these surfactants in preparing water-based GNPs nanofluids for heat transfer applications because of the negative effects of foam on heat transfer efficiency and fluid flow. Furthermore, after two months from the date of preparation, Figure 4.4b clearly shows a full separation between pristine GNPs and distilled water, which is due to the hydrophobic nature of pristine GNPs. This finding agrees well with a previous research which proved that covalent and non-covalent functionalizations are the two possible methods to increase the dispersibility of pristine GNPs in water (Amiri et al., 2015a). Therefore, it can be concluded that covalent or non-covalent functionalization is essential for the stable dispersion of GNPs and similar carbon-based nanostructures in aqueous media. But, due to the problem of formation of foam associated with using surfactants for non-covalent functionalization, covalent functionalization is recommended for preparing aqueous dispersions of GNPs and similar carbon-based nanostructures in heat transfer and fluid flow applications where foam-free working fluids are required.

Measurement of zeta potential for a colloidal dispersion is one of the procedures used by the researchers to evaluate the stability of the prepared nanofluids by investigating its electrophoretic behavior (H. Zhu et al., 2007; Ghadimi et al., 2011). The importance of zeta potential is that its value can be linked directly to the stability of a colloidal suspension (Amrollahi et al., 2009). The relationship between dispersion stability and zeta potential arises from the mutual repulsion that occurs between like-charged particles. For this reason, particles with a high surface charge tend not to agglomerate, since contact is opposed (J.-H. Lee et al., 2008; Vandsburger, 2010). So, a nanofluid suspension with an absolute value of the measured zeta potential above 30 mV is considered to have a good colloidal stability (Vandsburger, 2010; Wei Yu & Xie, 2012). For water-based GNPs nanofluids shown in Figure 4.3, the values of zeta potential were measured and presented in Figure 4.5 and Table 4.1. The highest value of zeta potential (45.6 mv absolute) is shown for the (1-1) SDBS-GNPs sample, which is the most stable sample in the UV-vis tests. While the four remaining samples showed absolute value of zeta potential less than 30 mv. These results confirmed the trend of data obtained with the UV-vis tests and validated that from the surfactants investigated in this study, using SDBS surfactant for non-covalent functionalization of GNPs could provide the highest colloidal stability. Furthermore, Figure 4.5 illustrates the measured average particle size for water-based GNPs nanofluids shown in Figure 4.3. The values of average particle size and polydispersity index (PDI) measured by Zetasizer Nano ZS are presented in Table 4.1. In spite of the fact that lower average particle size indicates higher stability of the colloidal suspension (X. Li et al., 2007; X. F. Li et al., 2008; Huang et al., 2009; X.-j. Wang et al., 2009; Gowda et al., 2010), the average particle size for the (1-1) SDBS-GNPs sample is the second lowest value after the SDS-GNPs sample, but still lower than those for the other three samples.

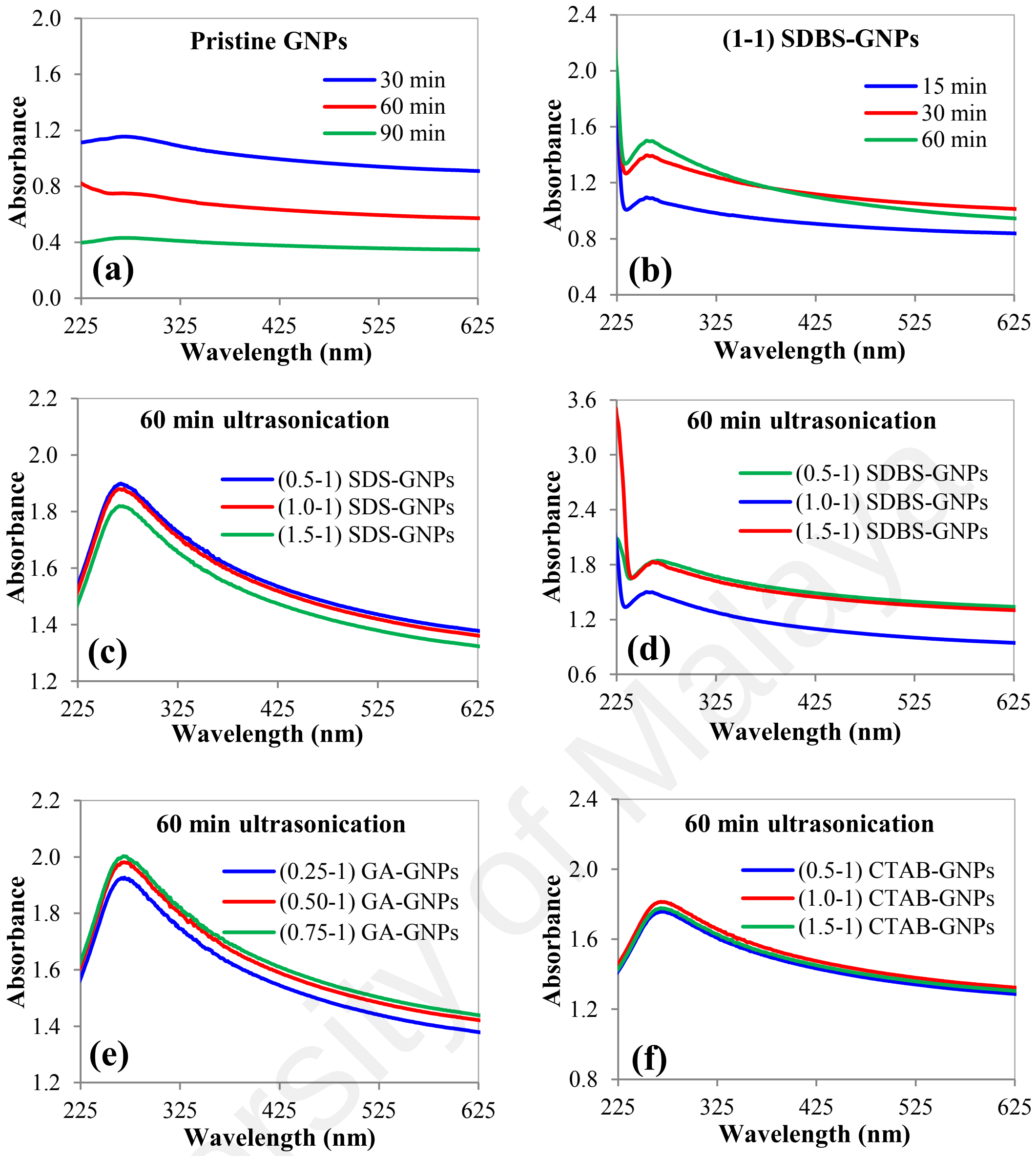

Figure 4.1: UV–vis spectrum of the diluted water-based 0.1-wt% GNPs 300 nanofluids at a ratio of 1:20. (a, b) Pristine GNPs and (1-1) SDBS-GNPs water-based nanofluids at different ultrasonication times, and (c-f) water-based GNPs nanofluids with different surfactants and 60 minutes ultrasonication time.

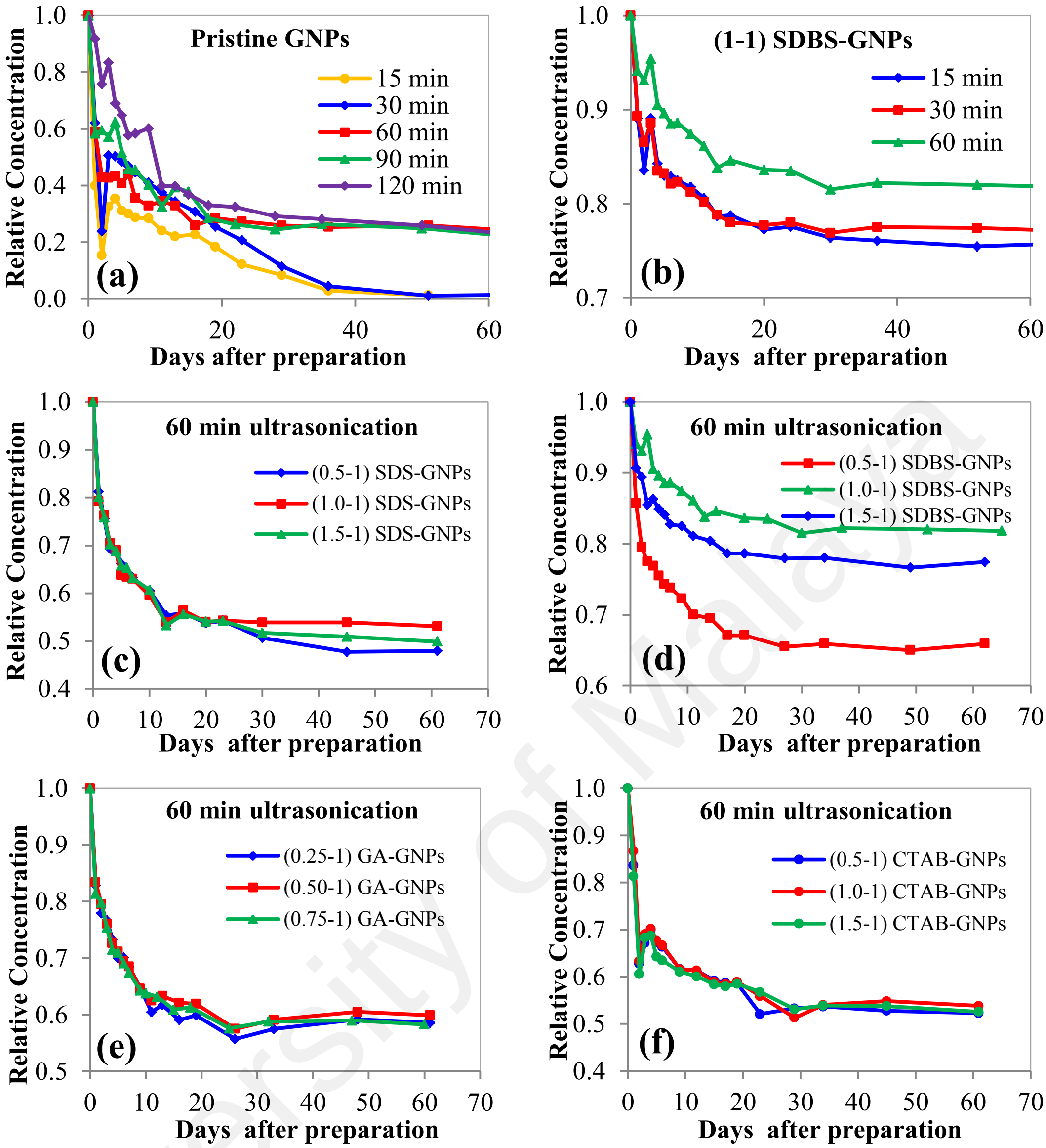

Figure 4.2: Variation of relative concentration with number of days after preparation for water-based 0.1-wt% GNPs 300 nanofluids. (a, b) Pristine GNPs and (1-1) SDBD-GNPs water-based nanofluids at different ultrasonication times, and (c-f) water-based GNPs nanofluids with different surfactants and 60 minutes ultrasonication time.

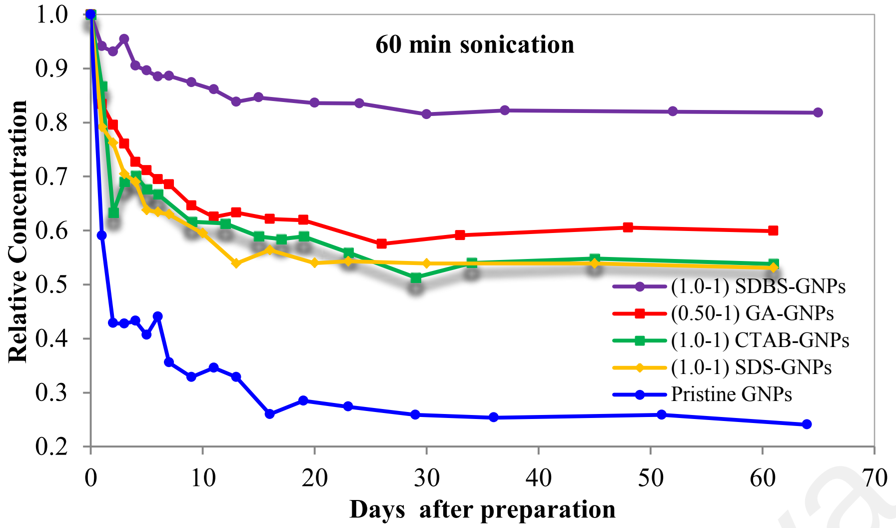

Figure 4.3: Relative concentration versus number of days after preparation for selected water-based 0.1-wt% GNPs 300 nanofluids with the highest stability from those shown in Figure 4.2.

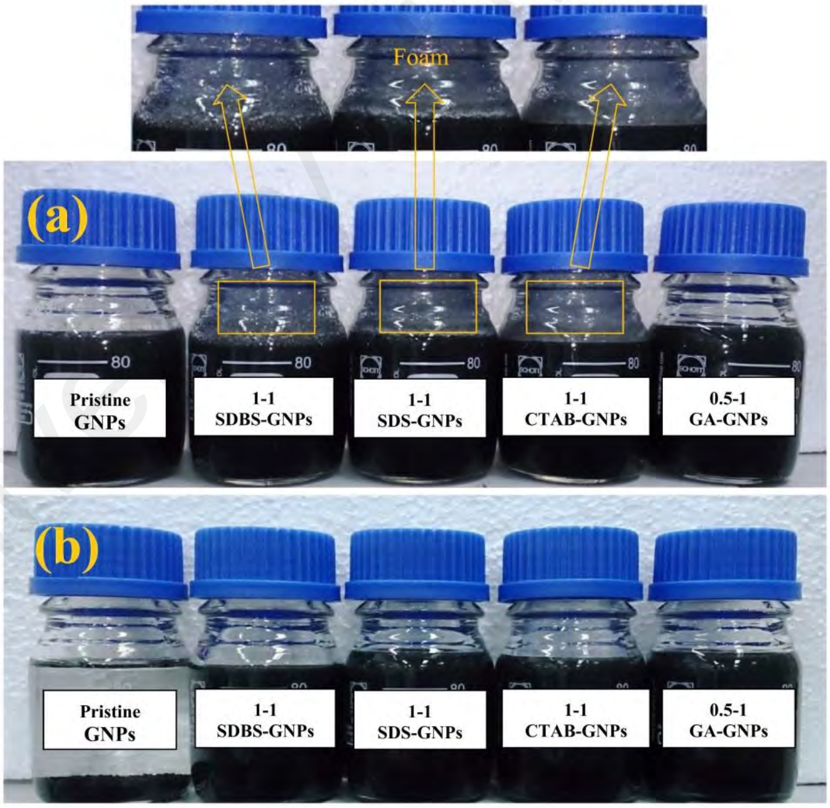

Figure 4.4: Photographs of the nanofluids shown in Figure 4.3. (a) After preparation with shaking of samples, and (b) After two months from preparation without any motion.

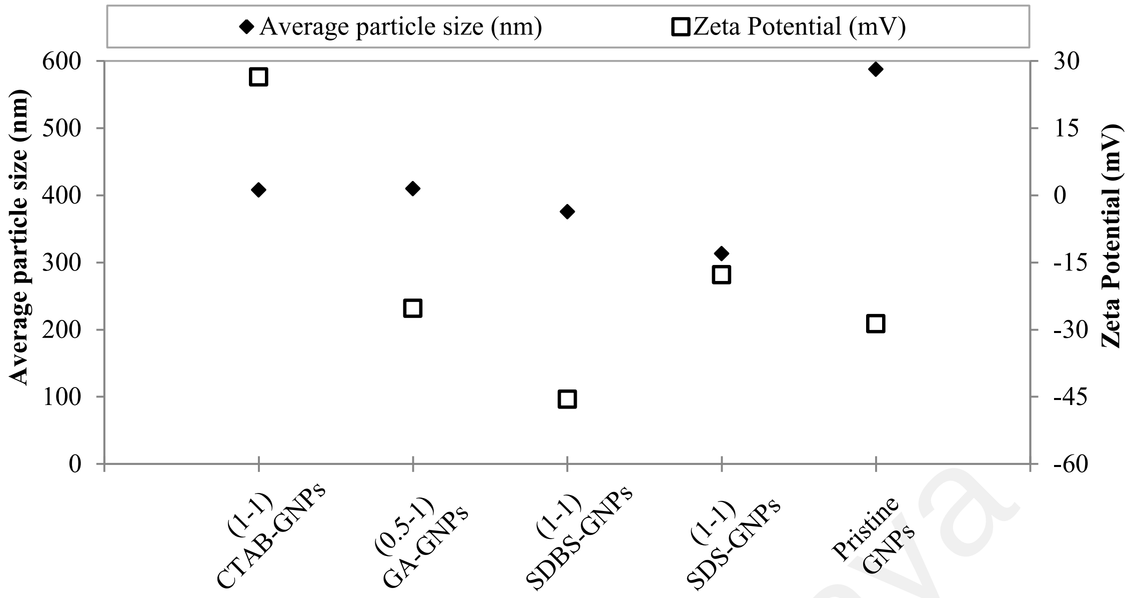

Figure 4.5: Zeta potential values and average particle size for the 0.1-wt% water-based GNPs 300 nanofluids shown in Figure 4.3.

Table 4.1: Values of zeta potential, average particle size (Z-average), and polydispersity index (PDI) for water-based 0.1-wt% GNPs 300 nanofluids.

Samples	Z-Average (nm)	Polydispersity Index (PDI)	Zeta Potential (mV)
(1-1) CTAB-GNPs	408.0 ± 2.1	0.372 ± 0.036	26.4 ± 0.6
(0.5-1) GA-GNPs	409.6 ± 0.7	0.390 ± 0.016	-25.3 ± 0.4
(1-1) SDBS-GNPs	375.4 ± 3.4	0.518 ± 0.047	-45.6 ± 0.3
(1-1) SDS-GNPs	312.8 ± 4.6	0.340 ± 0.038	-17.8 ± 0.2
Pristine GNPs	587.6 ± 4.5	0.426 ± 0.031	-28.7 ± 0.4

4.2.2 Stability of TEA-GNPs nanofluids

To prepare water-based TEA-GNPs nanofluid, the accurately measured amount of the TEA-GNPs was added to a known amount of distilled water as base fluid and the mixture was sonicated for 60 min. This sonication time was selected for preparing all the aqueous dispersions of covalently functionalized nanomaterials in this study based on the results obtained from the previous section. Twelve samples were synthesized using four weight concentrations, i.e., 0.025%, 0.05%, 0.075%, and 0.1%, for each SSA of the TEA-GNPs, i.e., 300, 500, and 750 m^2/g. Sonication process was performed at

60%-amplitude of power output and using a two-seconds on/off sequential scheme. Colloidal stability of the nanofluids that were prepared was investigated using UV–vis spectroscopy and measurement of zeta potential and average particle size.

The UV–vis spectrum for the diluted water-based TEA-GNPs nanofluids with different SSAs and weight concentrations is presented in Figure 4.6, from which it can be noted that the peak value of absorbance for all samples due to the presence of TEA-GNPs lies in the wavelength range of 261–266 nm. Photometric analysis of the UV-vis spectrometer was used to track the weight concentration of all the samples that were prepared at different times for more than 100 days. For this aim, a standard curve was prepared for each nanofluid sample relating its weight concentration with the value of absorbance. Figure 4.7 shows the colloidal stability for water-based TEA-GNPs nanofluids that were prepared as a function of time. Due to agglomeration and sedimentation, weight concentrations of the samples decrease with time at different rates, as shown in Figure 4.7a. From which, it can be realized that the remaining weight concentrations for all the samples after 100 days were (0.0101, 0.0169, and 0.0182 for the 0.025 wt% fresh samples), (0.0331, 0.0411, and 0.0418 for the 0.05 wt% fresh samples), (0.0556, 0.0634, and 0.0628 for the 0.075 wt% fresh samples), and (0.0769, 0.0875, and 0.083 for the 0.1 wt% fresh samples) for the SSAs of 300, 500, and 750 m^2/g, respectively. Thus, it can be concluded that with different weight concentrations and SSAs, the rate of sedimentation among the samples was different. This fact coincides with the findings of previous researchers (Yujin Hwang et al., 2008; Behi & Mirmohammadi, 2012; Nasiri et al., 2012).

The relative concentration could be very helpful in specifying the highest stability sample between all the prepared samples. From Figure 4.7 (b–d), the relative concentrations after a period of 100 days for the 0.025 wt%, 0.05 wt%, 0.075 wt%, and 0.1 wt% fresh samples, respectively, were (0.404, 0.662, 0.741, and 0.769 for the TEA-

GNPs 300), (0.676, 0.822, 0.844, and 0.876 for the TEA-GNPs 500), and (0.728, 0.836, 0.838, and 0.830 for the TEA-GNPs 750). From these results, the highest colloidal stability was reached by the 0.1-wt% TEA-GNPs 500 sample with a relative concentration of 0.876, i.e., sedimentation of 12.4% after 100 days. While the lowest colloidal stability was attained by the 0.025-wt% TEA-GNPs 300 sample with a relative concentration of 0.404, i.e., sedimentation of 59.6% after 100 days. Furthermore, it can be noted that the samples with the lowest weight concentration, i.e., 0.025 wt%, had the lowest stability, which coincides with the trend of results for the average particle size found by the Nano ZS Zetasizer, shown in Figure 4.8a. From this figure, it can be noted that the highest particle size went for the lowest weight concentration, i.e., 0.025 wt%, and knowing that the highest particle size results in the lowest colloidal stability (X. Li et al., 2007; X. F. Li et al., 2008; Huang et al., 2009; X.-j. Wang et al., 2009; Gowda et al., 2010), it can be concluded that the 0.025-wt% samples have the lowest dispersion stability. From Figure 4.7 (b–d), it can also be distinguished that water-based TEA-GNPs nanofluids with SSA of 300 m^2/g have the lowest colloidal stability when compared with other SSAs, which might be attributed to the larger particle size associated with lower SSA (Warzoha & Fleischer, 2014). This behavior is in agreement with that of the average particle size found by the Nano ZS Zetasizer, shown in Figure 4.8b. From this figure it can be found that the 300-m^2/g SSA sample had the highest particle size, i.e., the lowest colloidal stability when compared with the 500- and 750-m^2/g SSAs samples. Figure 4.8 shows the zeta potential results found from the Nano ZS Zetasizer for different weight concentrations and SSAs of water-based TEA-GNPs nanofluids. From which, it can be found that all the samples have absolute values of zeta potential close to 30 mV or higher, i.e., have good colloidal stability (Vandsburger, 2010; Wei Yu & Xie, 2012).

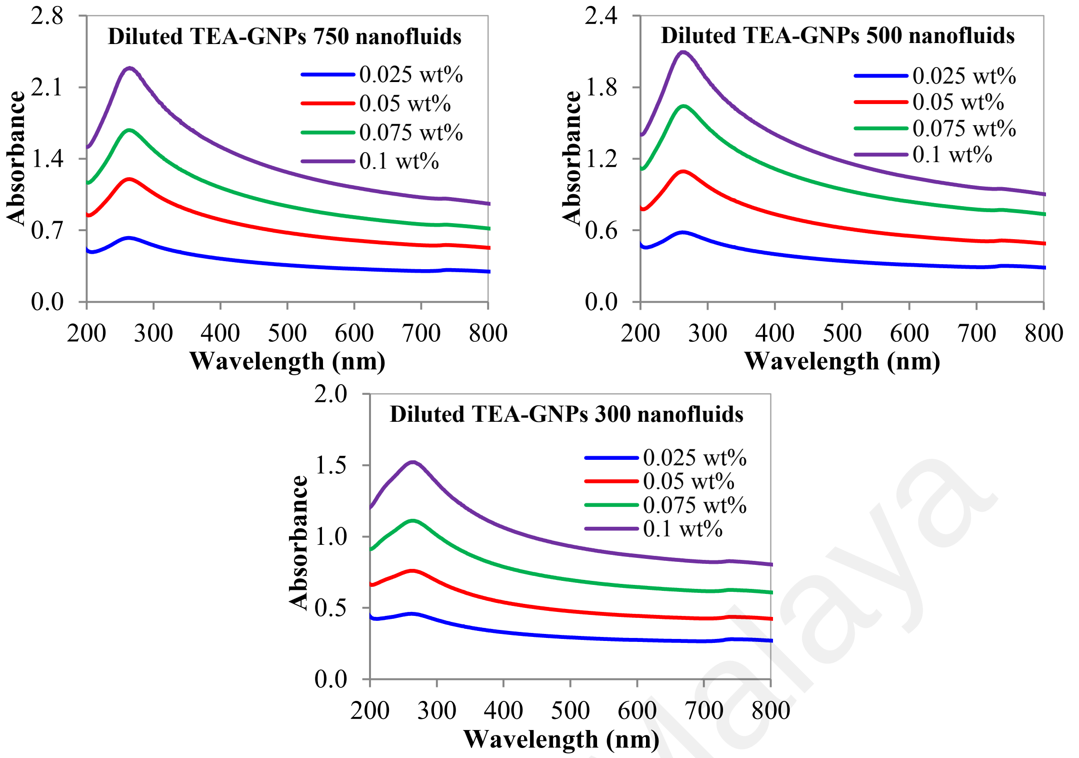

Figure 4.6: UV–Vis absorbance spectrum for the three different SSAs of the diluted water-based TEA-GNPs nanofluids at a ratio of 1:20.

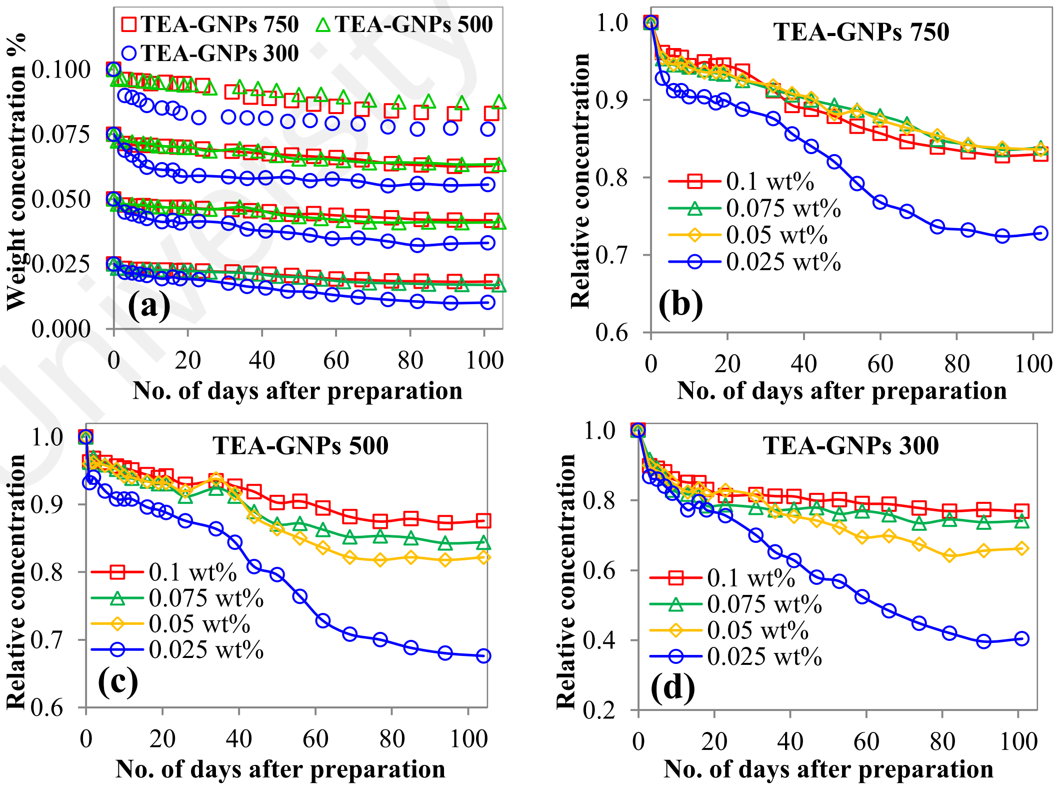

Figure 4.7: Weight and relative concentrations versus number of days after the nanofluids were prepared for different SSAs of TEA-GNPs dispersed in distilled water.

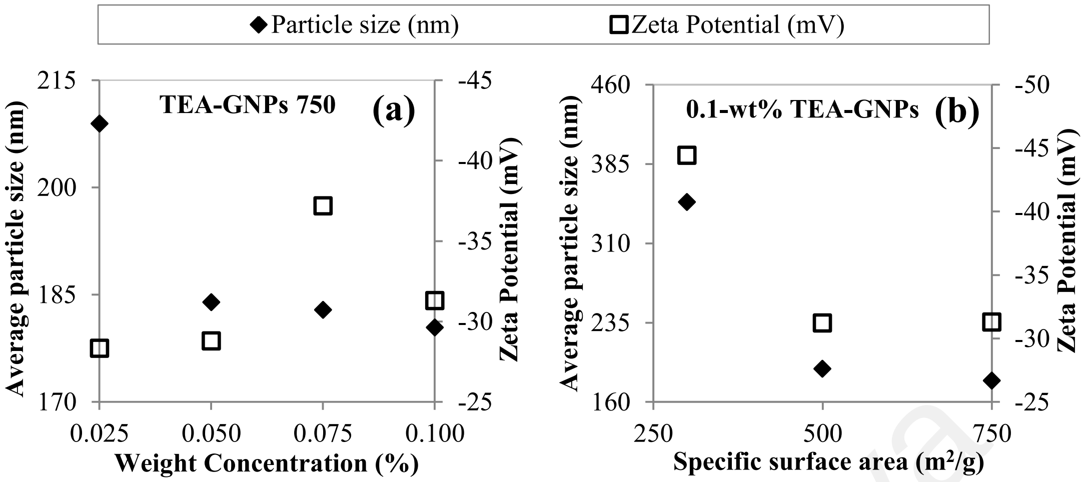

Figure 4.8: Values of average particle size and zeta potential found by Zetasizer Nano ZS for water-based nanofluids containing (a) different weight concentrations of TEA-GNPs 750 and (b) various SSAs of 0.1-wt% TEA-GNPs.

4.2.3 Stability of Ala-MWCNTs nanofluids

The two-step method with 60-min ultrasonication was used to prepare eight samples of water-based nanofluids containing Ala-MWCNTs with two different outside diameters, i.e., less than 8 nm and 20–30 nm, each with four weight concentrations, i.e., 0.025%, 0.05%, 0.075%, and 0.1%. Sonication process was performed at 60%-amplitude of power output and using a two-seconds on/off sequential scheme. Colloidal stability of the nanofluids that were prepared was investigated by UV–vis spectroscopy. The UV–vis spectrum for the two water-based Ala-MWCNTs nanofluids, diluted at a ratio of 1:20, at different weight concentrations is presented in Figure 4.9 (a, b). From which, it can be noticed that the highest value of absorbance due to the presence of Ala-MWCNTs for all nanofluids lies in the wavelength range of 248 −259 nm. Using UV-vis spectrometer, the photometric analysis was used to check the weight concentration at different times for all the samples that were prepared for more than 50 days. Weight concentrations versus number of days after preparation for all the samples are presented in Figure 4.9 (c, e). From which, it is clear that weight concentrations of the samples decreased at different rates with time as a result of agglomeration and sedimentation. After 50 days from preparation, the weight concentrations for the two Ala-MWCNTs nanofluids, i.e., less than 8 nm and 20–30 nm, were (0.0222 and 0.0218 for the 0.025 wt% fresh samples), (0.0468 and 0.0462 for the 0.05 wt% fresh samples), (0.0715 and 0.0702 for the 0.075 wt% fresh samples), and (0.0873 and 0.0925 for the 0.1 wt% fresh samples), respectively.

In order to identify the sample with the highest stability between all the nanofluids that were prepared, the relative concentrations for the two Ala-MWCNTs nanofluids as a function of time are presented in Figure 4.9 (d, f) at different weight concentrations. After 50 days from preparation, the relative concentrations for the 0.025 wt%, 0.05 wt%, 0.075 wt%, and 0.1 wt% fresh samples, respectively, were (0.888, 0.936, 0.955, and 0.863 for the Ala-MWCNTs with outside diameter less than 8 nm) and (0.872, 0.924, 0.939, and 0.925 for the Ala-MWCNTs with outside diameter of 20–30 nm). From the data presented, the highest colloidal stability after 50 days from preparation was achieved by the 0.075-wt% samples of Ala-MWCNTs < 8 nm and Ala-MWCNTs 20–30 nm with relative concentrations of 0.955 and 0.939, respectively, i.e., sedimentations of 4.5% and 6.1%. Furthermore, after 50 days from preparation, the lowest colloidal stability with relative concentrations of 0.863 and 0.872 was reached by the 0.1-wt% Ala-MWCNTs < 8 nm and 0.025-wt% Ala-MWCNTs 20–30 nm samples, respectively, i.e., sedimentations of 13.7% and 12.8%.

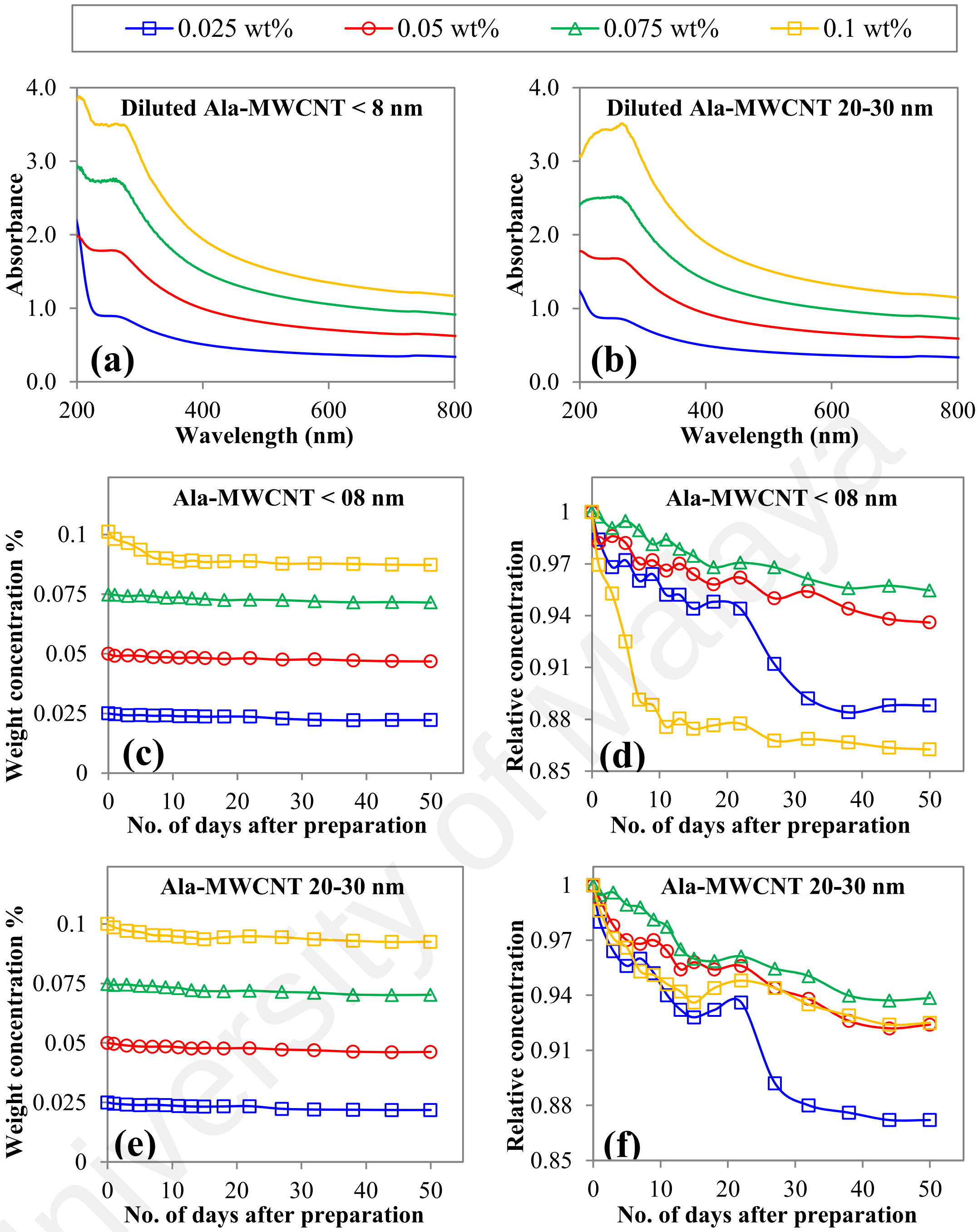

Figure 4.9: (a, b) UV–Vis absorbance spectrum for the two water-based Ala-MWCNTs nanofluids diluted at a ratio of 1:20; and (c–f) weight and relative concentrations versus number of days after preparation for the two water-based Ala-MWCNTs nanofluids.

4.3 Characterization of nanomaterials and nanofluids

Several methods were used to characterize the carbon-based nanostructures and water-based nanofluids that were used and synthesized in this study which will be presented in the following sections.

4.3.1 Characterization of water-based GNPs nanofluids with surfactants

Aqueous nanofluids that were prepared by non-covalent functionalization with surfactants were characterized using TEM from Hitachi (HT7700). The TEM images for the lowest and highest stability samples that were prepared, i.e., the 0.1 wt% pristine GNPs and the (1-1) SDBS-GNPs, respectively, are displayed in Figure 4.10. All the TEM images reveal the presence of some multi-layer structure of GNPs. Images of the pristine GNPs sample (Figure 4.10 (a, b)) illustrate flakes with relatively smooth layer's surface and edge. On the other hand, images of the SDBS-GNPs sample (Figure 4.10 (c and d)) provide layer's surface full of wrinkles. Although TEM images are not able to show minute SDBS surfactant, some changes in morphology and surface deterioration can be considered as an evidence for non-covalent functionalization. The wrinkles (waviness) seen in the TEM images are attributed to the inherent instability of 2D structures, which is increased during the ultrasonication process, resulting from appropriate flexibility of GNP flakes after treatment (Q. Zhang et al., 2013; Amiri et al., 2015a). Undoubtedly, SDBS can increase the wettability of GNP layer's surface, implying higher tendency for wrinkling during ultrasonication and/or drying process in preparing the TEM samples. Consequently, higher dispersion stability was obtained as a result of higher wettability of the GNP layer's surface (Wei et al., 2011; Kamiya et al., 2012).

The pH of water-based GNPs nanofluids in the presence and absence of surfactants has been measured and presented in Table 3.3. From which, it can be concluded that all the prepared nanofluids were non-corrosive since the values of pH were higher than 4 and less than 9 (F. Anderson, 2013).

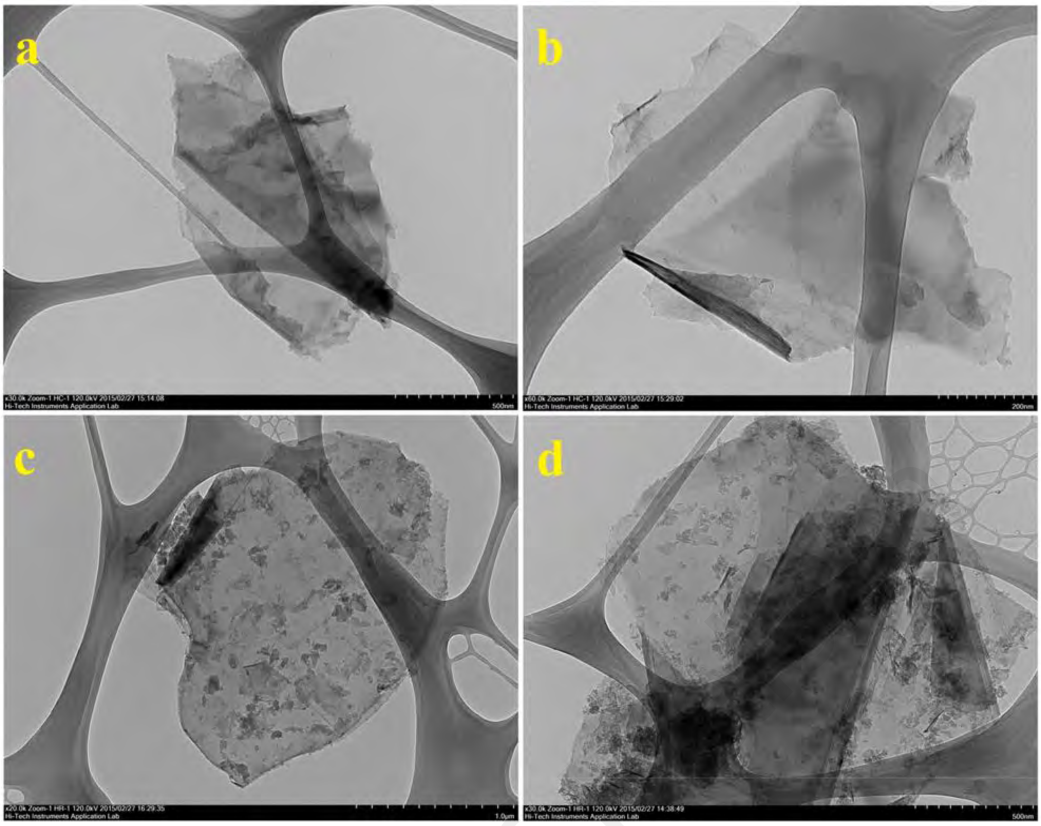

Figure 4.10: TEM images of water-based 0.1-wt% GNPs 300 nanofluids. (a, b) Pristine GNPs, and (c, d) (1-1) SDBS-GNPs.

4.3.2 Characterization of the TEA-GNPs nanofluids

Characterization of the water-based nanofluids containing triethanolamine-treated GNPs with different SSAs was performed using FTIR, Raman spectroscopy, TEM, and EDS. The FTIR spectra of the pristine and TEA-GNPs 750 are shown in Figure 4.11a. Clearly, in contrast to the pristine GNP 750, the TEA-GNPs 750 sample demonstrates some obvious cues of the TEA molecule. The detailed list of the peaks along with their interpretations is given in Table 4.2. The spectrum of TEA-GNPs 750 shows a board peak at 3359 cm^{-1}, which could be attributed to the O–H stretching vibration. Both symmetric and antisymmetric fundamental vibrations of CH bonds are observed at 2894-2950 cm^{-1} for the TEA-GNPs 750. Also, the peaks in the range of 1587-1645 cm^{-1} are attributable to the C=C stretching vibration of the graphene flakes after opening as a result of the electrophilic addition reaction of the main structure or edge of the GNP with –OH band of TEA. Furthermore, TEA functionalization was confirmed by the appearance of peaks at 1455, 1405, 1128, and 1070 cm^{-1} for the CH_2 bending vibration, out of plane CH vibration, C–N, and C–O stretching vibrations, respectively. The peaks at 1031 and 891 cm^{-1} are in agreement with stretching vibration of C–C and COH out of plane deformation.

Raman spectral analysis of the pristine and the TEA-GNPs 750 is shown in Figure 4.11b. At wavenumbers around 1349 and 1589 cm^{-1}, the Raman spectra of both samples exhibit D and G bands, respectively. The D band is related to the amorphous/disordered carbon (sp^3) and the G band to the graphitic carbon (sp^2) (Hodkiewicz, 2010). The increase in the Raman intensity ratio (I_D/I_G) means that some of the hybridized carbons have changed from sp^2 to sp^3 because of the covalent functionalization (Jeon et al., 2011; Amiri et al., 2015b). While pristine GNP 750 shows a ratio of 0.508 for the I_D/I_G, the TEA-GNPs 750 depicts a ratio of 0.999. Larger (I_D/I_G) ratio indicates the presence of higher number of sp^3 carbons and the happening of an electrophilic addition reaction. Since the same functionalizing procedure was followed for all the SSAs of the GNPs in this study, similar results for FTIR and Raman spectra were obtained. Therefore, they were not repeated and reported.

To confirm the electrophilic addition reaction, elemental analysis was performed by EDS spectroscopy for the three SSAs used in this study (i.e., 300, 500, and 750 m^2/g) and presented in Figure 4.11 (c–e). The EDS spectra of the TEA-GNPs illustrate traces amount of nitrogen, oxygen, and carbon in their chemical structures. Furthermore, EDS results are presented in Table 4.3 to accurately ascertain the exact amount of each element. EDS analysis illustrates the same degree of functionalization for the different SSAs of GNPs. Note that the presence of O and N elements in the TEA-GNPs is a good evidence of successful functionalization.

Using Hitachi TEM (HT7700), the TEM images for water-based pristine and TEA-GNPs nanofluids are presented in Figure 4.12. Obviously, all TEM images demonstrate some multi-layered graphene flakes with diameter around 2 µm. Images of the pristine GNP 300 samples (Figure 4.12 (a, b)) illustrate flakes with relatively smooth layer's surface and edge. Although TEM images for the TEA-GNPs (Figure 4.12 (c–h)) are not able to distinguish minute functional groups, surface deterioration and wrinkles of the GNPs that formed as a result of covalent functionalization with TEA can clearly been observed. According to the TEM results, the TEA-GNPs flakes preserved their shape and size as compared with the pristine sample. The presence of so many lines and wrinkles within the TEA-GNPs flakes can be attributed to the inherent instability of the 2D structures and the improved flexibility of GNP flakes after treatment (Q. Zhang et al., 2013; Amiri et al., 2015a). Obviously, higher tendency for wrinkling indicates an increase in the wettability of GNP's surface due to covalent functionalization with TEA. The easily-miscible TEA functionalities may explain the increased wettability of the treated GNPs. Consequently, higher dispersion stability was obtained (Wei et al., 2011; Kamiya et al., 2012).

The values of pH were measured after preparation and the results for the 0.025%, 0.05%, 0.075%, and 0.1 wt% were: TEA-GNPs 300 (6.86, 6.71, 6.63, and 6.54); TEA-GNPs 500 (7.86, 7.62, 7.52, and 7.48); and TEA-GNPs 750 (7.82, 7.71, 7.67, and 7.57), respectively. Since all pH values were higher than 4 and less than 9, it could be decided that the prepared water-based TEA-GNPs nanofluids were non-corrosive (F. Anderson, 2013), i.e., they can be used as working fluids in heat transfer applications.

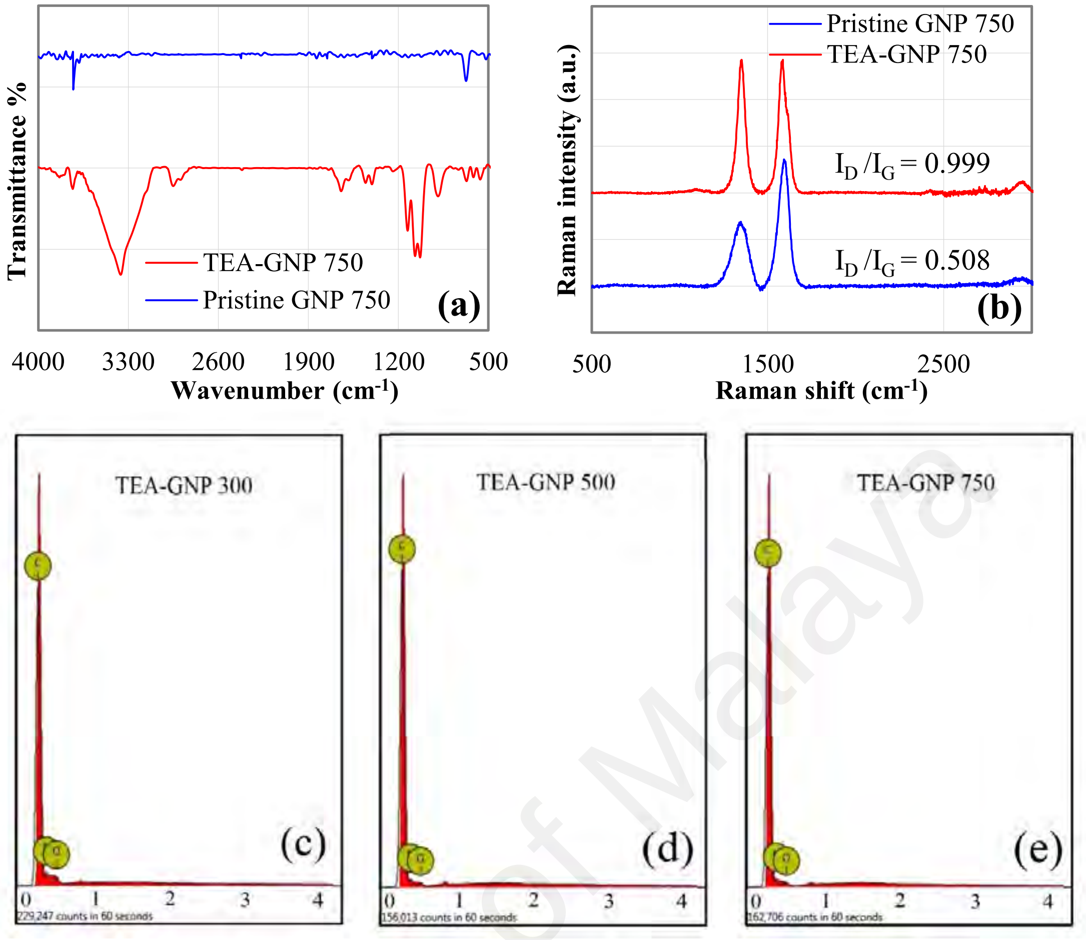

Figure 4.11: Characterization of the pristine and TEA-GNPs using: (a) FTIR spectral measurement, (b) Raman spectral measurement, and (c–e) EDS traces for different SSAs of the TEA-GNPs: (c) 300, (d) 500, and (e) 750 m^2/g.

Table 4.2: Ranges of FTIR vibration peaks and their corresponding chemical bonds for the covalently functionalized TEA-GNPs with 750-m^2/g SSA.

Wavenumber (cm^{-1})	Interpretation
3359	O-H stretching vibration
2950	CH_2 antisymmetric stretching vibration
2894	CH_2 symmetric stretching vibration
1587-1645	C=C stretching vibration
1455	CH_2 bending vibration
1405	Out of plane CH vibration
1128	C–N stretching vibration
1070	C–O stretching vibration
1031	C-C stretching vibration
891	COH out of plane deformation

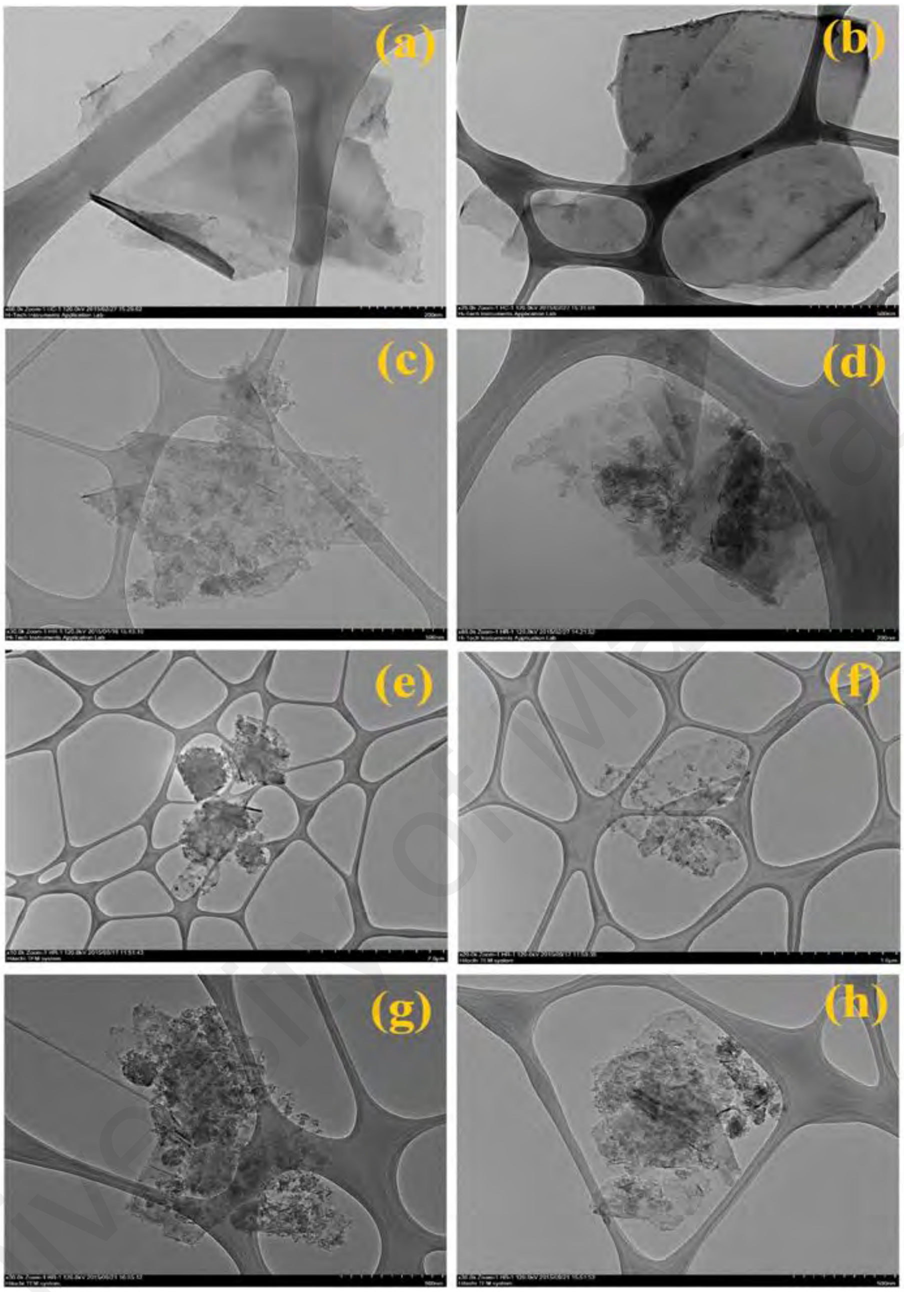

Figure 4.12: (a, b) TEM images for the pristine GNPs 300. (c–h) TEM images for the three different SSAs of the TEA-GNPs: (c, d) 300, (e, f) 500, and (g, h) 750 m^2/g.

Table 4.3: EDS results for TEA-GNPs with different SSAs.

Material/Element	Carbon	Oxygen	Nitrogen
TEA-GNPs 300	80.3 ±0.8	10.1±2.9	5.4±1.2
TEA-GNPs 500	79.9±0.9	9.8±1.1	5.1±0.6
TEA-GNPs 750	81.1±0.8	10.2±2.5	5.2±1.1

4.3.3 Characterization of the Ala-MWCNTs nanofluids

Water-based nanofluids containing Ala-MWCNTs with different outside diameters were characterized using FTIR, Raman spectroscopy, and TEM. The FTIR spectra of pristine and Ala-MWCNTs with outside diameter of 20–30 nm are illustrated in Figure 4.13a. Furthermore, the obtained infrared peaks and their assigned bonds are listed in Table 4.4. According to Figure 4.13a, the pristine MWCNTs show no sharp or even small peaks of any functional groups, representing the high purity of pristine samples. In contrast to the pristine MWCNTs, the Ala-MWCNTs sample illustrates meaningful peaks, demonstrating the presence of –OH, $–NH_2$, C–H, C=O, CH_2, C–N, and C–O bonds. These bonds and their interpretation can verify the successful functionalization of MWCNTs with β-Alanine.

Raman spectroscopy can also be utilized as a strong evidence for the covalent functionalization of MWCNTs. The Raman spectra of pristine and Ala-MWCNTs with outside diameter of 20–30 nm are presented in Figure 4.13b. From which, it can be seen that both samples display D and G bands at around 1346 cm^{-1} and 1577 cm^{-1}, respectively (Hodkiewicz, 2010). Intensity ratio of D–band to G–band (I_D/I_G) is known to show the proportion of sp^3 hybridized carbon (disordered C) to sp^2 hybridized carbon (graphitic C). As a great evidence, the hybridization of sp^2 carbons changes to sp^3 once the functionalization of MWCNTs occurs, resulting in an enhancement in I_D/I_G ratio (Amiri et al., 2015e; Amiri et al., 2016a). As could be seen in Figure 4.13b, the I_D/I_G ratio of Ala-MWCNTs is higher than that of pristine sample, representing 0.97 for the Ala-MWCNTs and 0.40 for pristine MWCNTs. The enhancement of I_D/I_G for the functionalized Ala-MWCNTs is in good agreement with the presence of different bands in the above-mentioned FTIR results.

TEM images taken using LEO 912 AB electron microscope for water-based nanofluids containing pristine and Ala-MWCNTs nanofluids with different outside diameters are displayed in Figure 4.14. In the pristine MWCNTs images (Figure 4.14a, b), MWCNTs with quite smooth and intact walls can be observed. In contrast, MWCNTs with increased roughness on the surface of the two Ala-MWCNTs samples are obvious after treatment (Figure 4.14c–g), resulting from the functionalization procedure under severe sonication process (Schwarz et al., 2004; Xu et al., 2008). Furthermore, open-end MWCNTs (Figure 4.14c–f) can also be considered as another evidence for successful functionalization (Zardini et al., 2012). Moreover, Figure 4.14g clearly depicts the high surface roughness on the surface of Ala-MWCNTs. In fact, reactive semi-stable diazonium ion can simply make a radical reaction with surface and caps of MWCNTs, causing the partial damage defect sites in graphitic sidewall of MWCNTs and disrupting the sp^2 carbon in the graphitic network of MWCNTs (Balasubramanian & Burghard, 2005). The reaction procedure can be accelerated under sonication condition. These observations are in appropriate agreements with the higher I_D/I_G in the Raman results (Figure 4.13b) and confirming functionalization of MWCNTs with β-Alanine.

Furthermore, the values of pH were measured after preparation and the results for the Ala-MWCNTS nanofluids with outside diameters of less than 8 nm and 20–30 nm were (7.00, 6.97, 6.96, and 6.64) and (6.41, 5.47, 6.62, and 5.53) for weight concentrations of 0.025%, 0.05%, 0.075%, and 0.1%, respectively. As all the recorded values of pH were higher than 4 and less than 9, it can be concluded that prepared water-based Ala-MWCNTS nanofluids were non-corrosive (F. Anderson, 2013), i.e., they might be used as working fluids in heat transfer applications.

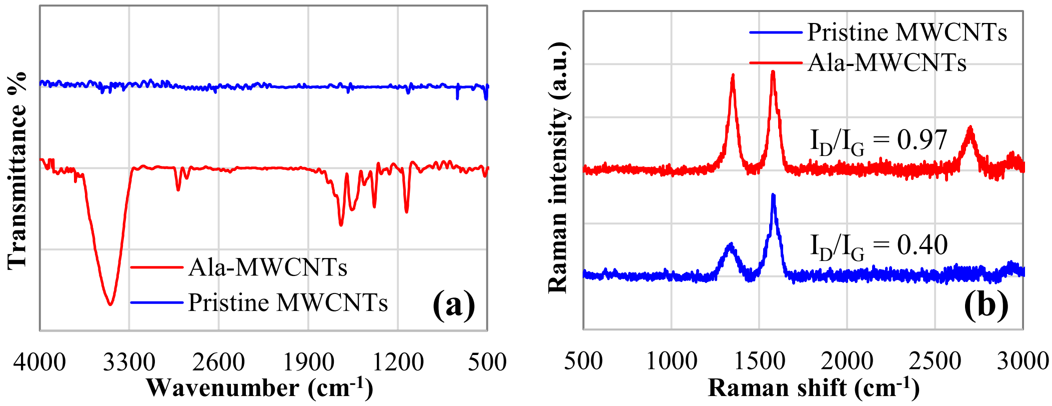

Figure 4.13: Characterization of pristine and Ala-MWCNTs with outside diameter of 20–30 nm using: (a) FTIR spectral measurement and (b) Raman spectral measurement.

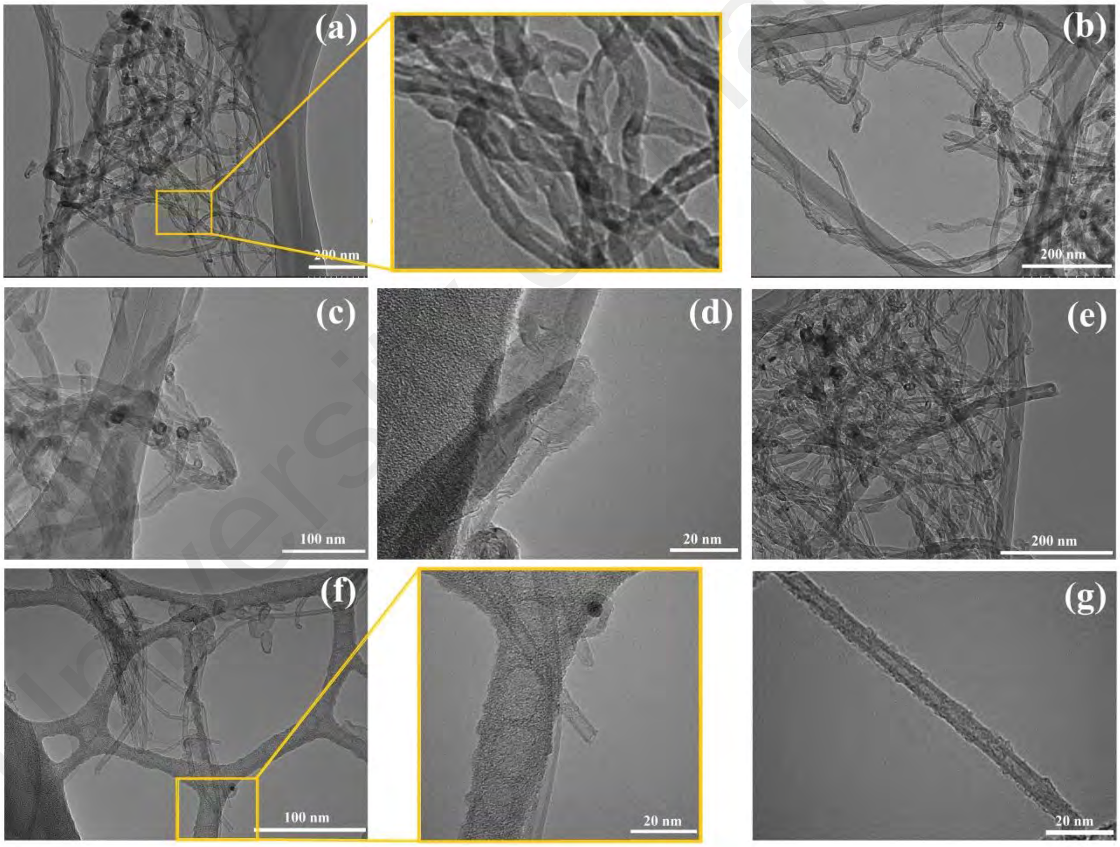

Figure 4.14: TEM images of water-based nanofluids containing pristine MWCNTs with outside dimeter of 20–30 nm (a, b) and Ala-MWCNTs with outside diameter of 20–30 nm (c–e) and less than 8 nm (f, g).

Table 4.4: Ranges of FTIR vibration peaks and their corresponding chemical bonds for the functionalized Ala-MWCNTs with outside diameter of 20–30 nm.

Wavenumber (cm^{-1})	Interpretation
3448	−OH stretching vibration and/or −NH stretching vibration of primary amine
2854 and 2919	sp^3 C− H and sp^2 C− H stretching vibration
1644	–C=O stretching vibration
1560	$–NH_2$ bending vibration
1455	$–CH_2$ bending vibration
1380	–C–N stretching vibration
1132	–C–O stretching vibration

4.4 Thermophysical properties of nanofluids

The availability of accurately predicted data for the thermophysical properties of the base fluid is essential to precisely calculate the thermophysical properties of nanofluids required in the MATLAB code. Accordingly, a comparison was made and found that the data obtained from the set of correlations presented in the previous chapter for the calculation of thermophysical properties of water reproduced the standard values listed in Arnold (1970) within the temperature range used in this study. The thermophysical properties of water-based nanofluids that were prepared in this study are presented in the following sections.

4.4.1 Thermal conductivity of nanofluids

Thermal conductivity was measured using the KD2 Pro thermal properties analyzer in the temperature range of 20–40 °C. In order to validate and check whether the KD2 Pro is working within the limits of the designed accuracy, the measured data for distilled water was compared with standard data presented by Arnold (1970), as shown in Figure 4.15. From which, it can be found that the measured thermal conductivity increases as temperature increases, as expected, and that the KD2 Pro underestimated the standard values of thermal conductivity with a maximum difference of 4.08%. Consequently, it can be concluded that the KD2 Pro is satisfactory working within its designed accuracy.

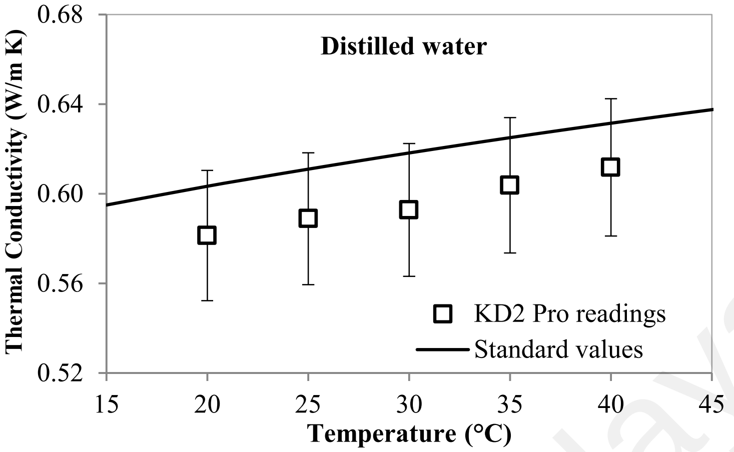

Figure 4.15: The measured thermal conductivity for distilled water using KD2 Pro thermal properties analyzer versus the standard values presented by Arnold (1970).

4.4.1.1 Thermal conductivity of GNPs nanofluids with surfactants

The values of measured thermal conductivity for distilled water and the non-covalently functionalized water-based 0.1wt% GNPs nanofluids shown in Figure 4.3 were plotted against temperature in Figure 4.16. From which, it can be found that the thermal conductivity increases as temperature increases. Also, from the four surfactants that were used in this work, the thermal conductivity of the GNPs nanofluids significantly increased in the presence of three surfactants only, i.e., GA, SDBS, and CTAB. For the range of temperatures studied, the enhancements in thermal conductivity were 6.519−10.80% for GA, 5.09−8.36% for SDBS, and 4.07−5.80% for CTAB. Obviously, GA is superior to both SDBS and CTAB because the GA-GNPs nanofluid has higher thermal conductivity, followed by the SDBS- and CTAB-GNPs nanofluids, respectively. On the other hand, with an enhancement in thermal conductivity of 0.89−1.44%, the presence of the SDS surfactant clearly suppressed the improvement in thermal conductivity of water-based GNPs nanofluids that were prepared. In previous research and in both laminar and turbulent flow, it was proved that nanofluids with better thermal conductivities than their base fluids will also have greater convective heat transfer coefficients (Sarit Kumar Das et al., 2003; Xuan & Li, 2003; Faulkner et al., 2004; Sarit K Das et al., 2007; Kwon et al., 2013; Amiri et al., 2015c). Consequently, water-based GNPs nanofluids containing GA, SDBS, and CTAB are expected to have higher heat transfer performance than that of distilled water. Moreover, due to extremely low enhancement in thermal conductivity, it can also be concluded that the SDS-GNPs nanofluid is not an appropriate working fluids for heat transfer applications.

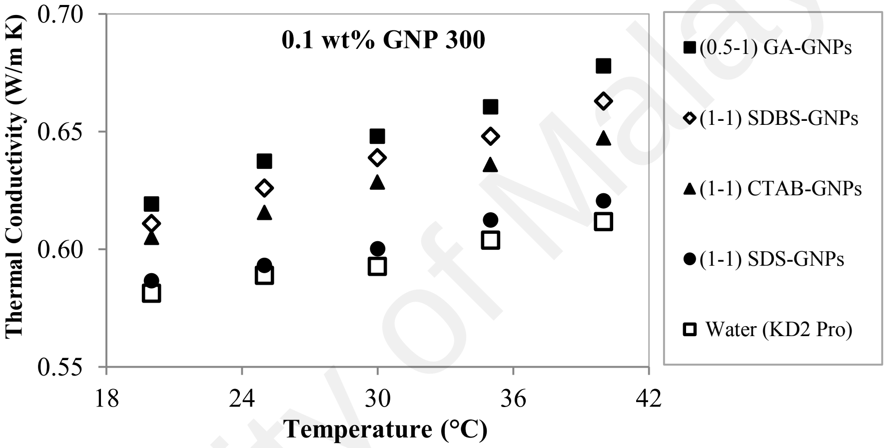

Figure 4.16: Thermal conductivity values for distilled water and the non-covalently functionalized water-based 0.1-wt% GNPs 300 nanofluids shown in Figure 4.3.

4.4.1.2 Thermal conductivity of TEA-GNPs nanofluids

The values of thermal conductivity that were measured for water and water-based TEA-GNPs nanofluids are plotted against temperature in Figure 4.17 at different weight concentrations and SSAs. As the temperature increases from 20 to 40 °C, Figure 4.17a indicates that the thermal conductivity of water-based TEA-GNPs 750 nanofluids increases from 0.627 to 0.662 W/m K at 0.025 wt%; from 0.641 to 0.713 W/m K at 0.05 wt%; from 0.651 to 0.729 W/m K at 0.075 wt%; and from 0.673 to 0.752 W/m K at 0.1 wt%. In comparison to water, the corresponding percentage enhancements in thermal conductivity are from 7.84% to 12.45% at 0.025 wt%; from 10.25% to 16.54% at 0.05

wt%; from 11.97% to 19.15% at 0.075 wt%; and from 15.76% to 22.91% at 0.1 wt%. For water-based TEA-GNPs nanofluids at 0.1 wt%, Figure 4.17b shows that the increase in temperature from 20 to 40 °C results in an increase in the thermal conductivity from 0.673 to 0.752 W/m K for 750-m^2/g SSA; from 0.647 to 0.708 W/m K for 500-m^2/g SSA; and from 0.626 to 0.672 W/m K for 300-m^2/g SSA. When compared to water, the corresponding percentage enhancements in thermal conductivity are from 15.76% to 22.91% for 750-m^2/g SSA; from 11.28% to 15.72% for 500-m^2/g SSA; and from 7.67% to 9.83% for 300-m^2/g SSA. It can be concluded that the increase in weight concentration, SSA, and temperature enhances the thermal conductivity, up to 22.91% for TEA-GNPs with 750-m^2/g SSA. The aforementioned conclusion about the effect of SSA on the thermal conductivity of water-based TEA-GNPs nanofluids agrees with the findings of previous researchers (Xuan & Li, 2000; Sen Gupta et al., 2011; Nasiri et al., 2012; Fang et al., 2015; Mehrali et al., 2015; Amiri et al., 2017a; Amiri et al., 2017b).

Four models of thermal conductivity that previously were presented in the literature review chapter, i.e., the models of MG-EMT (Gong et al., 2014), Nan et al. (2003), Nan et al. (1997), and Chu et al. (2012a), were compared with experimental data obtained using the KD2 Pro at different temperatures, SSAs, and weight concentrations, as shown in Figure 4.18. A MATLAB code using an iterative loop was developed in order to solve the model of Chu et al. (2012a) and find the value of nanofluid thermal conductivity. From Figure 4.18, it can be established that both models that neglected the effect of interfacial thermal resistance, i.e., MG-EMT (Gong et al., 2014) and Nan et al. (2003), overestimate the values of thermal conductivity. On the other hand, the models of Nan et al. (1997) and Chu et al. (2012a) that incorporated the effect of interfacial thermal resistance show better agreement with the experimental data in this study. However, using an interfacial thermal resistance value in the range of 1.95×10^{-9} to 4.05

× 10^{-9} m^2 K/W for both models, higher accuracy was obtained with the model of Chu et al. (2012a) with a maximum difference of 3.34%. Therefore, it will be used in the current study for evaluating the thermal conductivity values of water-based TEA-GNPs nanofluids. The range of interfacial thermal resistances obtained coincides with that found by Lin et al. (2010), and it is one order of magnitude smaller than that for CNTs with 8.33×10^{-8} m^2 K/W found by Huxtable et al. (2003), which may be attributed to the large lateral length of the GNPs (ordinarily around 2 μm) in comparison with that of the CNTs (typically around 10 nm) (Lin et al., 2010).

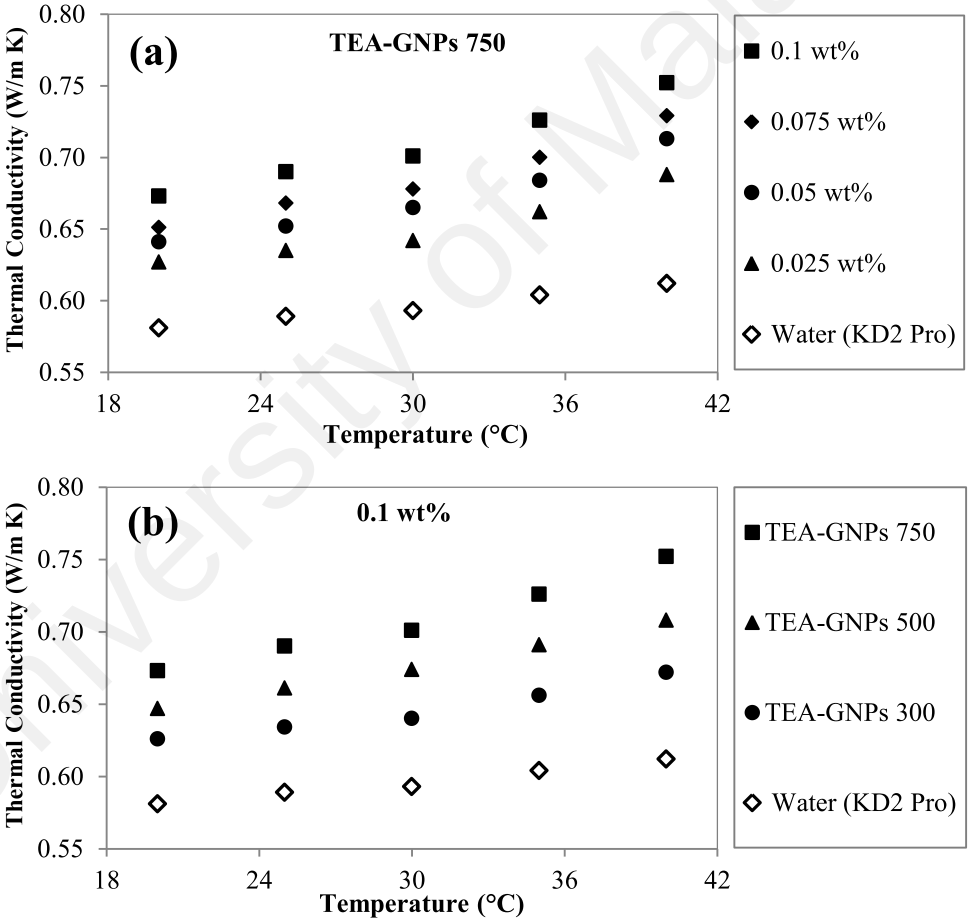

Figure 4.17: Measured values of thermal conductivity for water and water-based TEA-GNPs nanofluids versus temperature at different; (a) weight concentrations of TEA-GNPs 750 and (b) SSAs of 0.1-wt% TEA-GNPs.

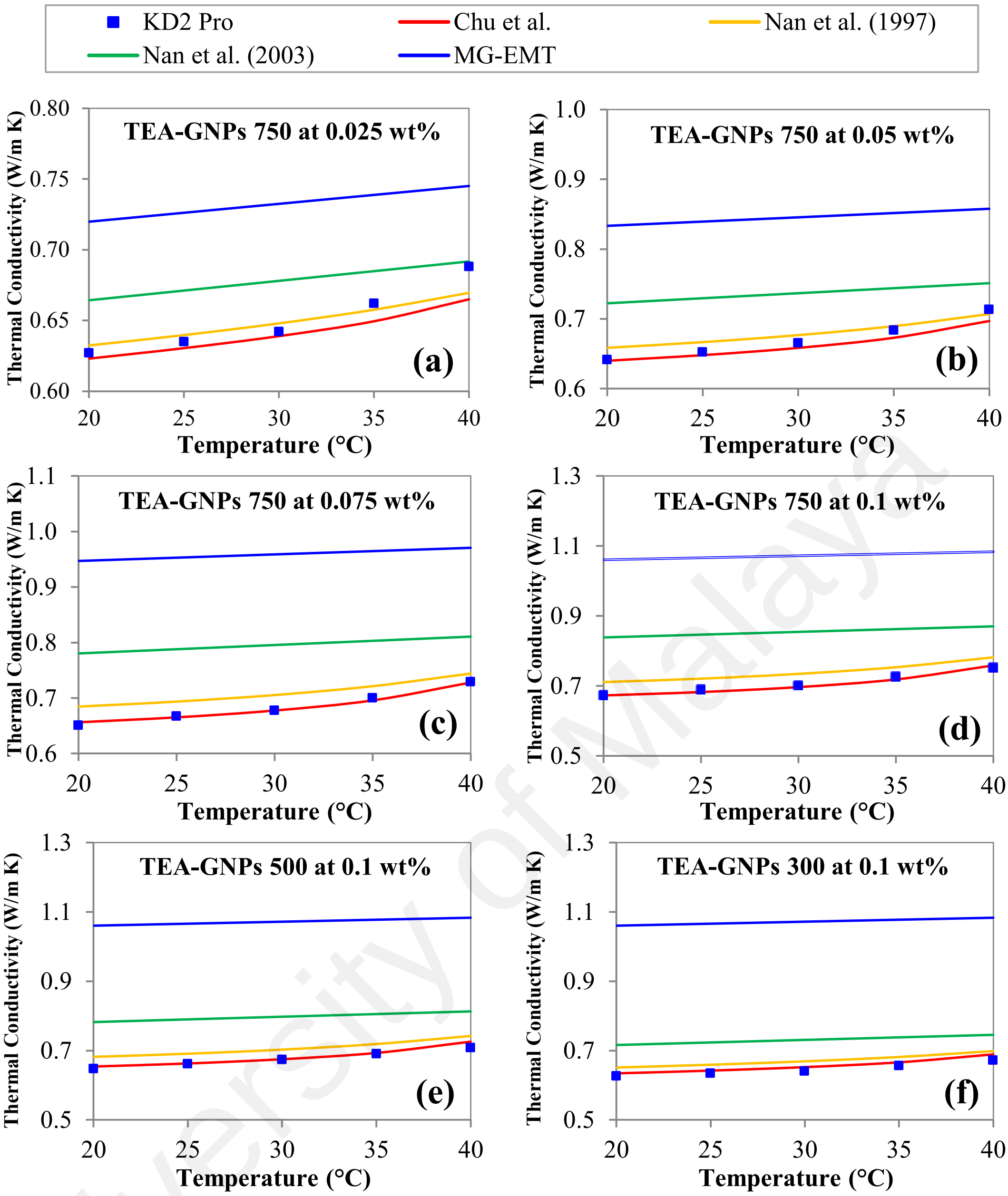

Figure 4.18: Values of thermal conductivity for water-based TEA-GNPs nanofluids at different temperatures, SSAs, and weight concentrations using the KD2 Pro versus the calculated values from the models of MG-EMT (Gong et al., 2014), Nan et al. (2003), Nan et al. (1997), and Chu et al. (2012a).

4.4.1.3 Thermal conductivity of Ala-MWCNTs nanofluids

The measured values of thermal conductivity for water and two water-based Ala-MWCNTs nanofluids at different temperatures and weight concentrations are presented in Figure 4.19. From Figure 4.19a and as the temperature increases from 20 to 40 °C, the thermal conductivity of water-based nanofluids containing Ala-MWCNTs with outside diameter < 8 nm increases from 0.61 to 0.664 W/m K at 0.025 wt%; from 0.616 to 0.675 W/m K at 0.05 wt%; from 0.626 to 0.689 W/m K at 0.075 wt%; and from 0.637 to 0.702 W/m K at 0.1 wt%. In comparison to water, the corresponding percentage enhancements in thermal conductivity are from 4.92% to 8.53% at 0.025 wt%; from 5.95% to 10.32% at 0.05 wt%; from 7.67% to 12.61% at 0.075 wt%; and from 9.56% to 14.74% at 0.1 wt%. Furthermore, from Figure 4.19b, the thermal conductivity of water-based nanofluids containing Ala-MWCNTs with outside diameter of 20−30 nm increases from 0.596 to 0.644 W/m K at 0.025 wt%; from 0.602 to 0.663 W/m K at 0.05 wt%; from 0.609 to 0.678 W/m K at 0.075 wt%; and from 0.624 to 0.687 W/m K at 0.1 wt% as the temperature increases from 20 to 40 °C. When compared to water, the corresponding percentage enhancements in thermal conductivity are from 2.51% to 5.26% at 0.025 wt%; from 3.54% to 8.36% at 0.05 wt%; from 4.75% to 10.81% at 0.075 wt%; and from 7.33% to 12.29% at 0.1 wt%. The enhancement in the measured values of thermal conductivity for Ala-MWCNTs < 8 nm (with SSA > 500 m^2/g) was higher than that for Ala-MWCNTs 20−30 nm (with SSA > 110 m^2/g). This result coincides with the findings of previous researchers (Nasiri et al., 2011; Nasiri et al., 2012), which may be attributed to the fact that Ala-MWCNTs with outside diameter < 8 nm have higher SSA than Ala-MWCNTs with outside diameter of 20−30 nm (Xuan & Li, 2000; Sen Gupta et al., 2011; Nasiri et al., 2012; Fang et al., 2015; Mehrali et al., 2015; Amiri et al., 2017a; Amiri et al., 2017b). Thus, it can be concluded that for water-based Ala-MWCNTs nanofluids, the thermal conductivity increases as weight concentration, SSA, and temperature increase, up to 14.74% and 12.29% for Ala-MWCNTs with outside diameters of < 8 nm and 20−30 nm, respectively.

The measured values of thermal conductivity for water-based nanofluids containing Ala-MWCNTs with outside diameter < 8 nm at different temperatures and weight concentrations were compared with the models of Nan et al. (2003) and Nan et al. (1997), as shown in Figure 4.20. From which, it can be recognized that the model of Nan et al. (2003) that neglected the effect of interfacial thermal resistance overestimates the values of thermal conductivity. Instead, the model of Nan et al. (1997) that considered the effect of interfacial thermal resistance shows good agreement with the experimental data with a maximum difference of 2.09%. Consequently, it can be used for calculating the thermal conductivity values of water-based Ala-MWCNTs nanofluids.

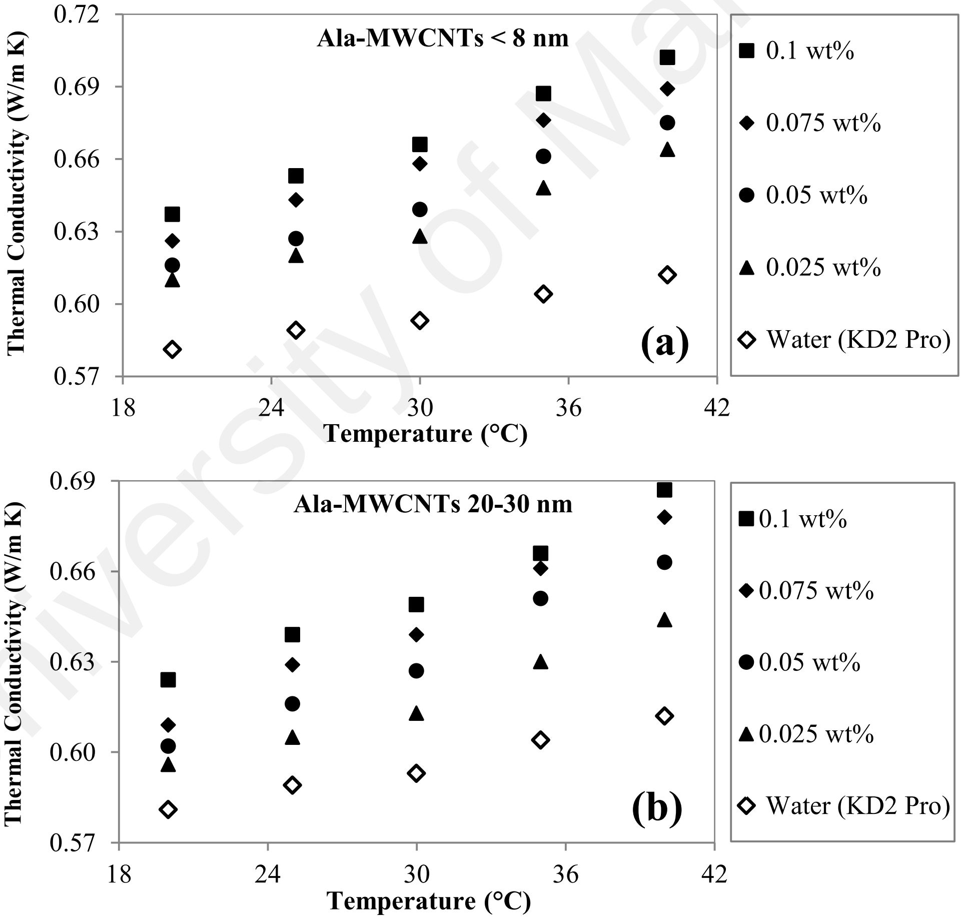

Figure 4.19: Measured values of thermal conductivity for water and water-based Ala-MWCNTs nanofluids with outside diameters of (a) < 8 nm and (b) 20–30 nm.

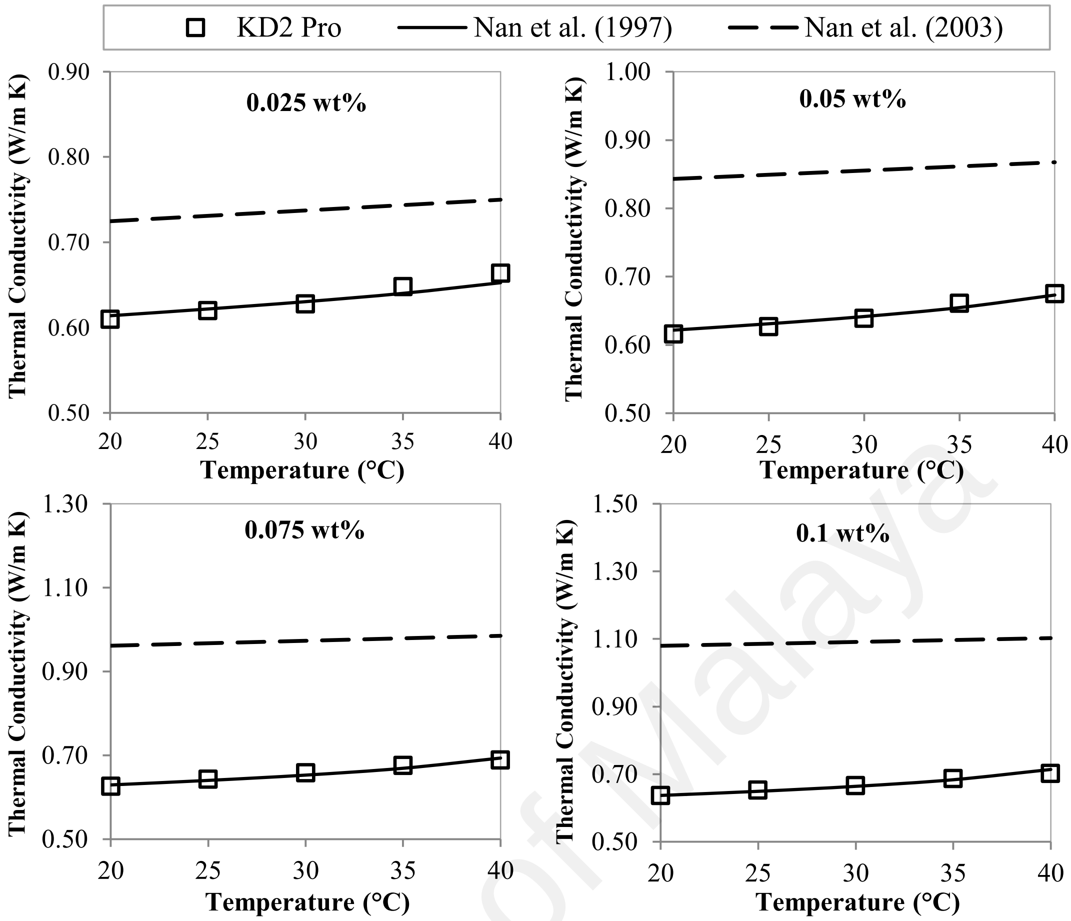

Figure 4.20: Measured values of thermal conductivity for water-based nanofluids containing Ala-MWCNTs < 8 nm at different temperatures and weight concentrations versus calculated values from the models of Nan et al. (2003) and Nan et al. (1997).

4.4.2 Dynamic viscosity of nanofluids

The accuracy and reliability of the rheometer was validated by comparing the measured values of viscosity for distilled water at 200-1/s shear rate with the standard values presented by Arnold (1970), as shown in Figure 4.21, and a maximum difference of 1.04% was found. Thus, it was concluded that the rheometer is reliable for measuring the viscosity of nanofluids with an acceptable accuracy.

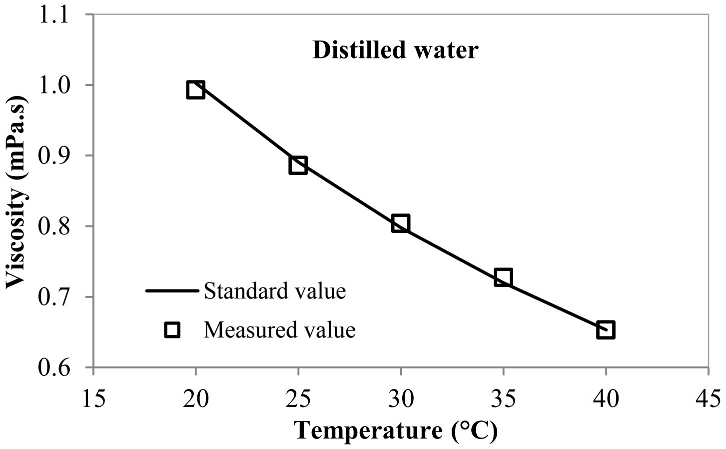

Figure 4.21: Comparison between the measured values of viscosity for distilled water at 200-1/s shear rate with the standard values presented by Arnold (1970).

4.4.2.1 Dynamic viscosity of GNPs nanofluids with surfactants

Plots of viscosity versus shear rate at different temperatures for distilled water and the water-based GNPs nanofluids shown in Figure 4.3 in the absence and presence of surfactants are displayed in Figure 4.22. The range of shear rate was 20–200 1/s, while for temperature was 25–55 °C. From Figure 4.22, the behavior of water-based (1-1) SDBD-, SDS-, and CTAB-GNPs nanofluids is almost Newtonian in the whole range of shear rate, and the average values of viscosity are higher than that of distilled water with (7.4%, 4.5%, and 6.9% at 25°C), (3.9%, 4.8%, and 5.4% at 30°C), (0.9%, 2.4%, and 1.7% at 35 °C), (3.7%, 7.6%, and 5.0% at 40°C), (5.4%, 13.6%, and 6.8% at 45°C), (5.2%, 17.5%, and 7.1% at 50°C), and (5.9%, 20.8%, and 7.7% at 55°C), respectively. On the other hand, pristine GNPs nanofluid showed a non-Newtonian (shear-thinning) behavior in a certain region of shear rate with Newtonian behavior prevailing afterward and in all the investigated temperatures except at 35°C, at which, a Newtonian behavior prevailed in the whole shear rate range. Also, the average values of viscosity are higher than that of distilled water with (14.1%, 11.4%, 4.1%, 9.8%, 25.7%, 37.6%, and 45.7%) at (25, 30, 35, 40, 45, 50, and 55 °C), respectively. But for the (0.5-1) GA-GNPs nanofluid, a severe shear-thinning behavior was observed along the major part of the shear rate region, and this behavior continued afterwards with a slight slope. This non-Newtonian behavior of the 0.5-1 GA-GNPs nanofluid was previously reported by some researchers (Sanchez et al., 2002; Ding et al., 2006; Garg et al., 2009; X Li et al., 2011), which may be attributed to the unique properties of the GA surfactant, since GA/water in a low concentration of 0.25 wt% showed this behavior in previous research (Ding et al., 2006; Garg et al., 2009). Moreover, the average values of viscosity are much higher than that of the distilled water with (116.9%, 83.6%, 63.7%, 76.5%, 59.7%, 79.3%, and 108.9%) at (25, 30, 35, 40, 45, 50, and 55 °C), respectively. Therefore, it is clear that the effect of GA on the viscosity of GNPs nanofluid is much higher than the other investigated surfactants (with 116.9% maximum increase in the average viscosity in comparison to water) whereas its concentration is half of them. Thus, the use of GA as a surfactant in fluid flow applications could result in a large increase in the pressure loss and pumping power, which is an undesirable effect. In contrast, the SDBS-GNPs sample caused a maximum increase of 7.4% in the average viscosity of the base fluid, and has the highest colloidal stability. Some of the main considerations for the successful use of nanofluids as working fluids in heat transfer applications are high colloidal stability and lowest increase in base fluid viscosity (Duangthongsuk & Wongwises, 2010; Behi & Mirmohammadi, 2012). Accordingly, SDBS can be considered as the most effective surfactant among the four surfactants considered in the present study.

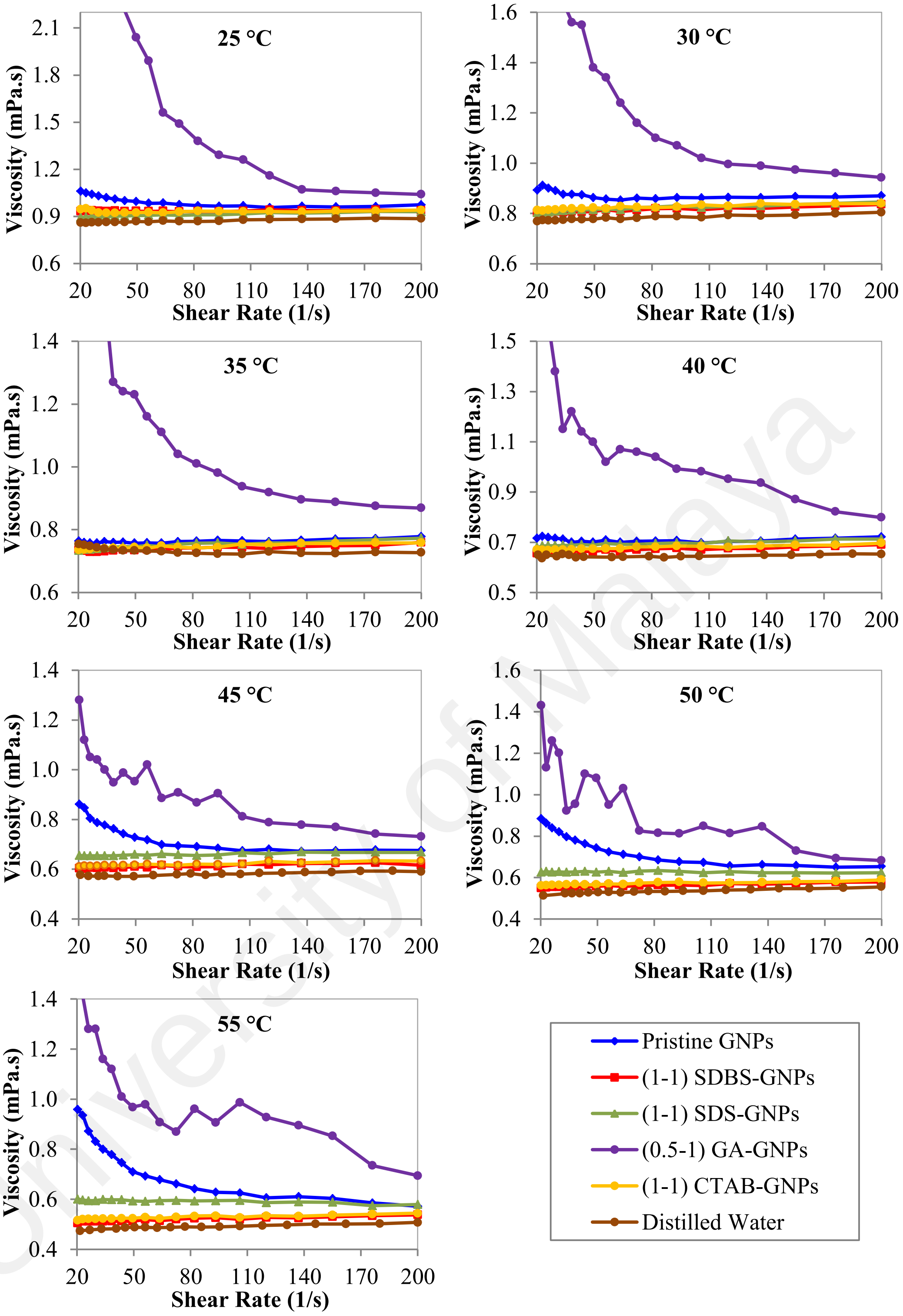

Figure 4.22: Plots of viscosity versus shear rate at different temperatures for distilled water and the water-based 0.1-wt% GNPs 300 nanofluids shown in Figure 4.3.

4.4.2.2 Dynamic viscosity of TEA-GNPs nanofluids

The measured values of viscosity for water-based TEA-GNPs nanofluids versus shear rate at different temperatures, SSAs, and weight concentrations are plotted in Figure 4.23. From which, it can be found that the behavior of water-based TEA-GNPs nanofluids is quite Newtonian with almost constant viscosity at different values of shear rate. Furthermore, the measured values of viscosity for water and water-based TEA-GNPs nanofluids versus temperature are presented in Figure 4.24 at different SSAs and weight concentrations. From Figure 4.24a, it can clearly be found that viscosity of TEA-GNPs 750 nanofluids is higher than water and increases as weight concentration increases. Also, referring to Figure 4.24b, very close values of viscosity for different SSAs of 0.01-wt% TEA-GNPs are found, especially at temperatures above 30 °C, with slightly higher viscosity for higher SSA. Thus, it can be concluded that the viscosity increases as weight concentration increases and decreases as temperature increases. In comparison to water, the highest increase of 23.66% in the viscosity was observed for the TEA-GNPs 750 at 0.1 wt%. The measured values of viscosity at 30 and 40 °C for the TEA-GNPs 750 nanofluids are compared with the classical models of Einstein, Brinkman, and Batchelor, which have previously been presented in the literature review chapter, and displayed in Figure 4.25. From which, it is obviously proved that all the classical models have under-predicted the values of viscosity for the TEA-GNPs 750 nanofluids. Therefore, a correlation has been developed, equation (4.1), by modifying the factor in the original Einstein model for spheres from a value of 2.5 to a fitted value of 550 that represents the TEA-GNPs of this study. The predicted values of viscosity from the developed correlation are in good agreement with the measured values with a maximum difference of 2.3%, as shown in Figure 4.25. Thus, it can reliably be used for determining the values of viscosity for water-based TEA-GNPs nanofluids.

Suggested correlation, $$\frac{\mu_{nf}}{\mu_{bf}} = 1 + 550\, \emptyset_v \qquad (4.1)$$

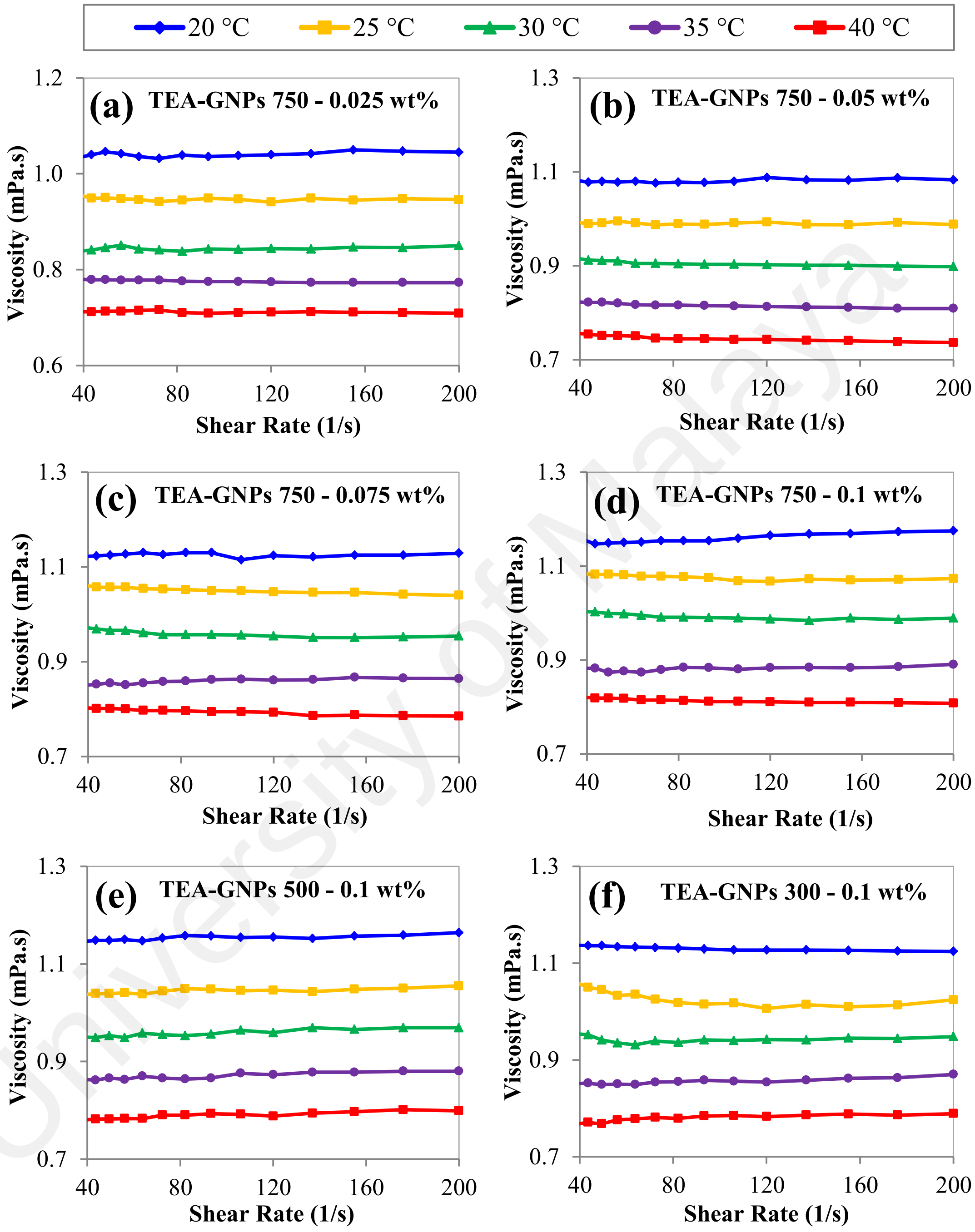

Figure 4.23: Plots of the measured values of viscosity versus shear rate for water-based TEA-GNPs nanofluids at different temperatures, SSAs, and weight concentrations.

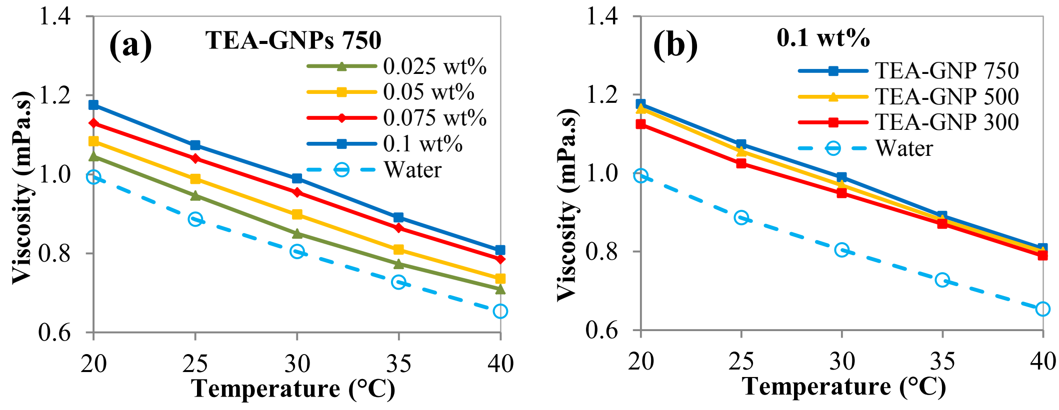

Figure 4.24: Plots of measured values of viscosity versus temperature for distilled water and water-based TEA-GNPs nanofluids at a shear rate of 200 1/s; (a) different weight concentrations of TEA-GNPs 750, and (b) different SSAs of TEA-GNPs.

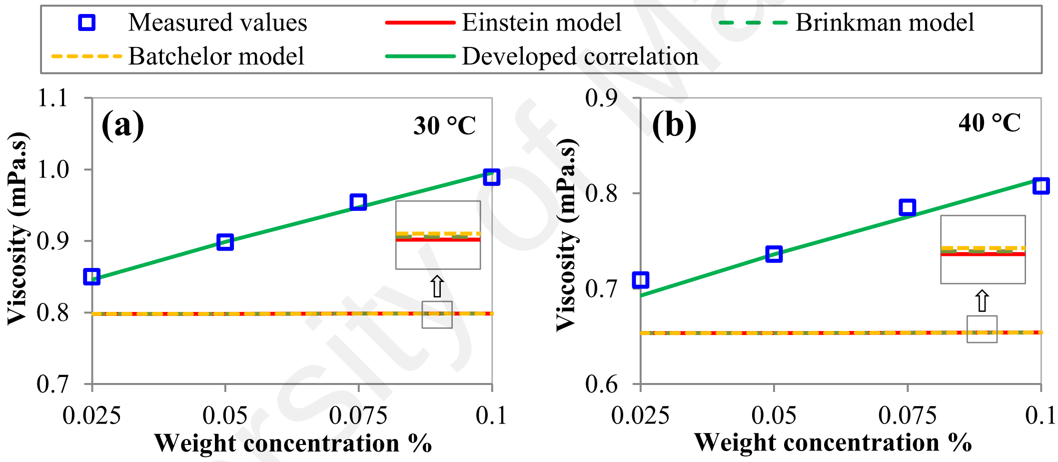

Figure 4.25: Comparison between the measured values of viscosity for water-based TEA-GNPs 750 nanofluids at (a) 30 °C and (b) 40 °C with the classical viscosity models of Einstein (1906) (as cited in Mahbubul et al. (2012), Brinkman (1952), and Batchelor (1977) (as cited in Y. Li et al. (2009)) and with the developed correlation.

4.4.2.3 Dynamic viscosity of Ala-MWCNTs nanofluids

The measured values of viscosity for water-based Ala-MWCNTs nanofluids at different weight concentrations versus temperature are presented in Figure 4.26 at a shear rate of 200 1/s. From which, it can be concluded that the viscosity decreases as temperature increases and increases as weight concentration increases. The viscosity increased up to 25.04% and 25.69% for 0.1-wt% water-based Ala-MWCNTs nanofluids with outside diameters of less than 8 nm and 20–30 nm, respectively, in comparison to water. The classical models of Einstein, Brinkman, and Batchelor in addition to the formerly suggested correlation for viscosity, i.e., equation (4.1), have all been compared with the measured values of viscosity at 30 and 40 °C for the water-based Ala-MWCNTs nanofluids and presented in Figure 4.27. From which, it can be found that the predicted values of viscosity by all the classical models are significantly lower than the measured values. However, the data obtained from the suggested correlation showed good agreement with the measured values of viscosity with a maximum difference of 3.79%. Accordingly, it can be used for calculating the values of viscosity for water-based Ala-MWCNTs nanofluids with a reasonable accuracy.

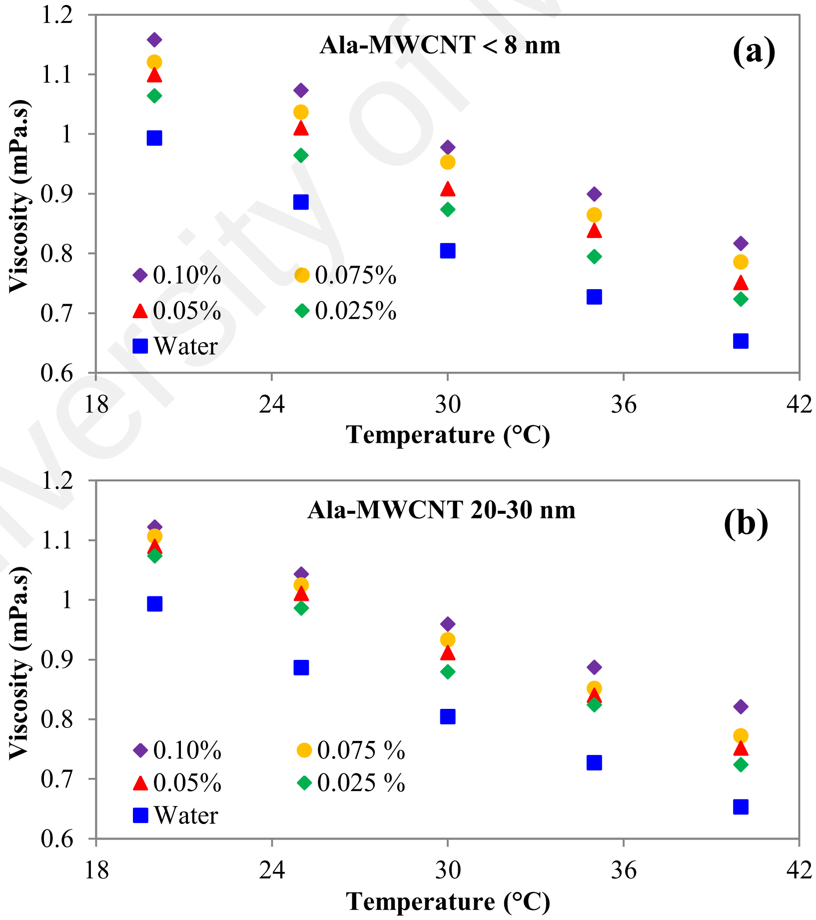

Figure 4.26: The measured values of viscosity versus temperature at 200-1/s shear rate for water and different weight concentrations of water-based Ala-MWCNTs nanofluids with outside diameters of (a) < 8 nm, and (b) 20–30 nm.

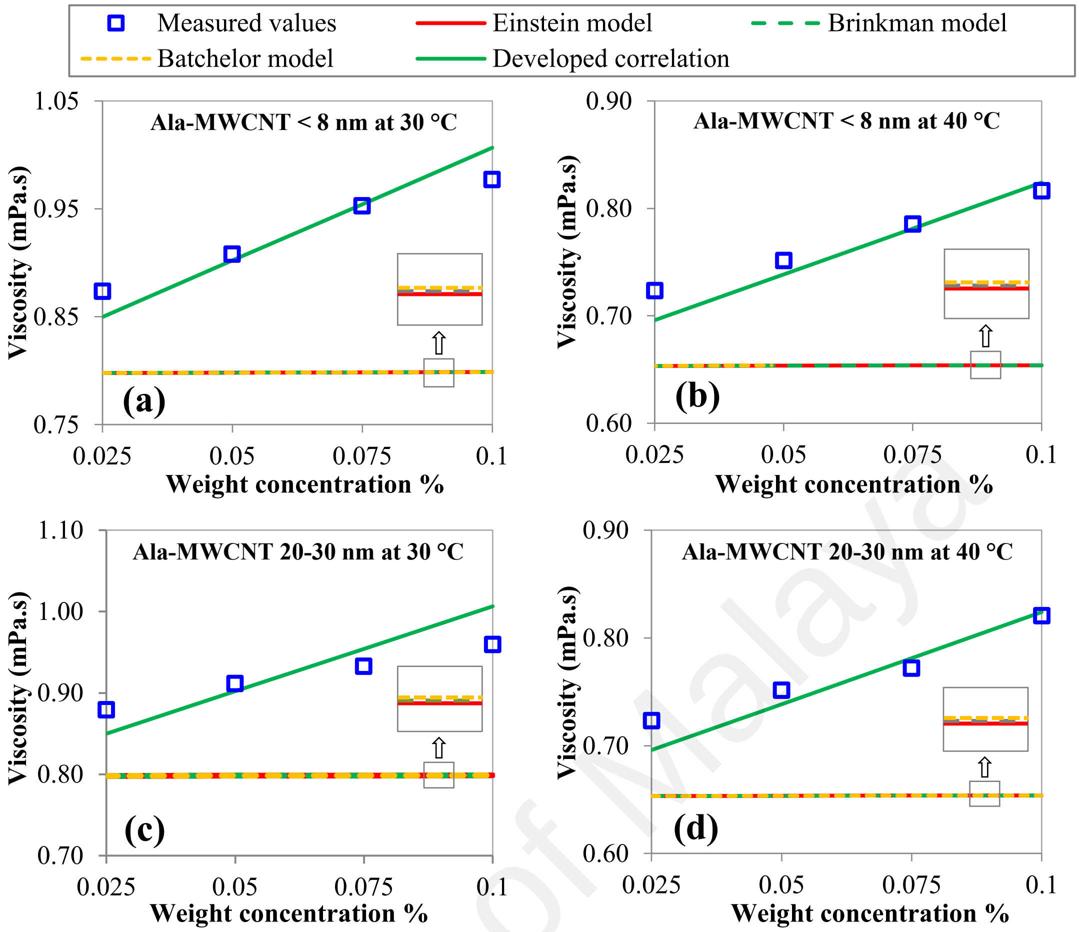

Figure 4.27: The measured values of viscosity for aqueous Ala-MWCNTs nanofluids with outside diameters of (a, b) < 8 nm and (c, d) 20–30 nm versus the classical models of Einstein (1906) (as cited in Mahbubul et al. (2012), Brinkman (1952), and Batchelor (1977) (as cited in Y. Li et al. (2009)) and with the developed correlation.

4.4.3 Density of nanofluids

Since the density of solid nanomaterials is generally higher than that of water, the density of water-based nanofluid increases as the weight concentration of nanomaterials in the base fluid increases (Chandrasekar et al., 2012). The accuracy and reliability of the density meter was confirmed by comparing the measured values of density for distilled water at different temperatures with the standard values presented by Arnold (1970), as shown in Figure 4.28, and a maximum difference of 0.041% has been found. Accordingly, it has been concluded that the density meter is appropriate for measuring the density of nanofluid with a very good reliability.

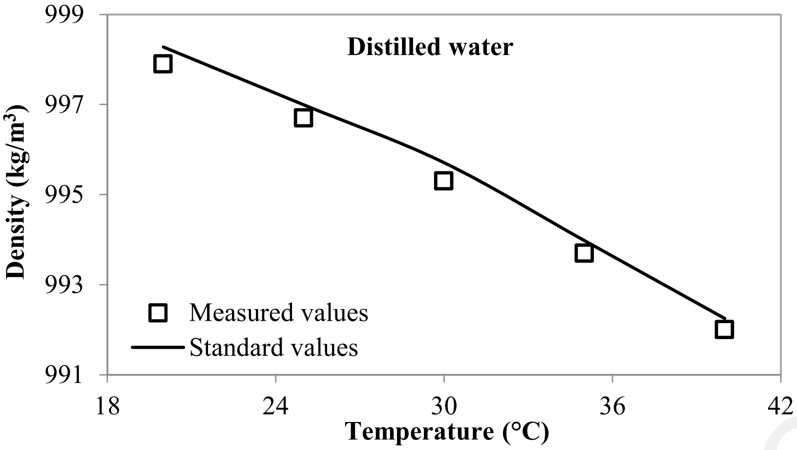

Figure 4.28: Comparison between the measured values of density for distilled water at different temperatures with the standard values presented by Arnold (1970).

4.4.3.1 Density of TEA-GNPs nanofluids

The measured values of density for water-based TEA-GNPs nanofluids with 500-m^2/g SSA at different temperatures and weight concentrations are presented in Figure 4.29. From which, it can be noticed that the density of water and water-based nanofluids decreases as the temperature increases. Also, as weight concentration increases from 0.025% to 0.1%, a slight increase has been noticed in the density of the nanofluids up to 0.070% in comparison to water. The measured values of density were compared with those calculated using the equation of Pak & Cho (1998) and showed a very good agreement with a maximum difference of 0.04%, as shown in Figure 4.30. Therefore, it can be determined that the equation of Pak & Cho (1998) is highly reliable for calculating the density values of water-based TEA-GNPs nanofluids.

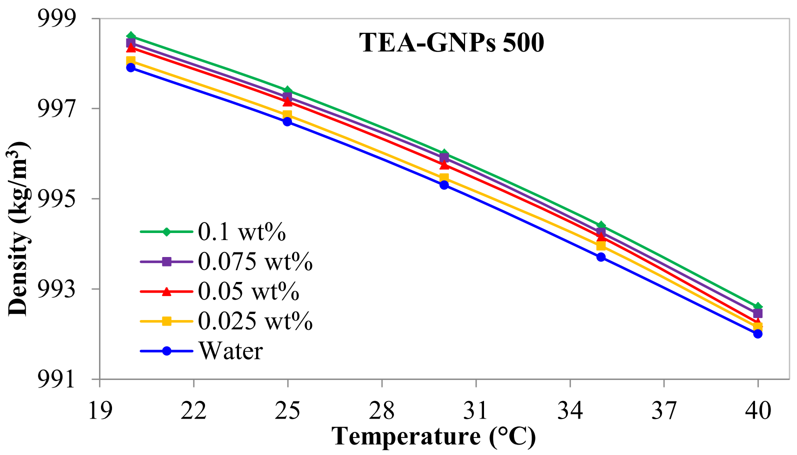

Figure 4.29: The values of density at different temperatures and weight concentrations for water-based TEA-GNPs nanofluids with SSA of 500 m^2/g.

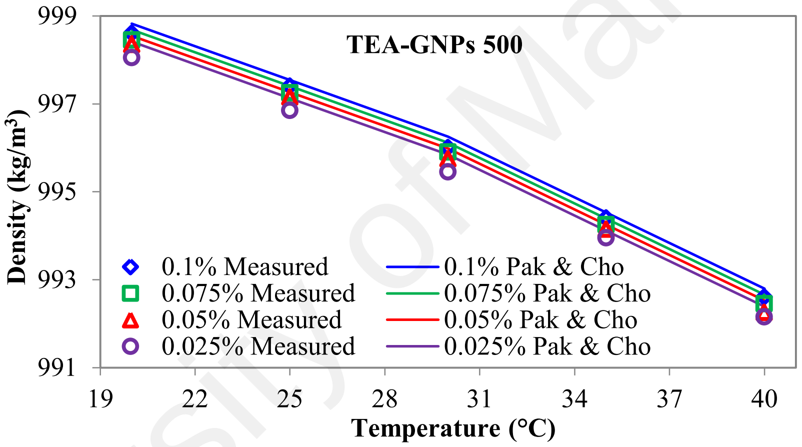

Figure 4.30: Comparison between the measured values of density for water-based TEA-GNPs 500 nanofluids with the equation of Pak & Cho (1998).

4.4.3.2 Density of Ala-MWCNTs nanofluids

The measured values of density for distilled water and two water-based Ala-MWCNTs nanofluids, i.e., less than 8 nm and 20–30 nm, at different temperatures and weight concentrations are presented in Figures 4.31 and 4.32, respectively. These two figures clearly show that the loading of nanomaterials from 0.025 wt% to 0.1 wt% causes an insignificant increase in the density of water-based Ala-MWCNTs nanofluids, up to 0.065% and 0.055%, respectively, when compared to water. Furthermore, the density of water and water-based nanofluids decreases as temperature increases. A comparison between the measured values of density for the two water-based Ala-MWCNTs nanofluids with those calculated using the equation of Pak & Cho (1998) has been performed and presented in Figures 4.33 and 4.34, which indicate very good agreements with maximum differences of 0.049% and 0.047% for the Ala-MWCNTs with outside diameters of < 8 nm and 20–30 nm, respectively. Accordingly, it can be decided that the equation of Pak & Cho (1998) can be used for predicting the density of water-based Ala-MWCNTs nanofluids with high accuracy.

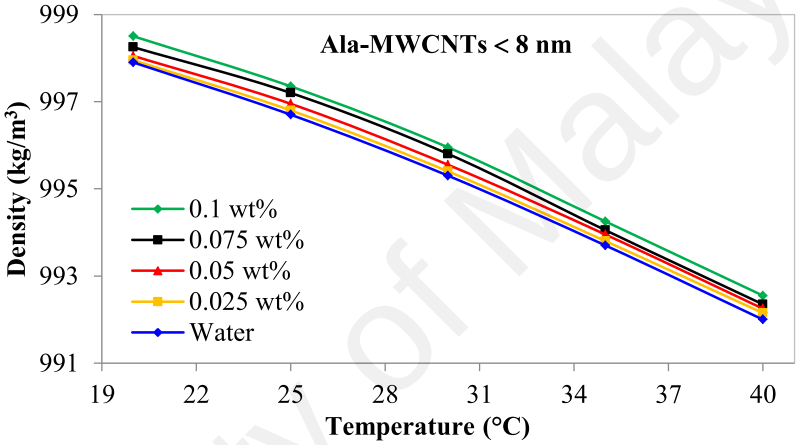

Figure 4.31: The measured values of density versus temperature for water and water-based Ala-MWCNTs < 8 nm nanofluids at different weight concentrations.

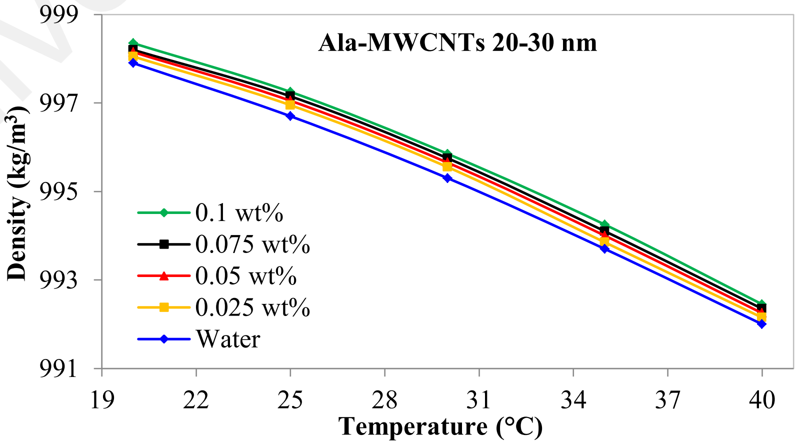

Figure 4.32: The measured values of density versus temperature for water and water-based Ala-MWCNTs 20–30 nm nanofluids at different weight concentrations.

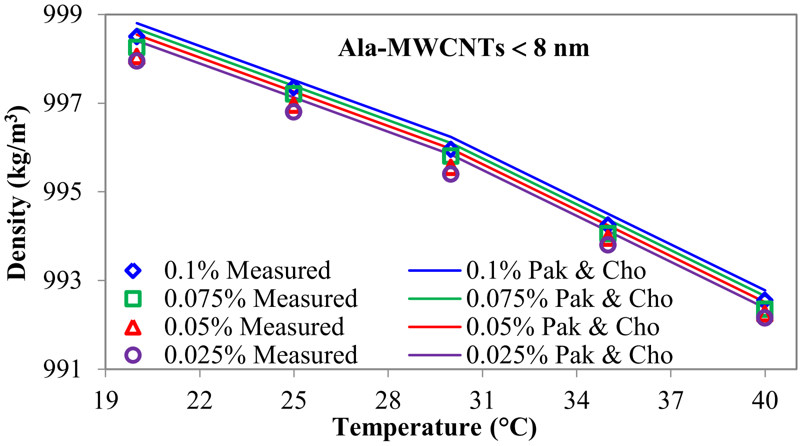

Figure 4.33: Comparison between the measured values of density with the equation of Pak & Cho (1998) for water-based Ala-MWCNTs < 8 nm nanofluids.

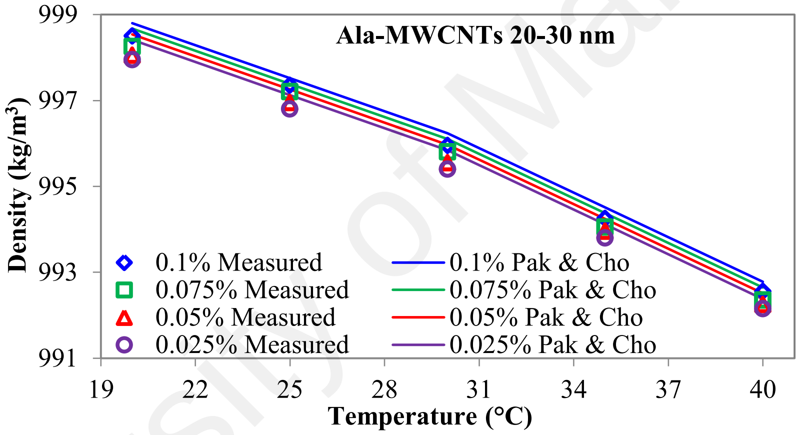

Figure 4.34: Comparison between the measured values of density with the equation of Pak & Cho (1998) for water-based Ala-MWCNTs 20–30 nm nanofluids.

4.4.4 Specific heat of nanofluids

The measured values of specific heat for distilled water at different temperatures were compared with the standard values presented by Arnold (1970) and displayed in Figure 4.35. This comparison aimed at testing the reliability and accuracy of the DSC, and showed a maximum difference of 2.75%. Therefore, the DSC was considered dependable for measuring the specific heat of nanofluids in the present study.

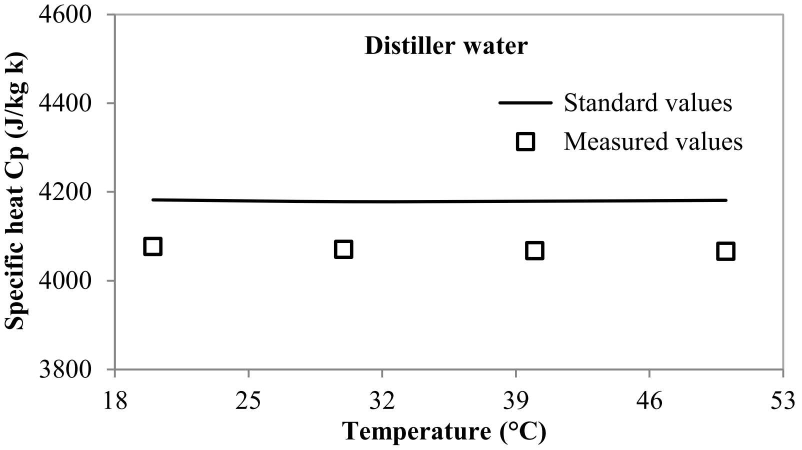

Figure 4.35: The measured values of specific heat versus the standard values presented by Arnold (1970) for distilled water at different temperatures.

4.4.4.1 Specific heat of TEA-GNPs nanofluids

The specific heat of water-based TEA-GNPs nanofluids with SSAs of 300, 500, and 750 m^2/g was measured at different temperatures and weight concentrations and presented in Figure 4.36 (a–c) along with the specific heat values of distilled water. It can be observed that all the measured values of specific heat decrease as temperature increases. Also, when compared with water, the specific heat of water-based TEA-GNPs nanofluids decreases as weight concentration increases down to 0.26%, 0.23%, and 0.28% for 0.1-wt% of water-based TEA-GNPs nanofluids with SSAs of 300, 500, and 750 m^2/g, respectively. This decrease may be explained by the fact that the specific heat values of solid nanomaterials are generally lower than water (Chandrasekar et al., 2012; Said et al., 2015b; Arzani et al., 2016).

For water-based TEA-GNPs nanofluids with three SSAs, the calculated values of specific heat using the equations of Pak & Cho (1998) and Xuan & Roetzel (2000) were compared with the experimentally measured values at different temperatures and weight concentrations. A sample of the comparison is presented in Figure 4.36d for the 0.1-wt% TEA-GNPs with 500-m^2/g SSA, which clearly shows that both equations overestimate the measured values. The maximum differences found for the TEA-GNPs with SSAs of 300, 500, and 750 m^2/g were (3.01%, 2.97%, and 3% for Xuan & Roetzel (2000)) and (3.05%, 3.02%, and 3.05% for Pak & Cho (1998)), respectively. The equation of Xuan & Roetzel (2000) shows slightly lower error than that of Pak & Cho (1998) and therefore it will be used for calculating the specific heat values for water-based TEA-GNPs nanofluids in this study.

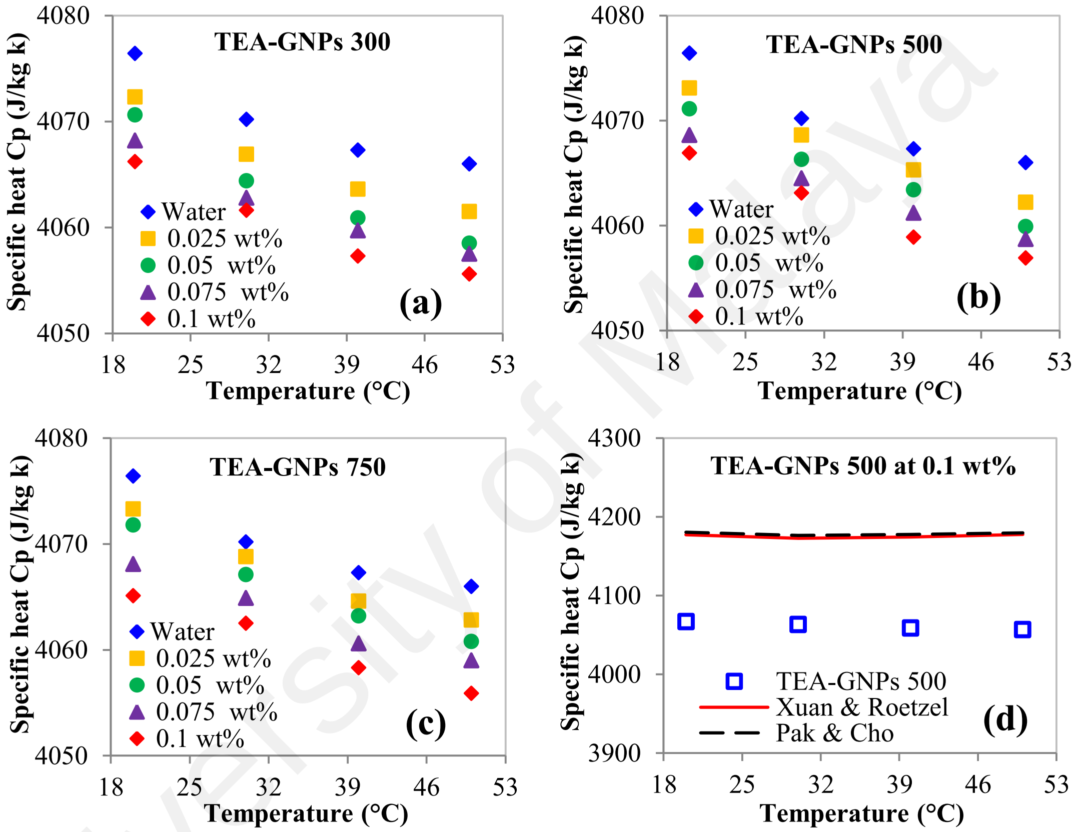

Figure 4.36: The measured values of specific heat for water-based TEA-GNPs nanofluids (a–c) at different temperatures, weight concentrations, and SSAs, and (d) at 0.1- wt% versus with the equations of Pak & Cho (1998) and Xuan & Roetzel (2000).

4.4.4.2 Specific heat of Ala-MWCNTs nanofluids

The measured values of specific heat at different temperatures and weight concentrations for water-based Ala-MWCNTs nanofluids with outside diameters of < 8 nm and 20–30 nm are presented in Figures 4.37a and 4.38a, respectively, in addition to the specific heat values of distilled water. From these two figures, it can be found that as temperature and weight concentration increase, the measured values decrease, down to 0.4% and 0.95% for water-based Ala-MWCNTs nanofluids with 0.1-wt% and outside diameters of < 8 nm and 20–30 nm, respectively, in comparison to water.

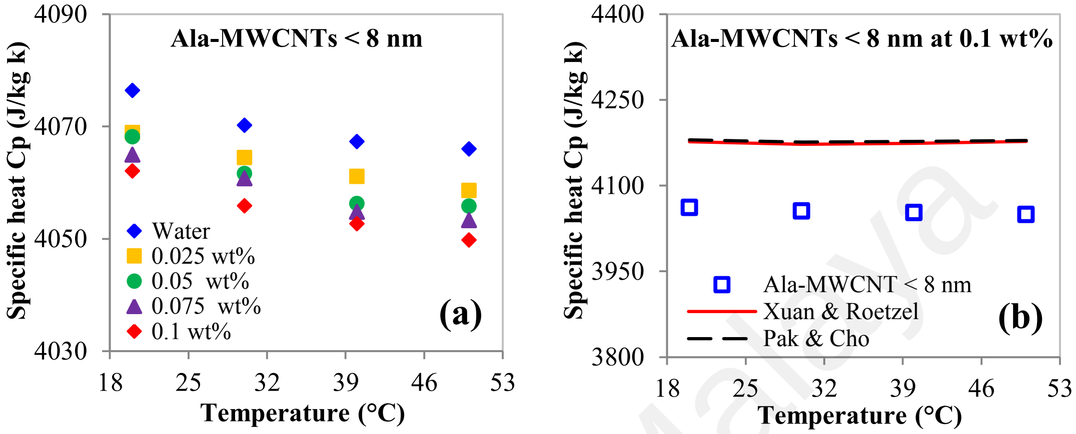

Figure 4.37: The measured values of specific heat for water-based Ala-MWCNTs < 8 nm nanofluids (a) at different temperatures and weight concentrations, and (b) at 0.1-wt% versus the equations of Pak & Cho (1998) and Xuan & Roetzel (2000).

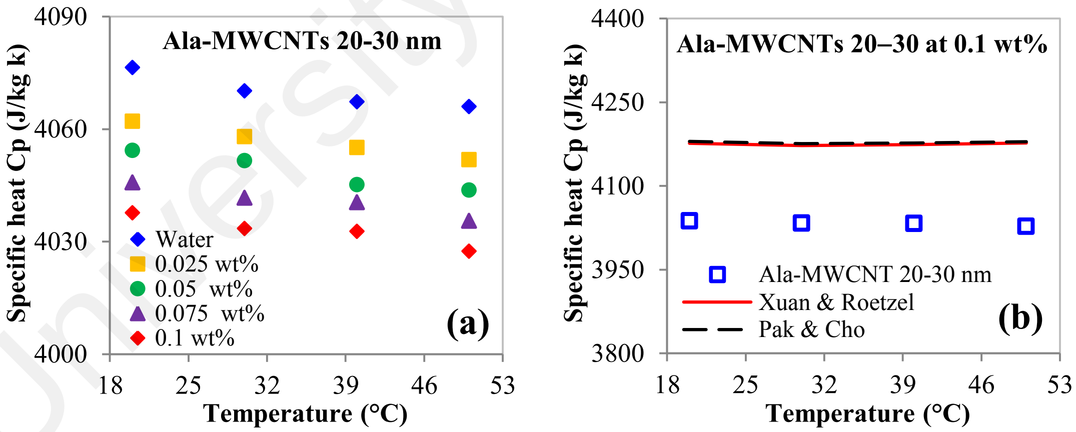

Figure 4.38: The measured values of specific heat for water-based Ala-MWCNTs 20–30 nm nanofluids (a) at different temperatures and weight concentrations, and (b) at 0.1- wt% versus the equations of Pak & Cho (1998) and Xuan & Roetzel (2000).

The calculated values of specific heat at different temperatures and weight concentrations using the equations of Pak & Cho (1998) and Xuan & Roetzel (2000) were compared with the experimentally measured values for water-based Ala-

MWCNTs nanofluids with outside diameters of < 8 nm and 20–30 nm. Samples of the comparison at weight concentration of 0.1 wt% are presented in Figures 4.37b and 4.38b. From which, it can again be noticed that both equations overestimate the measured values up to (3.15% and 3.72% for Xuan & Roetzel (2000)) and (3.2%, and 3.77% for Pak & Cho (1998)) for water-based Ala-MWCNTs nanofluids with outside diameters of < 8 nm and 20–30 nm, respectively. The equation of Xuan & Roetzel (2000) once again shows somewhat less error than that of Pak & Cho (1998) and thus it will be used in this study for determining the values of specific heat for water-based Ala-MWCNTs nanofluids.

4.4.5 Measurement of contact angle for nanofluids

The wettability is governed by the balance between adhesive and cohesive forces that can be characterized by evaluating the contact angle (C. Choi & Kim, 2011; Ortiz-Young et al., 2013). The contact angle has been measured in this work using OCA15EC of Dataphysics. For distilled water and water-based TEA-GNPs nanofluids, the contact angle was measured when they spread on a solid surface (glass slide) at room temperature and presented in Figure 4.39. The results revealed a decrease in contact angle from 50.7° for distilled water to about 47.1°–47.9° for water-based TEA-GNPs fluids. This decrease in the contact angle implies increased surface wettability with the resulting enhancement in heat transfer performance (Rosengarten et al., 2006; Sarit K Das et al., 2007; C. Choi & Kim, 2011). In previous research, it was proved that larger viscosity associate with smaller contact angle (Ortiz-Young et al., 2013). Accordingly, the viscosity of the water-based TEA-GNPs fluids that were prepared should be higher than distilled water, which has been experimentally validated from the viscosity data presented in a previous section.

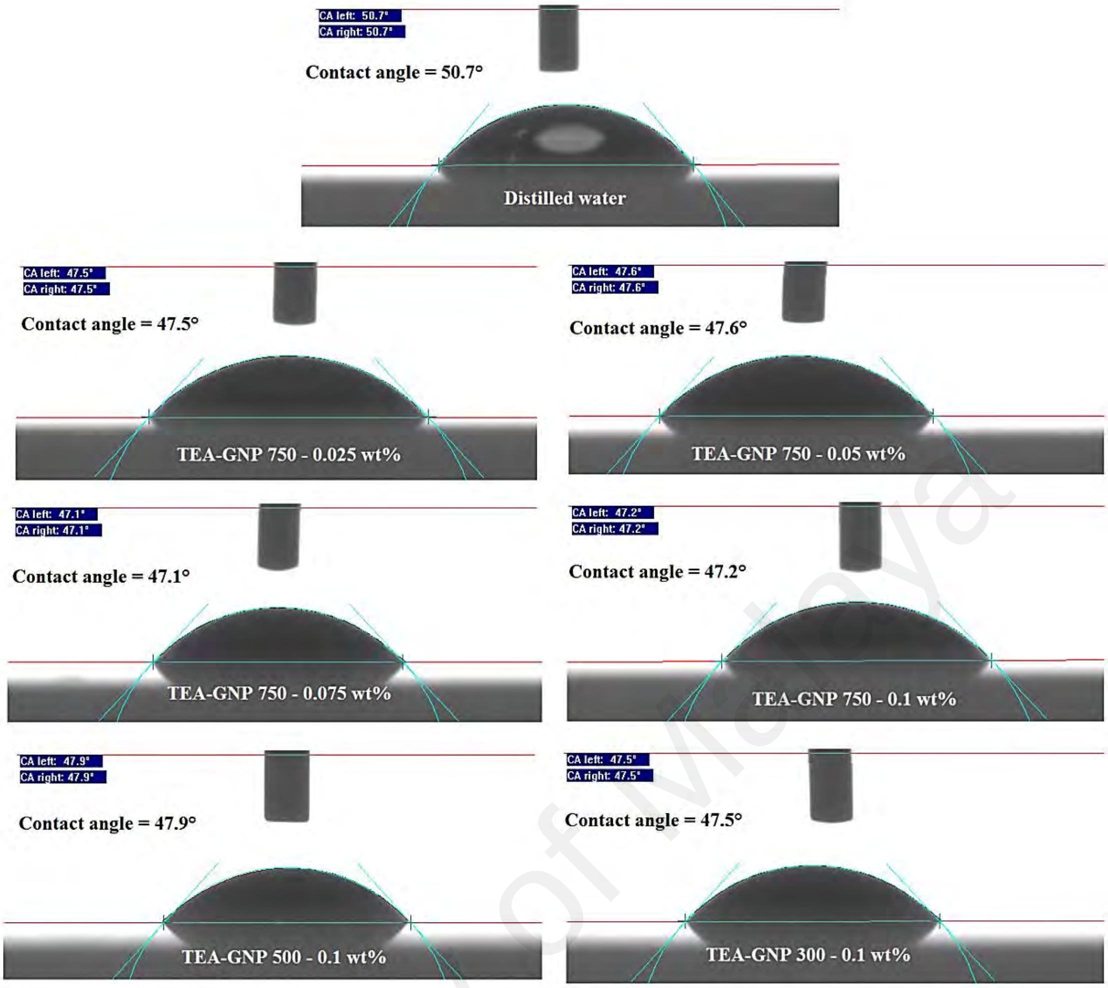

Figure 4.39: Images of contact angle for distilled water and water-based TEA-GNPs nanofluids with different weight concentrations and SSAs.

4.5 Thermal performance of the experimental FPSC

In this section, the data collected from the experimental test runs and MATLAB code on the thermal performance of the developed FPSC's test setup are comprehensively presented in graphical format, explained, and compared for validation. Distilled water and five aqueous colloidal dispersions of carbon-based nanostructures with four weight concentration of 0.025%, 0.05%, 0.075%, and 0.1% were used as working fluids. The effects of inlet fluid temperature, heat flux intensity, and mass flow rate on the thermal performance of the FPSC were experimentally and theoretically investigated. Inlet fluid temperatures of 30, 40, and 50 °C, heat flux intensities of 600, 800, 1000 W/m^2, and mass flow rates of 0.6, 1.0, and 1.4 kg/min were used in the present study. Accordingly, the total number of test runs that were performed for each of the experimental setup and MATLAB code were (27) and (540) for distilled water and water-based nanofluids, respectively.

The outside wall temperatures of the two riser tubes in the middle and the center line temperature of the absorber plate (abbreviated as AP) were measured at four different locations along the x-axis as shown in Figure 3.10. From which, it can be found that the locations are at 114, 343, 572, and 801 mm from the edge of the absorber plate, i.e., at dimensionless axial distances (x/d) of about 11.3, 34.0, 56.6, and 79.3, respectively. The outside wall temperatures of the two riser tubes were averaged at each location and abbreviated as (TW). For each test run, the outlet fluid temperature, surface temperatures of the absorber plate, ambient temperature, pressure loss, and outside wall temperatures of the two riser tubes in the middle were all recorded after reaching a steady state condition with respect to temperature.

4.5.1 Thermal performance during water run

The experimental test runs for the FPSC were initially performed using distilled water as a working fluid to check the validity, repeatability, and accuracy of the recorded data. Tests were repeated to check the repeatability of the data obtained from the experimental setup. Figures 4.40, 4.41, and 4.42 present the measured values of AP and TW versus x/d along the direction of flow in the FPSC at different mass flow rates, heat flus intensities, and inlet fluid temperatures, respectively. From these figures, it can be inferred that the values of AP and TW decrease as flow rate increases (Figure 4.40), and increase as heat flux intensity (Figure 4.41) and inlet fluid temperature (Figure 4.42) increase, which are characteristic features for the convective mode of heat transfer under constant heat flux.

The experimentally calculated values of energy efficiency for the water-based FPSC versus the reduced temperature parameter are presented in Figure 4.43 at different mass flow rates. In this figure, a linear trend line is added to each flow rate group to clarify the effect of flow rate on efficiency. From which, it is clear that the collector's efficiency increases as flow rate increases, which may attributed to the decreased AP temperature (Figure 4.40) resulting in lower heat losses from the collector, i.e., increased collector's efficiency. This behavior is confirmed through Figure 4.44, which displays the variation of energy efficiency versus flow rate at different heat flus intensities and inlet fluid temperatures. Here it can also be concluded that the FPSC's efficiency is in direct proportion to heat flux intensity (Figure 4.44a) and inverse proportion to inlet fluid temperature (Figure 4.44b).

Using the same range of values for mass flow rate, heat flus intensity, and inlet fluid temperature that were used to perform the experimental test runs in addition to the recorded ambient temperature, the MATLAB code was run to find the corresponding predicted values of AP, TW, pressure loss, and energy efficiency. Then, a comparison between the experimental and simulated values was performed in order to validate the accuracy and reliability of the collected data. At 1000-W/m^2 heat flux intensity and 30-°C inlet fluid temperature, the recorded and calculated values of AP and TW versus x/d are displayed in Figure 4.45, which visibly demonstrates a very good agreement between them with maximum differences of 3.02% and 3.19% for AP and TW, respectively. This good agreement can further be confirmed thorough Figure 4.46, which shows the experimental and predicted distributions of temperature along y-axis for the FPSC's absorber plate between the two riser tubes in the middle at different values of x/d. The location (y = 0) represents the center line between the two riser tubes at which the first boundary condition presented by equation (3.10) applies (i.e., dT/dy = 0). Therefore, the temperature is higher at this location. Furthermore, a comparison between the calculated values of collector's efficiency at different flow rates using the experimental data and the MATLAB code is presented in Figure 4.47, which clearly reveals that both values are very well matched with a difference up to 3.26% at 1.4 kg/min. Accordingly, it can be concluded that the collected data from the experimental test setup and MATLAB code are reasonably accurate and reliable.

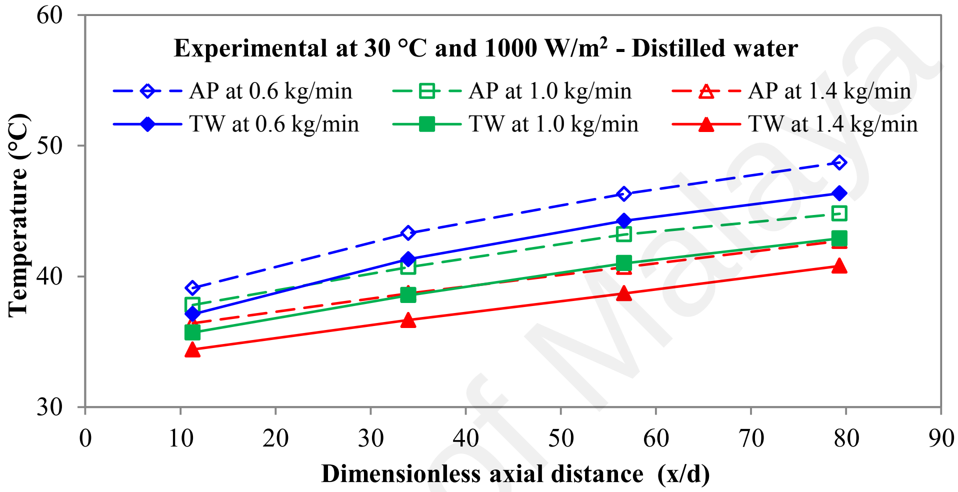

Figure 4.40: Variation of measured AP and TW with x/d along the FPSC using distilled water as a working fluid at different mass flow rates.

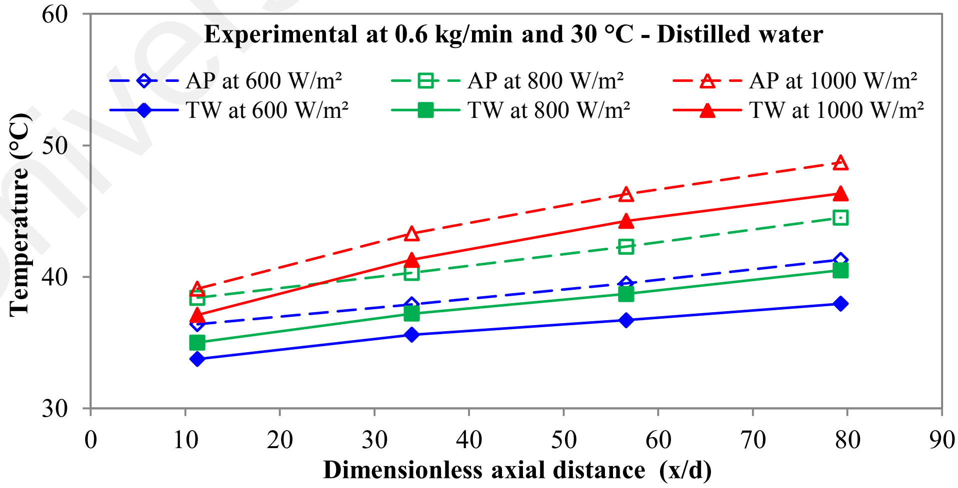

Figure 4.41: Variation of measured AP and TW with x/d along the FPSC using distilled water as a working fluid at different heat flus intensities.

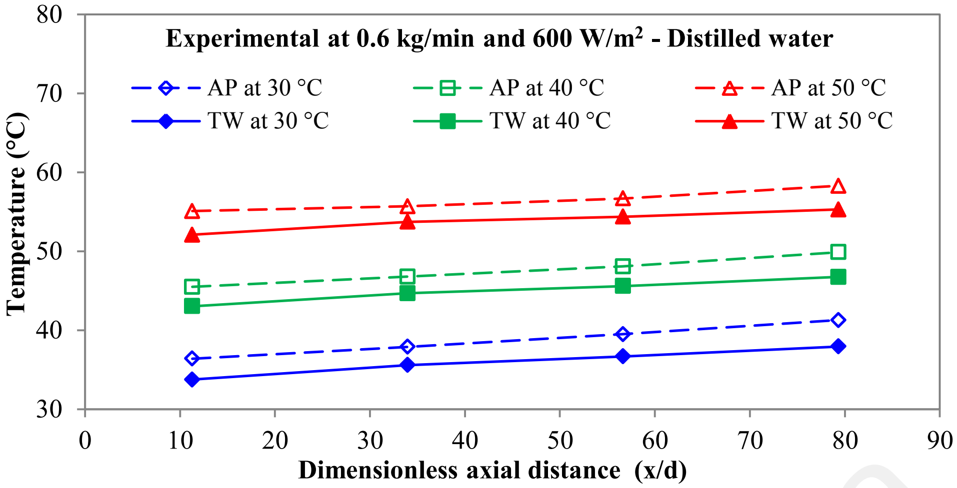

Figure 4.42: Variation of measured AP and TW with x/d along the FPSC using distilled water as a working fluid at different inlet fluid temperatures.

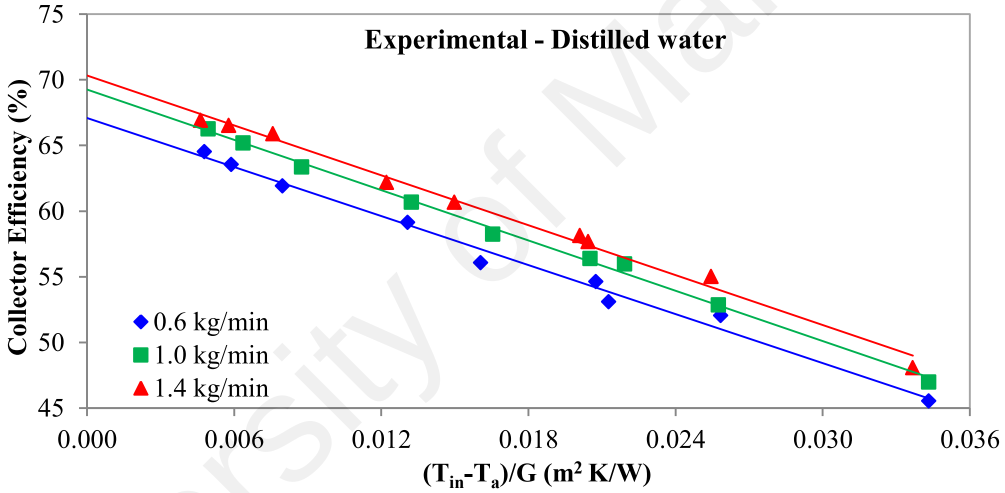

Figure 4.43: The experimental values of FPSC's efficiency versus reduced temperature parameter at different mass flow rates during water run.

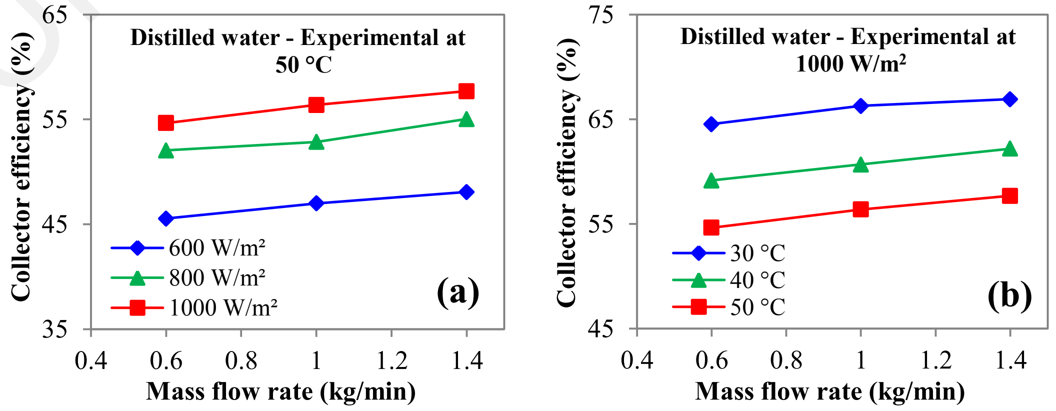

Figure 4.44: The experimental values of FPSC's efficiency during water run versus mass flow rate at different (a) heat flux intensities and (b) inlet fluid temperatures.

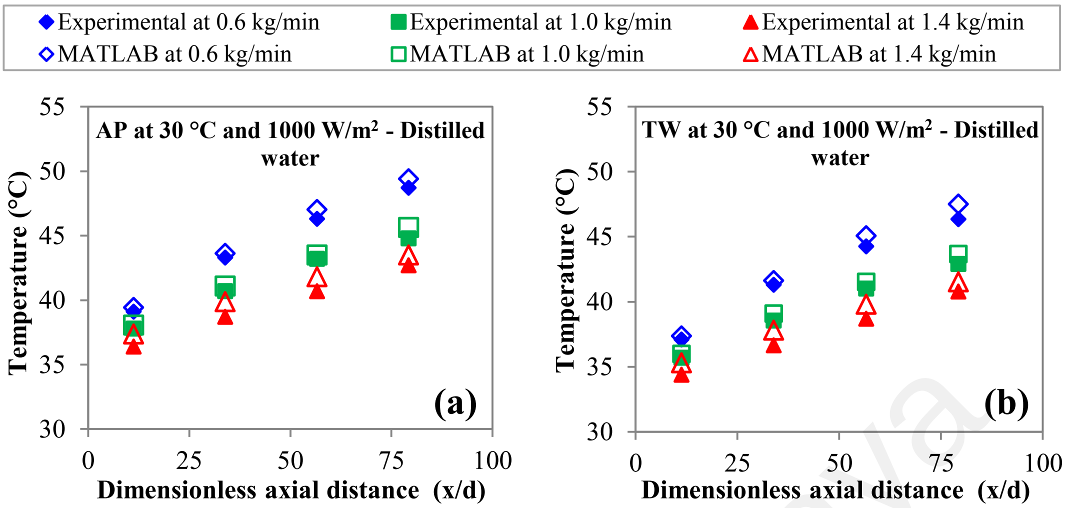

Figure 4.45: Measured values of AP (a) and TW (b) for distilled water at 1000-W/m^2 heat flux intensity and 30-°C inlet fluid temperature versus MATLAB predictions.

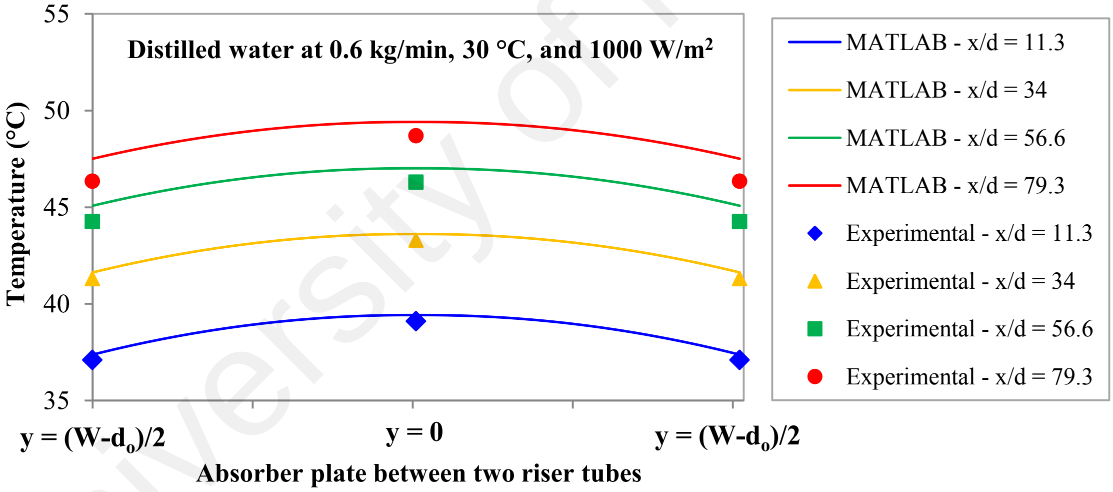

Figure 4.46: Experimental values versus MATLAB predictions for the temperature distribution along y-axis of the FPSC's absorber plate between the two riser tubes in the middle for distilled water at 1000-W/m^2 heat flux intensity, 0.6-kg/min mass flow rate, and 30-°C inlet fluid temperature and at different values of x/d.

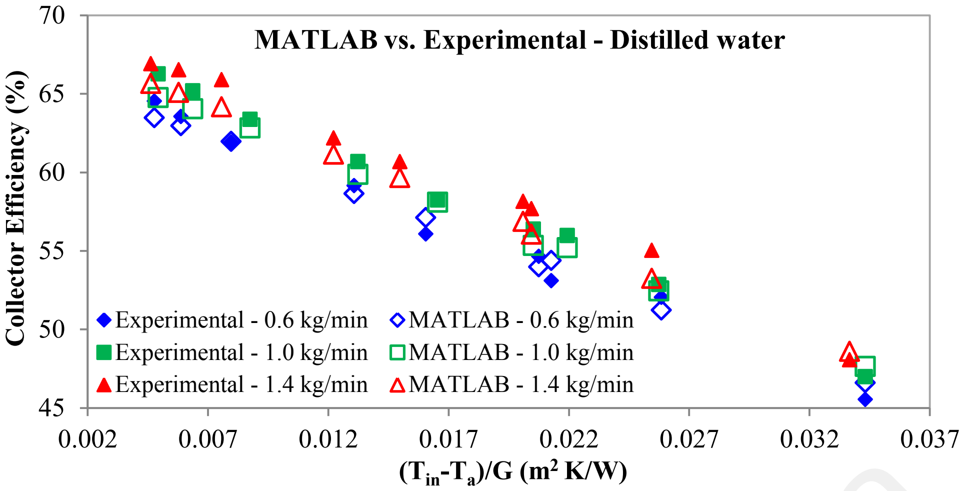

Figure 4.47: Comparison of the calculated values of collector's efficiency using the experimental data and the MATLAB code for distilled water at various mass flow rates.

4.5.2 Thermal performance using water-based nanofluids

Aimed at investigating the thermal performance of FPSCs using alternative and improved working fluids instead of the conventional heat transfer fluids, experimental test runs were performed using four different weight concentrations of aqueous colloidal dispersions containing five covalently-functionalized carbon-based nanostructures that were prepared in this work. The effect of using these water-based nanofluids on the values of AP, TW, pressure loss, energy efficiency, and performance index (PI) of the experimental FPSC will be presented, interpreted, and discussed in the subsequent sections.

4.5.2.1 Using aqueous colloidal dispersions of TEA-GNPs

The measured values of AP and TW versus x/d along the direction of flow in the FPSC at 1000-W/m² heat flux intensity and 30-°C inlet fluid temperature are presented in Figure 4.48 for water and 0.1-wt% water-based TEA-GNPs nanofluids with different SSAs. This figure clearly shows that the addition of TEA-GNPs with any SSA to the base fluid results in a decrease of AP and TW at different rates, down to 3.35% and 3.51% for TEA-GNPs with 750-m^2/g SSA at 0.6 kg/min, respectively. This decrease in temperature may be attributed to the enhanced thermal conductivity in the presence of

TEA-GNPs with the resulting augmentation of convective heat transfer coefficient. Knowing that in previous research and in both laminar and turbulent flow, it was proved that nanofluids with better thermal conductivities than their base fluids will also have greater convective heat transfer coefficients (Faulkner et al., 2004; Sarit K Das et al., 2007; Kwon et al., 2013; Amiri et al., 2015c). Furthermore, Figures 4.49 and 4.50 present the measured values of AP and TW for water and water-based TEA-GNPs nanofluids with different weight concentrations and SSAs, respectively. From these figures and in comparison to water, it can easily be found that AP and TW decrease as weight concentration and SSA increase, which can explained by remembering that in this study the thermal conductivity of nanofluids was previously proved to increase as weight concentration and SSA increased, consequently, it can further be concluded that the convective heat transfer coefficient and thermal performance of water-based TEA-GNPs nanofluids increase as weight concentration and SSA increase. This conclusion coincides with the findings of previous researchers (Xuan & Li, 2000; Sen Gupta et al., 2011; Nasiri et al., 2012; Fang et al., 2015; Mehrali et al., 2015; Amiri et al., 2017a; Amiri et al., 2017b). A comparison between the measured and simulated values of AP and TW at 30-°C inlet fluid temperature and 1000-W/m² heat flux intensity was performed at different mass flow rates for water-based TEA-GNPs nanofluids with 0.1-wt% and 750-m^2/g SSA and presented in Figure 4.51. From which, it can be clearly revealed that the MATLAB code always overestimate the measured values up to 4.74% and 4.7% for AP and TW, respectively.

The values of FPSC's efficiency calculated from the experimental versus mass flow rate for 0.1-wt% water-based TEA-GNPs nanofluids are presented in Figure 4.52 at different inlet fluid temperatures and heat flux intensities. From which, a trend similar to that of distilled water is found, i.e., the efficiency increases as heat flux intensity and mass flow rate increase, and decreases as inlet fluid temperature increases. The experimental values of FPSC’s energy efficiency versus reduced temperature parameter at 0.6-kg/min mass flow rate for water and water-based TEA-GNPs nanofluids are presented in Figure 4.53 at different SSAs of 0.1-wt% TEA-GNPs and in Figure 4.54 at different weight concentrations of TEA-GNPs 750. From these two figures, it is apparent that the presence of TEA-GNPs with any SSA and weight concentration in water enhances the energy efficiency of the FPSC. Larger FPSC’s efficiency is observed for higher loading and SSA of TEA-GNPs nanomaterial, up to 10.53% for 0.1-wt% TEA-GNPs 750 in comparison with water. This trend of results coincides with that previously found for the effects of SSA and weight concentration on the values of AP and TW. Also, the experimentally calculated values of collector’s efficiency were compared with MATLAB code predictions and presented in Figures 4.55 and 4.56 at different mass flow rates and weight concentrations, respectively. From these two figures, it can be observed that the MATLAB code under-predicted the experimental values of energy efficiency with a maximum difference of 13.47% for the 0.1-wt% TEA-GNPs 750 at 1.4-kg/min mass flow rate, 50-°C inlet fluid temperature, and 600-W/m^2 heat flux intensity. This difference may be attributed to the uncertainty in the experimentally measured values and also to the errors in the MATLAB code originated from different sources, such as the dependence on correlations for calculating some of the numerous factors required, numerical errors, and the assumptions made to simplify the solution of the mathematical model. Thus, it can be concluded that the developed MATLAB code is suitable for simulating the thermal performance of a FPSC using water-based TEA-GNPs nanofluid as its working fluid with an acceptable accuracy.

The positive effect of SSA on thermal conductivity, heat transfer performance, and energy efficiency may be explained mainly by two methods; first by the fact that the increase in SSA means a drop in the size of the dispersed particles, which in turn produces a better and more effective dispersion in terms of higher efficiency of the dispersed particles in transferring heat to the base fluid as a results of reduced effect of the Kapitza resistance (Fang et al., 2015); and second by the effect Brownian motion. Here, with the decreased size of particles, the Brownian motion velocity will be higher, which improves the positive role of the dispersed particles to the total heat transfer performance through the persistent formation of extra paths for heat flow in the base fluid (Özerinç et al., 2009; Sen Gupta et al., 2011).

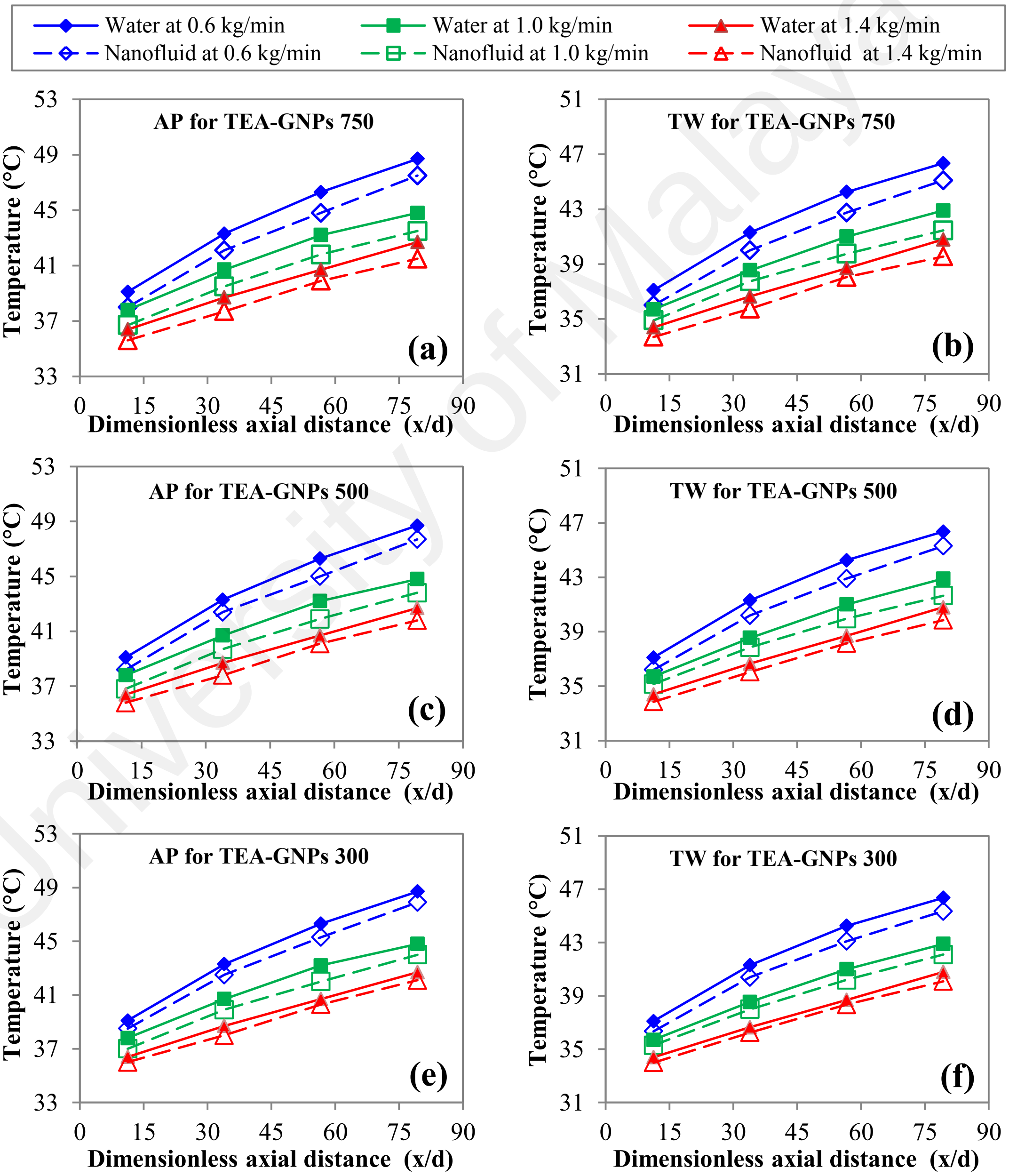

Figure 4.48: The measured values of AP and TW at 30-°C inlet fluid temperature and 1000-W/m² heat flux intensity for water and 0.1-wt% water-based TEA-GNPs nanofluids with SSAs of (a, b) 750 m^2/g, (c, d) 500 m^2/g, and (e, f) 300 m^2/g.

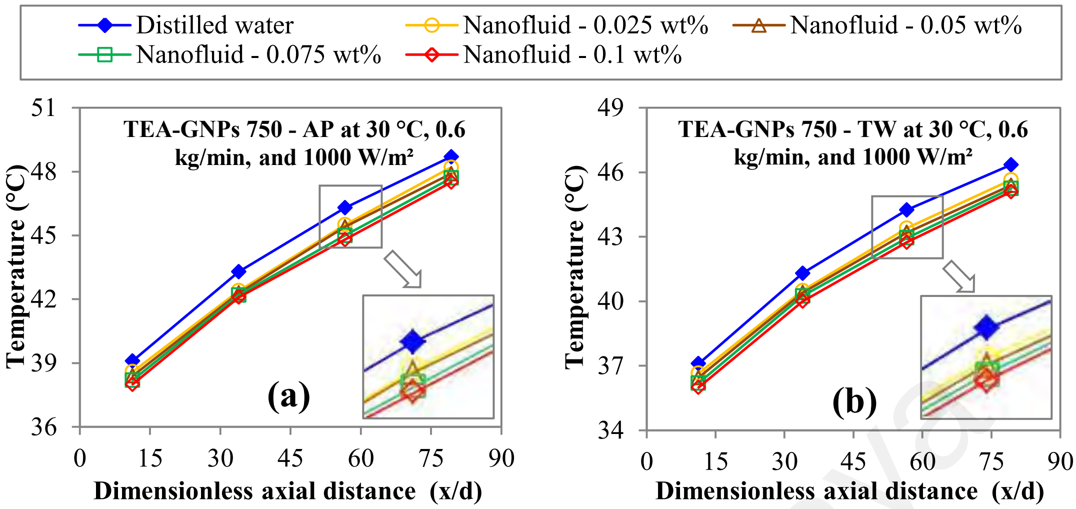

Figure 4.49: Values of AP (a) and TW (b) measured at 30-°C inlet fluid temperature, 0.6-kg/min mass flow rate, and 1000-W/m² heat flux intensity for water and different weight concentrations of water-based 750-m^2/g SSA TEA-GNPs nanofluids.

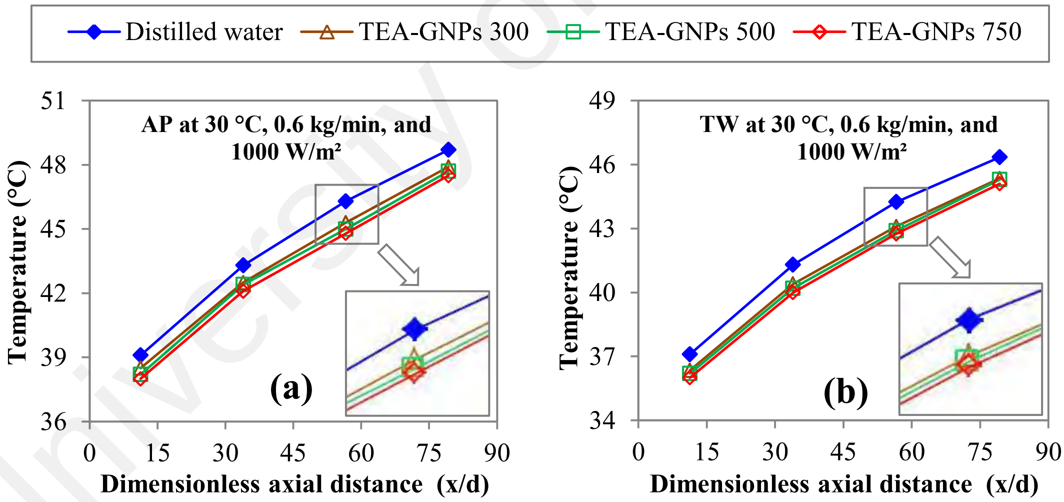

Figure 4.50: Measured values of AP (a) and TW (b) at 30-°C inlet fluid temperature, 0.6-kg/min mass flow rate, and 1000-W/m² heat flux intensity for water and different SSAs of 0.1-wt% water-based TEA-GNPs nanofluids.

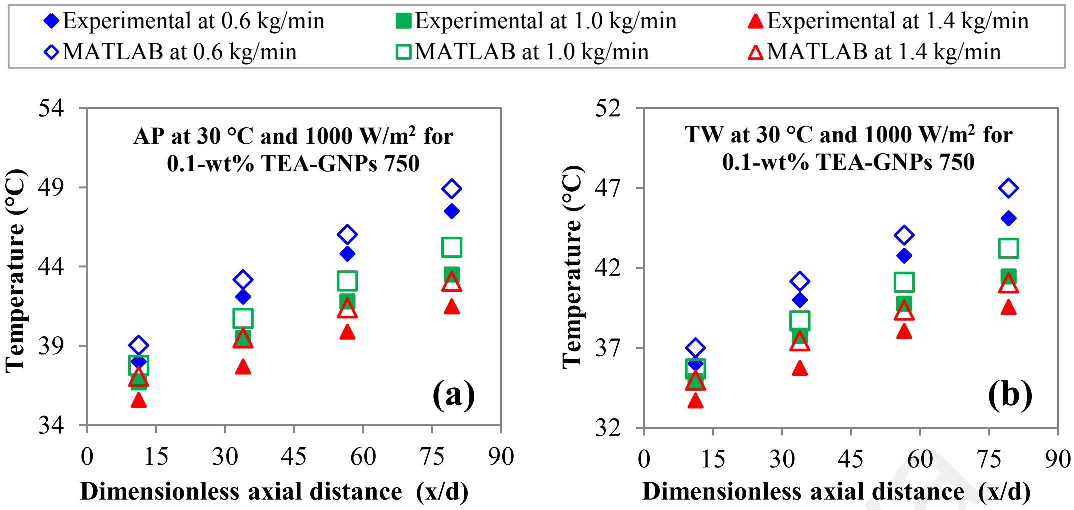

Figure 4.51: Measured values of AP (a) and TW (b) versus MATLAB predictions at 30-°C inlet fluid temperature and 1000-W/m² heat flux intensity for 0.1-wt% and 750-m^2/g SSA water-based TEA-GNPs nanofluids at different mass flow rates.

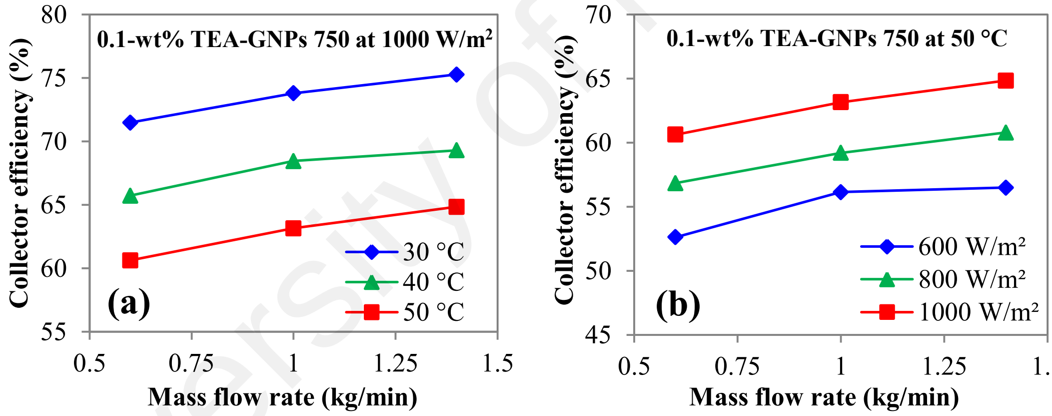

Figure 4.52: Experimental values of FPSC's energy efficiency versus mass flow rate for water-based TEA-GNPs nanofluids at weight concentration of 0.1% and different (a) inlet fluid temperatures and (b) heat flux intensities.

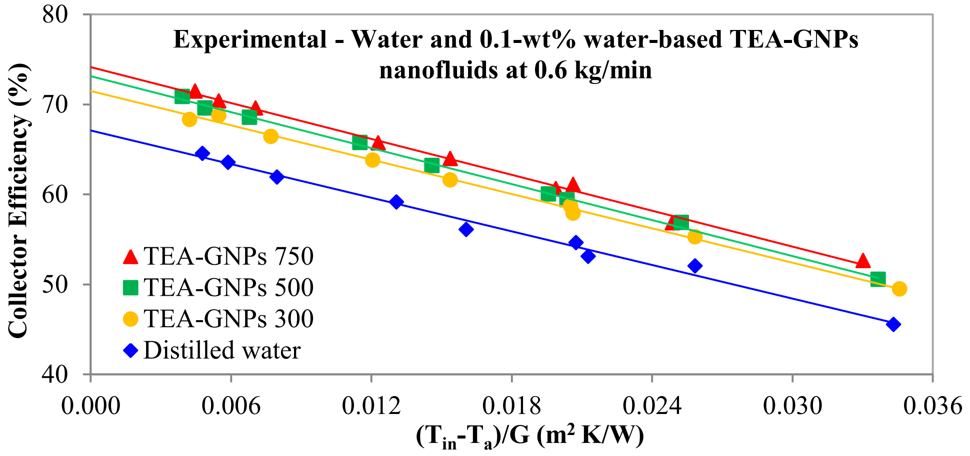

Figure 4.53: Experimentally calculated values of collector's efficiency for water and 0.1-wt% water-based TEA-GNPs nanofluids with different SSAs.

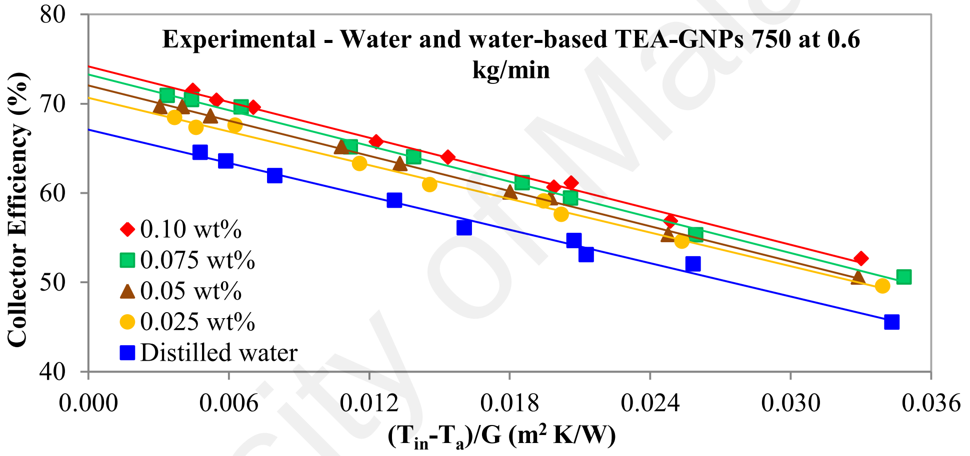

Figure 4.54: Experimentally calculated values of collector's efficiency for water and water-based TEA-GNPs 750 nanofluids with different weight concentrations.

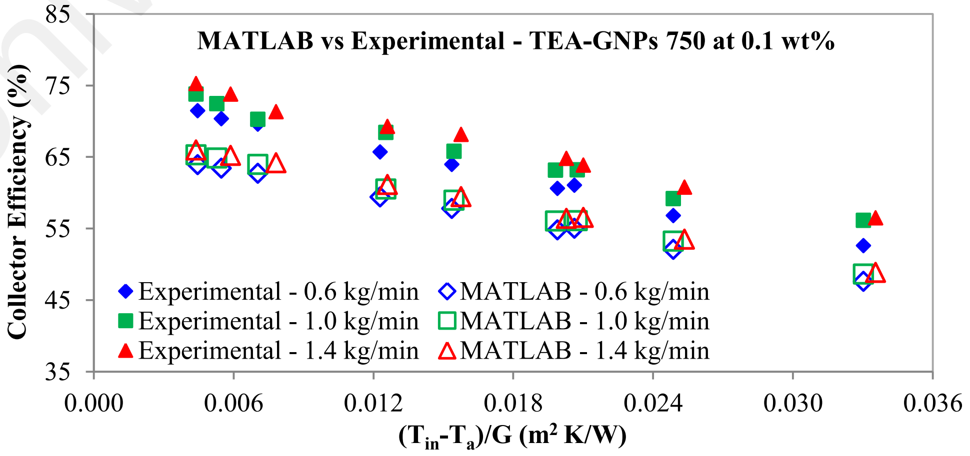

Figure 4.55: Comparison of the experimentally calculated values of FPSC's efficiency with MATLAB code predictions for water-based 0.1-wt% TEA-GNPs 750 nanofluids at different mass flow rates.

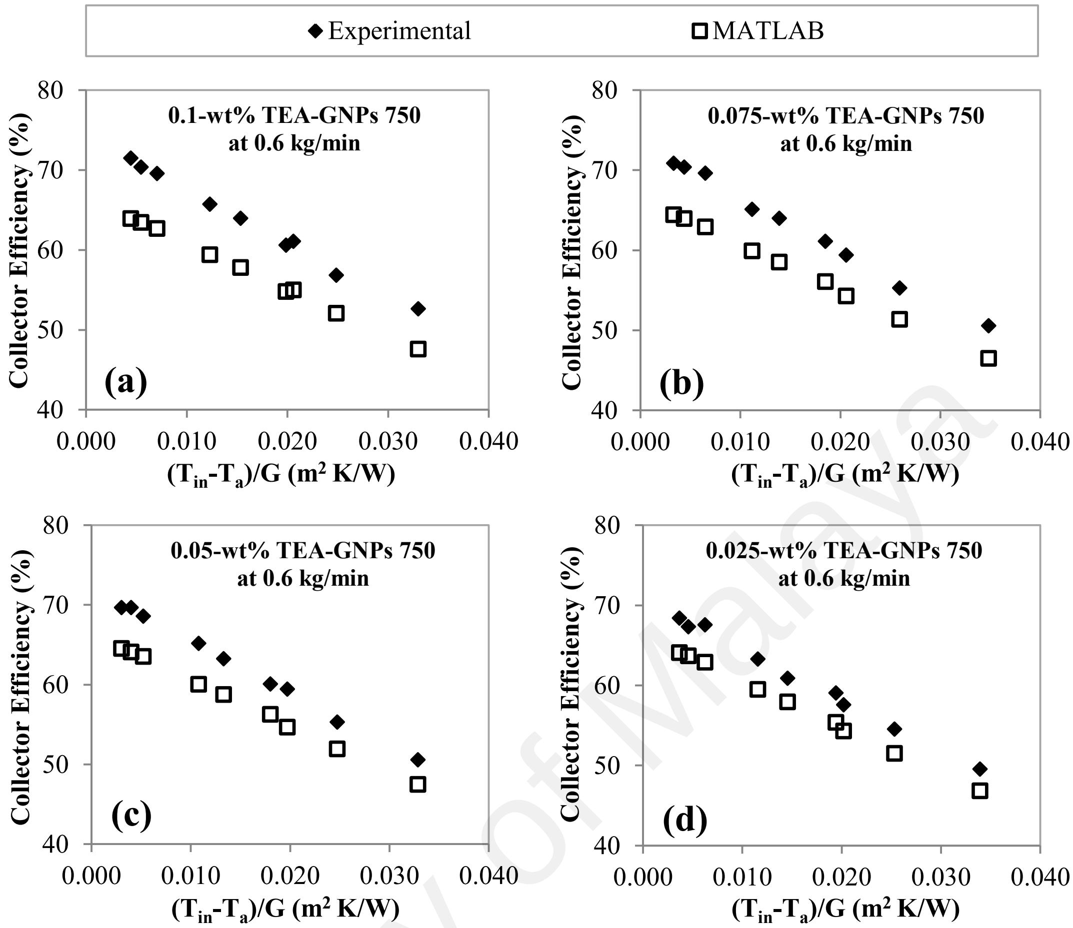

Figure 4.56: Experimentally calculated values of FPSC's energy efficiency versus MATLAB code predictions at different weight concentrations of water-based TEA-GNPs 750 nanofluids.

4.5.2.2 Using aqueous colloidal dispersions of Ala-MWCNTs

The variations of the measured values of AP and TW with x/d along the direction of flow in the FPSC for water and 0.1-wt% water-based Ala-MWCNTs nanofluids with different outside diameters are presented in Figure 4.57 at 1000-W/m² heat flux intensity and 30-°C inlet fluid temperature. It can be seen from this figure that the measured values of AP and TW decrease as flow rate increases and their values for water-based Ala-MWCNTs nanofluids are less than their corresponding values for water, down to 2.86% at 1 kg/min and 3.03% at 0.6 kg/min, respectively, for Ala-MWCNTs < 8 nm. In addition, at 30-°C inlet fluid temperature, 0.6-kg/min mass flow rate, and 1000-W/m² heat flux intensity, the measured values of AP and TW versus x/d along the direction of flow are presented in Figures 4.58 and 4.59 for water and water-based Ala-MWCNTs nanofluids at different weight concentrations and outside diameters, respectively. In comparison to water, it can be recognized from these figures that the values of AP and TW for Ala-MWCNTs decrease as weight concentration and SSA increase, which can be justified in a similar way to that mentioned in the previous section. At 30-°C inlet fluid temperature and 1000-W/m² heat flux intensity, the measured values of AP and TW along with MATLAB code predictions versus x/d along the direction of flow are displayed in Figure 4.60 for water-based 0.1-wt% Ala-MWCNTs < 8 nm nanofluids at different mass flow rates. From which, it can be visibly shown that the measured values are always lower than the predictions of the MATLAB code, down to 4.24% and 3.94% for AP and TW, respectively.

The experimental values of FPSC's efficiency for 0.1-wt% water-based Ala-MWCNTs nanofluids at different inlet fluid temperatures and heat flux intensities are presented in Figure 4.61 versus mass flow rate. From which, it can found that the efficiency increases as heat flux intensity and mass flow rate increase, and decreases as inlet fluid temperature increases, this trend is similar to that for distilled water presented in a previous section. At a mass flow rate of 0.6 kg/min, the experimental values of FPSC's energy efficiency versus reduced temperature parameter for water and water-based Ala-MWCNTs nanofluids are presented at different outside diameters of 0.1-wt% Ala-MWCNTs in Figure 4.62 and at different weight concentrations of Ala-MWCNTs < 8 nm in Figure 4.63. From which, it is obvious that the energy efficiency of the FPSC increases with the loading of Ala-MWCNTs in water. Furthermore, as the SSA of Ala-MWCNTs with outside diameter of < 8 nm is higher than that with 20–30 nm, it can be concluded from Figure 4.62 that the FPSC's energy efficiency increases as SSA increases. When compared with water, a maximum increase in energy efficiency of

9.55% was found for the 0.1-wt% Ala-MWCNTs < 8 nm at 1.4 kg/min. Furthermore, the experimental values of collector's energy efficiency along with their corresponding MATLAB code predictions versus reduced temperature parameter are presented at different mass flow rates in Figure 4.64 and weight concentrations in Figure 4.65. From these two figures, it can be found that the predicted values of energy efficiency are lower than their corresponding experimental values with a maximum difference of 12.64% for the 0.1-wt% Ala-MWCNTs < 8 nm at 1.4-kg/min mass flow rate, 50-°C inlet fluid temperature, and 800-W/m^2 heat flux intensity. Hence, it can be decided that the thermal performance of a FPSC using water-based Ala-MWCNTs nanofluid as its working fluid can properly be simulated by the developed MATLAB code with a reasonable accuracy.

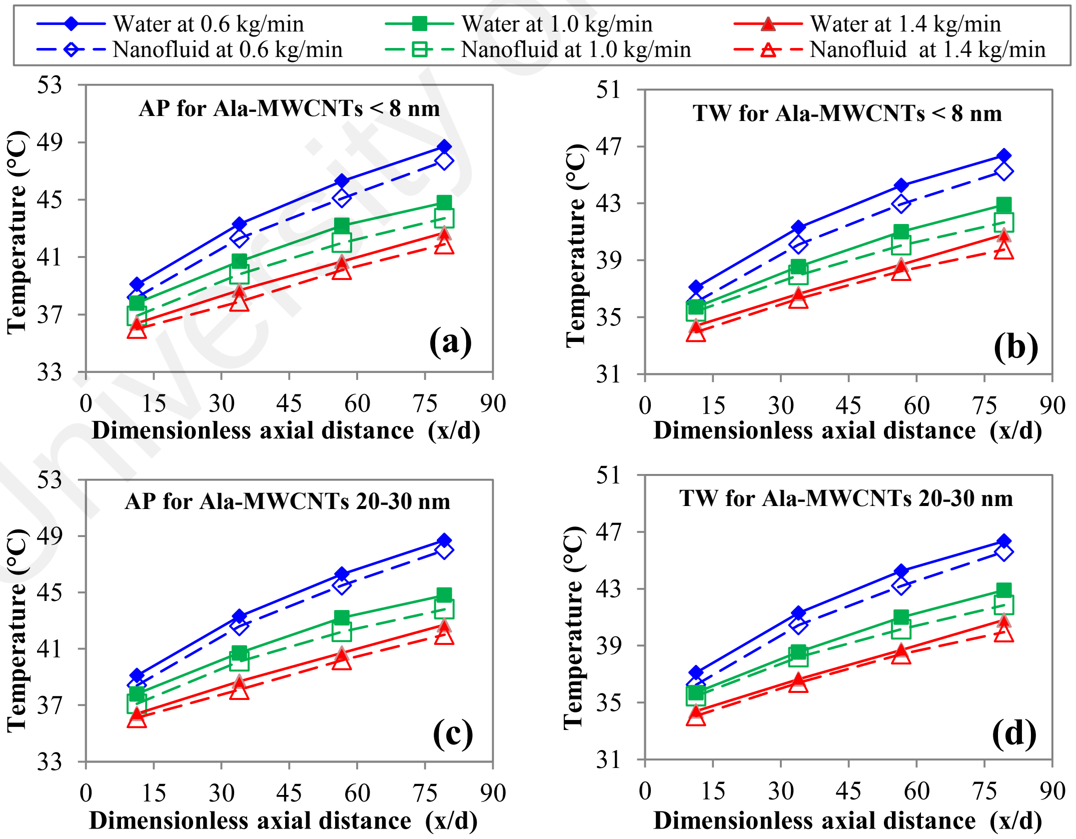

Figure 4.57: The measured values of AP and TW at 30-°C inlet fluid temperature and 1000-W/m² heat flux intensity for water and 0.1-wt% water-based Ala-MWCNTs nanofluids with outside diameters of (a, b) < 8 nm, and (c, d) 20–30 nm.

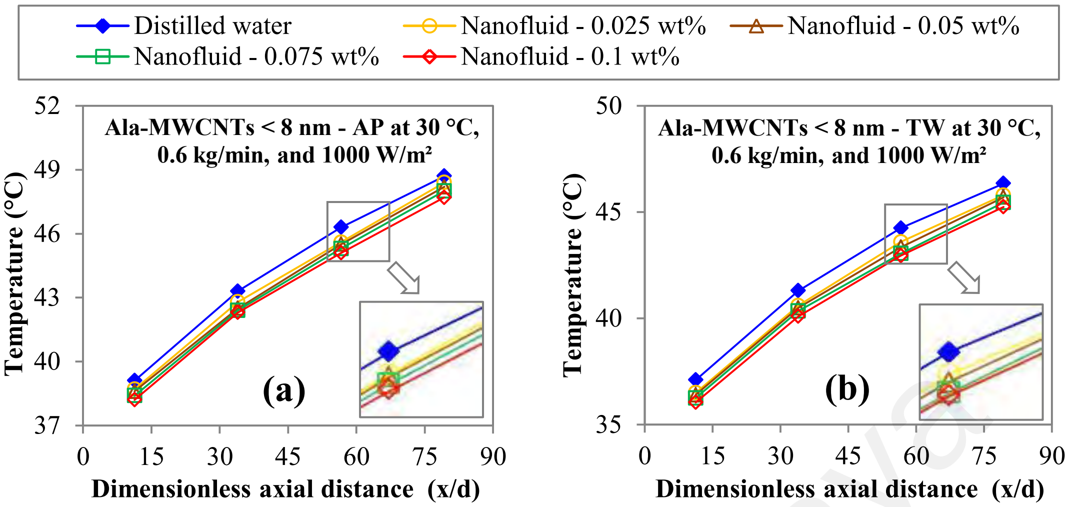

Figure 4.58: Values of AP (a) and TW (b) measured at 30-°C inlet fluid temperature, 0.6-kg/min mass flow rate, and 1000-W/m² heat flux intensity for water and different weight concentrations of water-based Ala-MWCNTs < 8 nm nanofluids.

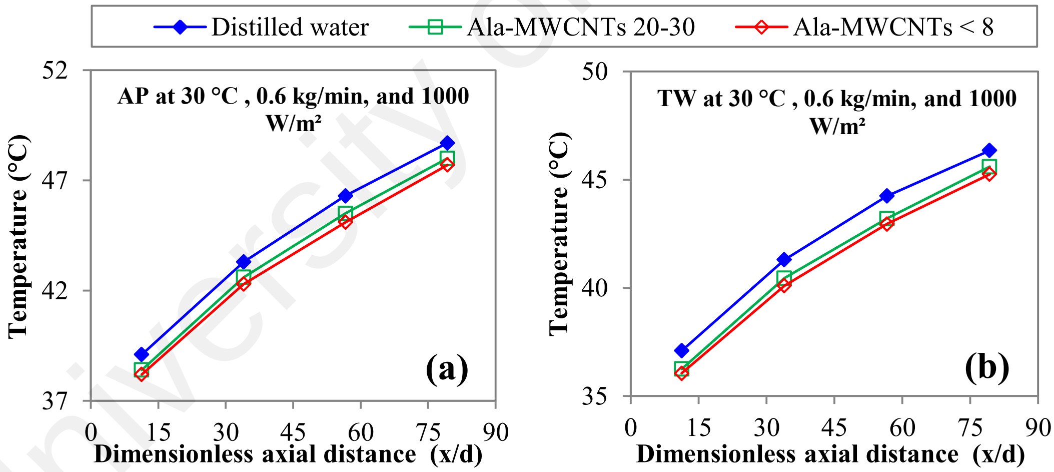

Figure 4.59: Values of AP (a) and TW (b) measured at 30-°C inlet fluid temperature, 0.6-kg/min mass flow rate, and 1000-W/m² heat flux intensity for water and 0.1-wt% water-based Ala-MWCNTs nanofluids with different outside diameters.

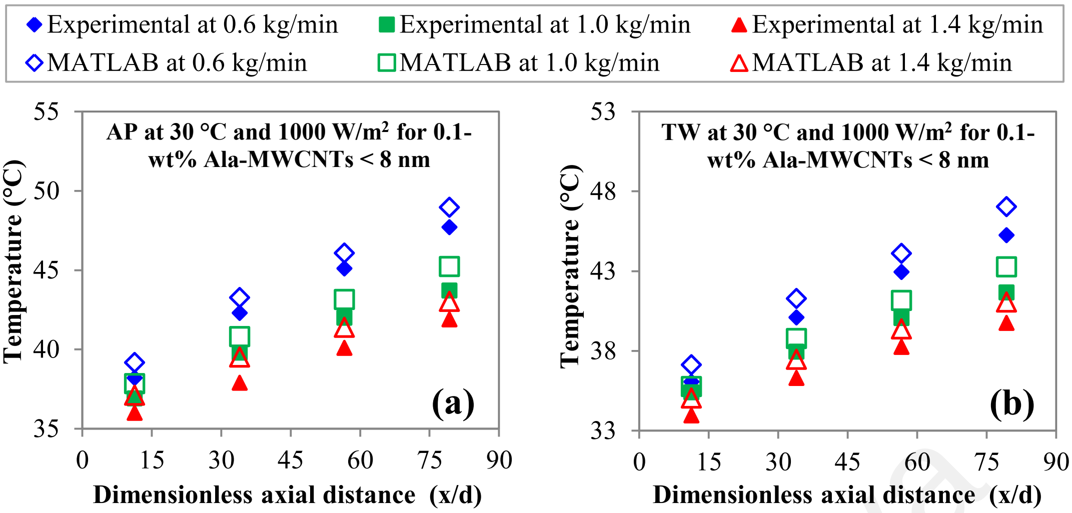

Figure 4.60: Measured values of AP (a) and TW (b) versus MATLAB predictions at 30-°C inlet fluid temperature and 1000-W/m² heat flux intensity for 0.1-wt% water-based Ala-MWCNTs < 8 nm nanofluids at different mass flow rates.

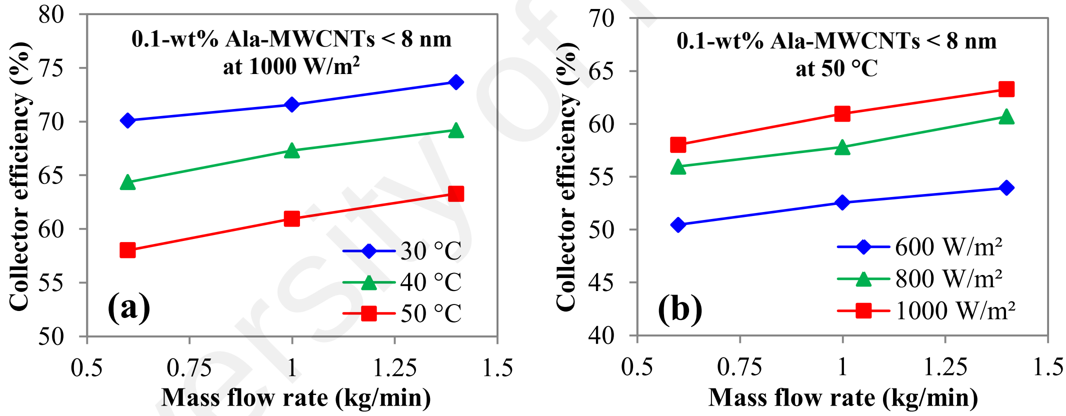

Figure 4.61: Experimental values of FPSC's energy efficiency versus mass flow rate for 0.1-wt% water-based Ala-MWCNTs nanofluids at different (a) inlet fluid temperatures and (b) heat flux intensities.

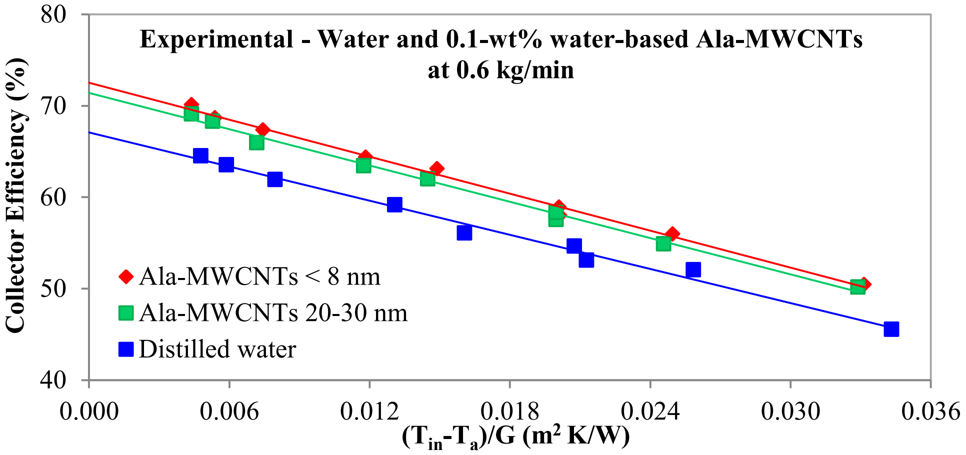

Figure 4.62: Experimentally calculated values of collector's efficiency for water and 0.1-wt% water-based Ala-MWCNTs nanofluids with different outside diameters.

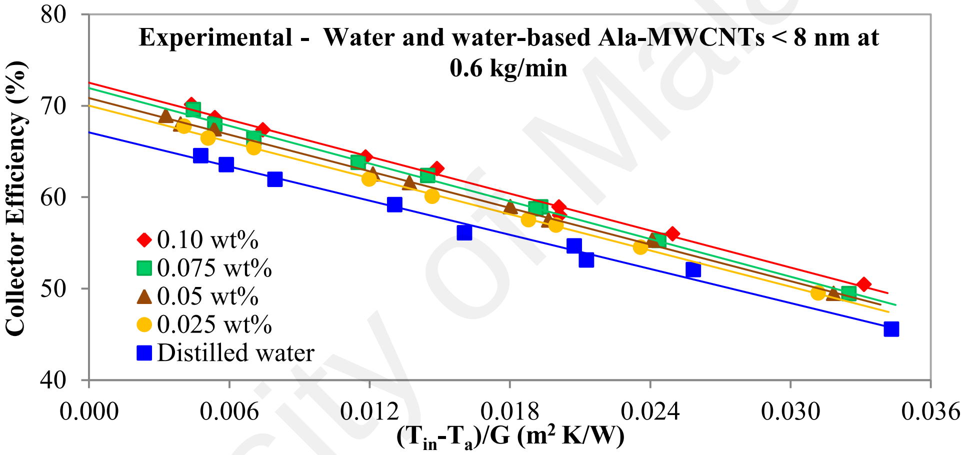

Figure 4.63: Experimentally calculated values of collector's efficiency for water and water-based Ala-MWCNTs < 8 nm nanofluids with different weight concentrations.

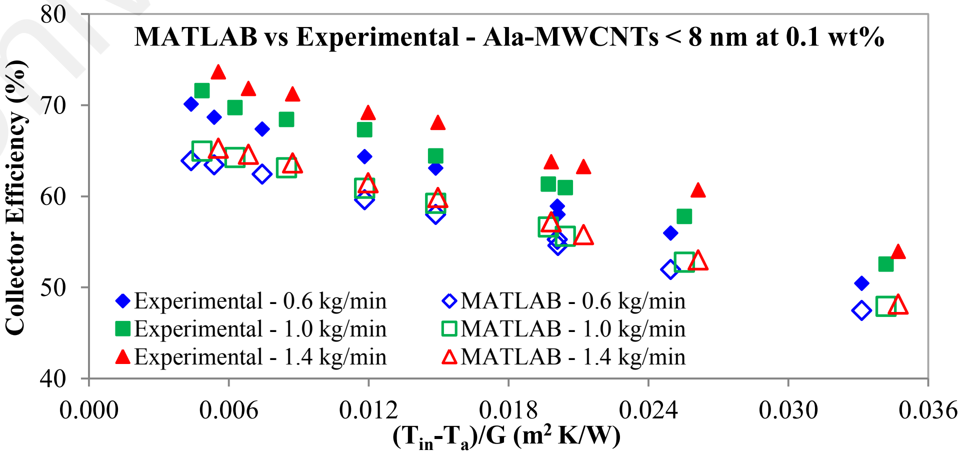

Figure 4.64: Comparison of the experimentally calculated values of FPSC's efficiency with the MATLAB code predictions for water-based 0.1-wt% Ala-MWCNTs < 8 nm nanofluids at different mass flow rates.

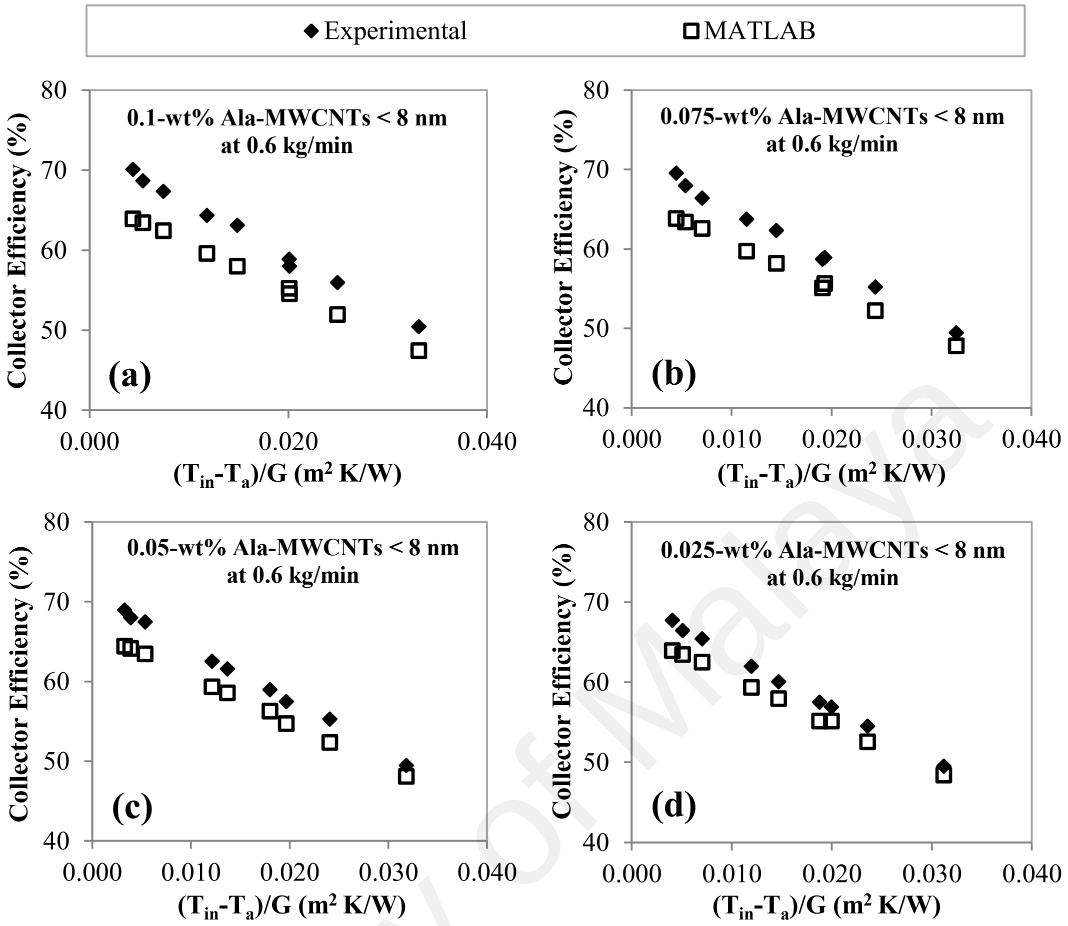

Figure 4.65: Experimentally calculated values of FPSC's energy efficiency versus MATLAB code predictions for water-based Ala-MWCNTs < 8 nm nanofluids at different weight concentrations.

4.5.2.3 Comparison of all the nanofluids at the highest concentration

In the previous sections, the individual effects of using five aqueous colloidal dispersions of covalently functionalized carbon-based nanostructures with different weight concentrations as working fluids on the thermal performance of a FPSC have been comprehensively presented. In the present section and at a weight concentration of 0.1%, a final comparison between all these five water-based nanofluids will be performed in terms of their positive effect on the thermal performance of the experimental FPSC in order to clarify and select the optimal nanofluid that can efficiently be utilized as a successful alternative working fluid in FPSCs.

The effect of experimentally using distilled water and 0.1-wt% water-based nanofluids that were prepared in this study as working fluids in the FPSC on the values of AP and TW at different values of x/d along the direction of flow is presented in Figure 4.66. The data were recorded at a mass flow rate of 1.4 kg/, inlet fluid temperature of 30 °C, and heat flux intensity of 1000 W/m². When compared with water, Figure 4.66 clearly shows that water-based nanofluids in the presence of TEA-GNPs with 750-m^2/g SSA relativity cause the largest decrease in AP and TW in comparison to other nanomaterials. This finding is logical and coincides with the fact that the same nanomaterial had previously showed, in this study, the highest increase in the thermal conductivity of base fluid. Since it was previously proved that the convective heat transfer coefficient for nanofluids with higher thermal conductivities in comparison to their base fluids will consequently be greater (Faulkner et al., 2004; Sarit K Das et al., 2007; Kwon et al., 2013; Amiri et al., 2015c), thus, it can be reasonably concluded the water-based TEA-GNPs nanofluids with 750-m^2/g SSA have relatively higher heat transfer coefficient and heat transfer performance.

The experimental values of FPSC's energy efficiency versus reduced temperature parameter are presented in Figure 4.67 for water and 0.1-wt% water-based nanofluids at different mass flow rates. From which and in comparison to water, it is very obvious that from all the nanofluids that were used in the present study, the water-based TEA-GNPs nanofluids with 750-m^2/g SSA is again superior in terms of the percentage enhancement in the energy efficiency of the FPSC, up to 10.53% at a mass flow rate of 0.6 kg/min. Based on the percentage enhancement in FPSC's energy efficiency that was obtained at 0.6-kg/min mass flow rate, the 0.1-wt% water-based nanofluids can be sequenced as (TEA-GNPs 750) > (TEA-GNPs 500) > (Ala-MWCNTs < 8 nm) > (TEA-GNPs 300) > (Ala-MWCNTs 20–30 nm) with values of 10.53% > 9.03% > 8.11% > 6.55% > 6.42%, respectively, in comparison to water. The same sequence was found for the 1.0-kg/min mass flow rate but with corresponding values of 9.19% > 8.44% > 7.09% > 6.0% > 4.87%. While for the mass flow rate of 1.4 kg/min, a different sequence of (TEA-GNPs 750) > (Ala-MWCNTs < 8 nm) > (TEA-GNPs 500) > (Ala-MWCNTs 20–30 nm) > (TEA-GNPs 300) was found with percentage enhancements of 10.07% > 9.55% > 8.96% > 8.08% > 5.16%, respectively, in comparison to water.

The variation of the performance index values with mass flow rate for the various water-based nanofluids that were prepared in this study are displayed in Figure 4.68 at different loadings of the nanomaterials in the based fluid. It is noteworthy that all the values of performance index irrespective to weight concentration and mass flow rate are greater than 1, indicating that all water-based nanofluids that were prepared in this work can be nominated as appropriate alternative working fluids in FPSCs. In this study, the 0.1-wt% water-based nanofluids can be arranged in terms of the calculated value of performance index at a mass flow rate of 0.6 kg/min as (TEA-GNPs 750) > (TEA-GNPs 500) > (Ala-MWCNTs < 8 nm) > (TEA-GNPs 300) > (Ala-MWCNTs 20–30 nm) with values of 1.104 > 1.089 > 1.079 > 1.064 > 1.063, respectively. Similar order was obtained for the 1.0-kg/min mass flow rate but with corresponding values of 1.092 > 1.084 > 1.07 > 1.06 > 1.048. While for the 1.4-kg/min mass flow rate, a different order was observed as (TEA-GNPs 750) > (Ala-MWCNTs < 8 nm) > (TEA-GNPs 500) > (Ala-MWCNTs 20–30 nm) > (TEA-GNPs 300) and values of 1.1 > 1.095 > 1.089 > 1.08 > 1.051, respectively. Furthermore, the values of performance index versus weight concentration are presented in Figure 4.69 at a mass flow rate of 0.6 kg/min. From which, it can easily be found that the performance index increases as weight concentration of nanomaterials in the base fluid increases, indicating that the enhancement in the energy efficiency of the FPSC is higher than the increase in pressure drop. These results strengthened the ability to conclude that the aqueous colloidal dispersions of covalently functionalized carbon-based nanostructures that were prepared in this study have positive effects on the thermal performance of the FPSC superior than their negative effects on pressure drop. Thus, they can effectively be used as promising and novel alternative working fluid in FPSCs or any other similar heat transfer application. Based on the aforementioned values for the enhancement in energy efficiency and performance index of the FPSC, it can be soundly decided that from all nanofluids that were prepared in this study, water-based TEA-GNPs nanofluid with 750-m^2/g SSA is the most effective unconventional working fluid that can be used in FPSCs or any other comparable thermal equipment or engineering process instead of the traditional working fluids for higher energy efficiency.

The calculated values of the performance index at different mass flow rates are displayed in Figure 4.70 for different weight concentrations of TEA-GNPs with SSA of 750m^2/g in water. From this figure, the values of performance index can be listed as follows; 1.052, 1.072, 1.09, and 1.104 at 0.6 kg/min; 1.053, 1.071, 1.083, and 1.092 at 1.0 kg/min; 1.059, 1.078, 1.091, and 1.1 at 1.4 for weight concentrations of 0.025%, 0.05%, 0.075%, and 0.1%, respectively. Here, it is important to notice that water-based TEA-GNPs 750 have the highest value of performance index at the lowest mass flow rate used in this study, i.e., 0.6 kg/min. At this flow rate, the difference between the maximum value of performance index at 0.1-wt% and the lower one at 0.075-wt% is around 1.28%. Since the additional initial cost of nanomaterials from a weight concentration of 0.075% to 0.1%, i.e., 0.25 gram of nanomaterials for each kilogram of base fluid, is quite low, it can reasonably and economically be concluded that from all the weight concentrations investigated in the present study, the 0.1-wt% is an appropriate selection that can be used for superior enhancements in energy efficiency and performance index of FPSCs.

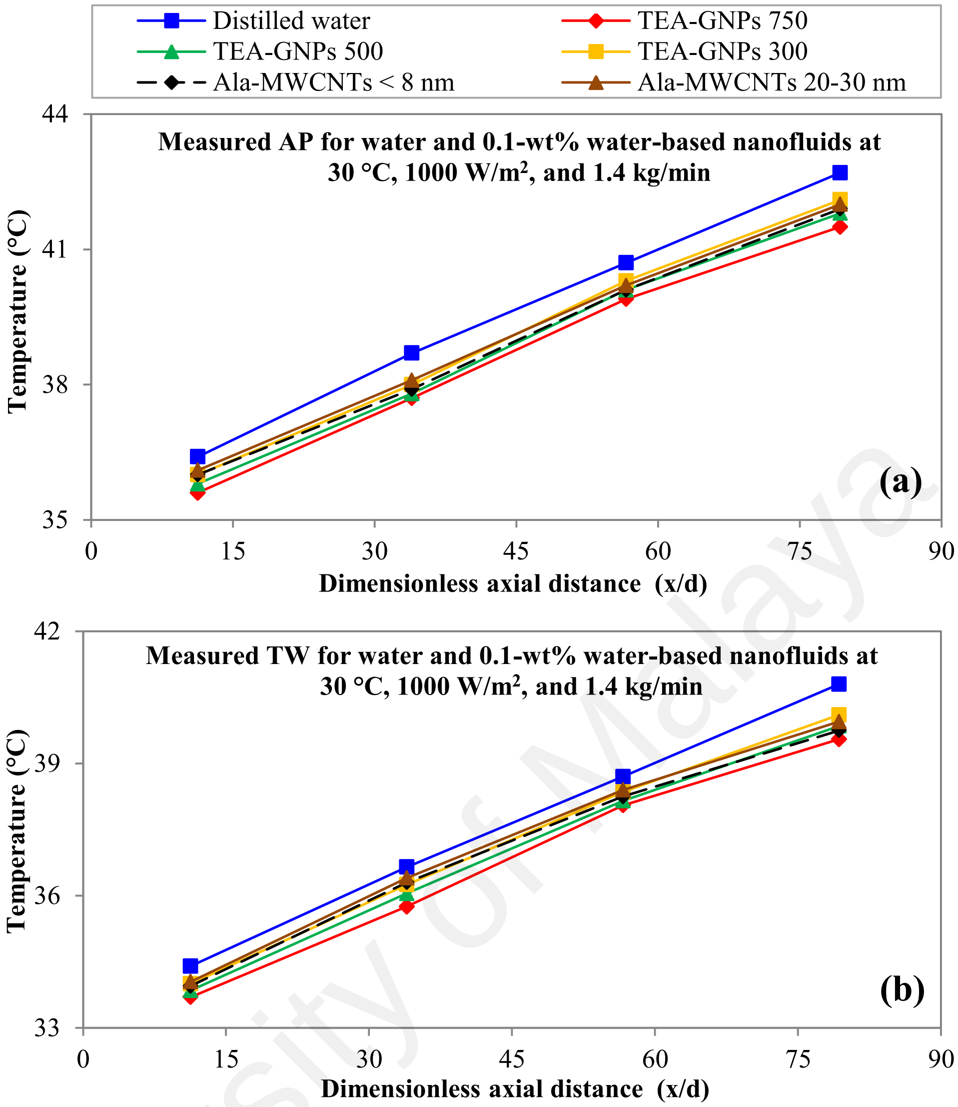

Figure 4.66: The values of AP (a) and TW (b) measured at 1.4-kg/min mass flow rate, 30-°C inlet fluid temperature, and 1000-W/m² heat flux intensity for water and 0.1-wt% carbon-based nanostructures aqueous nanofluids.

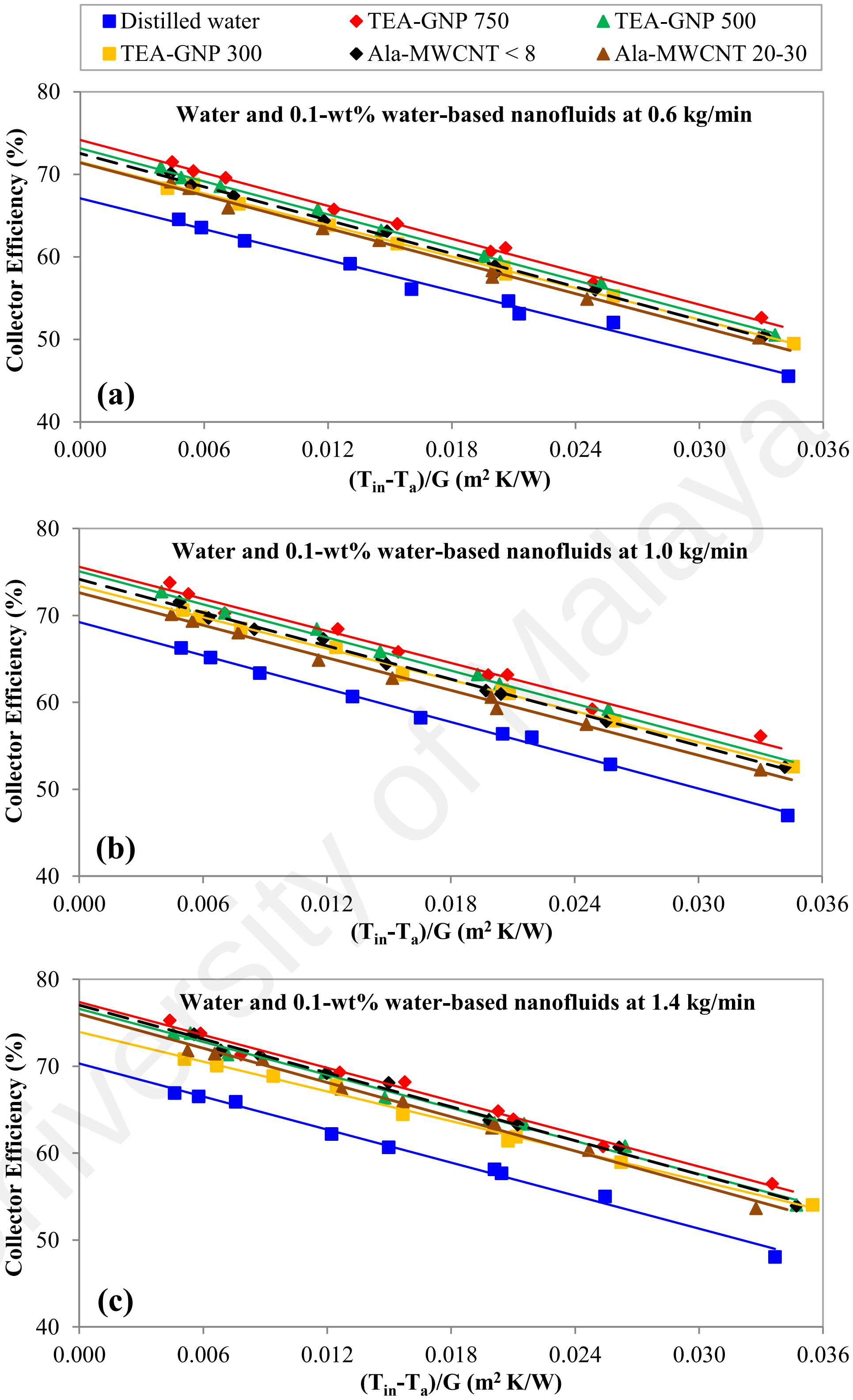

Figure 4.67: The calculated values of FPSC’s efficiency using the experimental data for water and 0.1-wt% carbon-based nanostructures aqueous nanofluids at mass flow rates of (a) 0.6 kg/min, (b) 1.0 kg/min, and (c) 1.4 kg/min.

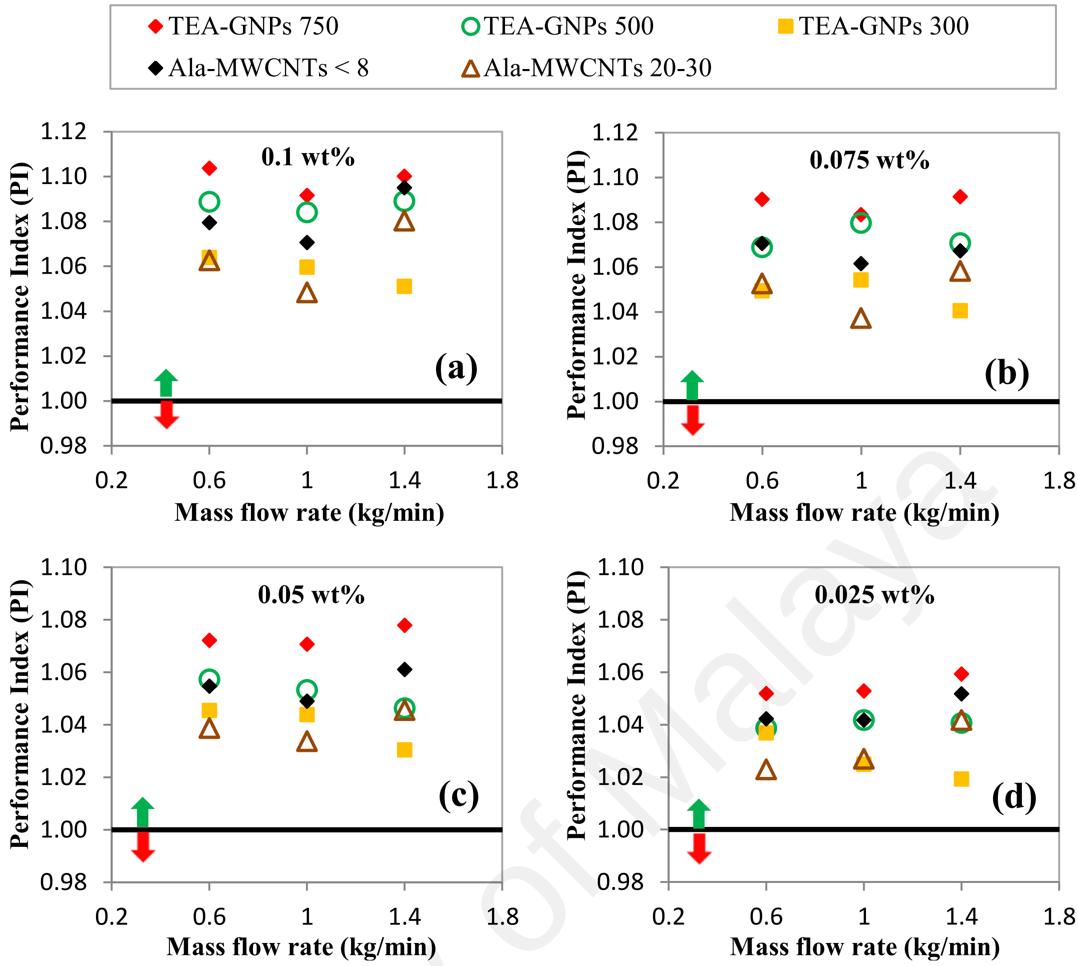

Figure 4.68: Performance index versus mass flow rate for water-based nanofluids at weight concentrations of (a) 0.1%, (b) 0.075%, (c) 0.05%, and (c) 0.025%.

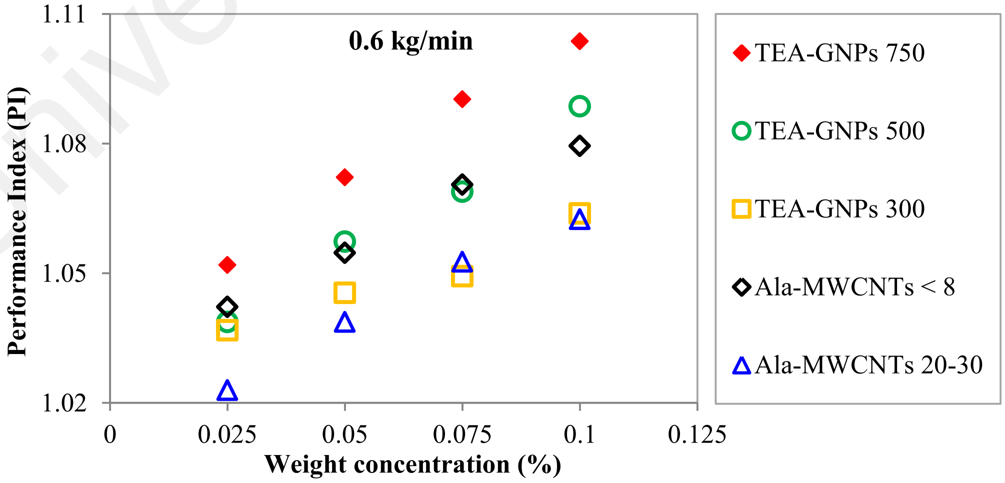

Figure 4.69: Variation of performance index with weight concentration for water-based nanofluids at 0.6-kg/min mass flow rate.

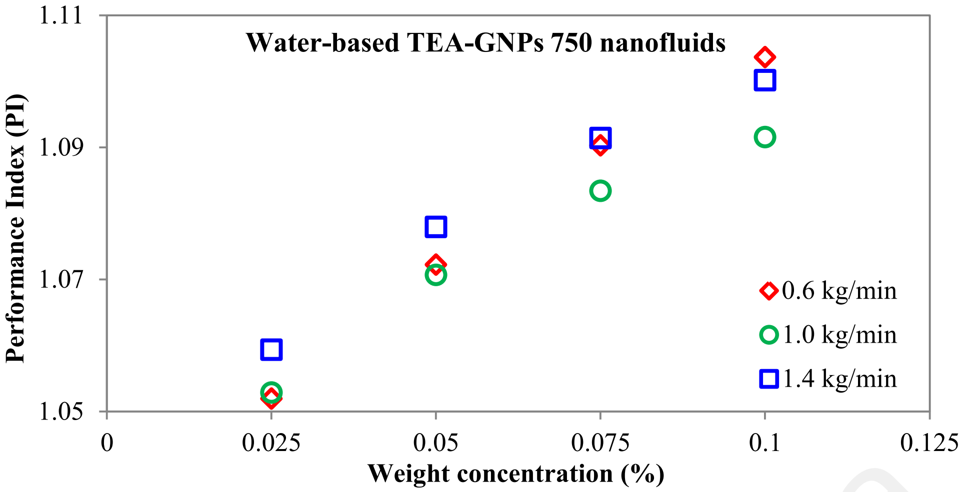

Figure 4.70: Variation of performance index with weight concentration for water-based TEA-GNPs 750 nanofluids at different mass flow rates.

CHAPTER 5: CONCLUSIONS AND RECOMMENDATIONS

5.1 Introduction

The conclusions of the current research observations are presented along with the suggestions for further work which could be performed as an extension of the research conducted in this thesis.

5.2 Conclusions

The target of this research is to study, theoretically and experimentally, the effect of using aqueous colloidal dispersions of carbon-based nanostructures with different types and weight concentrations as alternative working fluids on the thermal performance of a FPSC. From all the results presented and discussions made in the previous chapter, the following conclusions could be extracted.

1. Using ultrasonication times of 15, 30, 60, 90, and 120 min, higher colloidal stability could be obtained at 60-min ultrasonication time. Full separation of water-based pristine GNPs nanofluids was observed. The addition of GA, CTAB, SDS, and SDBS surfactants for non-covalent functionalization improved the colloidal stability but created excessive foam. Covalent functionalization revealed higher colloidal stability and the rate of sedimentation among the nanofluids was dependent on the type of nanomaterial, SSA, and weight concentration.

2. The thermal conductivity, viscosity, and density increased, while the specific heat decreased as weight concentration of various carbon-based nanostructures in the base fluid increased. The increase in temperature resulted in an increase in thermal conductivity and a decrease in viscosity, density, and specific heat of nanofluids. For each type of nanomaterials, the increase in SSA caused a visible increase in nanofluid thermal conductivity. Since the classical viscosity models of Einstein, Brinkman, and

Batchelor underestimated the measured values of viscosity, a correlation was developed and showed good agreement.

3. An experimental test rig was designed and built. With reference to the obtained results, the values of AP and TW were directly proportional to heat flux intensity and inlet fluid temperature, and inversely proportional to mass flow rate. The collector's efficiency increased as mass flow rate and heat flux intensity increased, and decreased as inlet fluid temperature increased. The presence of nanomaterials with any SSA and weight concentration in water resulted in a decrease in the values of AP and TW and an increase in FPSC's energy efficiency. In the presence of nanofluids, the FPSC's efficiency increased as the weight concentration and SSA increased, up to 10.53% for 0.1-wt% TEA-GNPs 750. Performance index values were directly proportional to the weight concentration of nanomaterial. Water-based TEA-GNPs nanofluid with 750-m^2/g SSA was the best alternative working fluid between all prepared nanofluids in this study which can be used in FPSCs for enhanced energy efficiency.

4. A mathematical model was set and a MATLAB code was developed for simulating the FPSC's performance during steady-state operation and using water-based nanofluids as its working fluids. Based on the comparison made between experimental and simulated data for water and nanofluids, it can be concluded that the MATLAB code is capable of simulating the thermal performance of nanofluid-based FPSCs with acceptable accuracy. While for other types of nanomaterials, the code can easily be modified by creating new MATLAB functions for calculating the thermophysical properties of their water-based nanofluids.

5.3 Recommendations for future work

The present work has focused on studying the thermal performance of a FPSC using novel aqueous colloidal dispersions of covalently-functionalized carbon-based nanostructures as its working fluids. In addition to the present research findings, a lot of work can be done to upgrade and expand the knowledge level in this field. Based on the findings of the present study, some specific subjects that could be addressed in future work on nanofluid-based FPSCs are stated below:

1. Further investigations are encouraged on preparing nanomaterials with higher SSA and study the colloidal stability, thermophysical properties, and thermal performance of their nanofluids.

2. In numerical simulation of nanofluid-based heat transfer applications, the availability of general correlations for the precise prediction of the thermophysical properties of any nanofluid or at least a wide range of nanofluids is essential for building computer code to simulate the thermal performance irrespective of the type of nanofluid used.

3. Further research can be implemented in the future to investigate the thermal performance of FPSCs at higher mass flow rates using the novel nanofluids prepared in this study and/or other types of nanomaterials with higher thermal conductivity at lower weight concentrations which can ultimately produce nanofluids with higher thermal performance and lower viscosity, i.e., higher performance index.

4. The present review of literature on the use of nanofluids in FPSCs revealed a lack of agreement between the findings of different researchers in terms of thermophysical properties and thermal performance. Therefore, additional work is required to identify the main factors responsible for this discrepancy in the experimental and theoretical data.

REFERENCES

Abdin, Z., Alim, M. A., Saidur, R., Islam, M. R., Rashmi, W., Mekhilef, S., & Wadi, A. (2013). Solar energy harvesting with the application of nanotechnology. *Renewable and Sustainable Energy Reviews, 26*, 837-852.

Ahmadi, A., Ganji, D. D., & Jafarkazemi, F. (2016). Analysis of utilizing Graphene nanoplatelets to enhance thermal performance of flat plate solar collectors. *Energy Conversion and Management, 126*, 1-11.

Ahuja, A. S. (1975a). Augmentation of heat transport in laminar flow of polystyrene suspensions. I. Experiments and results. *Journal of Applied Physics, 46*(8), 3408-3416.

Ahuja, A. S. (1975b). Augmentation of heat transport in laminar flow of polystyrene suspensions. II. Analysis of the data. *Journal of Applied Physics, 46*(8), 3417-3425.

Akhtar, N., & Mullick, S. (2007). Computation of glass-cover temperatures and top heat loss coefficient of flat-plate solar collectors with double glazing. *Energy, 32*(7), 1067-1074.

Amiri, A., Ahmadi, G., Shanbedi, M., Etemadi, M., Mohd Zubir, M. N., Chew, B. T., & Kazi, S. N. (2016d). Heat transfer enhancement of water-based highly crumpled few-layer graphene nanofluids. *RSC Advances, 6*(107), 105508-105527.

Amiri, A., Ahmadi, G., Shanbedi, M., Savari, M., Kazi, S. N., & Chew, B. T. (2015e). Microwave-Assisted Synthesis of Highly-Crumpled, Few-Layered Graphene and Nitrogen-Doped Graphene for Use as High-Performance Electrodes in Capacitive Deionization. *Sci Rep, 5*, 17503.

Amiri, A., Arzani, H. K., Kazi, S. N., Chew, B. T., & Badarudin, A. (2016c). Backward-facing step heat transfer of the turbulent regime for functionalized graphene nanoplatelets based water–ethylene glycol nanofluids. *International Journal of Heat and Mass Transfer, 97*, 538-546.

Amiri, A., Maghrebi, M., Baniadam, M., & Zeinali Heris, S. (2011). One-pot, efficient functionalization of multi-walled carbon nanotubes with diamines by microwave method. *Applied Surface Science, 257*(23), 10261-10266.

Amiri, A., Sadri, R., Shanbedi, M., Ahmadi, G., Chew, B. T., Kazi, S. N., & Dahari, M. (2015a). Performance dependence of thermosyphon on the functionalization approaches: An experimental study on thermo-physical properties of graphene nanoplatelet-based water nanofluids. *Energy Conversion and Management, 92*, 322-330.

Amiri, A., Sadri, R., Shanbedi, M., Ahmadi, G., Kazi, S. N., Chew, B. T., & Zubir, M. N. M. (2015b). Synthesis of ethylene glycol-treated Graphene Nanoplatelets with one-pot, microwave-assisted functionalization for use as a high performance engine coolant. *Energy Conversion and Management, 101*, 767-777.

Amiri, A., Shanbedi, M., Ahmadi, G., & Rozali, S. (2017a). Transformer oils-based graphene quantum dots nanofluid as a new generation of highly conductive and stable coolant. *International Communications in Heat and Mass Transfer, 83*, 40-47.

Amiri, A., Shanbedi, M., Chew, B. T., Kazi, S. N., & Solangi, K. H. (2016a). Toward improved engine performance with crumpled nitrogen-doped graphene based water–ethylene glycol coolant. *Chemical Engineering Journal, 289*, 583-595.

Amiri, A., Shanbedi, M., Rafieerad, A. R., Rashidi, M. M., Zaharinie, T., Zubir, M. N. M., . . . Chew, B. T. (2017b). Functionalization and exfoliation of graphite into mono layer graphene for improved heat dissipation. *Journal of the Taiwan Institute of Chemical Engineers, 71*, 480-493.

Amiri, A., Shanbedi, M., Yarmand, H., Arzani, H. K., Gharehkhani, S., Montazer, E., . . . Kazi, S. N. (2015c). Laminar convective heat transfer of hexylamine-treated MWCNTs-based turbine oil nanofluid. *Energy Conversion and Management, 105*, 355-367.

Amrollahi, A., Rashidi, A. M., Meibodi, M. E., & Kashefi, K. (2009). Conduction heat transfer characteristics and dispersion behaviour of carbon nanofluids as a function of different parameters. *Journal of Experimental Nanoscience, 4*(4), 347-363.

Amrutkar, S. K., Ghodke, S., & Patil, K. N. (2012). Solar flat plate collector analysis. *IOSR Journal of Engineering (IOSRJEN), Vol. 2*(2), 207-213.

Anderson, F. (2013). *A guide to working with corrosive substances*. Raleigh, NC: North Carolina, Occupational Safety and Health Division.

Anderson, T. N., Duke, M., & Carson, J. K. (2010). The effect of colour on the thermal performance of building integrated solar collectors. *Solar Energy Materials and Solar Cells, 94*(2), 350-354.

Aravind, S. S. J., Baskar, P., Baby, T. T., Sabareesh, R. K., Das, S., & Ramaprabhu, S. (2011). Investigation of Structural Stability, Dispersion, Viscosity, and Conductive Heat Transfer Properties of Functionalized Carbon Nanotube Based Nanofluids. *The Journal of Physical Chemistry C, 115*(34), 16737-16744.

Ardente, F., Beccali, G., Cellura, M., & Lo Brano, V. (2005). Life cycle assessment of a solar thermal collector. *Renewable Energy, 30*(7), 1031-1054.

Arnold, E. (1970). *UK steam tables in SI units*. London, UK: United Kingdom Committee on the Properties of Steam.

Arzani, H. K., Amiri, A., Arzani, H. K., Rozali, S. B., Kazi, S. N., & Badarudin, A. (2016). Toward improved heat transfer performance of annular heat exchangers with water/ethylene glycol-based nanofluids containing graphene nanoplatelets. *Journal of Thermal Analysis and Calorimetry*, 1-10.

ASHRAE Standard 93. (2003). *Methods of testing to determine the thermal performance of solar collectors*. Atlanta, GA: American Society of Heating, Refrigerating and Air-Conditioning Engineers.

Assael, M. J., Metaxa, I. N., Arvanitidis, J., Christofilos, D., & Lioutas, C. (2005). Thermal conductivity enhancement in aqueous suspensions of carbon multi-walled and double-walled nanotubes in the presence of two different dispersants. *International Journal of Thermophysics, 26*(3), 647-664.

Azari, A., Kalbasi, M., Derakhshandeh, M., & Rahimi, M. (2013). An experimental study on nanofluids convective heat transfer through a straight tube under constant heat flux. *Chinese Journal of Chemical Engineering, 21*(10), 1082-1088.

Badran, A. A., Mustafa, M. F., Dawood, W. K., & Ghazzawi, Z. K. (2008). On the measurement of bond conductance in solar collector absorber plate. *Energy Conversion and Management, 49*(11), 3305-3310.

Bahr, J. L., & Tour, J. M. (2001). Highly functionalized carbon nanotubes using in situ generated diazonium compounds. *Chemistry of materials, 13*(11), 3823-3824.

Bakari, R., Minja, R. J. A., & Njau, K. N. (2014). Effect of glass thickness on performance of flat plate solar collectors for fruits drying. *Journal of Energy, 2014*, 8.

Balasubramanian, K., & Burghard, M. (2005). Chemically functionalized carbon nanotubes. *Small, 1*(2), 180-192.

Behi, M., & Mirmohammadi, S. A. (2012). *Investigation on thermal conductivity, viscosity and stability of nanofluids.* (Master's thesis), Royal Institute of Technology (KTH), Stockholm, Sweden. Retrieved from http://www.diva-portal.org/smash/record.jsf?pid=diva2:561791

Bender, E. (1969). Druckverlust bei laminarer Strömung im Rohreinlauf. *Chemie Ingenieur Technik, 41*(11), 682-686.

Bhatt, M. K., Gaderia, S. N., & Channiwala, S. A. (2011). Experimental investigations on top loss coefficients of solar flat plate collector at different tilt angle. *World Academy of Science, Engineering and Technology, 5*, 361-365.

Bisen, A., Das, P. P., & Jain, R. (2011). Parametric studies of top heat loss coefficient of double glazed flat plate solar collectors. *MIT Internation Journal of Mechanical Engineering, 1*(2).

Bogaerts, W., & Lampert, C. (1983). Materials for photothermal solar energy conversion. *Journal of Materials Science, 18*(10), 2847-2875.

Brinkman, H. (1952). The viscosity of concentrated suspensions and solutions. *The Journal of Chemical Physics, 20*(4), 571-571.

Camel-solar. (2012). "Flat-plate solar collector" Online image. Retrieved from http://www.camel-solar.com/cs/wp-content/uploads/2012/01/flat-plate-cross-section.jpg

Çengel, Y. A. (2003). *Heat transfer : A practical approach*. Boston, MA: McGraw-Hill.

Cengel, Y. A., & Cimbala, J. M. (2006). Fluid mechanics fundamentals and applications. *McGraw-Hill Publication, 2*, 136-138.

Chaji, H., Ajabshirchi, Y., Esmaeilzadeh, E., Heris, S. Z., Hedayatizadeh, M., & Kahani, M. (2013). Experimental study on thermal efficiency of flat plate solar collector using TiO_2/water nanofluid. *Modern Applied Science, 7*(10).

Chandrasekar, M., Suresh, S., & Chandra Bose, A. (2010a). Experimental investigations and theoretical determination of thermal conductivity and viscosity of Al_2O_3/water nanofluid. *Experimental Thermal and Fluid Science, 34*(2), 210-216.

Chandrasekar, M., Suresh, S., & Senthilkumar, T. (2012). Mechanisms proposed through experimental investigations on thermophysical properties and forced convective heat transfer characteristics of various nanofluids – A review. *Renewable and Sustainable Energy Reviews, 16*(6), 3917-3938.

Chen, L., Xie, H., Li, Y., & Yu, W. (2008). Nanofluids containing carbon nanotubes treated by mechanochemical reaction. *Thermochimica Acta, 477*(1-2), 21-24.

Chen, Z., Furbo, S., Perers, B., Fan, J., & Andersen, E. (2012). Efficiencies of flat plate solar collectors at different flow rates. *Energy Procedia, 30*, 65-72.

Choi, C., & Kim, M. (2011). *Wettability Effects on Heat Transfer*: INTECH Open Access Publisher.

Choi, S. U. S., & Eastman, J. A. (1995). *Enhancing thermal conductivity of fluids with nanoparticles*. Paper presented at the ASME International Mechanical Engineering Congress & Exposition, San Francisco, CA.

Choi, S. U. S., & Eastman, J. A. (2001). *Enhanced heat transfer using nanofluids.* Argonne National Laboratory (ANL), Argonne, IL, Patent No. (US 6,221,275). U.S. Patent and Trademark Office.

Choi, S. U. S., Zhang, Z. G., Yu, W., Lockwood, F. E., & Grulke, E. A. (2001). Anomalous thermal conductivity enhancement in nanotube suspensions. *Applied Physics Letters, 79*(14), 2252.

Chu, K., Jia, C.-c., & Li, W.-s. (2012b). Effective thermal conductivity of graphene-based composites. *Applied Physics Letters, 101*(12), 121916.

Chu, K., Li, W.-s., Dong, H.-f., & Tang, F.-l. (2012a). Modeling the thermal conductivity of graphene nanoplatelets reinforced composites. *EPL (Europhysics Letters), 100*(3), 36001.

Codd, D. S., Carlson, A., Rees, J., & Slocum, A. H. (2010). A low cost high flux solar simulator. *Solar Energy, 84*(12), 2202-2212.

Corcione, M. (2011). Empirical correlating equations for predicting the effective thermal conductivity and dynamic viscosity of nanofluids. *Energy Conversion and Management, 52*(1), 789-793.

Das, S. K., Choi, S. U., Yu, W., & Pradeep, T. (2007). *Nanofluids: science and technology*: John Wiley & Sons.

Das, S. K., Choi, S. U. S., & Patel, H. E. (2006). Heat transfer in nanofluids - a review. *Heat Transfer Engineering, 27*(10), 3-19.

Das, S. K., Putra, N., Thiesen, P., & Roetzel, W. (2003). Temperature dependence of thermal conductivity enhancement for nanofluids. *Journal of Heat Transfer, 125*(4), 567-574.

Daungthongsuk, W., & Wongwises, S. (2007). A critical review of convective heat transfer of nanofluids. *Renewable and Sustainable Energy Reviews, 11*(5), 797-817.

Ding, Y., Alias, H., Wen, D., & Williams, R. A. (2006). Heat transfer of aqueous suspensions of carbon nanotubes (CNT nanofluids). *International Journal of Heat and Mass Transfer, 49*(1-2), 240-250.

Ding, Y., Chen, H., He, Y., Lapkin, A., Yeganeh, M., Šiller, L., & Butenko, Y. V. (2007a). Forced convective heat transfer of nanofluids. *Advanced Powder Technology, 18*(6), 813–824.

Duangthongsuk, W., & Wongwises, S. (2010). An experimental study on the heat transfer performance and pressure drop of TiO2-water nanofluids flowing under a turbulent flow regime. *International Journal of Heat and Mass Transfer, 53*(1-3), 334-344.

Duffie, J. A., & Beckman, W. A. (2013). *Solar engineering of thermal processes* (Fourth ed.). New York: John Willey & Sons.

Eastman, J. A., Choi, S. U. S., Li, S., Yu, W., & Thompson, L. J. (2001). Anomalously increased effective thermal conductivities of ethylene glycol-based nanofluids containing copper nanoparticles. *Applied Physics Letters, 78*(6), 718.

Eastman, J. A., Phillpot, S., Choi, S., & Keblinski, P. (2004). Thermal transport in nanofluids. *Annu. Rev. Mater. Res., 34*, 219-246.

Faizal, M., Saidur, R., & Mekhilef, S. (2013a). Potential of size reduction of flat-plate solar collectors when applying MWCNT nanofluid. *IOP Conference Series: Earth and Environmental Science, 16*, 012004.

Faizal, M., Saidur, R., Mekhilef, S., & Alim, M. A. (2013b). Energy, economic and environmental analysis of metal oxides nanofluid for flat-plate solar collector. *Energy Conversion and Management, 76*, 162-168.

Fang, X., Ding, Q., Fan, L.-W., Lu, H., & Yu, Z.-T. (2015). Effects of inclusion size on thermal conductivity and rheological behavior of ethylene glycol-based suspensions containing silver nanowires with various specific surface areas. *International Journal of Heat and Mass Transfer, 81*, 554-562.

Faulkner, D. J., Rector, D. R., Davidson, J. J., & Shekarriz, R. (2004, November 13-20). *Enhanced heat transfer through the use of nanofluids in forced convection.* Paper presented at the ASME International Mechanical Engineering Congress and Exposition IMECE04, Anaheim, CA.

Foster, R., Ghassemi, M., & Cota, A. (2010). *Solar energy - renewable energy and the environment* A. Ghassemi (Ed.) *Energy and the Environment* Retrieved from http://www.scribd.com/doc/130838250/Solar-Energy

Garg, P., Alvarado, J. L., Marsh, C., Carlson, T. A., Kessler, D. A., & Annamalai, K. (2009). An experimental study on the effect of ultrasonication on viscosity and heat transfer performance of multi-wall carbon nanotube-based aqueous nanofluids. *International Journal of Heat and Mass Transfer, 52*(21-22), 5090-5101.

Ghadimi, A., & Metselaar, I. H. (2013). The influence of surfactant and ultrasonic processing on improvement of stability, thermal conductivity and viscosity of titania nanofluid. *Experimental Thermal and Fluid Science, 51*, 1-9.

Ghadimi, A., Saidur, R., & Metselaar, H. S. C. (2011). A review of nanofluid stability properties and characterization in stationary conditions. *International Journal of Heat and Mass Transfer, 54*(17-18), 4051-4068.

Gillett, W. B., & Moon, J. E. (1985). *Solar collectors : Test methods and design guidelines*. Dordrecht, Holland: D. Reidel Pub. Co. for the Commission of the European Communities.

Godson, L., Raja, B., Lal, D. M., & Wongwises, S. (2010). Experimental Investigation on the Thermal Conductivity and Viscosity of Silver-Deionized Water Nanofluid. *Experimental Heat Transfer, 23*(4), 317-332.

Godson, L., Raja, B., Mohan Lal, D., & Wongwises, S. (2010). Enhancement of heat transfer using nanofluids - an overview. *Renewable and Sustainable Energy Reviews, 14*(2), 629-641.

Goldstein, J., Newbury, D., Joy, D., Lyman, C., Echlin, P., Lifshin, E., . . . Michael, J. (2003). *Scanning Electron Microscopy and X-ray Microanalysis* (Third ed.). NY: Plenum.

Gong, F., Bui, K., Papavassiliou, D. V., & Duong, H. M. (2014). Thermal transport phenomena and limitations in heterogeneous polymer composites containing carbon nanotubes and inorganic nanoparticles. *Carbon, 78*, 305-316.

Goodwin, J. W. (2004). *Colloids and Interfaces with Surfactants and Polymers - An Introduction* (pp. i-ix). Retrieved from http://www.slideshare.net/ivancastaneda925/colloids-and-interfaces-with-surfactants-and-polymers-an-introduction

Gowda, R., Sun, H., Wang, P., Charmchi, M., Gao, F., Gu, Z., & Budhlall, B. (2010). Effects of particle surface charge, species, concentration, and dispersion method on the thermal conductivity of nanofluids. *Advances in Mechanical Engineering, 2010*, 1-10.

Gupta, A. K., & Gupta, M. (2005). Synthesis and surface engineering of iron oxide nanoparticles for biomedical applications. *Biomaterials, 26*(18), 3995-4021.

Gupta, H. K., Agrawal, G. D., & Mathur, J. (2015). Investigations for effect of Al2O3–H2O nanofluid flow rate on the efficiency of direct absorption solar collector. *Case Studies in Thermal Engineering, 5*, 70-78.

Halelfadl, S., Maré, T., & Estellé, P. (2014). Efficiency of carbon nanotubes water based nanofluids as coolants. *Experimental Thermal and Fluid Science, 53*, 104-110.

Hamilton, R. L., & Crosser, O. K. (1962). Thermal conductivity of heterogeneous two-component systems. *Industrial & Engineering Chemistry Fundamentals, 1*(3), 187-191.

Harish, S., Ishikawa, K., Einarsson, E., Aikawa, S., Inoue, T., Zhao, P., . . . Maruyama, S. (2012). Temperature dependent thermal conductivity increase of aqueous nanofluid with single walled carbon nanotube inclusion. *Materials Express, 2*(3), 213-223.

He, Q., Wang, S., Zeng, S., & Zheng, Z. (2013). Experimental investigation on photothermal properties of nanofluids for direct absorption solar thermal energy systems. *Energy Conversion and Management, 73*, 150-157.

Heris, S. Z., Ahmadi, F., & Mahian, O. (2013). Pressure drop and performance characteristics of water-based Al2O3 and CuO nanofluids in a triangular duct. *Journal of Dispersion Science and Technology, 34*(10), 1368-1375.

Hetsroni, G., & Rozenblit, R. (1994). Heat transfer to a liquid—solid mixture in a flume. *International Journal of Multiphase Flow, 20*(4), 671-689.

Ho, C. D., & Chen, T. C. (2006). The recycle effect on the collector efficiency improvement of double-pass sheet-and-tube solar water heaters with external recycle. *Renewable Energy, 31*(7), 953-970.

Hodkiewicz, J. (2010). Characterizing carbon materials with Raman spectroscopy. *Thermo Scientific Application Note, 51946*.

Holman, J. P. (2012). *Experimental methods for engineers* (Eight ed.). New York: McGraw-Hill series in mechanical engineering.

Hordy, N., Rabilloud, D., Meunier, J.-L., & Coulombe, S. (2014). High temperature and long-term stability of carbon nanotube nanofluids for direct absorption solar thermal collectors. *Solar Energy, 105*, 82-90.

Hottel, H. C., & Whillier, A. (1958). *Evaluation of flat-plate solar-collector performance.* Paper presented at the Transactions of the conference on the use of solar energy, University of Arizona, Tucson, AZ.

Huang, J., Wang, X., Long, Q., Wen, X., Zhou, Y., & L. Li. (2009). *Influence of ph on the stability characteristics of nanofluids.* Paper presented at the Symposium on photonics and optoelectronics (SOPO '09).

Huxtable, S. T., Cahill, D. G., Shenogin, S., Xue, L., Ozisik, R., Barone, P., . . . Keblinski, P. (2003). Interfacial heat flow in carbon nanotube suspensions. *Nat Mater, 2*(11), 731-734.

Hwang, Y., Lee, J.-K., Lee, J.-K., Jeong, Y.-M., Cheong, S.-i., Ahn, Y.-C., & Kim, S. H. (2008). Production and dispersion stability of nanoparticles in nanofluids. *Powder Technology, 186*(2), 145-153.

Hwang, Y., Lee, J. K., Lee, C. H., Jung, Y. M., Cheong, S. I., Lee, C. G., . . . Jang, S. P. (2007). Stability and thermal conductivity characteristics of nanofluids. *Thermochimica Acta, 455*(1-2), 70-74.

Hwang, Y., Park, H. S., Lee, J. K., & Jung, W. H. (2006). Thermal conductivity and lubrication characteristics of nanofluids. *Current Applied Physics, 6*, e67-e71.

Jamal-Abad, M. T., Zamzamian, A., Imani, E., & Mansouri, M. (2013). Experimental Study of the Performance of a Flat-Plate Collector Using Cu–Water Nanofluid. *Journal of Thermophysics and Heat Transfer, 27*(4), 756-760.

Jang, S. P., & Choi, S. U. S. (2004). Role of brownian motion in the enhanced thermal conductivity of nanofluids. *Applied Physics Letters, 84*(21), 4316.

Javadi, F. S., Saidur, R., & Kamalisarvestani, M. (2013). Investigating performance improvement of solar collectors by using nanofluids. *Renewable and Sustainable Energy Reviews, 28*, 232-245.

Jeon, I.-Y., Chang, D. W., Kumar, N. A., & Baek, J.-B. (2011). Functionalization of carbon nanotubes. In D. S. Yellampalli (Ed.), *Carbon Nanotubes - Polymer Nanocomposites*: INTECH Open Access.

Jiang, L., Gao, L., & Sun, J. (2003). Production of aqueous colloidal dispersions of carbon nanotubes. *Journal of Colloid and Interface Science, 260*(1), 89-94.

Kahani, M., Zeinali Heris, S., & Mousavi, S. M. (2013). Comparative study between metal oxide nanopowders on thermal characteristics of nanofluid flow through helical coils. *Powder Technology, 246*, 82-92.

Kalogirou, S. A. (2009). *Solar energy engineering - processes and systems* (1st ed.): Academic Press.

Kamiya, H., Gotoh, K., Shimada, M., Uchikoshi, T., Otani, Y., Fuji, M., . . . Miyahara, M. (2012). Chapter 3 - Characteristics and behavior of nanoparticles and its dispersion systems. In M. Hosokawa, K. Nogi, M. Naito & T. Yokoyama (Eds.), *Nanoparticle Technology Handbook (Second Edition)* (pp. 113-176). Amsterdam: Elsevier.

Kang, H. U., Kim, S. H., & Oh, J. M. (2006). Estimation of Thermal Conductivity of Nanofluid Using Experimental Effective Particle Volume. *Experimental Heat Transfer, 19*(3), 181-191.

Keblinski, P., Eastman, J. A., & Cahill, D. G. (2005). Nanofluids for thermal transport. *Materials Today, 8*(6), 36-44.

Keblinski, P., Phillpot, S. R., Choi, S. U. S., & Eastman, J. A. (2002). Mechanisms of heat flow in suspensions of nano-sized particles (nanofluids). *International Journal of Heat & Mass Transfer, 45*, 855-863.

Khalifa, A.-J. N. (1999). Thermal performance of locally made flat plate solar collectors used as part of a domestic hot water system. *Energy Conversion and Management, 40*(17), 1825-1833.

Khalifa, A. J. N., & Abdul Jabbar, R. A. (2010). Conventional versus storage domestic solar hot water systems: A comparative performance study. *Energy Conversion and Management, 51*(2), 265-270.

Khoukhi, M., & Maruyama, S. (2006). Theoretical approach of a flat-plate solar collector taking into account the absorption and emission within glass cover layer. *Solar Energy, 80*(7), 787-794.

Khullar, V., & Tyagi, H. (2010, December 16-18). *Application of nanofluids as the working fluid in concentrating parabolic solar collectors.* Paper presented at the 37th National & 4th International Conference on Fluid Mechanics and Fluid Power, Madras, Chennai, India.

Klein, S. A. (1975). Calculation of flat-plate collector loss coefficients. *Solar Energy, 17*(1), 79-80.

Kline, S. J., & McClintock, F. (1953). Describing uncertainties in single-sample experiments. *Mechanical engineering, 75*(1), 3-8.

Kole, M., & Dey, T. K. (2013). Investigation of thermal conductivity, viscosity, and electrical conductivity of graphene based nanofluids. *Journal of Applied Physics, 113*(8), 084307.

Kulkarni, D. P., Vajjha, R. S., Das, D. K., & Oliva, D. (2008). Application of aluminum oxide nanofluids in diesel electric generator as jacket water coolant. *Applied Thermal Engineering, 28*(14-15), 1774-1781.

Kwon, Y., Lee, K., Park, M., Koo, K., Lee, J., Doh, Y., . . . Jung, Y. (2013). Temperature Dependence of Convective Heat Transfer with Al2O3 Nanofluids in the Turbulent Flow Region. *Journal of Nanoscience and Nanotechnology, 13*(12), 7902-7905.

Labib, M. N., Nine, M. J., Afrianto, H., Chung, H. S., & Jeong, H. M. (2013). Numerical investigation on effect of base fluids and hybrid nanofluid in forced convective heat transfer. *International Journal of Thermal Sciences, 71*, 163-171.

Lee, G.-J., & Rhee, C. (2014). Enhanced thermal conductivity of nanofluids containing graphene nanoplatelets prepared by ultrasound irradiation. *Journal of Materials Science, 49*(4), 1506-1511.

Lee, J.-H., Hwang, K. S., Jang, S. P., Lee, B. H., Kim, J. H., Choi, S. U. S., & Choi, C. J. (2008). Effective viscosities and thermal conductivities of aqueous nanofluids containing low volume concentrations of Al_2O_3 nanoparticles. *International Journal of Heat and Mass Transfer, 51*(11-12), 2651-2656.

Lee, J., & Mudawar, I. (2007). Assessment of the effectiveness of nanofluids for single-phase and two-phase heat transfer in micro-channels. *International Journal of Heat and Mass Transfer, 50*(3-4), 452-463.

Lee, J. H. (2009). *Convection performance of nanofluids for electronics cooling.* (Doctoral dissertation), Stanford University, Stanford, CA. Retrieved from ProQuest Dissertations & Theses database. (UMI No. 3351458)

Lee, S.-H., & Jang, S. P. (2013). Extinction coefficient of aqueous nanofluids containing multi-walled carbon nanotubes. *International Journal of Heat and Mass Transfer, 67*, 930-935.

Lenert, A., & Wang, E. N. (2012). Optimization of nanofluid volumetric receivers for solar thermal energy conversion. *Solar Energy, 86*(1), 253-265.

Li, J., Li, Z., & Wang, B. (2002). Experimental viscosity measurements for copper oxide nanoparticle suspensions. *TSINGHUA SCIENCE AND TECHNOLOGY, 7*(2), 198 - 201.

Li, X., Zhang, H., Fang, Y., Al-Assaf, S., Phillips, G., & Nishinari, K. (2011). Rheological Properties of Gum Arabic Solution: the Effect of Arabinogalactan Protein Complex (AGP).

Li, X., Zhu, D., & Wang, X. (2007). Evaluation on dispersion behavior of the aqueous copper nano-suspensions. *Journal of Colloid and Interface Science, 310*(2), 456-463.

Li, X. F., Zhu, D. S., Wang, X. J., Wang, N., Gao, J. W., & Li, H. (2008). Thermal conductivity enhancement dependent ph and chemical surfactant for Cu-H_2O nanofluids. *Thermochimica Acta, 469*(1-2), 98-103.

Li, Y., Zhou, J. e., Tung, S., Schneider, E., & Xi, S. (2009). A review on development of nanofluid preparation and characterization. *Powder Technology, 196*(2), 89-101.

Lin, W., Zhang, R., & Wong, C. P. (2010). Modeling of Thermal Conductivity of Graphite Nanosheet Composites. *Journal of Electronic Materials, 39*(3), 268-272.

Liu, M.-S., Lin, M. C.-C., Tsai, C. Y., & Wang, C.-C. (2006). Enhancement of thermal conductivity with Cu for nanofluids using chemical reduction method. *International Journal of Heat and Mass Transfer, 49*(17-18), 3028-3033.

Madni, I., Hwang, C.-Y., Park, S.-D., Choa, Y.-H., & Kim, H.-T. (2010). Mixed surfactant system for stable suspension of multiwalled carbon nanotubes. *Colloids and Surfaces A: Physicochemical and Engineering Aspects, 358*(1-3), 101-107.

Mahbubul, I. M., Saidur, R., & Amalina, M. A. (2012). Latest developments on the viscosity of nanofluids. *International Journal of Heat and Mass Transfer, 55*(4), 874-885.

Mahian, O., Kianifar, A., Kalogirou, S. A., Pop, I., & Wongwises, S. (2013a). A review of the applications of nanofluids in solar energy. *International Journal of Heat and Mass Transfer, 57*(2), 582-594.

Mahian, O., Kianifar, A., Sahin, A. Z., & Wongwises, S. (2015). Heat Transfer, Pressure Drop, and Entropy Generation in a Solar Collector Using SiO2/Water Nanofluids: Effects of Nanoparticle Size and pH. *Journal of Heat Transfer, 137*(6), 061011.

Mahmood, A. (2012). *Numerical and analytical study of nanofluids thermal and hydrodynamic characteristics.* (Doctoral dissertation), University of Sherbrooke Sherbrooke (Quebec), Canada.

Maïga, S. E. B., Palm, S. J., Nguyen, C. T., Roy, G., & Galanis, N. (2005). Heat transfer enhancement by using nanofluids in forced convection flows. *International Journal of Heat and Fluid Flow, 26*(4), 530-546.

Marconnet, A. M., Panzer, M. A., & Goodson, K. E. (2013). Thermal conduction phenomena in carbon nanotubes and related nanostructured materials. *Reviews of Modern Physics, 85*(3), 1295-1326.

Martín, R. H., Pinar, G. A., & García, J. P. (2011). *Experimental Heat Transfer Research in Enhanced Flat-Plate Solar Collectors*. Paper presented at the World Renewable Energy Congress, Linköping, Sweden.

Mehrali, M., Sadeghinezhad, E., Rosen, M. A., Tahan Latibari, S., Mehrali, M., Metselaar, H. S. C., & Kazi, S. N. (2015). Effect of specific surface area on convective heat transfer of graphene nanoplatelet aqueous nanofluids. *Experimental Thermal and Fluid Science, 68*, 100-108.

Meibodi, M. E., Vafaie-Sefti, M., Rashidi, A. M., Amrollahi, A., Tabasi, M., & Kalal, H. S. (2010). The role of different parameters on the stability and thermal conductivity of carbon nanotube/water nanofluids. *International Communications in Heat and Mass Transfer, 37*(3), 319-323.

Meibodi, S. S., Kianifar, A., Niazmand, H., Mahian, O., & Wongwises, S. (2015). Experimental investigation on the thermal efficiency and performance characteristics of a flat plate solar collector using SiO2/EG–water nanofluids. *International Communications in Heat and Mass Transfer, 65*, 71-75.

Michael, J. J., & Iniyan, S. (2015). Performance of copper oxide/water nanofluid in a flat plate solar water heater under natural and forced circulations. *Energy Conversion and Management, 95*, 160-169.

Mingzheng, Z., Guodong, X., Jian, L., Lei, C., & Lijun, Z. (2012). Analysis of factors influencing thermal conductivity and viscosity in different kinds of surfactant solutions. *Experimental Thermal and Fluid Science, 36*, 22-29.

Moffat, R. J. (1985). Using Uncertainty Analysis in the Planning of an Experiment. *Journal of Fluids Engineering, 107*(2), 173-178.

Munich, C. T. (2013). *Modeling of the thermal output of a flat plate solar collector.* (Master's thesis), The University of Arizona, Arizona. Retrieved from ProQuest Dissertations & Theses database. (UMI No. 1537563)

Nan, C.-W., Birringer, R., Clarke, D. R., & Gleiter, H. (1997). Effective thermal conductivity of particulate composites with interfacial thermal resistance. *Journal of Applied Physics, 81*(10), 6692-6699.

Nan, C.-W., Shi, Z., & Lin, Y. (2003). A simple model for thermal conductivity of carbon nanotube-based composites. *Chemical Physics Letters, 375*(5-6), 666-669.

Nanda, J., Maranville, C., Bollin, S. C., Sawall, D., Ohtani, H., Remillard, J. T., & Ginder, J. (2008). Thermal conductivity of single-wall carbon nanotube dispersions: role of interfacial effects. *The Journal of Physical Chemistry C, 112*(3), 654-658.

Nasiri, A., Shariaty-Niasar, M., Rashidi, A., Amrollahi, A., & Khodafarin, R. (2011). Effect of dispersion method on thermal conductivity and stability of nanofluid. *Experimental Thermal and Fluid Science, 35*(4), 717-723.

Nasiri, A., Shariaty-Niasar, M., Rashidi, A. M., & Khodafarin, R. (2012). Effect of CNT structures on thermal conductivity and stability of nanofluid. *International Journal of Heat and Mass Transfer, 55*(5-6), 1529-1535.

Natarajan, E., & Sathish, R. (2009). Role of nanofluids in solar water heater. *Int. J. Adv. Manuf. Technol, 1*, 3-7.

Nawayseh, N. K., Farid, M. M., Omar, A. A., & Sabirin, A. (1999). Solar desalination based on humidification process—II. Computer simulation. *Energy Conversion and Management, 40*(13), 1441-1461.

Nguyen, C. T., Desgranges, F., Roy, G., Galanis, N., Maré, T., Boucher, S., & Angue Mintsa, H. (2007). Temperature and particle-size dependent viscosity data for water-based nanofluids – hysteresis phenomenon. *International Journal of Heat and Fluid Flow, 28*(6), 1492-1506.

Noghrehabadi, A. R., Hajidavaloo, E., & Moravej, M. (2016). Experimental investigation of efficiency of square flat-plate solar collector using SiO2/Water nanofluid. *Case Studies in Thermal Engineering*.

Okujagu, C. U., & Adjepong, S. K. (1989). Performance of a simple flat plate solar collector at an equatorial location. *Solar & Wind Technology, 6*(3), 283-289.

Oliva, A., Maldonado, R., Díaz, E., & Montalvo, A. (2013). *A high absorbance material for solar collectors' applications.* Paper presented at the IOP Conference Series: Materials Science and Engineering.

Ong, K. S. (1974). A finite-difference method to evaluate the thermal performance of a solar water heater. *Solar Energy, 16*, 137-147.

Ong, K. S. (1976). An improved computer program for the thermal performance of a solar water heater. *Solar Energy, 18*, 183-191.

Ortiz-Young, D., Chiu, H. C., Kim, S., Voitchovsky, K., & Riedo, E. (2013). The interplay between apparent viscosity and wettability in nanoconfined water. *Nat Commun, 4*, 2482.

Otanicar, T. P. (2009). *Direct absorption solar thermal collectors utilizing liquid-nanoparticle suspensions.* (Doctoral dissertation), Arizona State University, Arizona. Retrieved from ProQuest Dissertations & Theses database. (UMI No. 3353694)

Otanicar, T. P., Phelan, P. E., Prasher, R. S., Rosengarten, G., & Taylor, R. A. (2010). Nanofluid-based direct absorption solar collector. *JOURNAL OF RENEWABLE AND SUSTAINABLE ENERGY, 2*(3), 033102.

Özerinç, S., Kakaç, S., & Yazıcıoğlu, A. G. (2009). Enhanced thermal conductivity of nanofluids: a state-of-the-art review. *Microfluidics and Nanofluidics, 8*(2), 145-170.

Pak, B. C., & Cho, Y. I. (1998). Hydrodynamic and heat transfer study of dispersed fluids with submicron metallic oxide particles. *Experimental Heat Transfer an International Journal, 11*(2), 151-170.

Pantzali, M. N., Mouza, A. A., & Paras, S. V. (2009a). Investigating the efficacy of nanofluids as coolants in plate heat exchangers (PHE). *Chemical Engineering Science, 64*(14), 3290-3300.

Polvongsri, S., & Kiatsiriroat, T. (2011). *Enhancement of flat-plate solar collector thermal performancewith silver nano-fluid*. Paper presented at the The Second TSME International Conference on Mechanical Engineering, Krabi, Thailand.

Prasher, R., Song, D., Wang, J., & Phelan, P. (2006). Measurements of nanofluid viscosity and its implications for thermal applications. *Applied Physics Letters, 89*(13), 133108.

Price, B. K., & Tour, J. M. (2006). Functionalization of single-walled carbon nanotubes “on water”. *Journal of the American Chemical Society, 128*(39), 12899-12904.

Rastogi, R., Kaushal, R., Tripathi, S. K., Sharma, A. L., Kaur, I., & Bharadwaj, L. M. (2008). Comparative study of carbon nanotube dispersion using surfactants. *Journal of Colloid and Interface Science, 328*(2), 421-428.

Razi, P., Akhavan-Behabadi, M. A., & Saeedinia, M. (2011). Pressure drop and thermal characteristics of CuO–base oil nanofluid laminar flow in flattened tubes under constant heat flux. *International Communications in Heat and Mass Transfer, 38*(7), 964-971.

Rosengarten, G., Cooper-White, J., & Metcalfe, G. (2006). Experimental and analytical study of the effect of contact angle on liquid convective heat transfer in microchannels. *International Journal of Heat and Mass Transfer, 49*(21-22), 4161-4170.

Saeedinia, M., Akhavan-Behabadi, M. A., & Razi, P. (2012b). Thermal and rheological characteristics of CuO–Base oil nanofluid flow inside a circular tube. *International Communications in Heat and Mass Transfer, 39*(1), 152-159.

Said, Z., Sabiha, M. A., Saidur, R., Hepbasli, A., Rahim, N. A., Mekhilef, S., & Ward, T. A. (2015a). Performance enhancement of a Flat Plate Solar collector using Titanium dioxide nanofluid and Polyethylene Glycol dispersant. *Journal of Cleaner Production, 92*, 343-353.

Said, Z., Saidur, R., & Rahim, N. A. (2016). Energy and exergy analysis of a flat plate solar collector using different sizes of aluminium oxide based nanofluid. *Journal of Cleaner Production, 133*, 518-530.

Said, Z., Saidur, R., Sabiha, M. A., Rahim, N. A., & Anisur, M. R. (2015b). Thermophysical properties of Single Wall Carbon Nanotubes and its effect on exergy efficiency of a flat plate solar collector. *Solar Energy, 115*, 757-769.

Said, Z., Sajid, M. H., Alim, M. A., Saidur, R., & Rahim, N. A. (2013a). Experimental investigation of the thermophysical properties of AL_2O_3-nanofluid and its effect on a flat plate solar collector. *International Communications in Heat and Mass Transfer, 48*, 99-107.

Saidur, R., Leong, K. Y., & Mohammad, H. A. (2011). A review on applications and challenges of nanofluids. *Renewable and Sustainable Energy Reviews, 15*(3), 1646-1668.

Sanchez, C., Renard, D., Robert, P., Schmitt, C., & Lefebvre, J. (2002). Structure and rheological properties of acacia gum dispersions. *Food hydrocolloids, 16*(3), 257-267.

Sani, E., Barison, S., Pagura, C., Mercatelli, L., Sansoni, P., Fontani, D., . . . Francini, F. (2010). Carbon nanohorns-based nanofluids as direct sunlight absorbers. *OPTICS EXPRESS 5179, 18*(5).

Schmidt, E. (1981). *Properties of water and steam in SI-units* (U. Grigull Ed.): Springer.

Schwarz, J. A., Contescu, C. I., & Putyera, K. (2004). *Dekker encyclopedia of nanoscience and nanotechnology* (Vol. 3): CRC press.

Sekhar, Y. R., Sharma, K. V., & Rao, M. B. (2009). Evaluation of heat loss coefficients in solar flat plate collectors. *ARPN Journal of Engineering and Applied Sciences, 4*(5).

Sen Gupta, S., Manoj Siva, V., Krishnan, S., Sreeprasad, T., Singh, P. K., Pradeep, T., & Das, S. K. (2011). Thermal conductivity enhancement of nanofluids containing graphene nanosheets. *Journal of Applied Physics, 110*(8), 084302.

Shah, R. K. (1975). *Thermal entry length solutions for the circular tube and parallel plates.* Paper presented at the Proceedings of 3rd National Heat and Mass Transfer Conference, Bombay, India.

Skeiker, K. (2009). Optimum tilt angle and orientation for solar collectors in Syria. *Energy Conversion and Management, 50*(9), 2439-2448.

Smith, E., & Dent, G. (2013). *Modern Raman spectroscopy: a practical approach*: John Wiley & Sons.

Sohn, C. W., & Chen, M. M. (1981). Microconvective Thermal Conductivity in Disperse Two-Phase Mixtures as Observed in a Low Velocity Couette Flow Experiment. *Journal of Heat Transfer, 103*(1), 47-51.

Solangi, K. H., Kazi, S. N., Luhur, M. R., Badarudin, A., Amiri, A., Sadri, R., . . . Teng, K. H. (2015). A comprehensive review of thermo-physical properties and convective heat transfer to nanofluids. *Energy*.

Sundar, L. S., Singh, M. K., & Sousa, A. C. M. (2014). Enhanced heat transfer and friction factor of MWCNT–Fe_3O_4/water hybrid nanofluids. *International Communications in Heat and Mass Transfer, 52*, 73-83.

Taylor, R. (2011). *Thermal energy conversion in nanofluids.* (Doctoral dissertation), Arizona State University, Arizona. Retrieved from ProQuest Dissertations & Theses database. (UMI No. 3465706)

Taylor, R. A., Phelan, P. E., Otanicar, T. P., Adrian, R., & Prasher, R. (2011b). Nanofluid optical property characterization- towards efficient direct absorption solar collectors. *Nanoscale Research Letters, 6*(225).

Teng, C.-C., Ma, C.-C. M., Lu, C.-H., Yang, S.-Y., Lee, S.-H., Hsiao, M.-C., . . . Lee, T.-M. (2011). Thermal conductivity and structure of non-covalent functionalized graphene/epoxy composites. *Carbon, 49*(15), 5107-5116.

Teng, T.-P., & Hung, Y.-H. (2014). Estimation and experimental study of the density and specific heat for alumina nanofluid. *Journal of Experimental Nanoscience, 9*(7), 707-718.

Thermo, N. (2001). Introduction to fourier transform infrared spectrometry. *Thermo Nicolet Corporation: Madison-USA.*

Thirugnanasambandam, M., Iniyan, S., & Goic, R. (2010). A review of solar thermal technologies. *Renewable and Sustainable Energy Reviews, 14*(1), 312-322.

Timofeeva, E. V. (2011). Nanofluids for heat transfer – potential and engineering strategies. In D. A. Ahsan (Ed.), Two Phase Flow, Phase Change and Numerical Modeling (pp. 435-450). Retrieved from www.intechopen.com.

Timofeeva, E. V., Gavrilov, A. N., McCloskey, J. M., Tolmachev, Y. V., Sprunt, S., Lopatina, L. M., & Selinger, J. V. (2007). Thermal conductivity and particle agglomeration in alumina nanofluids: Experiment and theory. *Physical Review E, 76*(6), 061203.

Ting, K.-C. (1980). *Simulation and sizing of flat plate solar collectors for grain drying.* (Doctoral dissertation), University of Illinois at Urbana-Champaign, Urbana, Illinois.

Tiwari, A. K., Ghosh, P., & Sarkar, J. (2013). Solar water heating using nanofluids - a comprehensive overview and environmental impact analysis. *International Journal of Emerging Technology and Advanced Engineering, 3*(3), 221-224.

Tora, E. A.-H., & Moustafa, T. (2013). Numerical simulation of an Al_2O_3-H_2O nanofluid as a heat transfer agent for a flat-plate solar collector. *International Journal of Scientific & Engineering Research, 4*(5).

Vajjha, R. S., & Das, D. K. (2009a). Specific heat measurement of three nanofluids and development of new correlations. *Journal of Heat Transfer, 131*(7), 071601.

Vajjha, R. S., & Das, D. K. (2009b). Experimental determination of thermal conductivity of three nanofluids and development of new correlations. *International Journal of Heat and Mass Transfer, 52*(21-22), 4675-4682.

Vajjha, R. S., Das, D. K., & Mahagaonkar, B. M. (2009). Density measurement of different nanofluids and their comparison with theory. *Petroleum Science and Technology, 27*(6), 612-624.

Vakili, M., Hosseinalipour, S. M., Delfani, S., Khosrojerdi, S., & Karami, M. (2016). Experimental investigation of graphene nanoplatelets nanofluid-based volumetric solar collector for domestic hot water systems. *Solar Energy, 131*, 119-130.

Vandsburger, L. (2010). *Synthesis and covalent surface modification of carbon nanotubes for preparation of stabilized nanofluid suspensions.* (Master's thesis), McGill University, Montreal, Quebec, Canada.

Verma, S. K., Tiwari, A. K., & Chauhan, D. S. (2016). Performance augmentation in flat plate solar collector using MgO/water nanofluid. *Energy Conversion and Management, 124*, 607-617.

Verma, S. K., Tiwari, A. K., & Chauhan, D. S. (2017). Experimental evaluation of flat plate solar collector using nanofluids. *Energy Conversion and Management, 134*, 103-115.

Verma, V., & Kundan, L. (2013). Thermal performance evaluation of a direct absorption flat plate solar collector (DASC) using Al_2O_3-H_2O based nanofluids. *Journal of Mechanical and Civil Engineering (IOSR-JMCE), 6*(2), 29-35.

Vijayakumaar, S. C., Shankar, R. L., & Babu, K. (2013, 24 - 26 July, 2013). *Effect of CNT-H_2O nanofluid on the performance of solar flat plate collector-an experimental investigation.* Paper presented at the International Conference on Advanced Nanomaterials & Emerging Engineering Technologies, New Delhi, India.

Wang, X.-j., Zhu, D.-s., & yang, S. (2009). Investigation of ph and SDBS on enhancement of thermal conductivity in nanofluids. *Chemical Physics Letters, 470*(1-3), 107-111.

Wang, X.-Q., & Mujumdar, A. S. (2007). Heat transfer characteristics of nanofluids: A review. *International Journal of Thermal Sciences, 46*(1), 1-19.

Wang, X.-Q., & Mujumdar, A. S. (2008a). A review on nanofluids - part I: Theoretical and numerical investigations. *Brazilian Journal of Chemical Engineering, 25*(4), 613 - 630.

Wang, X.-Q., & Mujumdar, A. S. (2008b). A review on nanofluids - part II: Experiments and applications. *Brazilian Journal of Chemical Engineering, 25*(4), 631 - 648.

Warzoha, R. J., & Fleischer, A. S. (2014). Effect of Graphene Layer Thickness and Mechanical Compliance on Interfacial Heat Flow and Thermal Conduction in Solid–Liquid Phase Change Materials. *ACS Appl Mater Interfaces, 6*(15), 12868-12876.

Wei, D., Li, H., Han, D., Zhang, Q., Niu, L., Yang, H., . . . Ryhanen, T. (2011). Properties of graphene inks stabilized by different functional groups. *Nanotechnology, 22*(24), 245702.

Wen, D., & Ding, Y. (2004). Experimental investigation into convective heat transfer of nanofluids at the entrance region under laminar flow conditions. *International Journal of Heat and Mass Transfer, 47*(24), 5181-5188.

Wen, D., Lin, G., Vafaei, S., & Zhang, K. (2009). Review of nanofluids for heat transfer applications. *Particuology, 7*(2), 141-150.

Wong, K. V., & De Leon, O. (2010). Applications of nanofluids: Current and future. *Advances in Mechanical Engineering, 2010*, 1-11.

Xiaowu, W., & Ben, H. (2005). Exergy analysis of domestic-scale solar water heaters. *Renewable and Sustainable Energy Reviews, 9*(6), 638-645.

Xu, Y., Wang, X., Tian, R., Li, S., Wan, L., Li, M., . . . Wang, S. (2008). Microwave-induced electrophilic addition of single-walled carbon nanotubes with alkylhalides. *Applied Surface Science, 254*(8), 2431-2435.

Xuan, Y., & Li, Q. (2000). Heat transfer enhancement of nanofluids. *International Journal of Heat and Fluid Flow, 21*(1), 58-64.

Xuan, Y., & Li, Q. (2003). Investigation on convective heat transfer and flow features of nanofluids. *Journal of Heat Transfer, 125*(1), 151.

Xuan, Y., & Roetzel, W. (2000). Conceptions for heat transfer correlation of nanofluids. *International Journal of Heat and Mass Transfer, 43*(19), 3701-3707.

Yarmand, H., Gharehkhani, S., Shirazi, S. F. S., Amiri, A., Alehashem, M. S., Dahari, M., & Kazi, S. N. (2016b). Experimental investigation of thermo-physical properties, convective heat transfer and pressure drop of functionalized graphene nanoplatelets aqueous nanofluid in a square heated pipe. *Energy Conversion and Management, 114*, 38-49.

Yousefi, T., Shojaeizadeh, E., Veysi, F., & Zinadini, S. (2012c). An experimental investigation on the effect of ph variation of MWCNT–H_2O nanofluid on the efficiency of a flat-plate solar collector. *Solar Energy, 86*(2), 771-779.

Yousefi, T., Veisy, F., Shojaeizadeh, E., & Zinadini, S. (2012a). An experimental investigation on the effect of MWCNT-H_2O nanofluid on the efficiency of flat-plate solar collectors. *Experimental Thermal and Fluid Science, 39*, 207-212.

Yousefi, T., Veysi, F., Shojaeizadeh, E., & Zinadini, S. (2012b). An experimental investigation on the effect of Al_2O_3–H_2O nanofluid on the efficiency of flat-plate solar collectors. *Renewable Energy, 39*(1), 293-298.

Yu, W., France, D. M., Routbort, J. L., & Choi, S. U. S. (2008). Review and comparison of nanofluid thermal conductivity and heat transfer enhancements. *Heat Transfer Engineering, 29*(5), 432-460.

Yu, W., & Xie, H. (2012). A review on nanofluids: Preparation, stability mechanisms, and applications. *Journal of Nanomaterials, 2012*, 1-17.

Yu, W., Xie, H., & Bao, D. (2010). Enhanced thermal conductivities of nanofluids containing graphene oxide nanosheets. *Nanotechnology, 21*(5), 055705.

Yu, W., Xie, H., & Chen, L. (2012). Nanofluids. In Dr Abbass Hashim (Ed.), Smart Nanoparticles Technology (pp. 497-518).

Yu, W., Xie, H., Chen, L., & Li, Y. (2009). Investigation of thermal conductivity and viscosity of ethylene glycol based ZnO nanofluid. *Thermochimica Acta, 491*(1-2), 92-96.

Yu, W., Xie, H., Li, Y., & Chen, L. (2011). Experimental investigation on thermal conductivity and viscosity of aluminum nitride nanofluid. *Particuology, 9*(2), 187-191.

Zardini, H. Z., Amiri, A., Shanbedi, M., Maghrebi, M., & Baniadam, M. (2012). Enhanced antibacterial activity of amino acids-functionalized multi walled carbon nanotubes by a simple method. *Colloids Surf B Biointerfaces, 92*, 196-202.

Zhang, Q., Li, W., Kong, T., Su, R., Li, N., Song, Q., . . . Cheng, G. (2013). Tailoring the interlayer interaction between doxorubicin-loaded graphene oxide nanosheets by controlling the drug content. *Carbon, 51*, 164-172.

Zhang, Z., & Lockwood, F. E. (2004). *Preparation of stable nanotube dispersions in liquids.* Washington, DC Patent No. (US 6,783,746). U.S. Patent and Trademark Office.

Zhou, S.-Q., & Ni, R. (2008). Measurement of the specific heat capacity of water-based Al 2 O 3 nanofluid. *Applied Physics Letters, 92*(9), 093123.

Zhu, D., Li, X., Wang, N., Wang, X., Gao, J., & Li, H. (2009). Dispersion behavior and thermal conductivity characteristics of Al_2O_3–H_2O nanofluids. *Current Applied Physics, 9*(1), 131-139.

Zhu, H., Zhang, C., Tang, Y., Wang, J., Ren, B., & Yin, Y. (2007). Preparation and thermal conductivity of suspensions of graphite nanoparticles. *Carbon, 45*(1), 226-228.

Zubir, M. N. M., Muhamad, M. R., Amiri, A., Badarudin, A., Kazi, S. N., Oon, C. S., . . . Yarmand, H. (2016). Heat transfer performance of closed conduit turbulent flow: Constant mean velocity and temperature do matter! *Journal of the Taiwan Institute of Chemical Engineers*.

LIST OF PUBLICATIONS AND PAPERS PRESENTED

Journal articles published (ISI)

1. Sarsam, W. S., Kazi, S. N., & Badarudin, A. (2015). A review of studies on using nanofluids in flat-plate solar collectors. *Solar Energy*, 122, 1245-1265.

2. Sarsam, W. S., Amiri, A., Kazi, S. N., & Badarudin, A. (2016). Stability and thermophysical properties of non-covalently functionalized graphene nanoplatelets nanofluids. *Energy Conversion and Management*, 116, 101-111.

3. Sarsam, W. S., Amiri, A., Zubir, M. N. M., Yarmand, H., Kazi, S. N., & Badarudin, A. (2016). Stability and thermophysical properties of water-based nanofluids containing triethanolamine-treated graphene nanoplatelets with different specific surface areas. *Colloids and Surfaces A: Physicochemical and Engineering Aspects*, 500, 17-31.

Journal articles accepted for publication

1. Sarsam, W. S., Amiri, A., Shanbedi, M., Kazi, S. N., Badarudin, A., Yarmand, H., & Zaharinie, T. (2017). Synthesis, stability, and thermophysical properties of aqueous colloidal dispersions of multi-walled carbon nanotubes treated with beta-alanine. Accepted for publication in the journal of *International Communications in Heat and Mass Transfer.*

APPENDIX A

Numerical constants for the correlations of thermophysical properties of water

Table A.1: Values of numerical constants for equation (3.49) (Arnold, 1970).

$k_1 = -7.691234564 \times 10^o$ $k_2 = -2.608023696 \times 10^1$ $k_3 = -1.681706546 \times 10^2$
$k_4 = 6.423285504 \times 10^1$ $k_5 = -1.189646225 \times 10^2$ $k_6 = 4.167117320 \times 10^0$
$k_7 = 2.097506760 \times 10^1$ $k_8 = 10^9$ $k_9 = 6$

Table A.2: Values of numerical constants for equations (3.50) to (3.55) (Arnold, 1970).

$A_0 = 6.824687741 \times 10^3$ $A_1 = -5.422063673 \times 10^2$ $A_2 = -2.096666205 \times 10^4$
$A_3 = 3.941286787 \times 10^4$ $A_4 = -6.733277739 \times 10^4$ $A_5 = 9.902381028 \times 10^4$
$A_6 = -1.093911774 \times 10^5$ $A_7 = 8.590841667 \times 10^4$ $A_8 = -4.511168742 \times 10^4$
$A_9 = 1.418138926 \times 10^4$ $A_{10} = -2.01727113 \times 10^3$ $A_{11} = 7.982692717 \times 10$
$A_{12} = -2.616571843 \times 10^{-2}$ $A_{13} = 1.52241179 \times 10^{-3}$ $A_{14} = 2.2842279054 \times 10^{-2}$
$\mathrm{A}_{15} = 2.421647003 \times 10^2$ $\mathrm{A}_{16} = 1.269716088 \times 10^{-10}$ $\mathrm{A}_{17} = 2.074838328 \times 10^{-7}$
$\mathrm{A}_{18} = 2.17402035 \times 10^{-8}$ $\mathrm{A}_{19} = 1.105710498 \times 10^{-9}$ $A_{20} = 1.293441934 \times 10$
$A_{21} = 1.308119072 \times 10^{-5}$ $A_{22} = 6.047626338 \times 10^{-14}$ $a_1 = 8.438375405 \times 10^{-1}$
$a_2 = 5.362162162 \times 10^{-4}$ $a_3 = 1.72 \times 10$ $a_4 = 7.342278489 \times 10^{-2}$
$a_5 = 4.97585887 \times 10^{-2}$ $a_6 = 6.5371543 \times 10$ $a_7 = 1.15 \times 10^{-6}$
$a_8 = 1.5108 \times 10^{-5}$ $a_9 = 1.4188 \times 10^{-1}$ $a_{10} = 7.002753165 \times 10$
$a_{11} = 2.995284926 \times 10^{-4}$ $a_{12} = 2.04 \times 10^{-1}$

Table A.3: Values of numerical constants for equations (3.56) and (3.57) (Schmidt, 1981).

$AA_0 = 0.0181583,\quad AA_1 = 0.0177624,\quad AA_2 = 0.0105287,\quad AA_3 = -0.0036744$

	$BB_{i,j}$				
	$j = 0$	1	2	3	4
$i = 0$	0.501938	0.235622	-0.274637	0.145831	-0.0270448
1	0.162888	0.789393	-0.743539	0.263129	-0.0253093
2	-0.130356	0.673665	-0.959456	0.347247	-0.0267758
3	0.907919	1.207552	-0.687343	0.213486	-0.0822904
4	-0.551119	0.0670665	-0.497089	0.100754	0.0602253
5	0.146543	-0.084337	0.195286	-0.032932	-0.0202595

Table A.4: Values of numerical constants for equation (3.58) (Arnold, 1970).

$a_{\mathrm{o}} = -922.47$ $a_1 = 2839.5$ $a_2 = -1800.7$ $a_3 = 525.77$

$a_4 = -73.44$ $b_{\mathrm{o}} = -0.9473$ $b_1 = 2.5186$ $b_2 = -2.0012$

$b_3 = 0.5186$ $c_{\mathrm{o}} = 1.6563 \times 10^{-3}$ $c_1 = -3.8929 \times 10^{-3}$ $c_2 = 2.9323 \times 10^{-3}$

$c_3 = -7.1693 \times 10^{-4}$ $T_{\mathrm{o}} = 273.15\ °K$